UNIVERSITY OF SOUTHAMPTON

FACULTY OF ENGINEERING AND THE ENVIRONMENT

Aerodynamics and Flight Mechanics

Aerodynamics of surface-mounted ribs.

by

Jacques Van der Kindere

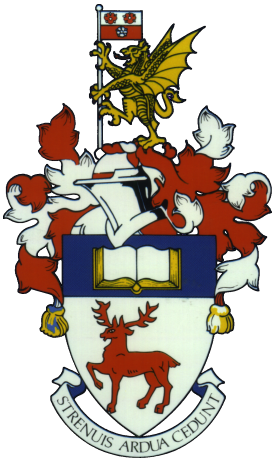

Thesis for the degree of Doctor of Philosophy

July 2017

UNIVERSITY OF SOUTHAMPTON

ABSTRACT

FACULTY OF ENGINEERING AND THE ENVIRONMENT
Aerodynamics and Flight Mechanics

Doctor of Philosophy

AERODYNAMICS OF SURFACE-MOUNTED RIBS.

by Jacques Van der Kindere

The flow over ribs consists of a forward-facing step followed by a backward-facing step. The interaction between the aerodynamics of these two canonical obstacles leads to complex patterns in an oscillating flow which depend on rib length. In order to study the aerodynamics of ribs, four steps were taken which involve multiple forms of velocity and pressure measurements. To begin, a method to estimate pressure fields from particle image velocimetry is applied and validated against pressure measurements. This provides pressure information necessary for the rest of the study. Second, the characteristics of the flow over ribs of varying length are studied in a statistical sense. Trends identified in previous work were found and extended to new quantities. The effect of free-stream turbulence on the characteristics of the flow is studied. It highlights the sensitivity of separation over short obstacles to free-stream turbulence in contrast with the unchanging separation over longer obstacles. Finally, the relationship between pressure and velocity is described using modelling of velocity components from surface pressure information. It shows that individual patterns in velocity fluctuations such as vortex shedding and shear layer flapping are closely linked to surface pressure fluctuations.

Contents

List of Figures

List of Tables

Declaration of Authorship

I, Jacques Van der Kindere , declare that the thesis entitled *Aerodynamics of surface-mounted ribs.* and the work presented in the thesis are both my own, and have been generated by me as the result of my own original research. I confirm that:

- this work was done wholly or mainly while in candidature for a research degree at this University;
- where any part of this thesis has previously been submitted for a degree or any other qualification at this University or any other institution, this has been clearly stated;
- where I have consulted the published work of others, this is always clearly attributed;
- where I have quoted from the work of others, the source is always given. With the exception of such quotations, this thesis is entirely my own work;
- I have acknowledged all main sources of help;
- where the thesis is based on work done by myself jointly with others, I have made clear exactly what was done by others and what I have contributed myself;
- none of this work has been published before submission

Signed:.....

Date:.....

Acknowledgements

First I would like to thank the people who followed me and helped me complete the work over more than three years. Bharath for his patience and guidance along the way, Roeland for his precise advice, Grégoire for helping me in the lab during the early stages, Jason for his "science", Davide for believing in my work and offering me a chance to finish on a high note.

I would also like to thank my colleagues and friends from campus and elsewhere. Angeliki who started on the same day as me and finished a week before me. Many long evenings were spent discussing and complaining with the "sailor" rather than working, but it was worth it. Javier and Jake for starting the bicycle craze and for the hours spent in the rain telling each other we're nearly home. Clemens and Vika for unforgettable moments. My housemate Mark for listening at home and taking care of the house while I was busy working. All of my office-mates and friends for the chats, the BBQs, and the drinks. The Awesome PGRs cycle club for the healthy and much needed dose of sports to balance all the drinking. All of my old and new friends in the U.K. and abroad for distracting me, joining me on vacation, taking care of me and staying in touch over the last years.

Finally I would also like to thank my parents, my three sisters and their partners and the rest of my family for the support and faith in me.

And now, as someone would say: "it's time to get serious!"

Nomenclature

Chapter 2

H	rib height
L	rib length
x	horizontal axis, parallel to the free-stream
y	vertical axis
$\delta_9 9$	boundary layer thickness (99% of U_e)
U_e	freestream velocity
W	rib width
ID	inner diameter
OD	outer diameter
PIV	Particle Image Velocimetry
FF	forward-facing
BF	backward-facing
dT	time interval between two laser pulses
f	focal length
f.p.s.	frames per second
CTA	Constant Temperature Anemometer
$T.E.$	trailing edge
$L.E.$	leading edge
L_R	recirculation length

Chapter 3

PTV	particle tracking velocimetry
3C	three-component
2D	two-dimensional
3D	three-dimensional
TH	Taylor's hypothesis
Eu	Eulerian
pLA	pseudo-Lagrangian
RANS	Reynolds-Average Navier-Stokes
p	pressure
ρ	density
u	velocity

ν	kinematic viscosity
NSE	Navier-Stokes equation
$\bar{u}$	average velocity
u'	velocity fluctuation
U_c	convection velocity
LIC	Line-Integral-Convolution
TR-PIV	time-resolved PIV
R_{xy}	correlation coefficient between x and y
VIC	vortex-in-cell
C_p	coefficient of pressure
U_∞	freestream velocity
$T.K.E$	turbulent kinetic energy
p_{rms}	root-mean-square of pressure
Chapter 4	
BFS	backward-facing step
FFS	forward-facing step
x_R	mean reattachment location
p'	standard deviation of pressure
p	pressure fluctuation
A_R	recirculation area in the plane of measurement
H_R	recirculation height in the plane of measurement
$P.D.F.$	probability density function
a	slope of the linear relationship between bubble height and area
ϕ_i	pre-multiplied frequency spectrum of quantity i
St	Strouhal number defined as fH/U_e
POD	Proper orthogonal decomposition
L_{UU}	integral length scale of the streamwise velocity component
Chapter 5	
FST	freestream turbulence
u'	standard deviation of the streamwise velocity component
u'_H	standard deviation of streamwise velocity component at rib height
τ_H	non-dimensional shear coefficient at rib height
L_x	horizontal integral length scale
xy	Reynolds stress term with quantity x and y
Chapter 6	
$t*$	non-dimensional time
u	streamwise velocity component
v	vertical velocity component
ω	vorticity
θ	phase angle in a periodic cycle
λ_i	energy proportion (out of 1) associated with POD mode

Chapter 7

p_k	Instantaneous pressure fluctuation from transducer k
u	Instantaneous velocity fluctuation
ΔT	$1/f_s$
R_{xy}	Correlation coefficient of x and y
R^*_{xy}	$\max(R_{xy})$
τ^*_{xy}	time-delay to obtain R^*_{xy}
N	number of samples
n	subset of POD modes up to mode n
$a_i(t)$	POD mode i coefficient a time t
$\hat{a}_i(t)$	POD mode i coefficient a time t estimated through LSE
w^k_j	the coefficient associated with each transducer k at time delay j from matrix W
ϕ^u_i	POD mode shape i of u
$\hat{u}(t,n)$	estimated velocity from POD reconstruction with n modes at time t
$u^n(t)$	Reduced-order velocity reconstructed with n POD modes
n_p	number of past time delays used in the estimator
n_f	number of future time delays used in the estimator

Chapter 1

Introduction

1.1 Topic of research

The wake behind blunt obstacles is turbulent and often presents multi-scale periodic fluctuations as well as recirculation regions. Historically turbulent separated flows have remained a small portion of interest in aerodynamic studies Sychev et al. (1998). The main cases studied were: forward-facing step, backward-facing step, fence/spoiler, parallelepipedic obstacles free hanging or surface-mounted, and cylinder. These types of obstacles have received little coverage due to the complexity of the flow requiring versatile instrumentation which posed difficulties for experimental studies. As a result of the limited understanding of flow separation, the general consensus was that flow separation should be avoided in most aerodynamic applications, as it was synonymous with drag, loss of efficiency, noise and vibration. However, as computational power increased, and more complex instrumentation became available, this type of flow is becoming more and more relevant (Sychev et al., 1998).

https://s-media-cache-ak0.pinimg.com/564x/5c/53/84/5c53848d67c37b2c0b5fc6a99349c733.jpg

https://www.tesla.com/en_GB/gigafactory

Figure 1.1: Example of two very different surface mounted obstacles. Key comfort elements such as heating, drafts or noise/vibration are dictated by wind which behaves differently on low and tall buildings.

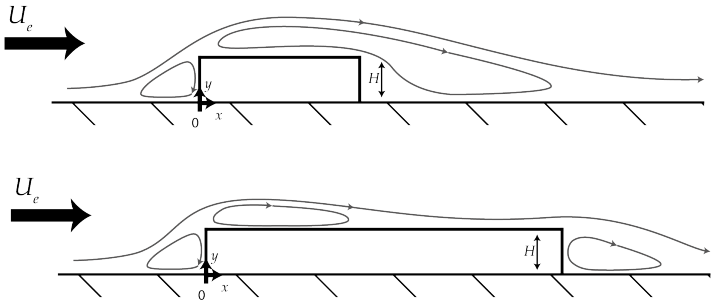

Figure 1.2: Elongated rib studied in this project. Image inspired by Antoniou and Bergeles (1988). Top: a short rib with two recirculation regions. Bottom: a long rib with three regions in total.

Although this PhD project is not targeted to a specific application but physical phenomena behind flow separation, a few examples of potential applications might help place this research in its context. Studying flow separation on a rib simplifies how air behaves near a building for instance (see figure 1.1), providing data for potential sources of noise, vibration, other phenomena detrimental to comfort or safety. Recent studies also reveal how it is possible to harness the properties of separated flows to achieve certain goals. For instance, Sherry et al. (2010) provide guidelines to position a wind-mill farm on top of hills to maximise their energy output based on the flow over a forward-facing step. In the chemical and pharmaceutical industry, it is possible to tune flow mixing devices to maximize separation and thus mixing at a minimal pressure or energy cost by carefully designing the shape of the obstacles creating the separated flow regions. Finally, flow separation still remains a challenge in accessible forms of computational fluid dynamics used by the aeronautical industry. Perhaps more detailed information about separated flows experimentally can be used to improve computer models.

We describe ribs as two-dimensional obstacles characterized by a finite height (H) and length (L) in the stream-wise direction, but an infinite length in the span-wise direction. As illustrated in Figure 1.2, a rib consists of a forward-facing step (FFS) followed by a backward-facing step (BFS). When studied independently, a forward-facing step or a backward-facing step produces unsteady flow features such as rolled-up vortices, large-scale vortical structures and flapping separation bubble (Liu et al., 2008) which also exist in the flow over ribs.

Varying L/H of a rib produces two distinct scenarios. On the one hand, a fence appears for the smallest length. On the other hand, two separate classical canonical problems (BFS and FFS) occur if the rib's stream-wise length is increased. Consequently, two or three regions of separated flow are produced depending on the length to height ratio (L/H) of the obstacle:

- the first one in the corner formed by the FFS vertical face and the floor
- the second one on top of the obstacle starting at the upstream/leading edge which extends past the trailing edge of short ribs, but is closed on the top surface of long ribs
- the third one separating at the trailing edge of long ribs and reattaching on the surface downstream.

1.2 Previous work on rib geometries

The following section describes the current state-of-the-art regarding flow separation occurring over these obstacles, additionally, FF and BF steps are covered to define the flow features of both types of obstacles which may be present on ribs, and how they may be modulated by properties of the rib and the incoming flow.

The flow over a rectangular rib is a composite of the flows occurring above a FF step, and a BF step. As mentioned above, two scenarios occur in the flow past an elongated rib. Bergeles and Athanassiadis (1983) isolate them through experiments with varying stream-wise lengths of the obstacle (L) for a fixed height (H). The first scenario arises for short ribs ($L/H < 4$). The bubble created on the top surface of a FF step merges with that of the BF step thus creating one long bubble from the leading edge to the surface downstream. The second scenario occurs for long ribs ($L/H \geq 4$), the mean velocity of the flow around such obstacle presents all the features of both the BF and FF steps. The total number of recirculation bubbles is preserved, and their effect on boundary layer velocity profile is consistent with that of independent obstacles although with some discrepancies. The threshold L/H between the two cases is said to b 4 as shown by the experiments of Bergeles and Athanassiadis (1983) as well as by Moss and Baker (1980) and Antoniou and Bergeles (1988) but is subject to incoming flow conditions such as boundary layer thickness, and turbulence.

The type of rib, short or long as defined above, has implications on the dimensions of the recirculation regions produced. In their study Bergeles and Athanassiadis (1983) study the length of recirculation regions around a rectangular rib of fixed height with varying length: $1 < L/H < 10$. It extends from wall to wall inside the wind-tunnel's test section thus forming a nominally 2D obstacle. The regime of the experiment is such that the obstacle protrudes from the boundary layer, at moderate Reynolds number ($\delta/H = 0.48$, and Reynolds number based on the obstacle's height is $Re_H = 26000$). The results suggest that for obstacle lengths between 1 and 4 the recirculation length of the region in the wake of obstacles decreases linearly from 11.5 to $2.8H$. For obstacles longer than $L/H = 4$, the recirculation length seems to stabilize at around $3H$. Recirculation length is defined as the distance from the separation edge of the obstacle to the reattachment

point on the surface downstream. The transition between both trends coincides with the apparition of reattachment on the top surface of sufficiently long ribs. According to the authors, the boundary layer velocity profile created at the trailing edge of long ribs in their case would have generated a separation bubble of $6H$ in length in the wake. However, it is measured to be only $3H$. This discrepancy is attributed to increased turbulent mixing in the wake bubble. On the other hand, the separated flow region on the top surface appears to be of same length as the one on top of a forward-facing step in similar flow conditions.

The dis/similarity between isolated obstacles and FF and BF sections of ribs is also found in the mean pressure distribution obtained by Leclercq et al. (2001). This study describes an experiment on a fixed elongated rib of $L/H = 10$. Mean pressure measurements show an increase upstream of the FF face, then a sharp decrease at the corner, to reach a measured minimum peak of $C_P = -0.5$. Mean pressure distribution flattens after the reattachment point on the top surface, before returning towards 0 again through the BF section. The authors note that the behaviour of the FF section is identical to an isolated FF step. This was also observed in previous studies, however blockage effects were a concern. The authors used acoustically transparent walls which release any pressure gradient and reinforce this claim. The BF section being affected by the FF section, it does not feature common properties found on isolated BF steps.

The existence of two distinct behaviours on ribs also has strong implications on the unsteadiness of the flow in the wake. Antoniou and Bergeles (1988) describe the flow over a similar arrangement as Bergeles and Athanassiadis (1983). However, they tackle the unsteady flow properties of such a configuration. The Reynolds number based on obstacle height was $Re_H = 20000$. The boundary layer to obstacle height ratio (δ/H) was 0.7. The incoming boundary layer was fully turbulent at the obstacle. Flow speed measurements were obtained using a filtered single hot-wire probe at five stations downstream of flow reattachment (between $x/h = 5$ and $x/h = 25$, and $0 < y/h < 7$) for all obstacle lengths. For reference, the results describe similar mean recirculation lengths to those of Bergeles and Athanassiadis (1983). Regarding averaged velocity profiles in the wake, both long and short ribs produce similar profiles near the wall far downstream. Indeed, Antoniou and Bergeles (1988) quote that up to $y/H = 1$ at $x/H = 25$ flow properties of a flat plate would be recovered over a shorter distance than in the outer portion. However, studying the measurements at $x/H = 5$, it appears that, in long ribs, obstacle length has a weaker effect on flow properties than in the case of short ribs. This is related to the lifetime of turbulence produced by each obstacle. Short ribs tend to produce larger thus longer lasting turbulent scales in the outer part which is paired with proportionally larger recirculation regions. A study of the integral time scale $T_{uu} = \int_0^\infty \frac{u(t)\bar{u(t+\tau)}}{u^2}$ provides good indication on the lifetime of turbulent fluctuations at different frequencies (Ramaprian and Shivaprasad, 1978). Short ribs showing a more uniform velocity profile downstream of the obstacle than long ribs also displays

values of T_{uu} indicating a longer lifetime of fluctuations. In the wake, the highest levels of turbulence intensity occur at the same height above the surface as the maximum $\partial U/\partial y$. However, in short ribs, this height is 50% higher than in long ribs, and the maximum intensity is higher by up to 50%. For long ribs, Leclercq et al. (2001) also found that the highest levels of turbulence occur downstream of the FF face, before the first reattachment. The mixing process in the wake between the uniform flow above the rib, and the "still" region downstream of the rib is compared by Arie et al. (1975b) to Görtler's theory on a uniform flow mixing with static fluid. The authors who also studied incoming flow effects quote the point of maximum turbulence intensity occurring at highest H/δ, and being located above the top surface of the obstacle. The exact height of maximum turbulence intensity varies with obstacle length (y/H=1.13 for short ribs and y/H=2.5 for a fence) which is explained by the Coandă effect deviating the shear layer .

As a consequence of the strong aerodynamic disturbance, ribs produce distinct pressure fluctuations causing noise and vibration along their surface. Arie et al. (1975a) provides a global overview of the behaviour of ribs immersed in a turbulent boundary layer by investigating the mean pressure drag generated at different inflow conditions. For obstacle lengths up to $L/H = 6$, within a range of obstacle height to boundary layer thickness ratio comparable to Bergeles and Athanassiadis (1983), it is clear that pressure drag coefficient decreases with rib length, and with H/δ. Arie et al. (1975b) supports the first experiment and adds detailed comparison of surface pressure distribution for two rib lengths ($L = 2H$ and $L = 4H$). A few trends are immediately visible: the pressure drop after the leading edge of the obstacle is stronger as δ/H decreases, the pressure on the downstream face is constant at all heights whereas it is not on the upstream face. Finally, it appears there is a degree of similarity between the pressure distribution across the cases of multiple rib lengths, especially for ribs with reattachment on top. However, the degree of similarity is not sufficient to call it an identical, merely scaled, surface pressure distribution.

Leclercq et al. (2001) aim to describe the pressure fluctuations of long ribs by analysing their acoustic signature. To that effect, an array of pressure transducers and microphones is used as well as Laser Doppler Anemometry (LDA). Flow conditions are the following: $Re_H = 170000$, pressure gradient is cancelled by adjusting ceiling height, and $\delta/H = 0.7$. Whether tripping of the boundary layer is present is not explicitly mentioned. As a reference, LDA measurements confirm the recirculation lengths of all three bubbles observed on a rib of $L/H = 10$ to be $L_R/H = 0.8$, then $L_R/H = 3.2$, and finally $L_R/H = 3.5$ in streamwise order. Wall pressure fluctuations were obtained with an array of microphones mounted to the surface of the model. It appears that the highest RMS levels are measured downstream of the BF step, upstream of the reattachment location at 0.26 times the dynamic pressure. Power Spectral Density (PSD) analysis shows that the frequency containing the most energy shifts from 145Hz at $x = 2H$ to

125Hz at $x = 9H$. This shift is simultaneous with a reduction in energy levels away from the BF face. Downstream of the BF face, upstream of the reattachment location one maximum is detected at 80Hz and the PSD shows a steep decline. Downstream of the reattachment point, the spectrum is shallower, and the peak disappears. In addition, a coherence is detected at 80Hz between microphones on top of the obstacle, and one located $2H$ downstream of the BF face. This testifies that phenomena occurring after the FF face are convected past the BF face.

Cross-spectral density reveals coherence exists on the top surface of the obstacle. It peaks at $\omega h/U_0 \simeq 1$, which matches the peak frequency in the PSD. Besides, coherence of the flow is computed to be most isotropic at that frequency downstream of the FF face. Downstream of the BF face, the pressure field presents strong stream-wise and span-wise isotropy at frequencies containing most energy in the PSD. This isotropy disappears beyond reattachment. Further on the subject of unsteadiness, Liu et al. (2008) describe the flow over a two-dimensional square rib, a short rib. Emphasis is put on large-scale structures and flapping of the separation bubble. The authors measured a continuous recirculation bubble from the leading edge to $9.75H$ downstream of the obstacle. Bergeles and Athanassiadis (1983) quotes a recirculation value closer to $L_R = 12.5$ for this L/H. Using spectral analysis and wavelet transform they identify large-scale vortical structures being shed at $fH/U_e = 0.03$, and a flapping of the bubble at $fH/U_e = 0.0075$. Using cross-correlation of pressure fluctuations, convection speeds were estimated between $U_c = 0.35U_e$ and $U_c = 0.45U_e$, where U_e is the free-stream velocity. Using conditional averaging based on the intermittency of reversed-flow, the authors were able to illustrate the relation between surface pressure and the shedding of large-scale structures from the obstacle. In conclusion, the unsteadiness in velocity above the square rib has a strong effect on surface pressure fluctuations. No similar study was found for a rib with reattachment on the top surface.

1.3 Comparable obstacles and their driving parameters

1.3.1 Fences

Raine and Stevenson (1977) describe the aerodynamic effects of a fence ("windbreak"): " The windbreak exerts a drag force on the wind field, causing a net loss of momentum in the incompressible airflow and thus a sheltering effect". As the incoming flow approaches the FF side of the fence, it separates shortly upstream of the obstacle. The flow above that bubble is deflected up and past the obstacle. A recirculation bubble forms immediately downstream of the fence accompanied by turbulent eddying. The separated flow impinges onto the floor several step heights downstream, thus delimiting the extent of the recirculation bubble. The extent of a recirculation bubble is commonly

Experiment	L_R/H	Re_H	δ/H
Arie and Rouse (1956)	17	100000	N/A
Mohsen (1967)	10-11	70000	4 and 2
Good and Joubert (1968)	13-14	176000	2.61-9.71
Raine and Stevenson (1977)	9		
Castro and Fackrell (1978)	9.5-18	5900-25000	0.3-2.1
Orellano and Wengle (2000)	12.8-13.6	3000-10500	

Table 1.1: Recirculation lengths behind fences in previous experiments.

given in length between the separation point and the mean reattachment location. Table 1.1 gives a summary of the results found in relevant publications. In general, fences produce a recirculation region ten times the height or more. After comparison with BF and FF steps, it will become clear that this configuration generates the largest mean recirculation bubble. As is the case for most strongly separated flows, the extent of the separation bubble fluctuates around an average value.

Provided that other flow conditions remain identical, an increase in incoming flow velocity (or Re_H) will not affect significantly the recirculation length behind a fence. Jensen (1958), van Eimern (1964), and Kaiser (1959) confirm this. However, the size of a separation region is sensitive to incoming boundary layer thickness δ. Castro and Fackrell (1978) describe the response of the flow over a fence of varying height in varying wind-tunnel blockage ratios(1% to 18%). These fences were studied at $15m/s$, with heights of $25.4mm$, $12.7mm$, and $6mm$. It appears that blockage affects significantly the aerodynamics of a fence. The maximum pressure on the front face of the fence decreases as the blockage ratio is increased. On the other hand, the drag coefficient of the fence increases with blockage ratio. This occurs because the base pressure (pressure used to normalize the coefficient), decreases sharply with blockage ratio, thus a high drag coefficient is maintained. Similarly, reattachment length behind the fence decreases as the blockage is increased. In conclusion, careful corrections should be applied when blockage is involved, especially since the effect of blockage seem stronger at small blockage ratios, rather than larger ones.

Raju et al. (1976) investigated the response of a 2D fence to varying turbulent inflow conditions. The authors tested the configuration on a smooth, rough and transitional flat plate. The results focus on the influence of these parameters on the drag generated by fences of varying height. It appears that fence drag coefficients are affected by roughness of the upstream wall, however, not necessarily by the exact velocity profile of the outer region of the boundary layer. There is a distinction between the outer region of the boundary layer, and the region affected by roughness. Castro and Fackrell (1978) continued to prove that drag coefficient of a fence can be approximated as a function of the ratio h/δ. This holds under the conditions that the fence has sharp edges and that are short enough to prevent reattachment on its top surface.

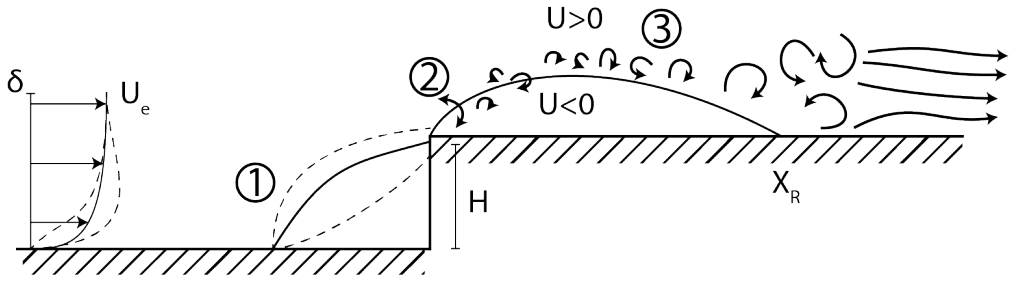

Figure 1.3: Flow topology around a forward-facing step inspired by Cherry et al. (1984). 1: the front recirculation region where Pearson et al. (2013) identified the effect of incoming flow on the slow large scale motions. 2: Location of the slow shear layer flapping reported by Cherry et al. (1984) which causes large slow motions of the bubble. 3: Growth of higher frequency fluctuations in the shear layer up to reattachment point (Cherry et al., 1984), then convection of turbulent flow with small and large scale oscillations downstream.

1.3.2 Forward-Facing Steps

In the case of FFS, most studies support the theory that the length of a recirculation bubble in these cases of strong separation depends mostly on step height, and only very little on flow velocity. Mohsen (1967) for instance compared three different obstacles causing strong flow separation from a known location, namely backward facing steps, forward facing steps, and fences. Each obstacle was also tested at various subsonic velocities. The authors conclude that turbulent separation length is independent of flow velocity. It appears to be directly linked to step height. Additionally, they notice that turbulent shear stress increases in the free shear layer with distance from the separation point. This last phenomenon is correlated with an increase in pressure fluctuations, being maximum at reattachment. However,the separation in this study was fully turbulent which is a critical condition.

Indeed, Sherry et al. (2010) studied the flow over a forward facing step of varying heights and at varying free-stream velocities producing laminar, transitional and fully turbulent shear layers around the separation region and found varying recirculation lengths as a function of Re_H. Three obstacle height to boundary layer thickness ratios were investigated: 0.83, 1.25, 2.5. The velocity was modified to cover a range of Reynolds numbers as follows: $1400 < Re_H < 19000$. Results show that recirculation lengths grow with velocity and step height for the lower Reynolds numbers. Above $Re_H = 8500$, a different regime occurs where the recirculation length varies only slightly with flow velocity. This change of regime coincides with the transition from laminar to turbulent flow separation at the corner of the step.

Largeau and Moriniere (2007) carried out experimental measurements of pressure fluctuations and velocity field in the flow over three FFS ($H = 30, 40, 50$mm), and varying speeds. The results show that surface pressure fluctuations increase from the separation corner to the mean reattachment point. This point moves upstream with increased free-stream velocity because higher turbulence levels exist in the free-stream. The main difference with previous studies is that this experiment is carried out on a nominally 2D obstacle in an open channel wind-tunnel. Consequently, there is significant bypassing around the obstacle. This affects the reattachment line on the top of the step. It is curved on the edges, but the centreline presents a clear reattachment location. Results which are extracted from the centreline describe an upstream separation bubble of $0.7H$ in length, and $0.5H$ in height. Downstream of the corner, large-scale vortical structures are shed from the corner. The recirculation length varies from $L_r/H \simeq 4.5 - 5$ for $U_e = 15m/s$ and $L_r/H \simeq 3.5 - 4$ for $U_e = 40m/s$.

Pearson et al. (2011) studied the flow over a FFS in a turbulent boundary layer using time-resolved PIV and "low-speed" PIV. Emphasis was placed on the relation between the regions before and after the corner of the step. Flow conditions are similar to those of the experiments in this thesis for the purpose of subsequent comparisons ($\delta_{nostep} = 4.9cm$, $U_e = 10m/s$, $H = 3cm$, $Re_H = 20500$). Results indicate that features of the incoming flow convect consistently past the obstacle. Evidence is found in the correlation of the extent of separation with upstream-wall shear stress, and that of displacement thickness upstream and downstream of the obstacle. The behaviour of the recirculation region with respect to incoming flow is described as well, however more details about the cyclic behaviour of the forward facing step is given in the following paper.

Pearson et al. (2013) uses 2D time-resolved PIV to break down the effect of fluctuations in the upstream separation bubble on the downstream one of a FFS (see figure 1.3). The experiment was run under similar flow conditions as the previous experiment (apart from $\delta_{nostep} = 4.4$cm). The authors describe that coherent structures of low-velocity fluid in the incoming turbulent boundary layer convect over the obstacle. These structures trigger the unsteadiness observed over the FF step. As a result of these slow structures, the upstream recirculation bubble, which would be of closed form, grows and "leaks" over the step. This results in a larger separated flow region on top of the step.

According to Camussi et al. (2008) the FF step generates stronger fluctuations in the wall pressure fields than the BF step. They aim to uncover the physical mechanisms behind pressure fluctuations through studying the FF step under different flow velocities. Through the use of high-speed PIV and synchronised pressure measurements at various locations, they describe that Reynolds number affects the size of the recirculation region ($Re_H \leq 8800$). The upstream recirculation bubble features a dual power law spectrum in its pressure signal. The transition between the two laws occur at a Strouhal number of 0.2 based on free-stream velocity and step height. From the leading edge of the step,

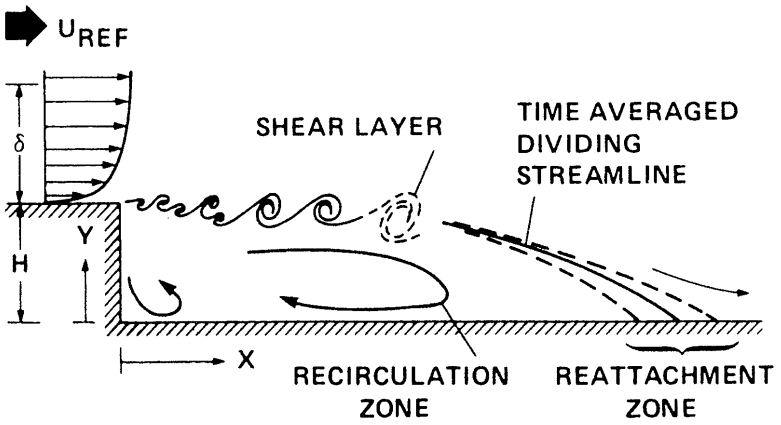

Figure 1.4: Flow topology behind a BF step (Driver et al. (1987))

fluctuations become progressively stronger to reach a peak two step heights downstream of the corner, where the flow reattaches.

Sigurdson (1995) attempted flow control on the separation occuring at the leading edge of a blunt faced cylinder oriented axially in the flow. Flow control requires a good understanding of the flow, as a result these types of studies generally contain good information about the physics of the flow in addition to the control strategy. The authors managed to reduce the drag produced by such object using a simple fixed frequency actuator. This actuator produced maximal drag reduction with a pulsed jet exiting on the circumference of the front face of the cylinder at a reduced frequency of 2 to 3 based on diameter D and free-stream velocity U_e. It affects both the Kelvin-Helmholtz instability of the free shear layer and the von Kármán vortex shedding occurring at a reduced frequency at much lower frequencies ($fh/U_e = 0.08$).

1.3.3 Backward-facing steps

Documentation about BF steps helps anticipate the response of such a singularity to the flow conditions imposed by the FF step upstream in the study of long ribs. Additionally, BF steps may cause phenomena with repercussions upstream of the face. In this section, various parameters driving the separation from BFS will be reviewed.

Bradshaw and Wong (1972), Driver et al. (1987), Armaly et al. (1983), Eaton and Johnston (1981), Adams and Johnston (1988), and Chandrsuda et al. (1978) describe the fundamentals of separated flows over a backward-facing step. This category of flows produces a recirculation bubble nested in the corner formed by the vertical face and the downstream plate. It is caused by the growing boundary layer on the top face meeting a strong adverse pressure gradient as it reaches the corner. The momentum carried by the flow prevents it from following the sharp corner, thus it separates. A curved shear layer forms between the top corner of the obstacle, and the plate downstream, where flow reattachment occurs. This shear layer bounds a recirculation bubble which can be

divided into two regions: the main recirculation bubble rotating in one direction, and its secondary contra-rotating recirculation bubble which is located between the main bubble and the step corner. As the flow reattaches past the obstacle, a new boundary layer forms containing features of the initial flow as well as new features caused by the perturbation.

The shear layer caused by the velocity gradient behind a BF step contains the source of the unsteady flow. This layer contains periodically shed vortices, rolling and pairing to form trains of vortical structures (Winant and Browand, 1974; Troutt et al., 1984). Winant and Browand (1974) describe the evolution from an instability (Kelvin-Helmholtz type) due to the velocity gradient, to progressively stronger waves until these break into vortices. Liu et al. (2005) describe the vortex pairing mechanism through which vortices amalgamate and form larger ones is associated with a Strouhal number of 0.13. As the vortices pair in the shear layer, they form coherent structures. As described by Hussain (1986): " A coherent structure is a connected turbulent fluid mass with instantaneously phase-correlated vorticity over its spatial extent". Winant and Browand (1974) describe how to determine the coherence of a structure by use of ensemble averaging. Understanding the characteristics of these coherent structures is of paramount importance in strongly separated flows. Indeed large coherent structures are related to heat, momentum and mass transfer. In addition, it appears that active control of these structures($St = 0.29$) leads to the largest changes in reattachment length behind a BF step (Roos and Kegelman, 1986). Chun and Sung (1996) found similar behaviour at $St = 0.27$. This result is associated with enhanced amalgamation, occurring sooner in the shear layer.

The reattachment location downstream of the obstacle is source of much discussion. It is not stationary, and strongly affected by pressure gradient, and incoming flow conditions. The instabilities occurring at the reattachment point originate in the impinging layer of flow, the shear layer. The large coherent structures produced in the shear layer may be advected downstream after reaching a maximum size of about one step height (Bradshaw and Wong, 1972; Farabee and Casarella, 1986). This advection was measured to occur at $St \approx 0.07$ according to Lee and Sung (2001), which is an order of magnitude lower than the pairing of vortical structures occurring shortly upstream described above. Hudy (2005) and Hudy et al. (2007) describe the distinction between the two phenomena behind axisymmetric BF steps.

The secondary vortex present in the corner of the backward facing step has also been extensively studied. Hall et al. (2003), and Spazzini et al. (2001) note that the secondary vortex responds as well to the fluctuations in the main recirculation bubble, furthermore this response occurs at a similar frequency than the flapping in the shear layer. Periodically, this secondary vortex may grow up to the step's full height (Spazzini et al., 2001).

As found in Eaton and Johnston (1981), the main parameters affecting the flow behind a backward facing step can be summarized as:

- Boundary layer's thickness and profile type
- Reynolds number based on step height
- Expansion ratio
- Step aspect ratio
- Free-stream turbulence state

As for the FF steps, it is essential to report these parameters when describing a study of BF steps. They are the minimum number of parameters which need to be considered when drawing comparisons between studies. While this chapter broadly covers the major studies involved in flow separation, we will return to these in more detail throughout the thesis as we analyse the experimental results.

1.4 Objectives and outline of research

The aim of this project is to characterize the flow over ribs of varying length in as much detail as possible. It has been noted in past studies that rib length affects drastically the flow separation caused by such obstacles. As seen in sections 1.3.2 and 1.3.3, ribs combine multiple unsteady phenomena which produce the unsteady recirculation regions and associated elements. The turbulent incoming boundary layer possibly causes shear layer flapping at the upstream corner. Regardless, the flapping and shear at the upstream corner produce the growth of a shear layer above the rib comparable to a classical mixing layer. If the flow reattaches on the top surface, this mixture of temporal and spatial scales stops growing and travels to the downstream corner. There, it modulates the "natural" shear layer formed in a backward-facing step. If the flow has not reattached on the top surface, then the structures of the FFS are still evolving as they reach the BFS. Consequently, it is difficult to predict what these combinations will result in around ribs. The two classical problems forming a rib, the forward-facing and backward-facing steps, are extensively studied, but the interaction between the separated flow from the forward-facing section with that of the backward-facing section remains widely undescribed.

In order to elucidate the physics of such separated flow, there will be five main parts to this project:

1. Estimate pressure from PIV measurements to provide a more complete information on flow separation around ribs and its effect on pressure. (Chapter 3)

2. Measure the spatial and temporal properties of the flow as a function of rib length, in a configuration that is comparable to previous literature on ribs and other "simpler" obstacles, and highlight the underlying mechanisms. (Chapter 4)

3. Study the effect of turbulence in the flow in order to obtain the response of the ribs to a change in the flow. (Chapter 5)

4. Study in depth the relationship between surface pressure and velocity fluctuations above a rib of critical length. (Chapter 6)

5. Modelling the separated flow over ribs based on surface pressure data to highlight the link between surface pressure fluctuations and velocity. (Chapter 7)

Chapter 2

Methodology

2.1 Wind-tunnel models

The experiments carried out during this study take place in the University of Southampton's "3x2" open return wind-tunnel. The air drawn through the test-section is expelled in the laboratory's room where it dilutes and mixes with almost stationary air and synthetic seeding smoke. This configuration requires under an hour of warming up the laboratory's air, and mixing it with smoke before obtaining a homogeneous mix at a stable temperature.

Upstream of the test section, a large intake with honeycomb and stainless steel mesh filters reduces the free stream turbulence to 0.6% according to hot-wire measurements. The flow is then contracted into the test section which measures 4.2m length, 90cm in width, and 60cm in height. The test section is a simple rectangular parallelepiped, without boundary layer suction. Consequently there is no device in the test section to alleviate the build up of blockage with boundary layer growth. The flow is then sucked through a diverging section by an electric fan with 12 blades. The number of blades should be recorded as acoustic noise may appear at a multiple of the number of blades, and the spinning frequency of the fan.

In order to control the incoming flow conditions for surface-mounted obstacles, an aluminium flat plate was used as a second floor hanging in mid-air. See figure 2.1. It is constructed with a sandwich method (aluminium skin/aluminium honeycomb/aluminium skin), as a result it is rigid and lightweight. It is suspended about 14cm above the floor of the wind-tunnel, and measuring only 1cm in thickness, produces very little blockage (less than 1.7%). Its length and position can be adjusted to form the required incoming boundary layer thickness, and pressure gradients. The importance of this technique is explained by Hanson et al. (2012).

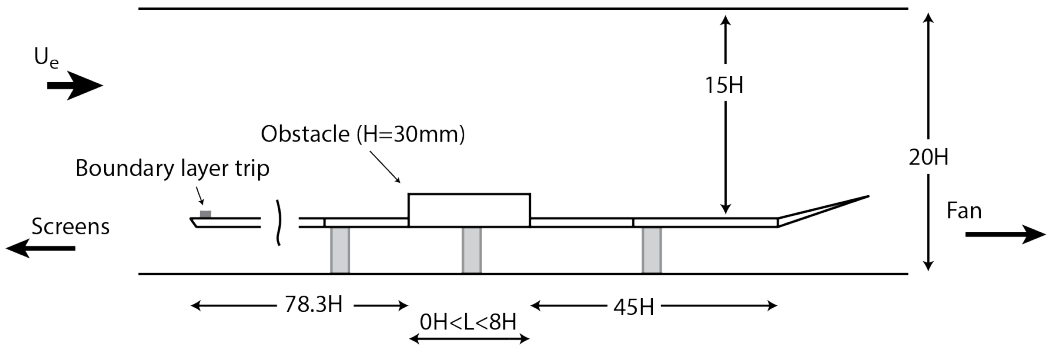

Figure 2.1: Installation of the model inside the wind-tunnel.

At the leading edge, a wedge splits the flow with very little perturbation to initiate the boundary layer. To prevent separation and thus a pulsating flow along the flat plate, a flap is mounted at the trailing edge. The flap is adjusted until the flow around the leading edge does not separate. It is checked using wool tufts, and surface oil visualization. The mean pressure gradient along the test section may not be neutral, however the flow is steady and predictable.

The test-section offers multiple optical access possibilities on three sides. Wide perspex windows enclose the area where the model is installed. A removable wooden floor also allows for the instrumentation cables/tubes to be channelled outside of the test-section. The test-section is surrounded by a large aluminium frame which allows stable support for the instrumental equipment. As a result, the lasers and their optics can be mounted on the same rigid frame as the recording cameras thus minimizing the chances of relative displacement between them.

Figure 2.1 displays the experimental layout inside the wind-tunnel in H units. Including the leading edge, the portion upstream measures 1.9m long. It is followed by 450mm of instrumented flat plate, then the model (between 3mm and 240mm long). Downstream of the model, another 450mm of instrumented plate and 900mm of aluminium flat plate. Finally, the trailing edge is fitted with the flap.

In the first experiment, the elongated rib is studied with varying distances between the FF and BF faces. Figure 2.2 offers a quick overview of the experimental setup along with key measurements for the testing conditions. The ribs extend along the full span of the wind-tunnel, thus creating a two-dimensional obstacle. They are mounted on a false-floor of the wind-tunnel. They are made of solid Perspex blocks to prevent reflections of the laser on the surface. Instrumentation is mounted inside the ribs, as well as on plates upstream and downstream. The following cases were studied:

- ribs: $H = 30$mm and $1H$, $2H$, $4H$, $6H$, $8H$ lengths

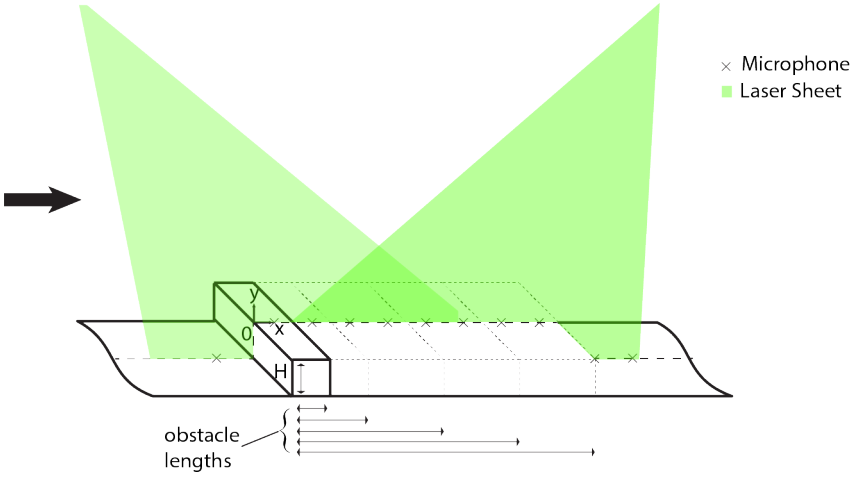

Figure 2.2: Schematic of the experimental setup. Five cases of elongated ribs are presented, as well as the location of instrumentation.

- a 30mm and a 15mm high fence (≈0.1H streamwise length)
- flat plate for unperturbed flow conditions

Measurements were performed in a plane near the centre line of the model. At this location, the nominally two-dimensional flow was expected to be homogeneous from a statistics standpoint in the spanwise direction. However, as described by Moss and Baker (1980) and Kiya and Sasaki (1983), this is incorrect in a closed-section wind tunnel unless the aspect ratio of the step (W/H) exceeds 10. Beyond that aspect ratio, we may expect a limited portion of acceptably spanwise homogeneous flow at the centre. In order to minimize the effects associated with the side walls of the test section on the recirculation region, the step was made such that $W/H = 30$. Additionally, homogeneity was verified for each case with surface oil flow visualisation techniques. Maltby (1962) and Smits and Lim (2000) provide details on the technique, but a summary of the method employed is described here. As recommended by Smits and Lim (2000), the model was wrapped in black heat shrinking polyester in order to produce a smooth uniform surface without absorbing oil. Silicon oil with a calibrated viscosity of 50 cps was used in conjunction with white polyamide pigments. This mixture offered good contrast with the black background, and the particles followed the oil well after visual inspection. A perforated steel mesh was used to position drops of mixture in an even pattern upstream, downstream, and on top of the step. Photos were taken from above the obstacle to record the pattern formed by the oil mixture before and after turning on the wind tunnel (see figure 2.3 for examples on $L/H = 6$). Overlapping the two images shows significantly different results for each case. The criterion used to determine spanwise homogeneity is the shape of the reattachment line both on top and downstream of the obstacle. The alignment of the flow upstream of the obstacle was also checked. It appears that ribs

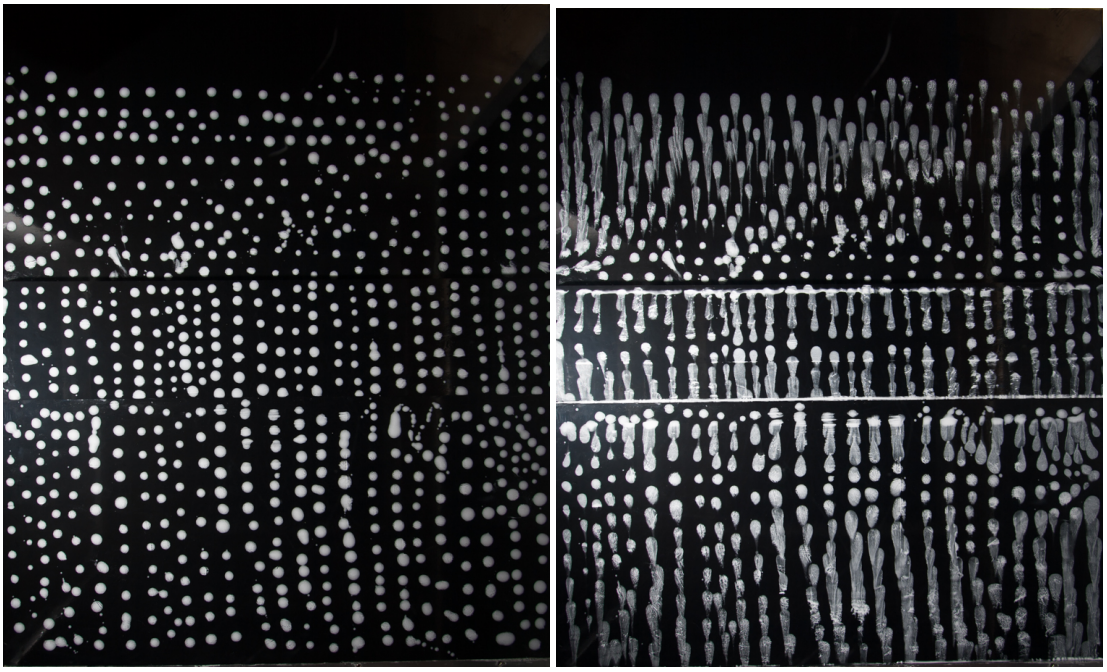

Figure 2.3: Top view of a rib ($L/H = 6$) during the oil flow visualization. Left is before, and right after wind is turned on. The wind travels from top to bottom. We distinguish the leading and trailing corners where oil accumulates. The mean reattachment lines are materialized by alignments of intact dots in the right photo.

with reattachment on top ($L/H \geq 4$) produced two straight reattachment lines, which are parallel to the obstacle for more than 75% of the span. Shorter ribs however produced a single reattachment line with a noticeable curvature. Curvature and position of this line varied with obstacle length. For $L/H = 2$, $L/H = 1$, and $L/H = 0.1$ the central portion parallel to the obstacle covered respectively 51%, 40% and 23% of the span. In conclusion, the longest obstacles produce acceptable flow conditions for a statistically homogeneous flow in the span. However, results for the three shortest obstacles must be considered affected by side-wall effects to an increasing degree which shortening length.

The models were machined on the same Sorotec CNC machine (SRT-FE 1507-V2S) which has a precision of ≤ 0.05mm. In practice, vibrations and thermal effects affect the quality of machining. An absolute accuracy of ± 0.1mm is achieved in the horizontal direction, and ± 0.3mm in the vertical direction. The holes for pressure taps and transducers were also drilled using the same machine, thus the same accuracy is obtained in positioning the holes relative to the obstacles.

2.2 Flow conditions without obstacle

The boundary layer conditions upstream of the obstacle are essential as they provoke different responses from the obstacle. They must be explicitly described in order to

compare different studies. To match Pearson et al. (2013), it was decided that the obstacle should be immersed in the boundary layer. In total 2.35m of flat plate create a turbulent boundary layer that is 42mm in height (δ_{99}) where the obstacle should begin. This was evaluated by measuring an average velocity profile over a flat plate using a hot-wire, at the location of the leading edge of the obstacle. At a freestream velocity of 10m/s, the Reynolds number based on step height is 20 000. The flow is tripped 8cm after the leading edge of the plate using zig-zag turbulator tape. As a result, the developing boundary layer is fully turbulent. The velocity of the flow was adjusted as close as possible to 10m/s by checking the readings of Pitot tubes installed on the ceiling of the wind tunnel, upstream and downstream of the obstacle. A difference of less than 0.4m/s existed between the two probes.

Flow conditions in the wind-tunnel were assessed through hot-wire, and pressure measurements. In this section, hot-wire data are used to establish boundary layer profiles of both fluctuating and averaged velocity at the location where the obstacle would stand. This data reveals most parameters required to characterize the boundary layer. See Table 2.1.

As plotted in Figure 2.4 the boundary layer is 1.4 times the height of the obstacle. This is the inverse scenario to what Bergeles and Athanassiadis (1983) describe ($\delta_{99}/H = 0.48$), but close to what Pearson et al. (2013) describes, thus comparison of results is possible. In addition, the boundary layer shape factor is consistent with typical turbulent boundary layers (Pope, 2000).

Figure 2.4 also presents the distribution of velocity fluctuations in the boundary layer at the location of the obstacle, concentrated in the turbulent boundary layer of height $1.4H$. It is obvious that the fluctuations found here plateau at approximately 0.6%.

In addition, a logarithmic profile was fitted to the measured boundary layer using Marusic et al. (2013)'s method:

$$u^+ = \frac{1}{\kappa} \ln y^+ + B$$

Quantity	**Value**	**Unit**
δ_{99}	1.4	H
	42	mm
$Re_{\delta_{99}}$	27600	
θ	4.9	mm
Re_θ	3213	
δ^*	6.7	mm
Re_{δ^*}	4356	
Shape Factor	1.36	
U_τ	0.39	m/s

Table 2.1: Boundary Layer characteristics.

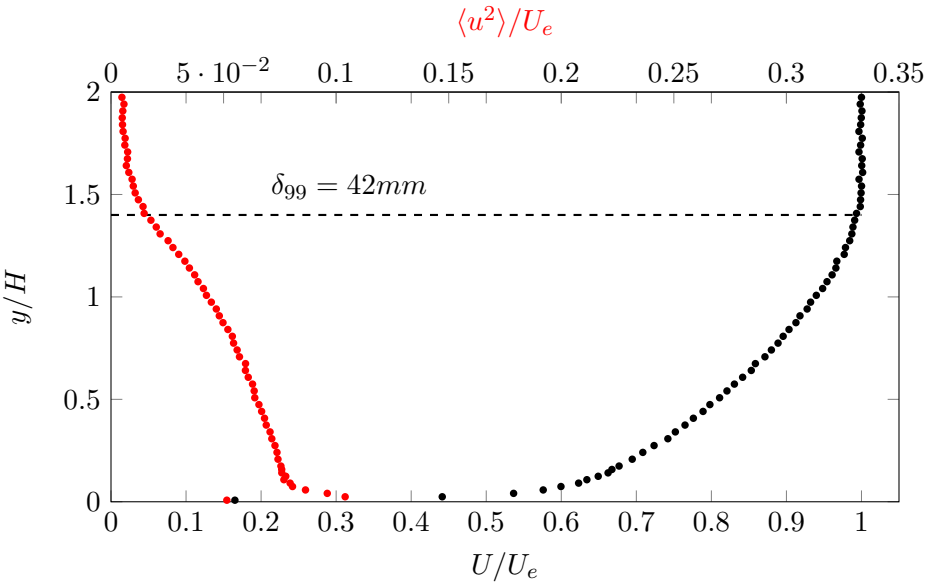

Figure 2.4: Velocity profiles of the boundary layer at the location of the obstacle without obstacle.

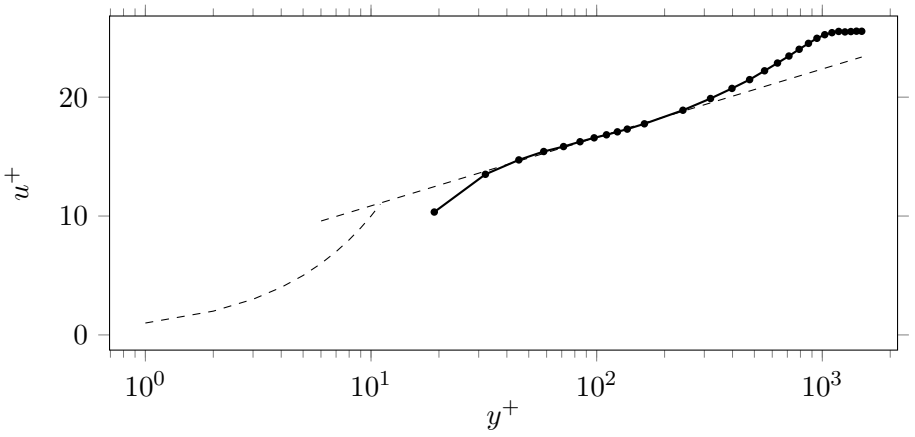

Figure 2.5: Velocity profile in wall units. The dashed lines represent theoretical results for the viscous sublayer, and the logarithmic region. The black dotted line corresponds to measured values.

The coefficients used are $\kappa = 0.4$, and $B = 5.1$. The value of u_τ used to fit the profile was obtained through a linear least squares fitting function. This function was applied to the recommended region ($3Re_\tau^{0.5} < y^+ < 0.15Re_\tau$). Figure 2.5 depicts the results. It is noticeable that the fit is acceptably close. Different coefficients for κ and B obtained in Pope (2000) were tested too but the fit was deemed less satisfactory.

The pressure distribution obtained in the first experiment described in section 4 is converted to pressure coefficient as follows:

$$C_P = \frac{P}{0.5 \times \rho \times U_e^2}$$

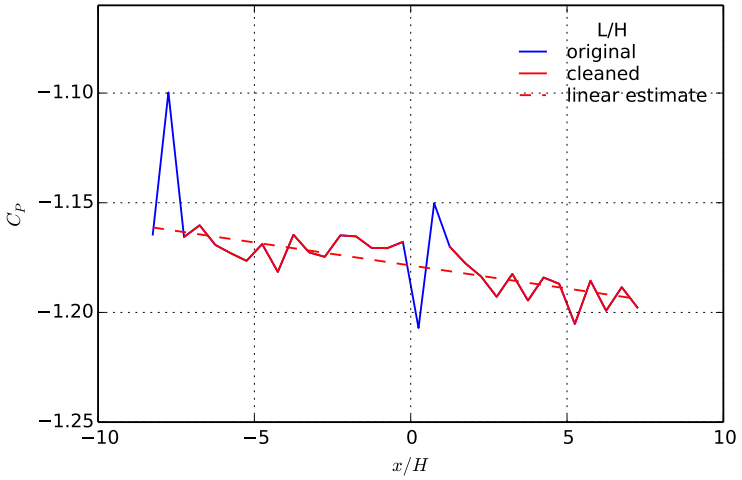

Figure 2.6: Pressure distribution along the surface of the initial flat plate.

where P is the pressure extracted from the mean pressure measurements zeroed at rest, ρ is the density of the air: $\rho = \frac{P_{atmo}}{RT_{atmo}}$, and U_e is the freestream velocity. The C_P values upstream of the ribs are then subtracted by the values obtained in the case without obstacle mounted in the test section. Finally the remaining pressure taps are compensated for the pressure gradient present in the test section. It was found that the pressure gradient followed a linear trend described by $C_P = -1.1786 - 0.0021x/H$. This is based on data from the initial flat plate where outliers were removed, see 2.6 for the data.

In order to characterize the flow around the obstacle, three techniques were used:

- Mean pressure measurements
- Fluctuating pressure measurements
- Velocity field measurements with PIV
- High-frequency point velocity measurements with hot-wire

The instrumentation should cover upstream and downstream regions of the obstacle in order to capture the incoming flow conditions, and the full range of reattachment lengths downstream of the obstacle. This last point fluctuates significantly (Armaly et al., 1983) for a backward-facing step. Shorter recirculation lengths were expected for cases $L \geq 4H$. They have been quoted to be near 3 or 4 obstacle heights in length with strong relative fluctuations on the reattachment location (based on BFS). However, for cases $L \leq 4H$, the total recirculation length increases significantly. In addition the fluctuations of the reattachment location behind a fence (worst case) are several step heights in magnitude Le et al. (1997). These can extend down to 19 fence heights.

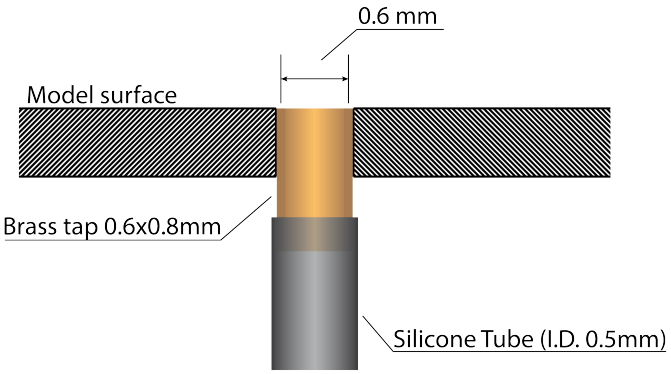

Figure 2.7: Typical configuration for pressure taps.

2.3 Mean pressure measurements

Pressure distribution was measured along the surface of the models. A 64-channel Scanivalve ZOC 33/64PxX2 - 20inH2O was used to acquire 1600 samples at each location. A maximum of 48 pressure taps were used with a streamwise separation of $0.5H$. Pressure taps were not aligned with the centreline of the model as this was reserved for potentially using a surface shear stress sensor. As a result, the measurement line is 70mm away from the centreline, and parallel to the freestream direction. They are spread in the following way (H=0 corresponds to the leading edge of the obstacle):

- 17 taps from $-8.25H$ to $-0.25H$
- 16 taps from $+0.25H$ to $+7.75H$
- 15 taps from $+8.25H$ to $+15.25H$

Each pressure tap is made up of a brass tube piercing through the surface of the obstacle. These measure 0.6mm ID, and 0.8mm OD. They are cut flush with the surface and glued in position. On the service side of the model, they are connected through fine silicon tubing (0.6mm ID) to the pressure sensor.

Pressure measurements last several minutes. As a result, these were acquired after settling of the temperature in the laboratory to avoid drifting values due to temperature changes. Zeroing of the pressure sensor was made with the wind-tunnel at rest, and the room at temperature. The Scanivalve transducer used to acquire the mean pressure measurements has an accuracy of 0.12% of full-scale (20 inH2O), this represents an error of 6Pa. Thermal drift is considered negligible since the wind-tunnel lab was preheated prior to the measurements. In addition, the sensor was zeroed prior to each measurement.

Damping due to the length and restricted diameter of the tubing would not allow us to measure fluctuations at a high enough rate through these taps. This phenomenon is explained and harnessed by Fuertes et al. (2014). As a consequence, a set of pressure transducers were used to measure pressure fluctuations. Section 3 describes the results obtained from the mean pressure measurements, including corrections made to the readings.

2.4 Fluctuating pressure measurements

Separated flows present strong fluctuations which are reflected in quantities such as velocity, but also in pressure. From an aerodynamics perspective, pressure information is part of the complete assessment of phenomena occurring in the flow over an obstacle. From an engineer's perspective, measurements of fluctuating pressure at the surface of a model is essential in determining unsteady mechanical loads on the surface, and generated acoustic noise (Naguib et al., 1996).

Two to four Endevco 8507C-2 pressure transducers and an Endevco 8510-1B were used to measure surface pressure fluctuations. These were mounted below the surface of the ribs by a 0.8mm hole, 2mm long. The first type were used to do measurements between $x/H = 1$ and 14.5, the second type was placed far upstream to gather data which could be used later in applying an optimal noise cancellation scheme as per Naguib et al. (1996). These transducers are used in several experiments, synchronously with velocity measurements both hot-wire, and PIV. In order to record measurements, a NI PXIe 1062Q data acquisition computer was used in conjunction with a NI PXIe-4330 card for Bridge-Based Measurements. These devices allow simultaneous measurements at up to 25.6kHz. The combined hysteresis of pressure fluctuation measurements made with the Endevco transducers is up to 1.5%.

Several steps are required prior to using the data from Endevco pressure transducers. First each transducer's sensitivity must be known, this is done by subjecting them to a known frequency and amplitude sound in a controlled environment. To this effect, a loudspeaker was connected to one end of a 2.5m long pipe which would emit sound-waves down the pipe to the other end, where a calibrated Endevco (8510-1B) and the transducer to be calibrated are listening. Simultaneous measurements were made through both transducers and the signal of the un-calibrated transducer was compared to the calibrated transducer. It was found that no time-lag appeared at various frequencies (from 20Hz to 20000Hz). Consequently, a simple gain is used to amplify the signal of the un-calibrated transducer to match that of the calibrated transducer. The values of each gain were recorded which is used in post-processing. The raw signal is therefore multiplied by this gain when it is used to produce results.

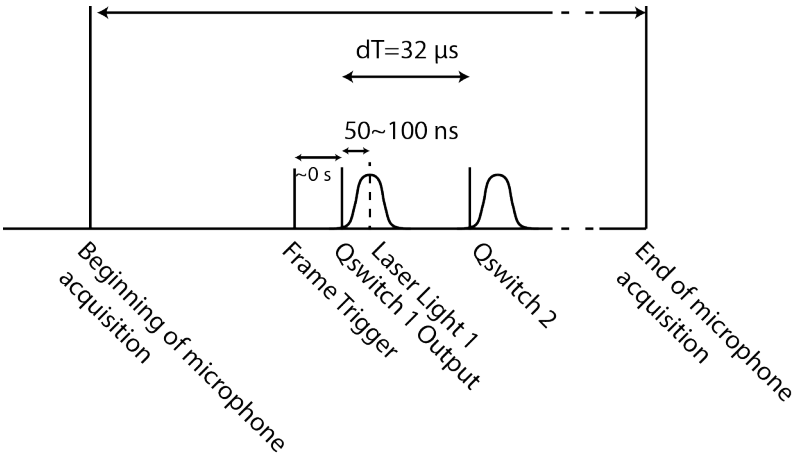

Figure 2.8: Timing strategy used to obtain PIV measurements synchronized with transducer measurements.

The second part of adjusting the transducer signal to become usable is to remove the acoustic noise present in the wind-tunnel. To that effect, the signal from the transducer far upstream inside the test-section is used as per Naguib et al. (1996). The noise cancellation method detects simultaneous signals far upstream, and on the rib and assumes this is acoustic sound travelling fast inside the test section as opposed to localized pressure fluctuations caused by the flow separation. Consequently, we remove this simultaneous sound and only the localized pressure fluctuations remain in the data. The method is robust, but requires a few elements to be successful, all of which can be found in the original document as well as application examples.

Finally the data is low-pass filtered down to 1280Hz in all of the results shown in this report. It was found that no detectable phenomenon occurs above this value which is a divider of the sampling frequency 25.6kHz.

2.5 Velocity field measurements

2.5.1 Low-speed setup

Flow field velocity measurements were accomplished using non-time-resolved particle image velocimetry (PIV). The field of interest stretches along the line of pressure transducers used to capture pressure fluctuations with an offset of less than 3mm. This was necessary in order to avoid laser light entering the cavity of the transducers. Past experience has shown that laser light may cause inaccurate pressure readings at the moment of impact on the sensing membrane. In addition flaring occurs when laser light intersects the edges of transducer cavities saturating the cameras' sensor.

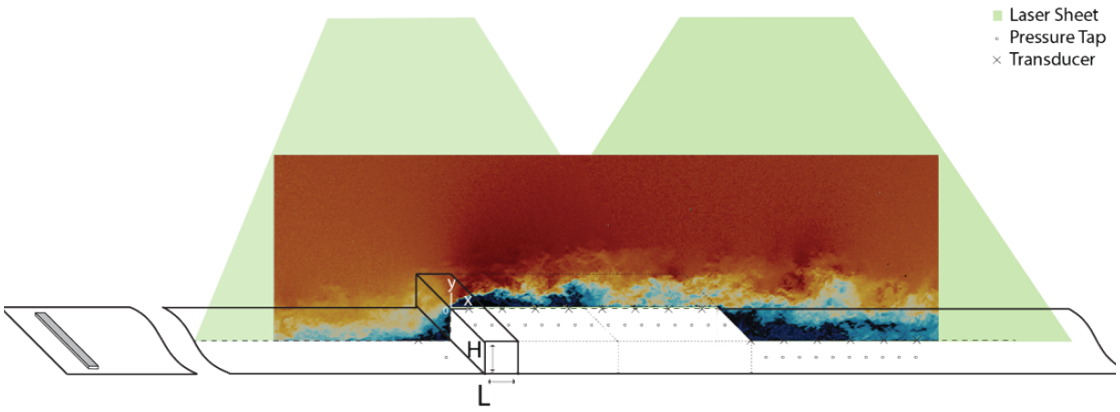

Figure 2.9: Illustration of the flow captured by the low-speed PIV setup.

The field of view of three cameras was adjusted to meet multiple criteria. The field of view must cover the region instrumented with transducers and mean pressure taps. This includes the flow in the upstream and downstream corners of the obstacle. As a result, the most upstream camera's optical axis must be upstream of the front face of the obstacle. Equally, the most downstream camera's optical axis must be downstream of the downstream face of the longest obstacle. In addition, the cameras must be able to capture the flow on the downstream face of the obstacle as its length reduce. Since the shortest obstacle may exit the field of view of the most downstream camera, a camera is added in between.

The best compromise found with the available equipment was three 16MPix "full frame" PIV cameras in conjunction with 105mm lenses. The exact model used are LaVision's LX Imager Pro 16MPix camera, and Sigma 105mm f2.8 Macro lens. Placed at approximately 1m from the laser sheet, the captured field of view covers 305mm horizontally per camera and 203mm vertically. With the conditions dictated above, the total field of view was 597mm by 180mm, starting from 160mm upstream of the FF face. It is shorter than desired, however it only truncates the upstream section of instruments. The full extent of sensors downstream is covered.

Standard deviation values of the velocity in the shear layer have been quoted to be 30% of the free stream velocity. As a result, in order to minimize the error on the estimation of the mean a large number of samples were necessary. 2500 vector fields per case would provide an error on estimation of the mean of 0.06m/s . This is an acceptable value for the scope of these experiments.

The images are processed using a commercial package (Davis 8.2) in five passes: 2 with square windows of 64x64 pixel, and 3 with square windows of 16x16 pixel. Each pass also includes an overlap of 50%. As a result, the vector fields contain ≈ 2 vectors/mm.

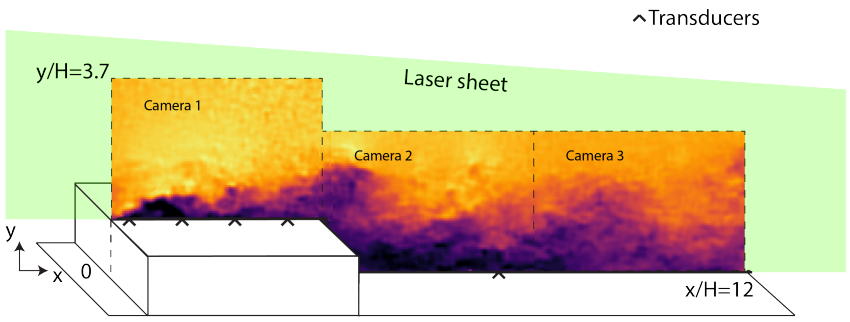

Figure 2.10: Illustration of the flow captured by the high-speed PIV setup. The configuration is identical to the low-speed PIV setup above, apart from the laser being horizontal rather than vertical.

Finally, the field of view was illuminated by two double cavity lasers from Litron lasers (Nano L 200-15 PIV). The timing was set to $dT = 32\mu$s which corresponds to nearly a 5 pixel displacement. This value is relatively short and leads to 2% correlation noise which is reflected in the minimum measurable FST. However, it was necessary as the strong shear present in the flow produced too much deformation in the groups of particles between two images for the correlation algorithm to function reliably with any longer time intervals. This value was chosen after several attempt at progressively shorter dT values beginning at the equivalent of 20 pixel displacement (128μs). In order to produce the laser sheet, the optical arrangement requires a collimator, 532nm-specific mirrors, and $f = -15$mm and $f = -20$mm cylindrical lenses.

The result of the velocity measurement is a set of three vector fields corresponding to each camera used. These vector fields are subsequently merged using an in-house code (`stitchPIV.m`) developed by Grégoire Fourrié. The method requires an overlap, and uses the coordinate system to blend the overlapping region by cubic-weighted average. The stitched fields are exported to a binary PLOT3D format compatible with Paraview and other in-house post-processing codes for CFD results ("FAT").

2.5.2 High-speed setup

In order to study in greater detail the flow of a rib of length $L/H = 4$, a high-speed PIV measurement was carried out in the "3x2 wind-tunnel". The same rib geometry and false-floor configuration was used as before. Three Phantom V641 cameras were installed next to each other in a streamwise alignment with Sigma 105mm f2.8 Macro lenses. The most upstream camera recorded the flow along the top surface, the following two recorded from the trailing edge downstream. Phantom V641 cameras operate at a maximum throughput of 6Gpx/s, in the current configuration a good compromise between spatial and temporal resolution was achieved using a recording frequency of 3200Hz (an effective vector field frequency of 1600 f.p.s.) and a sensor configuration of

1536 by 1028 pixel. No filter was used on the lenses, and the aperture was selected as f2.8. Calibration, acquisition and vector calculation were effectuated in Davis 8.3.1. .

In order to illuminate the flow, a Litron LDY 304 high-frequency laser was used with two laser-specific mirrors from Thorlabs to redirect the light. A LaVision beam focussing unit and cylindrical lens (f=-50mm) were used to produce the laser sheet at the right location in the section. Due to low power of the high-speed laser, the laser sheet needed to remain narrow in order to preserve sufficient illumination of the smoke particles. This is acceptable because we are interested in a long field of view in the streamwise direction, but low in the vertical direction. Consequently, unlike the low speed setup which illuminated the flow from top down, the high-speed laser was aligned horizontally from downstream of the ribs illuminating upstream, in a wall-normal streamwise plane. We used a vertical stainless-steel mirror mounted on a beam inside the test-section to reorient the light accordingly. This beam was downstream of the rib, at least $30H$ downstream of the trailing edge of the rib.

The effective field of view begins at $x/H = -0.15$ and ends at 8.5. The spatial resolution is 30.3 vector/H or 1.01 vector/mm in the vertical and horizontal directions. Stitching between the three cameras is made with the same algorithm as used in the low-speed data ("`stitchPara.m`" a parallelized version of "`stitchPIV.m`" from Dr. G. Fourrie).

The uncertainty associated with PIV measurements made with the high-speed setup for a single measurement was computed using Sciacchitano and Wieneke (2016)'s method. The result is approximately 2.5% uncertainty on velocity fluctuations.

The low-speed setup provides similar accuracy on fluctuations, but averaging over 2500 samples per case brings the error on mean velocity down to 0.6% in the most turbulent regions, and better in less turbulent regions.

2.6 Hot-wire measurements

The spectral form offers a clear representation of the composition of velocity fluctuations in terms of scales and strength. In order to obtain velocity measurements, a hot-wire system was used as this provides the best information for spectral analysis in the conditions dictated by the present experiment. Despite the presence of recirculating flow regions, the narrow measurement point of hot-wires can be placed outside the flow reversal, thus preserving the accuracy of the hot-wire calibrated for one flow direction. Consequently, it was only used in the outer parts of the shear layers to identify shedding frequencies from the corners of the ribs, as well as measuring boundary layer profiles in the absence of ribs to define the initial flow conditions.

The hot-wire system is identical in multiple experiments, as a result this section contains the information about the hardware. Each section of the thesis where the hot-wire

results are used will specify the treatments applied to the data such as thermal compensation, filtering, etc…A Dantec StreamLine Pro Constant Temperature Anemometer (CTA) system was used which includes a hot-wire probe, thermocouple, cabling, and an electronic Wheatstone bridge anemometer. The hot-wire probe (55P01) is illustrated in figure 2.11. The velocity measurement is made with a 1mm long and 5μm diameter sensing region of platinum-coated tungsten wire. In preparation for measurements, the Wheatstone bridge balancing electronics were adjusted to obtain a response frequency of the system above 40kHz. Note that the response may vary if the wire becomes dirty or ages. From the CTA system, a raw and conditioned signal are sampled through a NI TB-2709 card mounted on a PXI-6123 card inside a PXIe 1062Q acquisition computer. Preconditioning the raw signal (voltage) of the CTA system consists in applying a gain and an offset to match the range of voltages captured by the PXI system (0V to 10V). Carefully choosing gain and offset allows to maximize the usage of the dynamic range of the PXI card (16bit over 10V) when sampling the conditioned signal. In that respect, the hot-wire preconditioned signal was adjusted for 2m/s (the lowest velocity calibrated for) to be near but above 0V, and 13m/s (the highest velocity expected) to be near 9.5V. The gain settings are coarse so this is the best achieved range for the broad range of velocities present in the flow over ribs.

The relative expanded uncertainty for velocity measurements using this hot-wire system was evaluated to 2.8% with a 95% confidence interval following ISO uncertainty models.

The standard error on the mean evaluated with the length of the recordings (2 minutes at 25.6kHz), a turbulence intensity of 30%, and an integral time scale of 0.003s approaches 1.5% (see figure 4.28 for integral length scales).

Both the raw and conditioned signals are acquired as they are required to create a temperature dependent velocity calibration of the hot-wire probe prior to each set of measurements. Calibrations were done daily and each time the probe mount was adjusted to capture different regions of the flow. Velocity calibrations were made against a Pitot probe in the free-stream region of the test section. The calibration consists in finding the coefficients required to fit King's Law to a velocity vs voltage graph. Temperature and dynamic pressure as well as atmospheric pressure were recorded in parallel with the raw and conditioned signals.

The hot-wire anemometer was sampled at 25.6kHz, without analog filters for a duration of 30 seconds. Depending on the experiment the acquisition was repeated a number of times in order to obtain statistically converged data. The exact number should be compared to the integral time scales in order to check the convergence of statistics. Data is subsequently filtered below a threshold frequency specified in each experiment, a frequency above which the data is considered noisy from visual study of the velocity spectra. The filter is a box window applied in the frequency domain. Blocks of a few

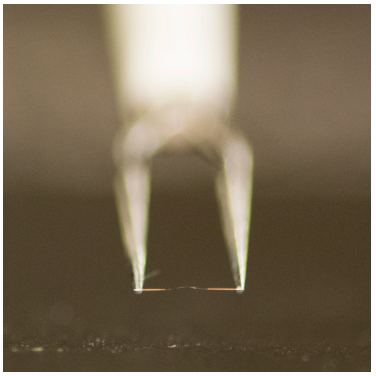

Figure 2.11: Picture of the hot-wire (Model: Dantec 55P01) used throughout the experiment.

$x/H =$		0.5	2	*T.E.*	L_R
	1	1.31	1.70		2.61
$L/H =$	4	1.36	1.68	1.91	1.65
	8	1.43	1.68	1	1.45

Table 2.2: Height (y/H) up to which flow is reversed above the surface of the obstacle.

seconds (detailed in results) are used to produce velocity spectra which are averaged to obtain a converged spectrum at each point of measurement.

Because the hot-wire has finite thickness, it was impossible to obtain data from the exact floor. As a result the probe was brought as close as possible to the floor and photos were taken to estimate the distance between it and the floor. Profiles have different resolutions and height due to the varying regions producing different flows, these ranges and spatial resolutions are specified for each profile in the results sections.

Furthermore, the type of hot-wire used in these experiments is designed to work in flows of uniform direction. In the presence of separated flows, reversed flow regions must be avoided in order to correctly measure velocity. To that effect, we used PIV data to determine in every captured frame how high the recirculation region would extend. The highest point of recirculating flow at each streamwise location is reported in table 2.2. Only one frame out of 2000 for each case displayed reversed flow up to that height. This information is used to locate the hot-wire and provide a valid point of comparison for spectra. Consequently velocity spectra displayed in the rest of this chapter are extracted from the height in table 2.2.

Chapter 3

Pressure distribution around ribs of varying length

The rapid development of particle image velocimetry (PIV) techniques in recent years has lead to a fast increase in temporal and spatial resolution of velocity data. On the other hand, conventional point-wise pressure measurements, crucial to a variety of industrial applications, are limited in the information they provide. Thus interest is growing in estimating pressure from flow velocity information. The alternative ways of obtaining pressure information involve using the Navier-Stokes equations, where all velocity terms can be measured directly through PIV measurements of varying degrees of complexity, and solving for the remaining pressure term.

Starting with the work of Gurka et al. (1999) when time-resolved data was not yet readily accessible, planar PIV velocity snapshots of a pipe and jet flow were used to get time-averaged pressure using a Poisson formulation of the Reynolds-averaged Navier-Stokes equations and results were compared with data from previous studies. In a similar line of work, Hosokawa et al. (2003), used both planar PIV and particle tracking velocimetry (PTV) data of a laminar liquid flow around bubbles to estimate time-averaged pressure using an iterative Poisson solver. Apart from a Poisson formulation, alternative schemes of pressure integration were also analysed, most notably in the work by Liu and Katz (2006) who employed an omni-directional virtual integration scheme to get pressure in a cavity shear flow. Later, van Oudheusden and al (2007) also evaluated time-averaged pressure and forces from planar PIV data in both compressible and incompressible flow cases using a control volume approach and a spatial integration scheme for the pressure gradients.

Building on these time-averaged studies, Fujisawa et al. (2005) were among the first to attempt instantaneous pressure determination, using snapshot PIV on the flow around a

cylinder, although the missing time information posed specific constraints in the boundary conditions used. As high-speed PIV systems started to develop, time-resolved velocity information became available and several studies on instantaneous pressure determination subsequently emerged (Liu and Katz, 2006; Murai et al., 2007; de Kat et al., 2008), effectively shifting the attention towards evaluation methods for the material acceleration term. In that context both Eulerian and Lagrangian approaches for the computation of the acceleration term were assessed in various flow scenarios, often with contradicting results (Jakobsen et al., 1997; Charonko et al., 2010; Violato et al., 2010; de Kat and Van Oudheusden, 2012; Ghaemi et al., 2012). A comprehensive review of these studies can be found in van Oudheusden (2013).

Very recently, new techniques that allow for accurate fully Lagrangian particle tracking were developed. Most notably, Schröder et al. (2015); Schanz and Schröder (2016) presented the 'Shake the Box' algorithm, which uses volumetric time-resolved particle images and reconstructs particle trajectories using previous time-steps to predict future particle positions and corrects accordingly using image matching. To further improve spatial resolution of these rapidly developing particle tracking techniques, Schneiders and Scarano (2016) proposed a method of velocity field reconstruction, which provides high spatial resolution velocity information especially in large-scale experiments where seeding density is low. Such particle tracking methods provide highly accurate velocity gradients and subsequently material acceleration estimations, significantly improving pressure reconstruction when compared to methods that use PIV velocity information which is known to suffer from averaging effects of the cross-correlation process involved (Blinde et al., 2016, for a detailed comparison on pressure estimation using different PIV and PTV based approaches).

These developments show that in a scientific context, the progress of pressure estimation techniques is clearly oriented towards state-of-the-art equipment and complex computational algorithms. On the other hand, for some cases such as industrial measurements, minimization of cost, complexity, and processing time is critical, even at the expense of accuracy. It is therefore valuable to quantify how loss of information (either in terms of time or space) affects the accuracy of pressure estimation methods, so that a balance between cost and performance can be found for different applications. To this end, there was some recent attention towards simpler methods that can provide accurate pressure results even in cases of lower quality input data. The use of Taylor's hypothesis (TH) was assessed in the case of time-resolved 3C-planar data (de Kat and Ganapathisubramani, 2013) and 3C-volumetric snapshots (Laskari et al., 2016) and it was shown to provide reliable pressure estimation in the case of missing either spatial or temporal information respectively, while it was the most robust approach with respect to noise and grid resolution. In a similar context, Schneiders et al. (2016) proposed a method based on the vorticity transport equation to estimate instantaneous pressure from 3D velocity snapshots when time information is not available.

In this chapter, we assess the performance of pressure determination with TH method and 2D velocity snapshots (effectively neglecting temporal and reducing spatial information). The applicability of Taylor's hypothesis when using 2D data is initially evaluated in two experiments over ribs using high-speed and low-speed PIV measurements. With high-speed data, we attempt to compare TH, Eu, and pLA methods to obtain the velocity terms required to estimate pressure using only planar data but keeping temporal resolution. In the second experiment, estimated pressure is obtained using TH and RANS from non time-resolved data. We compare estimates with experimental surface pressure measurements and sources of errors are discussed.

3.1 Obtaining pressure from PIV

PIV providing only velocity information, we must use Navier-Stokes equation rewritten assuming a divergence-free (constant density) and irrotational flow to obtain pressure:

$$\nabla p = -\rho\{\partial u/\partial t + (u \cdot \nabla)u - \nu\nabla^2 u\} \tag{3.1}$$

All terms of this equation are measurable directly through PIV measurements of varying degrees of complexity (2C or 3C, planar or volumetric, time-resolved or non-time resolved) and multiple methods are available to solve the equation for the pressure field (van Oudheusden, 2013) which suit each of the PIV techniques. Regrouping the multiple methods available, are four main concepts. The Lagrangian method, Eulerian method, RANS approach and Taylor's hypothesis approach to computing the acceleration terms in the NSE. The Eulerian and Langrangian approaches are the most reliable approaches in theory, however they require time-resolved information. In addition, the Eulerian approach is affected by measurement noise, and the Lagrangian approach requires reliable particle tracking. de Kat and Ganapathisubramani (2013) proposed an approach applying Taylor's hypothesis to the Eulerian approach, thus reducing the sensitivity to measurement noise on temporal gradients. This consists in replacing temporal gradients with spatial gradients and a local convection velocity. The selection of an appropriate convection velocity for Taylor's formulation of the acceleration term is critical, however it removes the necessity for time-resolved information. Laskari et al. (2016) compared the Langrangian, Eulerian and Taylor's methods in volumetric time-resolved PIV measurements showing that Taylor's hypothesis works best in turbulent boundary layers assuming the convection velocity of turbulent structures is equal to the local mean streamwise velocity.

The continuing improvements in camera technology in terms of acquisition frequency and resolution have made PIV an intensive instrument to measure velocity to the benefit of higher precision. For industrial applications, the complexity of experiments and processing time should be minimized. The usability of Taylor's hypothesis in 3C-planar

de Kat and Ganapathisubramani (2013) and 3C-volumetric Laskari et al. (2016) data shows that pressure can be obtained reliably without the need of expensive time-resolved data. To further test TH, we apply this method to the simplest form of PIV (2D-planar) in a complex but realistic industrial flow to show the possibilities and pinpoint the pitfalls of the methods.

Two experiments were carried out. The first attempts to compare TH, Eu, and pLA methods to obtain the velocity terms required to estimate pressure using only planar data but keeping temporal resolution. In the second experiment, estimated pressure is obtained using TH and RANS from non time-resolved data. We compare estimates with experimental surface pressure measurements and sources of errors are discussed.

3.2 Estimation models

3.2.1 RANS estimation of pressure from PIV statistics

We apply the Reynolds-averaged Navier-Stokes equation to statistics of PIV measurements to obtain the time-averaged pressure gradients as explained by van Oudheusden and al (2007) and Gurka et al. (1999). Assuming a divergence free flow:

$$\nabla p = -\rho\{(\bar{u}\cdot\nabla)\bar{u} + \nabla\cdot\overline{u'u'}\} \tag{3.2}$$

where $u = \bar{u} + u'$ from PIV measurements.

Then the divergence of this equation is integrated using a Poisson solver:

$$\nabla^2 p = \nabla\cdot(-\rho\{(\bar{u}\cdot\nabla)\bar{u} + \nabla\cdot\overline{u'u'}\}) \tag{3.3}$$

A detailed explanation of the use of Taylor's hypothesis in pressure estimation including error assessment is provided by de Kat and Ganapathisubramani (2013). The methodology used to solve the Poisson equation is similar to that used by de Kat and Van Oudheusden (2012). First the pressure gradients are obtained from the simplified Poisson formulation of the NSE. These gradients are then integrated. In this study, the region of integration is bounded by a Dirichlet boundary condition imposing a pressure determined by Bernoulli's equation along the top edge 3.4.

$$p = \frac{1}{2}\rho(\overline{U}^2 + \overline{u'u'}) \tag{3.4}$$

Free-stream pressure is used at the top left corner as a starting point for the integration. This pressure was measured by Pitot tube during the PIV data acquisition. Three Neumann boundary conditions are imposed on the upstream, downstream, and surface edges

of the integration window using the gradients found in the pressure gradient estimates from PIV.

3.2.2 Pressure estimation using Taylor's hypothesis on PIV snapshots

In order to obtain more detailed statistics, we also applied Taylor's hypothesis to Navier-Stokes equation written as follows:

$$\nabla p = -\rho\{du/dt + (u \cdot \nabla)u - \nu\nabla^2 u\} \tag{3.5}$$

assuming divergence-free, or incompressible flow. We use again the Reynolds decomposition throughout:
$u = \bar{u} + u'$

With Taylor's hypothesis:

$$Du'/Dt = \partial u'/\partial t + (U_c \cdot \nabla)u' = 0 \tag{3.6}$$

where we assume $U_c = \bar{u}$, the convection velocity of turbulent eddies is assumed to be equal to the local mean velocity. This is not a valid assumption in the case of separated flows, where the magnitude of the turbulent fluctuations is comparable to the local mean velocity Taylor (1938).

The incompressible Navier- Stokes equation becomes:

$$\nabla p = -\rho\{-(\bar{u} \cdot \nabla)u' + (u \cdot \nabla)u - \nu\nabla^2 u\} \tag{3.7}$$

All of the in-plane velocity components and gradients are available from a set of planar PIV, thus the 2D version of equation 3.7 can be solved. After integration using the same boundary conditions as the RANS estimation in the previous section (Dirichlet at the top edge of the window, and Neumann on the three other edges) we obtain an instantaneous pressure field. The validity of the procedure has been tested and presented by Laskari et al. (2016).

In this study, we consider the separated flow past a rib of given length and height. Time-resolved two-component planar PIV data was used to assess the validity of TH against pLA and EU methods for pressure estimation as well as surface pressure fluctuation measurements. Laskari et al. (2016) carried out an extensive study on the effect of noise and resolution over the results of pressure estimates of this type. Our experiment (reported in section 2.5.2) produced PIV measurements which lie within the range of tested values. The spatial resolution of our PIV grid can be converted to $l^+ = 26$ (13 for the low-speed experiment) and temporal resolution to $t^+ = 0.49$ in their terminology.

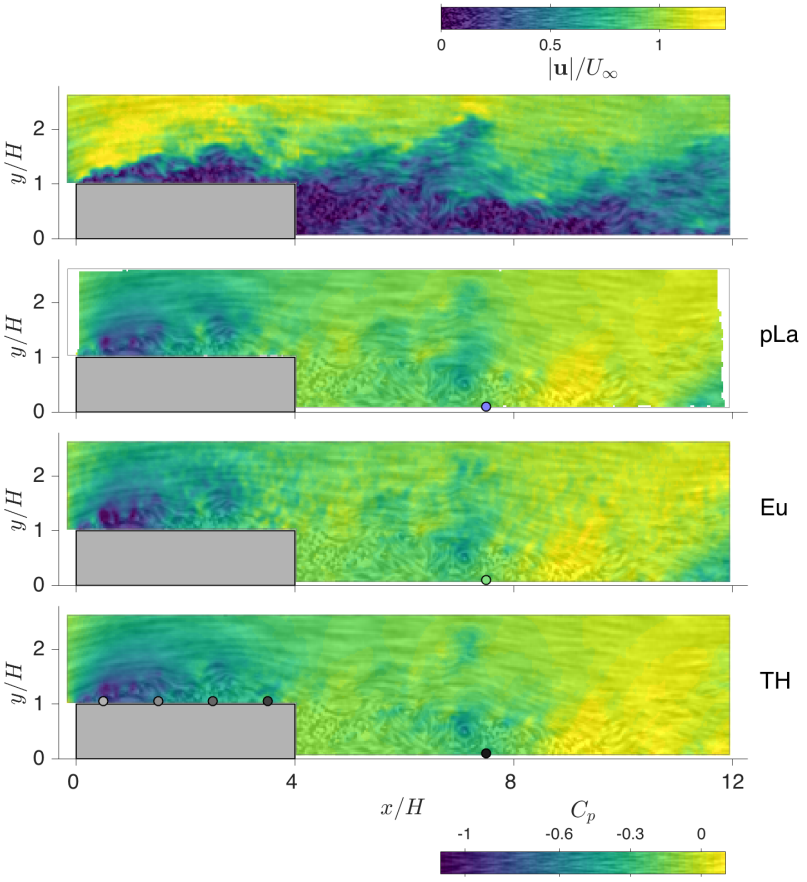

Figure 3.1: Instantaneous pressure snapshots obtained with three different techniques from planar PIV. Top: Instantaneous magnitude of velocity; The three subsequent rows show the pressure estimation from pLA, EU and TH. A video is included as supplementary material.

Although the PIV post-processing settings are not identical, this means these parameters which affect the performance of the estimator are of comparable magnitude. Thus, the estimator should behave with similar performance to that described by Laskari et al. (2016). At these values, Laskari et al. (2016) found that with measurement noise, TH produces better estimates the two other methods. This is encouraging to use in our case.

3.3 Pressure estimation from planar time-resolved data in separated flows

In order to establish the performance of TH with planar measurements compared to other common methods, pressure was obtained using three pressure estimation methods (pLA, EU, TH). Figure 3.1 contains a sample snapshot of the instantaneous pressure estimate (using the three different methods: EU, pLA an TH) around the rib. The evolution of flow trajectory is visualized with Line Integral Convolution inspired by Phillips et al. (2015) and Longmire et al. (2003). LIC was implemented in-house as per

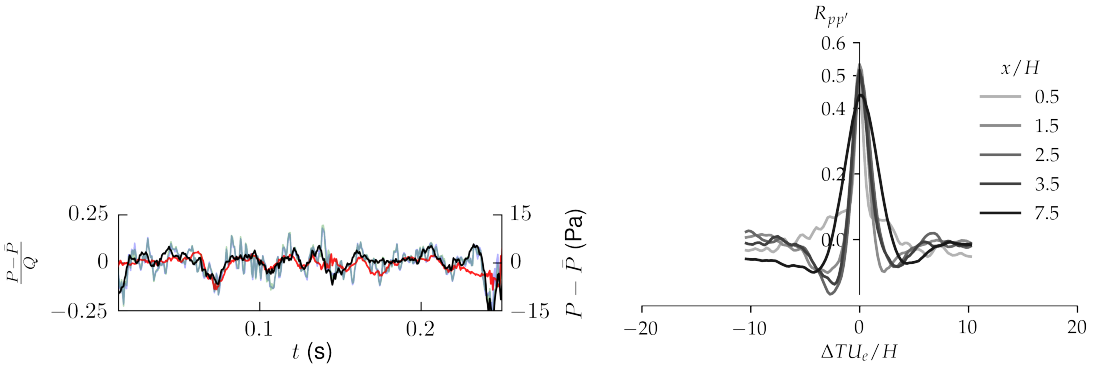

Figure 3.2: Left: Instantaneous time-series obtained from TR-PIV estimates, and corresponding pressure transducer measurements from the transducer located in the wake region ($x/H = 7.5$). Units are in Pascal and normalized by Q (C_P). **Red** corresponds to the reference signal measured with a pressure transducer. **Light blue**, the result of the pLA method. **Light green**, the result of the EU method (behind the transparent blue curve). **Black**, the result of the TH method. Right: Cross-correlation between pressure estimates using TH and the associated time-series for each transducer.

the description of Cabral and Leedom (1993) using the multi-frequency noise technique described by Kiu and Banks (1996). The combination of these techniques provides the clearest visualization of flow trajectory in our PIV snapshots with indications of coherent regions such as vortices shed from the obstacles. A supplementary video was also made using the dynamic LIC technique described by Sundquist (2003) (see supplementary material). The three methods appear to produce similar results behind the leading edge, where shear layer roll-up and vortex shedding occurs. The range of pressure computed within the domain is comparable across all methods. However, The pLA and EU methods tend to introduce more fluctuations towards the edges of the domain of integration. In addition, the Eulerian method shows what seems to be a more noisy result throughout the window of integration. This is not a physical feature of the flow as highlighted in the following section.

Surface pressure fluctuation measurements validate the estimates produced with TR-PIV. In order to do so, a pressure estimates time-series is extracted from the nearest valid point to the pressure transducer. The measured and estimated time-series are synchronized in time therefore direct comparison is possible. Figure 3.2 depicts a sample time-series obtained through direct measurements, and the estimates from pLA, EU and TH from the location $x/H = 7.5$ which is in the wake of the obstacle. The estimates follow the reference signal, but some deviations appear at times. Peaks appear at higher frequencies in the pressure estimates, especially from EU and pLA. TH seems to produce a smoother signal which follows the general trend of the two other estimates.

A more quantitative approach, which is also used by Schneiders et al. (2016), consists in computing the cross-correlation coefficient between pressure estimates p' and the

direct measurements p. Figure 3.2 shows the cross-correlation $R_{pp'}$ computed between the signal from five pressure transducers located by dots in figure 3.1 and the nearest pressure time-series estimated using TH method.

$$R_{pp'}(\tau) = \frac{\langle p(t+\tau)p'(t)\rangle}{\sqrt{\langle p^2\rangle\langle p'^2\rangle}}$$

The figure shows the peak correlation is at zero time lag indicating that there is no phase difference between measured and estimated pressure at these locations. Figure 3.2 also shows that the peak correlation value appears to decrease with increasing stream-wise location. The same procedure was repeated for the two other estimation methods and no measurable time-delay was found between signals. The other methods also show a decrease in peak correlation value with downstream distance.

The peak cross-correlation coefficient for all stream-wise locations and all three methods is reported in table 3.1. The TH method shows a maximum $R_{pp'}$ of 0.54 along the top surface of the obstacle, and 0.46 in the wake region. The highest correlation value is comparable to the other two methods. However, the other methods exhibit a larger decrease in the peak correlation with downstream distance (the maximum difference is approximately 40%). TH estimates are more consistent with spatial location with the maximum difference between points being less than 15%.

It must be noted that planar measurements neglect the span-wise velocity components in pressure estimates. Nevertheless the results appear to produce similar correlation coefficients to more advanced techniques which contain the third dimension as reported by Schneiders et al. (2016) in an attached flow (i.e. a turbulent boundary layer). For example, Table 3 in Schneiders et al. (2016) shows that a vortex-in-cell (VIC) approach together with snapshot 3D data and homogeneous boundary conditions results in a peak correlation coefficient of 0.61 while a Lagrangian approach that uses a three-point stencil produces a peak correlation coefficient of 0.45. Therefore, the range of peak correlation values obtained with the simple TH method and planar PIV data in a separated flow is within the range of 3D time-resolved methods in an attached flow.

The comparable accuracy could be due to the fact that the TH method attenuates noise compared to other Eulerian and Lagrangian methods (see de Kat and Ganapathisubramani 2012; Laskari et al 2016). Two different sources of noise amplification (spatial and temporal gradients) exist in the pLA and EU methods while the TH method is only sensitive to errors from the spatial aspect. This noise attenuation appears to be sufficient to overcome the lack of information along the third direction (velocity and gradients). The propagation of this noise through the Poisson equation and eventually in pressure requires further work and should be the subject of future investigations. In the meantime, the TH method provides the means to compute full-field pressure statistics (and instantaneous pressure) from simple planar PIV data.

Method/Location	0.5	1.5	2.5	3.5	7.5
TH	0.52	0.54	0.50	0.51	0.46
pLA	0.53	0.55	0.52	0.48	0.34
EU	0.57	0.57	0.52	0.48	0.34

Table 3.1: Table containing the peak correlation coefficient between estimated and measured surface pressure. The estimates come from the nearest point to the surface with valid data, this may be several vectors above the surface due to reflections.

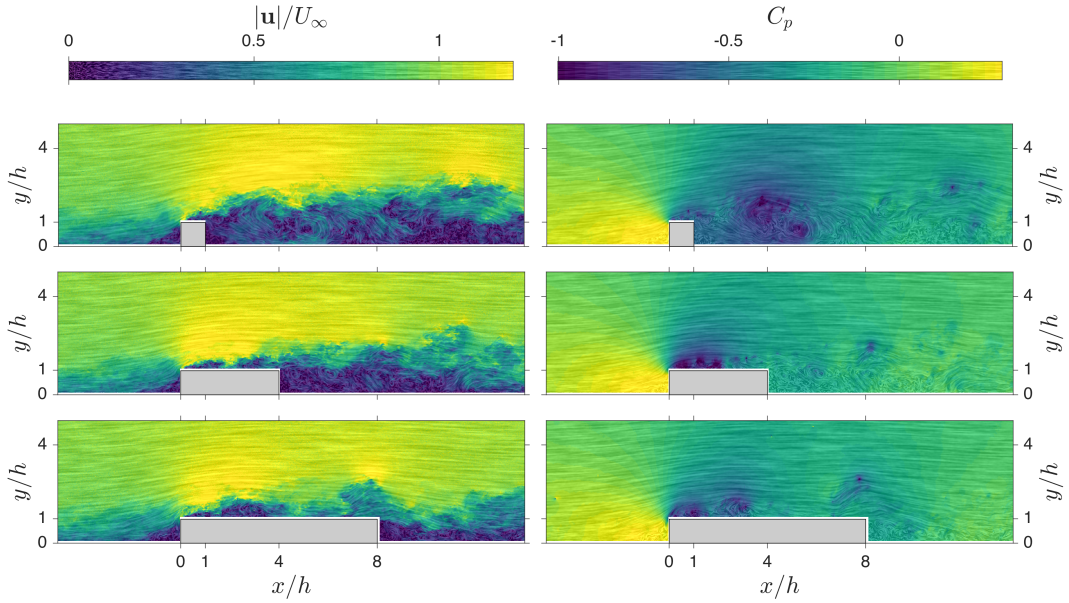

Figure 3.3: Overlay of velocity in the form of LIC and instantaneous pressure contours for three rib lengths ($L/H = 1, 4$ and 8).

3.4 Pressure estimation from snapshot PIV data in separated flows

In keeping with a simple PIV configuration, only uncorrelated snapshot PIV measurements were obtained in the rib experiments. This allows the use of TH method to obtain instantaneous pressure from the snapshot data and subsequently, pressure statistics.

Figure 3.3 shows a sample of the original velocity distribution around three ribs ($L/H = 1, 4$ and 8) in the form of line-integral-convolution (LIC) as well as the corresponding instantaneous pressure distribution obtained using the TH method. Qualitatively, known phenomena are well represented in the pressure field. Most notably, points of high vorticity near the leading edge of the ribs correspond to vortices being shed at this location and travelling downstream along the shear layer. This phenomenon appears in the form of trains of low pressure pulses, matching the centre of each vortex. Furthermore,

in the wake region, a large pocket of slow turbulent flow between appears as a strong disturbance in the estimated pressure field.

The instantaneous data from PIV snapshots can now be used to compute the statistics of pressure (both mean and standard deviation). The statistics thus obtained can then be compared to the direct pressure transducer measurements (for both mean and standard deviation) as well as to the RANS method (as described in section 3.2.1). The comparison to RANS method enables comparison of mean pressure while the TH method can also provide the standard deviation.

Figure 3.4 (left column) shows the mean pressure obtained from TH method (for three critical rib lengths, $L/H = 1, 4, 8$). All contour plots in the figure are obtained using the TH method. Additionally, line plots are shown where the mean pressure from the TH method is compared to the values obtained from RANS method and to direct pressure measurements obtained at select locations at the wall. The line plots for the PIV estimate are obtained along the lowest wall-normal location where there is a valid vector. This is located approximately 3mm from the surface. These comparative line plots show that the mean values from averaged instantaneous pressure estimates are close to the values obtained through the RANS approach. These line plots also indicate a good match between the direct measurements and estimates with a maximum error of 2.5Pa.

On the right of figure 3.4, fields of standard deviation of pressure obtained from TH method are represented along with graphs of surface pressure estimates and measurements for three rib lengths. Standard deviation estimates appear to follow directly measured values in most regions of the flow around ribs for all three cases. In the incoming boundary layer, the pressure estimates and direct measurements are similar. The ratio of the standard deviation of the pressure estimate to that of the direct measurement was found to be 0.91, 1.22 and 0.94 for ribs of length 8, 4 and 1 respectively. This is comparable results obtained in Schneiders et al. (2016) where this ratio was found to vary between 0.88 to 2.55, depending on the method that was employed to estimate the pressure. The best pressure estimate in their study was obtained using a Lagrangian method applied to tomographic PIV data (with 9 time-steps), which yielded a ratio of 1 and the cross correlation of 0.65. The best snapshot method (with snapshot tomographic PIV data) attained a ratio of 0.95 with a correlation of 0.59. This suggests that current TH method with snapshot planar data can perform as well as other methods in attached flows, but in separated flows.

In the top and wake regions, as seen in table 3.2, there are discrepancies in selected areas of the flow field. The worst differences appear to be near the leading edge of the rib where the ratio reaches to 1.6. There are two main factors that could explain this large difference and these are examined in more detail below.

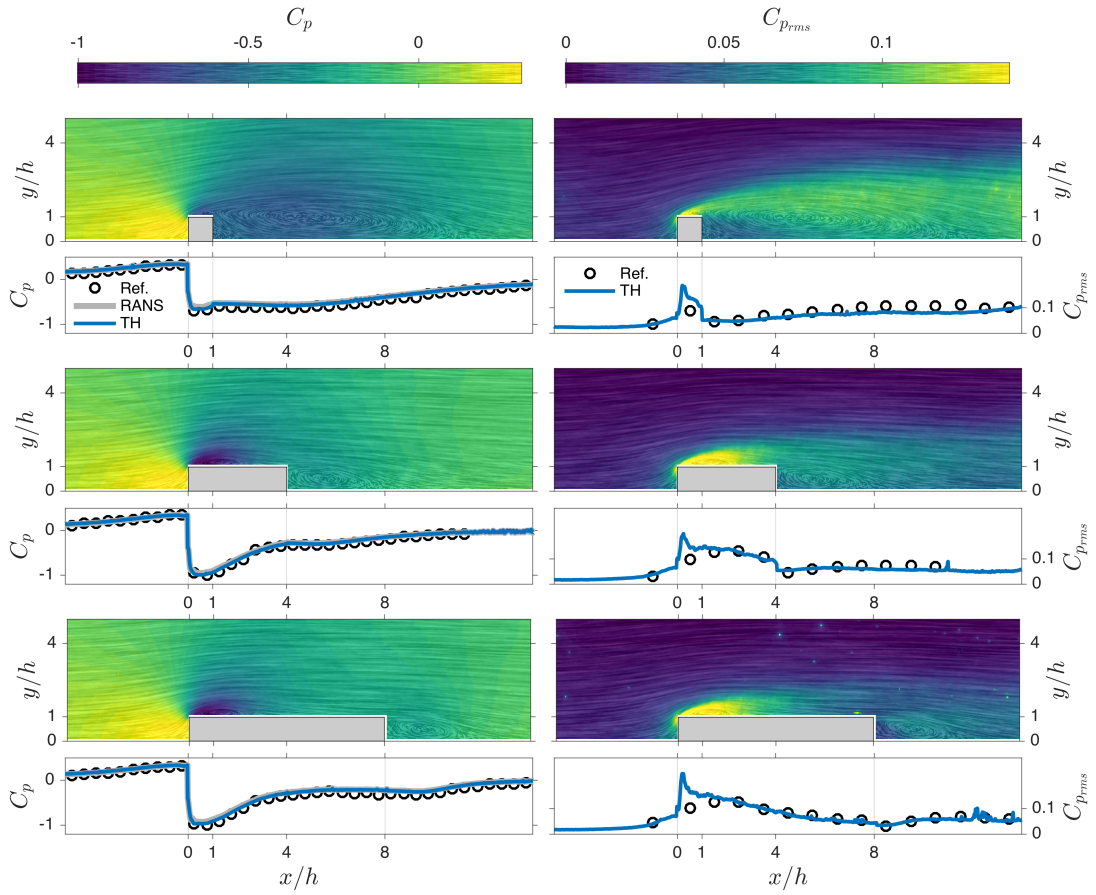

Figure 3.4: Statistics of pressure for $L/H = 1, 4, 8$. The left column shows average pressure ($\bar{P}$). The contours are obtained using TH method. The Grey line in the line-plot is using the RANS method, the blue line is using TH method while the symbols are from pressure tapping located at the wall. The right column shows standard deviation of pressure fluctuations (σP) where the blue line is from TH method and symbols are from pressure transducers located at the wall.

Difference	Smallest	Largest
$L/H = 1$	$x/H = 1.5$ (1.05)	$x/H = 0.5$ (1.6)
$L/H = 4$	$x/H = 2.5$ (0.96)	$x/H = 0.5$ (1.44)
$L/H = 8$	$x/H = 2.5$ (1.00)	$x/H = 0.5$ (1.6)

Table 3.2: Location and value of the largest and smallest difference between estimated and measured surface pressure standard deviation for each case of rib length. The value in parenthesis is the ratio between standard deviation of estimated surface pressure to measured values.

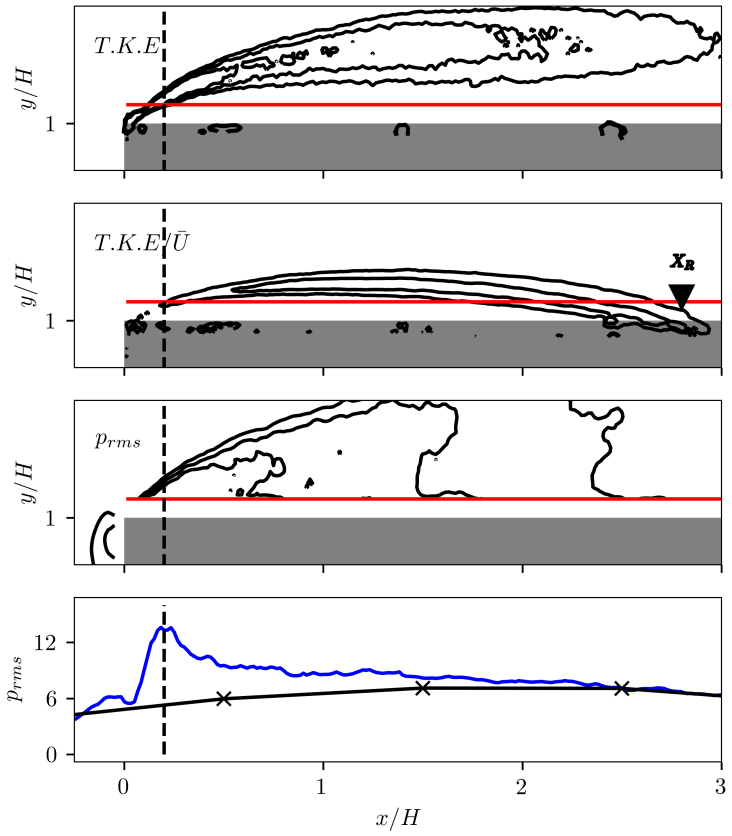

Figure 3.5: Discrepancies in pressure measurements and estimation near the leading edge of the long rib. Top to bottom: $T.K.E.$, $T.K.E./\bar{U}$, σ_P, σ_P estimated (blue) and measured (black) at surface. The black dashed line crosses through the peak in σ_P at the surface. The red line represents the bottom of the estimated pressure field.

The first is related to validity of Taylor's hypothesis, which is assumed to be true when computing the estimates. Taylor's hypothesis is valid only if the velocity fluctuations are much smaller than the convection velocity of these fluctuations. In this study, the convection velocity is assumed to be the local average velocity. This assumption is suitable in the case of an attached flow, however, near the leading edge of ribs, strong turbulence is present as shown in figure 3.5 ($T.K.E \approx 30\%$). In addition, these regions of strong turbulence also coincide with recirculation regions where local mean velocity is reduced to zero. When fluctuation levels are normalized by local mean velocity the ratio of the two becomes infinite as the flow stops. Consequently the TH method cannot be valid in this region.

As can be seen in the p_{rms} contours of figure 3.5, high $T.K.E$ regions match high p_{rms} regions. Consequently we would expect p_{rms} to decrease with $T.K.E$ as we approach

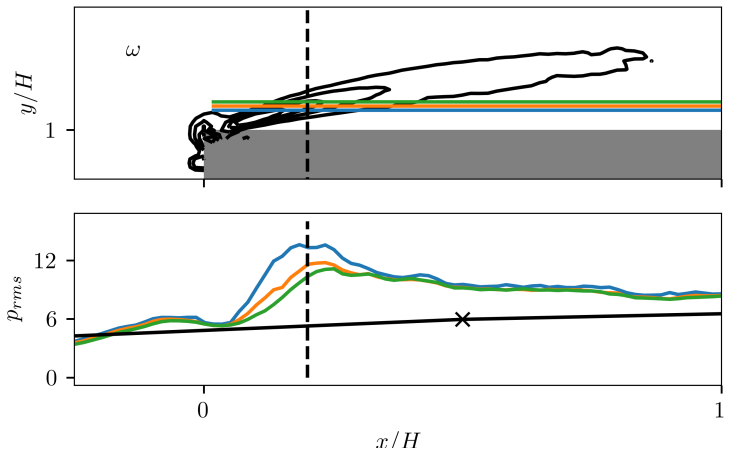

Figure 3.6: Effect of sample location when comparing estimates with measurements near the leading edge of rib ($L/H = 8$). Different colored lines in the vorticity map represent the sample location corresponding to the colored lines in the pressure distribution graph beneath. These are compared against surface measurements (black line with crosses).

the surface of the obstacle. On the other hand below the high $T.K.E$ plume, the p_{rms} contour still persists instead of reducing with decreasing $T.K.E$. This is because the high $T.K.E/\bar{U}$ ratio region begins below the high $T.K.E$ region. Here TH is invalid and the smallest velocity fluctuation will cause a very large fluctuation in TH, thus p_{rms} is inaccurate. This explains the broad regions between separation and reattachment over which p_{rms} measured and estimated at the surface are different. Despite this, the worst ratio of estimate pressure to measured pressure is only 1.6, which is comparable to (or better than) some estimation methods using 3D time-resolved data.

The second factor is linked to the region of integration for pressure estimates not reaching the surface of the rib, thus we are comparing measurements at the surface with estimates away from the surface. This is seen as a sharp peak present in the pressure estimates immediately after the leading edge of each rib. When studying the region of pressure estimation (its edge is illustrated in red in figure 3.5) it is clear the integration window ends some distance above the surface where pressure measurements are taken. The window of integration slices through the shear layer above the surface where strong vortices are shed. Since the location of the peak in estimated p_{rms} and the intersection with the shear layer match, it is possible that the low pressure cores of the vortices shed from the leading edge are included in the p_{rms} estimates. The effect of sample location can in fact be illustrated by shifting the sample location (red line). Figure 3.6 depicts that samples taken further from the surface show a peak in p_{rms} located further downstream. At the surface of the rib, there is no pressure tap close enough to the leading edge to capture the pressure drop inside these vortices.

Discrepancies are also found in the wake of the short rib. The largest discrepancy occurs

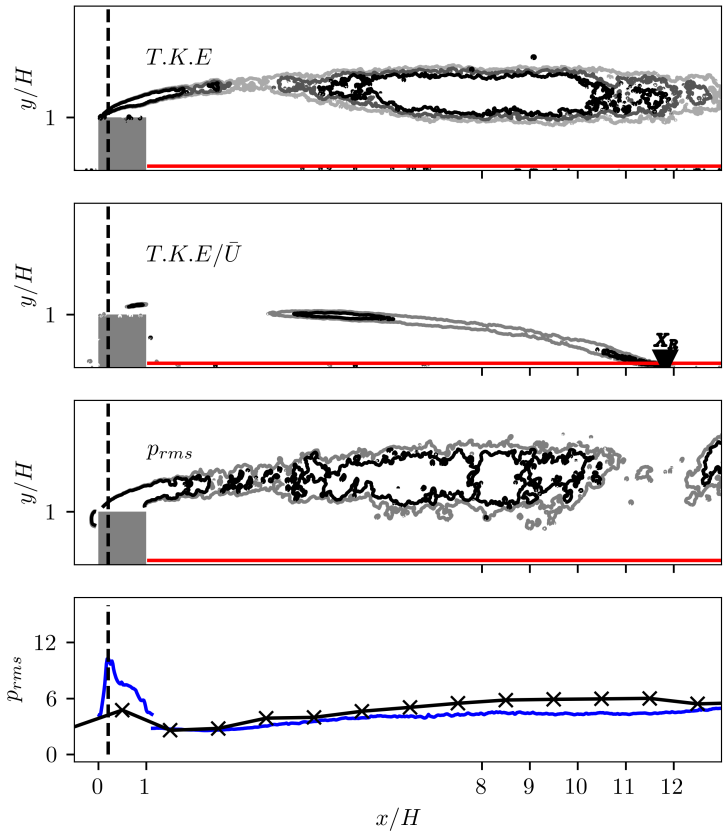

Figure 3.7: Discrepancies in pressure from estimation and measurements in the case of the short rib. Top to bottom: $T.K.E.$, $T.K.E./\bar{U}$, σ_P, σ_P estimated (blue) and measured (black) at surface. The black dashed line crosses through the peak in σ_P at the surface. The red line represents the bottom of the estimated pressure field.

near the reattachment point (x_R). It can be seen from figure 3.7 that in the wake of the short rib the high p_{rms} region follows broadly the high $T.K.E.$ regions, however as we approach the surface near the reattachment point the high $T.K.E/\bar{U}$ region intersects the window of pressure estimation. Once again, the large ratio invalidating Taylor's hypothesis causes the large error visible in the comparison of surface pressure measurements and estimation. In this region a small variation near the reattachment point could produce an actual convection velocity in the wrong direction thus creating unrealistic pressure estimates.

Chapter 4

Separation and reattachment over ribs of varying length

In this chapter, we review the main trends observed as we vary the distance between leading and trailing edges of a surface-mounted rib.

4.1 Trends of recirculation length with varying rib length

The flow over ribs of varying length produces up to three separation regions. Figure 4.1 summarizes the evolution of those recirculation regions as a function of rib length. At the top of the figure, long ribs produce three small recirculation regions: in front, on top and in the wake. The medium length ribs show the top and wake regions beginning to merge as they are brought closer to each other. Finally, the short ribs show one large recirculation region from the leading edge to the downstream surface. In relative terms, the recirculation region of long and medium ribs are much smaller than that of short ribs. The length of these regions is the first quantity of interest in this chapter.

We use the location at the surface where U, the stream-wise velocity component, switches from negative to positive to determine the size of each recirculation region. Due to laser reflections at the surface, the nearest row of valid velocity vectors is offset from the physical surface of the rib by typically $y/H = 0.1$ or less. The dimensions of the bubbles plotted against rib length highlight two trends which are depicted in figure 4.2. Long ribs produce a recirculation region length above the top surface which is steady at $2.7H$, and a wake region which asymptotes to $3.8H$. Short ribs on the other hand produce a single recirculation region of which the length decreases linearly from $13.3H$ in case $L/H = 0.1$ to $4.4H$ in case $L/H = 4$.

The size of recirculation regions is dictated by parameters such as incoming boundary layer thickness, Reynolds number, and the amount of turbulence in the flow. However,

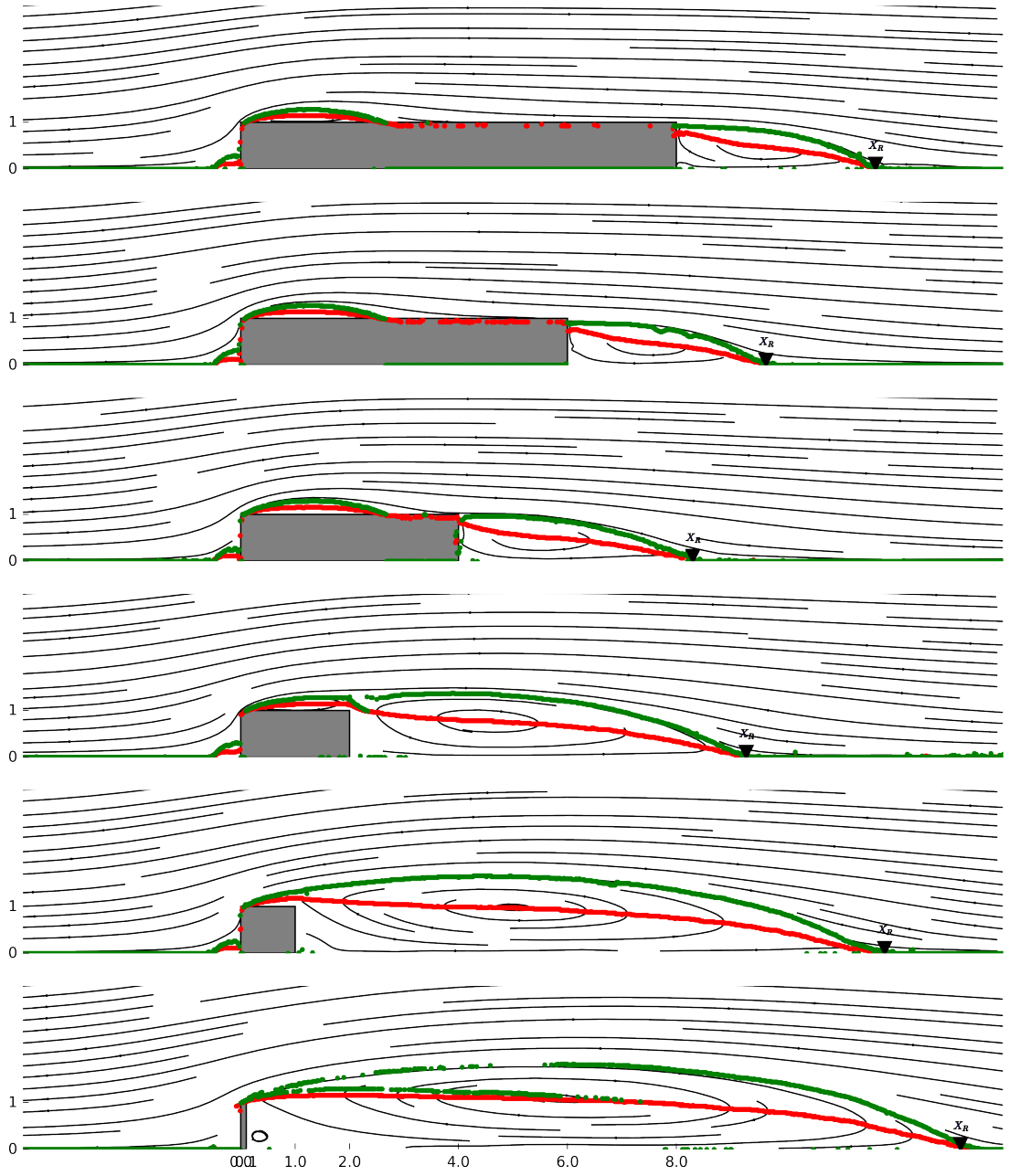

Figure 4.1: Organization of recirculation regions around ribs of varying length. The red line links points where $U = 0$. The green line bounds flow trapped inside the recirculation bubble.

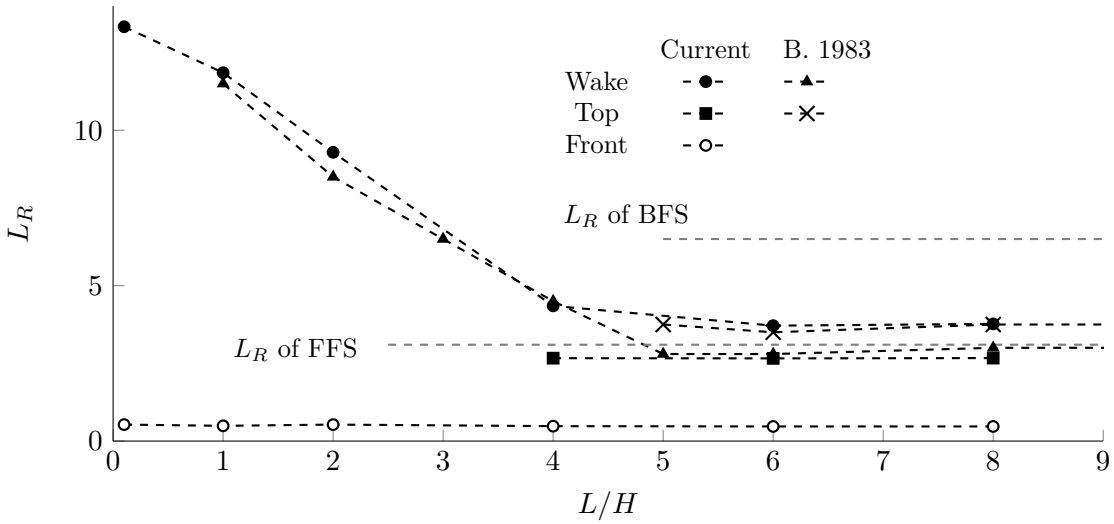

Figure 4.2: Length of three recirculation regions compared with Bergeles and Athanassiadis (1983), an isolated FFS Sherry et al. (2010), and an isolated BFS Adams and Johnston (1988).

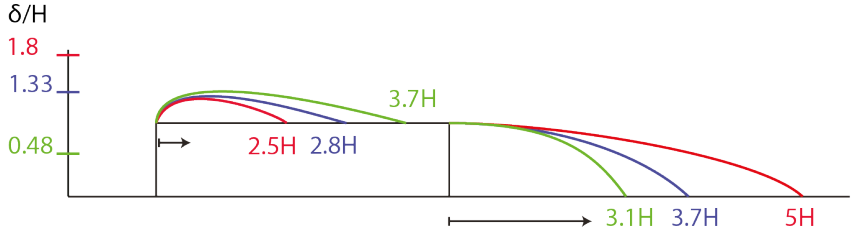

Figure 4.3: Effect of boundary layer thickness on length of recirculation regions of a rib $L/H = 4$. The forward and backward-facing steps behave in reverse with variation of incoming boundary layer thickness.- Arie et al. (1975a), - current study, - Bergeles and Athanassiadis (1983)

a debate exists around which parameter affects bubble size the most. We found two experiments with comparable governing parameters, only the thickness of the boundary layer is significantly different. We compare the bubble lengths of our configuration where the boundary layer is thicker than the rib $\delta/H = 1.33$ to the work of Bergeles and Athanassiadis (1983) with the opposite situation ($\delta/H < 1$), and Arie et al. (1975b) with $\delta/H = 1.8$. Both these publications quote a comparable Reynolds number based on step height. This isolates the effects of incoming boundary layer thickness over the ribs.

Figure 4.2 juxtaposes the recirculation region lengths measured by Bergeles and Athanassiadis (1983), and the present experiment for front, top and wake regions. Note that the top region does not exist for ribs shorter than $L/H = 4$. In comparison with Bergeles and Athanassiadis (1983), the recirculation length of the top region in this study

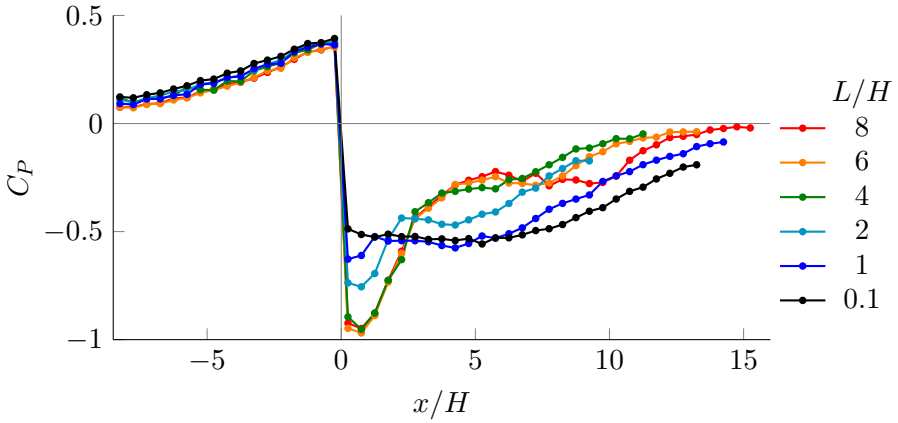

Figure 4.4: Mean surface pressure distribution measured for all rib lengths, corrected for the pressure gradient in the test-section.

is approximately 25% shorter. However, this is consistent with the behaviour of an "isolated" forward-facing step. According to Sherry et al. (2010) the larger δ/H of the present study should indeed yield a smaller recirculation region. On the contrary, the higher Reynolds number should yield a longer recirculation region. Nevertheless, it appears boundary layer thickness prevails on the size of recirculation length in the current regime.

The opposite situation appears in the wake region because the increased recirculation region length above the rib has a direct impact on the wake region downstream. Unlike the top region, in our experiments, the wake region is consistently longer than it is in Bergeles and Athanassiadis (1983), but still only 55% of the length of the recirculation region of a comparable isolated BFS (Adams and Johnston, 1988). Arie et al. (1975b), with $\delta/H = 1.8$ and $Re_H = 30000$, obtain an even longer $L_R/H = 5$. This is illustrated for case $L/H = 4$ in figure 4.3.

In conclusion, if we ranked all three studies by boundary layer thickness a trend becomes apparent where the longer recirculation region on the top surface possibly produces a flow with less momentum at the trailing edge of the rib, and produces a smaller wake recirculation region. This trend is driven mostly by incoming boundary layer thickness. This hypothesis is validated in the next chapter when we investigate the velocity profiles at the trailing edge of each rib.

4.2 Surface pressure distribution

4.2.1 Mean surface pressure distribution

Figure 4.4 summarizes the pressure distribution of all cases studied in this experiment. Figure 4.5 distinguishes the two cases identified by Bergeles and Athanassiadis (1983).

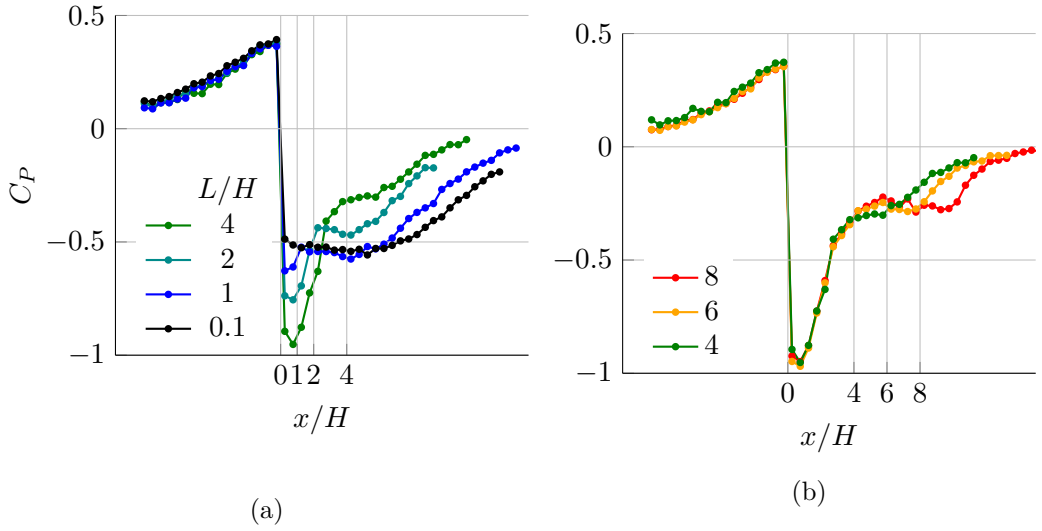

Figure 4.5: Pressure distribution on the surface of short ribs (a), and long ribs (b).

There exists a clear discrepancy in flow behaviour near the leading edge. In the case of short ribs, the magnitude of peak C_P increases with obstacle length. This behaviour extends to the fence case displaying the lowest C_P magnitude. However, the fence produces a rounder pressure distribution in its wake. For short ribs, the peak C_P is quickly reduced with streamwise distance from the leading edge along the top of the obstacle. From the trailing edge and further downstream, the rate of reduction in C_P reduces to values similar to those observed in the wake of the fence. One must keep in mind that according to previous literature, none of the short ribs should have flow reattachment on the top surface, yet the presence of this short horizontal surface has a strong effect on the pressure distribution in the wake. The absence of flow reattachment on the top surface is illustrated in figure 4.1.

In the case of long ribs, a different behaviour is observed. Long ribs, according to Bergeles and Athanassiadis (1983) and our measurements, present a mean reattachment point on the top surface as confirmed in figure 4.1. It appears that peak C_P occurring near the leading edge is -0.97 and is unaffected by obstacle length. It also seems that for longer obstacles, pressure on the top surface settles progressively before the trailing edge. Otherwise, the pressure distribution on the top surface is very similar for $L/H = 6$ and 8. However, there is no clear link between where the pressure settles and the location of the mean reattachment point. Discrepancies between long ribs only occur after the trailing edge, where the surface pressure returns to 0. The slope of pressure recovery near the obstacle is steeper as obstacle length increases. All three C_P distributions of this case seem to meet further downstream of the obstacle. It is not exact, but the recovery far downstream of the obstacle seems to occur at similar rates for all three obstacles.

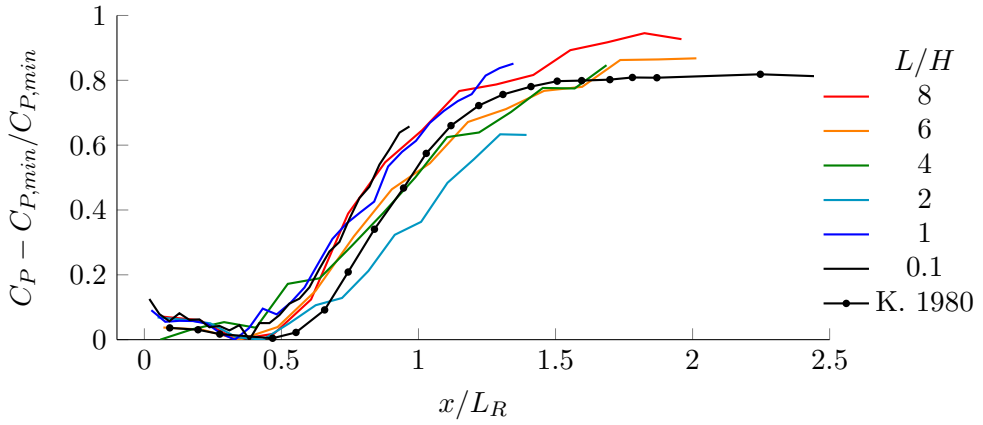

Figure 4.6: Rescaled wake region pressure distribution as per Kim et al. (1980).

We attempted to normalize C_P to show if there is a similarity in recovery rate, and figure 4.6 illustrates surface pressure distribution from the trailing edge of each rib downstream normalized by minimum and rescaled in relation to the mean reattachment point. This normalization is described by Kim et al. (1980) in the case of BFS by

$$\frac{C_P - C_{P,min}}{C_{P,min}}$$

In general, the pressure distribution in the wake of each rib matches somewhat the case of an isolated BFS (Kim et al., 1980) albeit the distributions for each rib length show slight variations. The initial part near the trailing edge appears to be similar for all rib cases and the BFS case. However, this similarity does not hold further downstream. The C_P distribution plateaus at a location which varies with rib length. The longest rib appears to stabilize 20% L_R further downstream of the mean reattachment point compared to a BFS. As rib length shortens, the plateau moves upstream. Case $L/H = 2$ has already plateaued 10% of L_R earlier than the BFS. Even shorter ribs appear to follow a different pattern, which recovers at the same rate as a BFS, but offset in stream-wise position.

Using the pressure estimates from PIV from chapter 3, we computed the pressure difference between the forward and backward-facing face of each obstacle studied with snapshot PIV ($L/H = 0.1, 1, 2, 4, 6, 8$) normalized by the dynamic pressure of the free-stream flow ($U_e = 10$m/s), as well as the height of the rib H. The results show that pressure drag follows a similar trend to that of bubble dimensions although not linear. Indeed, short ribs produce the largest amount of drag. Drag coefficient decreases with rib length up to $L/H = 4$, where it begins to converge to 0.45 for $L/H = 8$. Figure 4.7 depicts the trend observed in pressure drag.

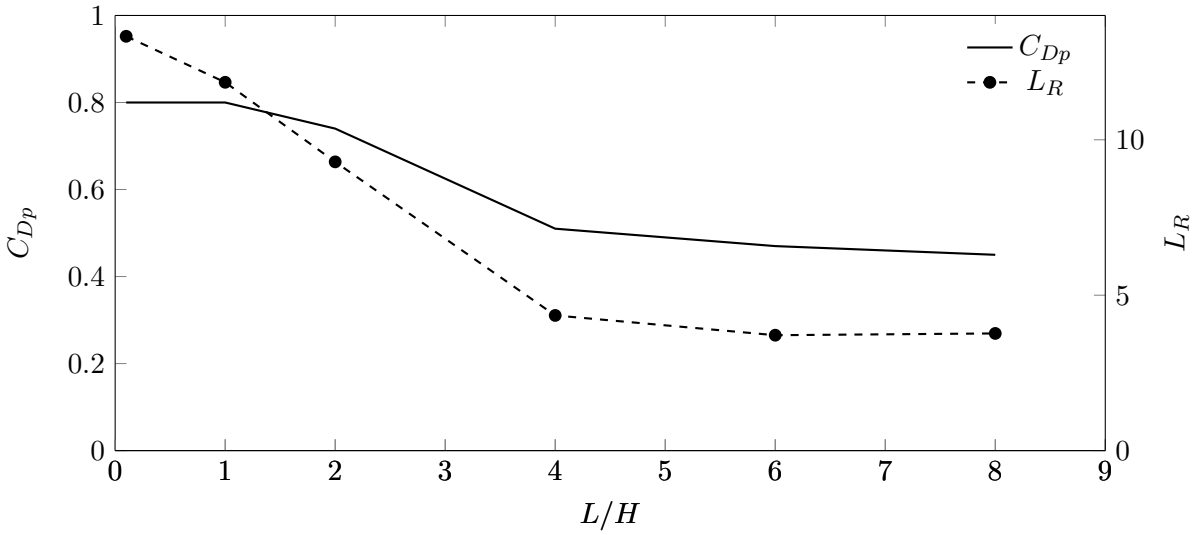

Figure 4.7: Pressure drag coefficient obtained by computing the pressure difference between front and back faces of each rib. Drag is normalized by dynamic pressure of the free-stream and rib height H.

4.2.2 Surface pressure fluctuations

Pressure transducers were installed at several stream-wise positions to measure surface pressure fluctuations for three rib lengths $L/H = 1, 4$ and 8. The measurements comprised four 30-second series at an acquisition frequency $f_s = 25.6$kHz. The pressure series are multiplied by a single transducer-specific gain, then low-pass filtered below 1.28kHz, and acoustic noise is cancelled. The standard deviation of the corrected pressure series is used in figure 4.8. It appears that all ribs produce two regions of high surface pressure fluctuations. The first one occurs after separation at the leading edge, the second near the mean reattachment location in the wake region. The longest ribs appear to produce similar pressure fluctuations on the top surface. The trailing edge produces a sharp drop in the magnitude of pressure fluctuations. Progressing downstream towards their respective mean reattachment point (x_R/H =8.3 and 11.8), both long ribs produce again high surface pressure fluctuations. However, $L/H = 4$ produces 9% more fluctuations. The short rib generates the lowest measured pressure fluctuations on the top surface. However, the wake region sees the highest fluctuation amplitude which is 55% higher at its mean reattachment point ($x_R/H = 11.8$) than the longest rib.

The pressure fluctuation measurements were made with several pressure transducers at once. Therefore, it is possible to use the correlation between transducer signals to determine the convection velocity across the surface of ribs. Figure 4.9 represents pressure fluctuations along the top surface of case $L/H = 4$ against time in seconds and stream-wise location normalized by step height H. It appears that this rib produces periodical events of low and high pressure travelling downstream with time. These are

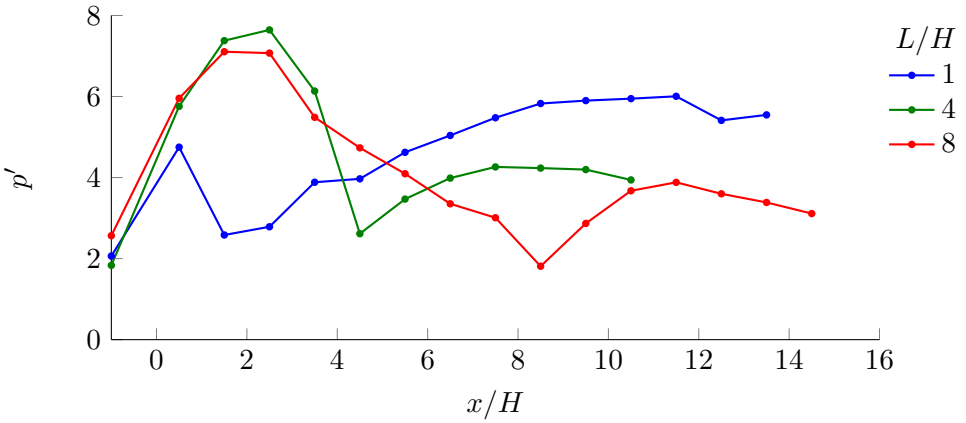

Figure 4.8: Standard deviation of surface pressure fluctuations at each streamwise location for three ribs of interest.

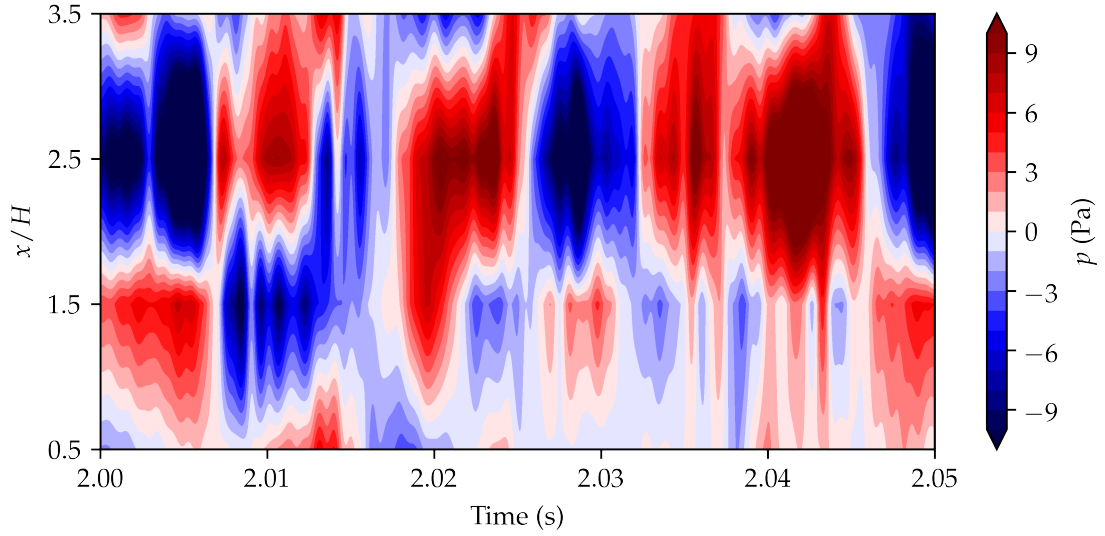

Figure 4.9: Evolution with time of pressure fluctuations along the top surface of $L/H = 4$.

visible as parallel blue and red regions laying diagonally in the figure. Their orientation provides an indication of convection velocity where a steeper pattern indicates a higher convection velocity, and vice versa. Along the top surface of $L/H = 4$, a pattern forms downstream of the leading edge where a region of low of high pressure appears immediately downstream of the edge. With time, it turns into an elongated region which travels from $x/H = 2.5$ at a nearly constant rate towards the trailing edge of the rib and beyond. One may conclude that relatively large amplitude fluctuations are generated by the leading edge separation and are modulated along the top surface before reaching the wake region.

In order to quantify the convection velocity of these high or low pressure events highlighted above, several techniques are available. We use cross-correlation in time between

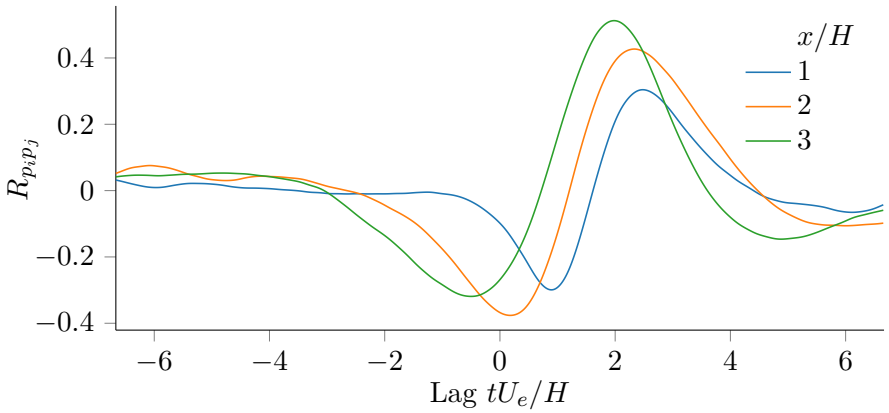

Figure 4.10: Two-point correlation of surface pressure data from the top of $L/H = 4$ between a location and the next one downstream. The legend denotes the mid-point between locations used in the correlation.

transducer signals to evaluate the time necessary for events to travel from one measurement location to the following one. A cross-correlation coefficient $R_{p_ip_j}$ is evaluated between a transducer i and the next one downstream j to evaluate a "local" convection velocity using a similar equation to the equation found in Clark et al. (2014):

$$R_{p_j,p_i}(\tau) = \frac{\langle p_j(t+\tau)p_i(t)\rangle}{\sqrt{\langle p_j^2\rangle\langle p_i^2\rangle}} \tag{4.1}$$

where p represents a pressure measurement point denominated by the subscript. τ is a time lag. t denotes time.

The result of this operation is plotted in figure 4.10 using data from measurements along the top surface of $L/H = 4$. The legend denotes the mid-point between transducers used in the cross-correlation. In other words, the curve denominated $x/H = 1$ is in fact the cross-correlation between microphones at $x/H = 0.5$ and $x/H = 1.5$. The operation is made with 6 second-long time series acquired at 25.6kHz.

From correlations such as the ones presented in figure 4.10 we may determine the lag between two signals by locating the peak value. Using the distance between successive microphones ($1H$), we obtain a convection velocity U_c. The evolution of this convection velocity is plotted against stream-wise position x/H for three obstacle lengths in figure 4.11.

Several features are consistent across the three studied cases. The cross-correlation of pressure series shows that a high convection velocity is reached between the transducer -$1H$ upstream of the rib and the first one after the leading edge ($0.5H$). This high convection velocity immediately drops to values between 43% and 80% of U_e along the top surface of the longest rib. This is consistent with Awasthi et al. (2014) quoting a convection velocity of 80% of U_e along the top surface of a forward-facing step. A similar

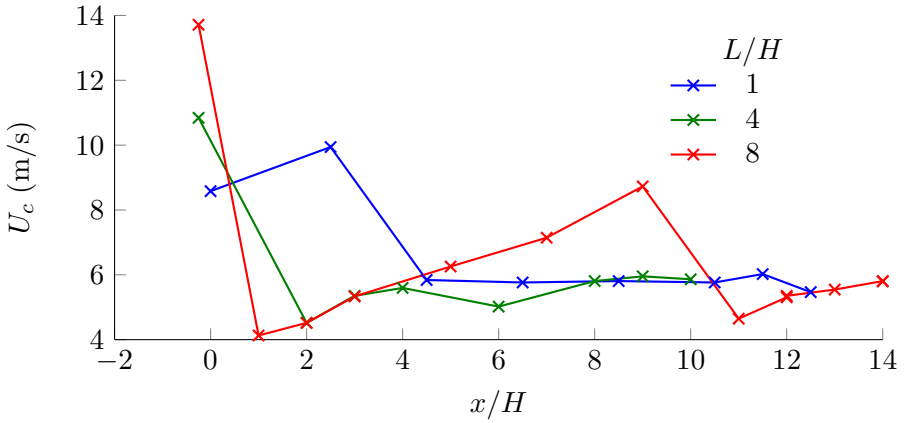

Figure 4.11: Convection velocity of pressure along the surface of three ribs plotted between successive pressure transducers.

observation is made for $L/H = 4$ at the leading edge. In contrast, shorter ribs seem to produce a faster convection along the top surface, which approaches 93% of U_e between the first and second microphone. In the wake of a square rib, Shi et al. (2010) quote a convection velocity of approximately 40% .

In average quantities, the similarities existing in L_R were also found in pressure. The FFS portion of long ribs produces a flow that is similar to an isolated FFS, whereas short ribs produce a more variable flow. In the next section, we study more statistics of these quantities to further highlight similarities and discrepancies between ribs.

4.3 Dimensions of the recirculation regions

The previous sections highlighted trends in mean recirculation bubble length, and surface pressure distribution on ribs of varying length. The following section investigates length, height and area of recirculation bubble in the plane of measurement and how fluctuations of these quantities may vary with rib length. These measurements are available because we used PIV to measure velocity around the rib. To the author's knowledge this is the first description of height and area of recirculation regions for various rib lengths in one single consistent experiment. It is also the first report of their fluctuations. These quantities matter in describing the full extent of a recirculation region. Indeed, most studies are limited to bubble length or reattachment point at the surface, but in some applications such as wind disturbance in the civil engineering sector, this is not sufficient.

The height of a recirculation region corresponds to the highest vector with negative stream-wise velocity U at each stream-wise point of measurement in the region of interest. The y/H coordinates of these vectors are then averaged to obtain a mean recirculation region height for each PIV snapshot. The area in the PIV plane is given by the

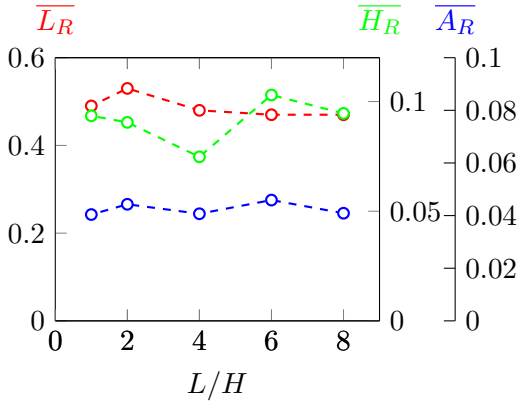

(a)

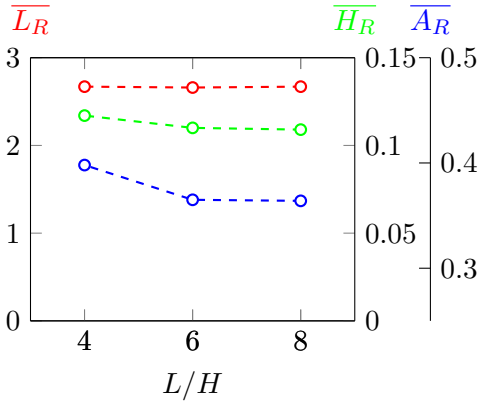

(b)

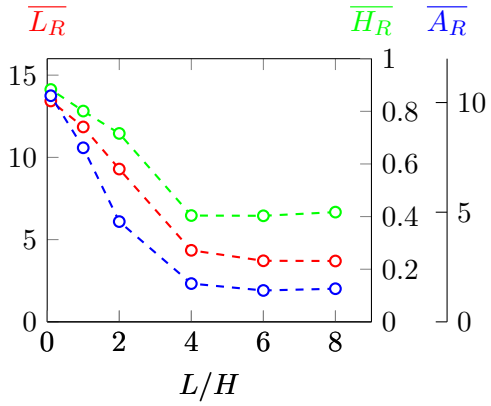

(c)

Figure 4.12: Average dimensions of recirculation region around ribs of varying length. (a) Front region, (b) Top region, (c) Wake region. A_R corresponds to the area in the plane of measurement and H_R the height of the recirculation region.

sum of vectors with $U \leq 0$ in each area of interest. The number of vectors is converted to units of area by the size of each vector window ($\approx 0.28 \times 10^{-3} H^2$).

Figure 4.12 contains a summary of average dimensions for all three recirculation regions in each case. The mean values for the front bubble are shown in figure 4.12a. The values for the top bubble (that only exists for the long ribs) are shown in figure 4.12b and the quantities for the wake bubble (whose length begins at the leading-edge for short ribs and the trailing edge for long ribs) are shown in figure 4.12c. Average height and area follow the same trends as observed in bubble length. Short ribs produce regions with area, height and length inversely proportional to rib length. Long ribs produce wake regions whose length asymptotes to a constant value. The top region remains of nearly constant dimension, as does the front recirculation region.

4.3.1 Dimensions of top recirculation regions

Figure 4.13 presents probability distributions of each quantity (area, height and length) of the recirculation region on top of the long ribs. The distributions are presented

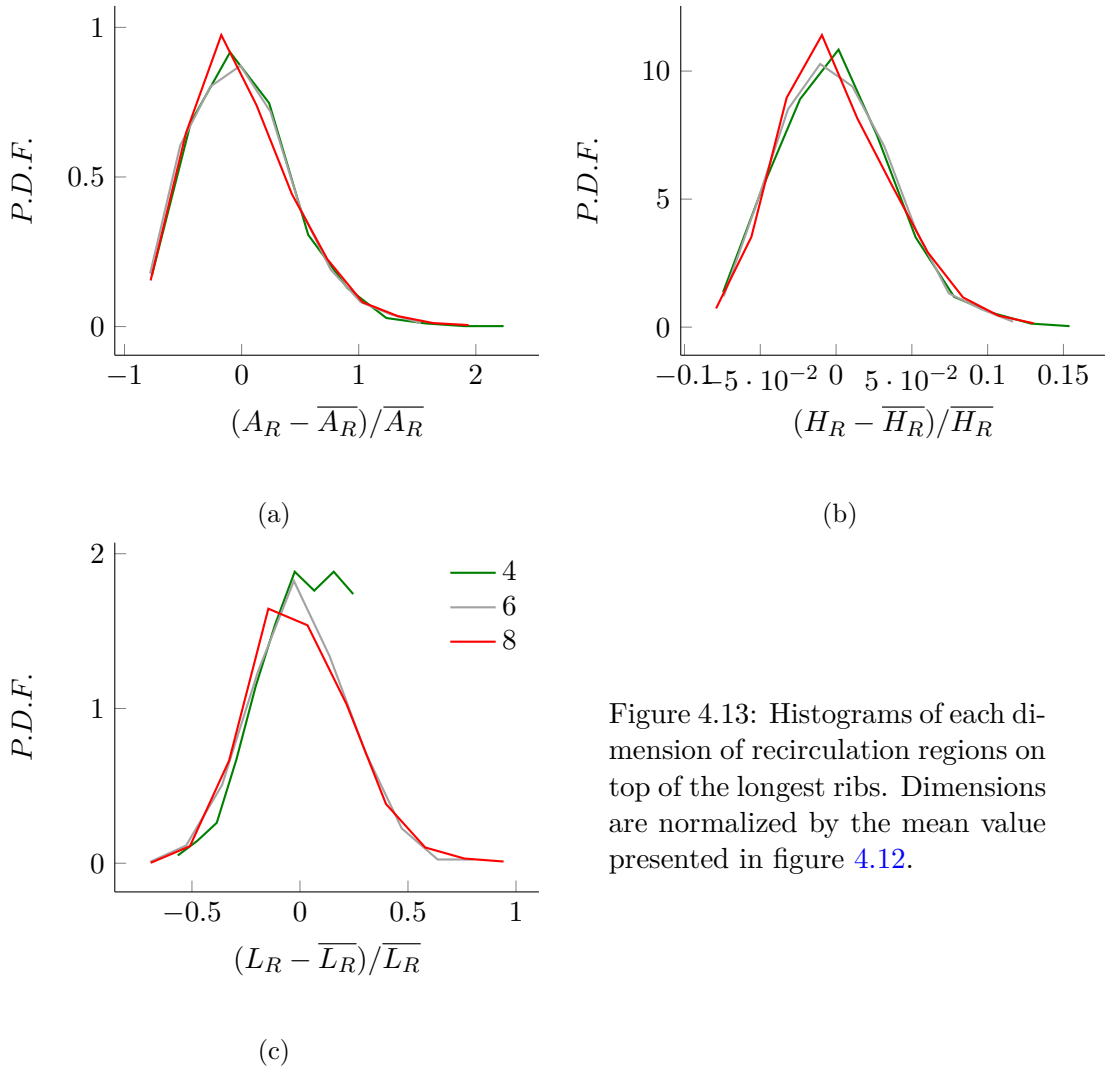

Figure 4.13: Histograms of each dimension of recirculation regions on top of the longest ribs. Dimensions are normalized by the mean value presented in figure 4.12.

relative to the mean dimension presented in figure 4.12. It is clear from the distribution that the fluctuations of the dimensions about the mean are similar for ribs of length $L/H = 4, 6$, or 8. These distributions show a mode that is marginally negative and a long tail on the positive side. This trend appears to be the same for all three dimensions. This indicates that the bubbles are often smaller than the mean value, but tend to grow far more than they shrink. Therefore, the recirculating flow regions are constrained in how small they can be, but are able to grow occasionally in size. The distribution of the recirculation length of $L/H = 4$ is clipped on the right side because in many instances the bubble extends past the trailing edge. This suggests the top bubble may merge with the recirculation region in the wake instantaneously.

The individual quantities which define the size of a recirculation region show similarities between different rib lengths. Studying the relationship between these quantities for each rib indicates further conclusions on the shape of these regions. A two-dimensional histogram made with the instantaneous bubble dimensions identifies links between height

and area, height and length or area and length. These histograms are split into 10 bins and normalized.

For the top region of case $L/H = 8$, figure 4.14 (a., c., e.) contains three two-dimensional histograms, which relate bubble length L_R with bubble height H_R, height with area in the plane of measurement A_R and length with area. It appears the relationship between bubble height and length is weak in the top region as indicated by the circular pattern of the histogram. Bubble length and area show some degree of correlation with a triangular shaped patch in the histogram. It appears the recirculation has a sharp minimum length for a given area, but no clear maximum. Thus, it can grow in length but maintain a small area, but a large area cannot be associated with very small lengths. Finally, height and area seem strongly correlated as indicated by the well-defined angled ellipse in the histogram. This ellipse describes a positive relationship between area and height, meaning that a large bubble area is often associated with a high bubble.

The data presented in 4.14 (a., c., e.) is extracted from the $L/H = 8$ case, but the same operation was executed for the three long ribs ($L/H = 4$, 6 and 8). The results of all three ribs are in agreement. However, it is relevant to know whether the relationship between area and height changes with rib length. Figure 4.14(b., d., f.) also contains two-dimensional histograms relating area with height of three long ribs. A linear least-square fit indicates that the slope of the ellipsoids present in these two-dimensional histograms remains constant regardless of rib length.

In conclusion, the shape of the instantaneous recirculation region on the top surface of the rib remains statistically unchanged with rib length.

4.3.2 Dimensions of wake recirculation regions

The probability distributions of the bubble dimensions can also be computed for the wake region. As previously, the data is presented relative the their corresponding mean values introduced in figure 4.12c. Figure 4.15 shows contours of variations in height, area and length of the wake recirculation region behind ribs $L/H = 2, 4, 6$ and 8. The abscissa in this contour map is the rib length while the ordinate shows the bins of normalised fluctuations. This contour map enables us to compare the fluctuations normalized by the mean in the recirculation regions across different cases. The shortest ribs ($L/H = 0.1$ and 1) are omitted as the PIV field of view did not capture the extent of the recirculation in every snapshot. From the distribution of length, height, and area, it appears the shortest and longest ribs produce marginally more steady values than the $L/H = 4$. The long rib shows the least relative fluctuation in the wake bubble length across all the cases. $L/H = 4$ and 6 produce a modestly wider spread in values of all three dimensions. $L/H = 4$ produces the least steady recirculation region in the wake due to the occasional merging of the top and wake recirculation regions. Unlike the observations

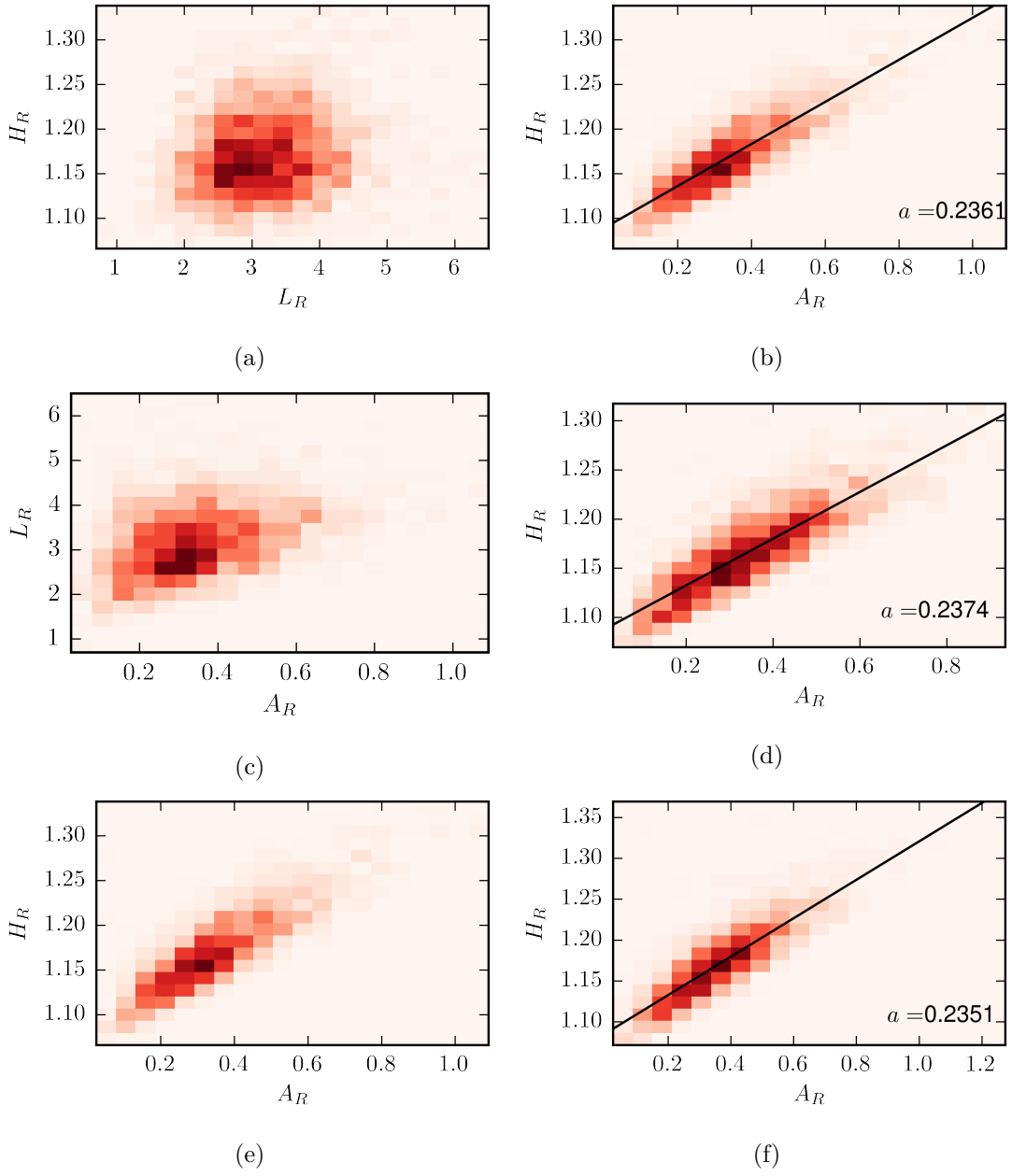

Figure 4.14: Joint probability density function of the dimensions of the recirculation region on top of a $L/H = 8$ rib (a. ,c. ,e.). Joint histogram of area and height of the recirculation region for three long ribs(L/H =8 b., 6 d., 4 f.). The inset text reports the slope a of a line fit through the distributions.

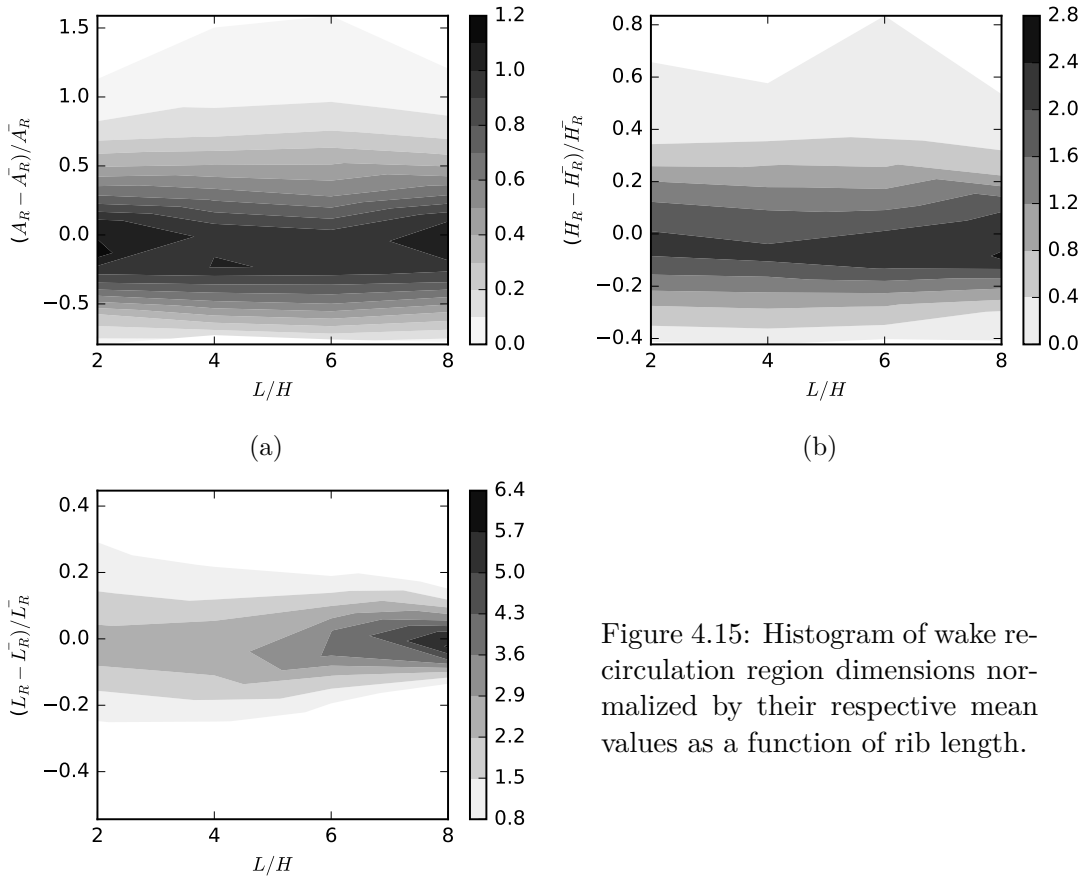

Figure 4.15: Histogram of wake recirculation region dimensions normalized by their respective mean values as a function of rib length.

of Bergeles and Athanassiadis (1983) on mean quantities, there is no monotonous trend in fluctuations that demarcates the long from the short ribs.

Similarly to the top region in section 4.3.1, joint histograms of the three measurements of the wake region provide an indication on its shape and the evolution with rib length. Figures 4.16 (a., c., e.) contain the relationship between height and length, length and area, and height and area respectively for case $L/H = 4$. Similarly to the top recirculation region, little or no correlation appears between length and height in the wake region. This is shown by the round patch in the joint histogram with no particular direction standing out. On the contrary, a slight relationship is visible between length and area in the plane of measurement through the triangular patch visible in the joint histogram. This triangular patch has a sharp lower limit indicating that a given area has a fixed minimum recirculation length associated with it. On the other hand the recirculation length can be much larger for the same area. Finally, as for the top region the relationship between height and area of the recirculation region is clearly defined by the oblique ellipse present in the joint histogram. It indicates a positive linear relationship where a large recirculation bubble leads necessarily to a high bubble. Figure 4.16 (b., d., f.) depicts the relationship between area and height for ribs $L/H = 2, 4, 6$. An ellipsoid is clearly apparent for all three rib lengths, however a linear fit through indicates that the

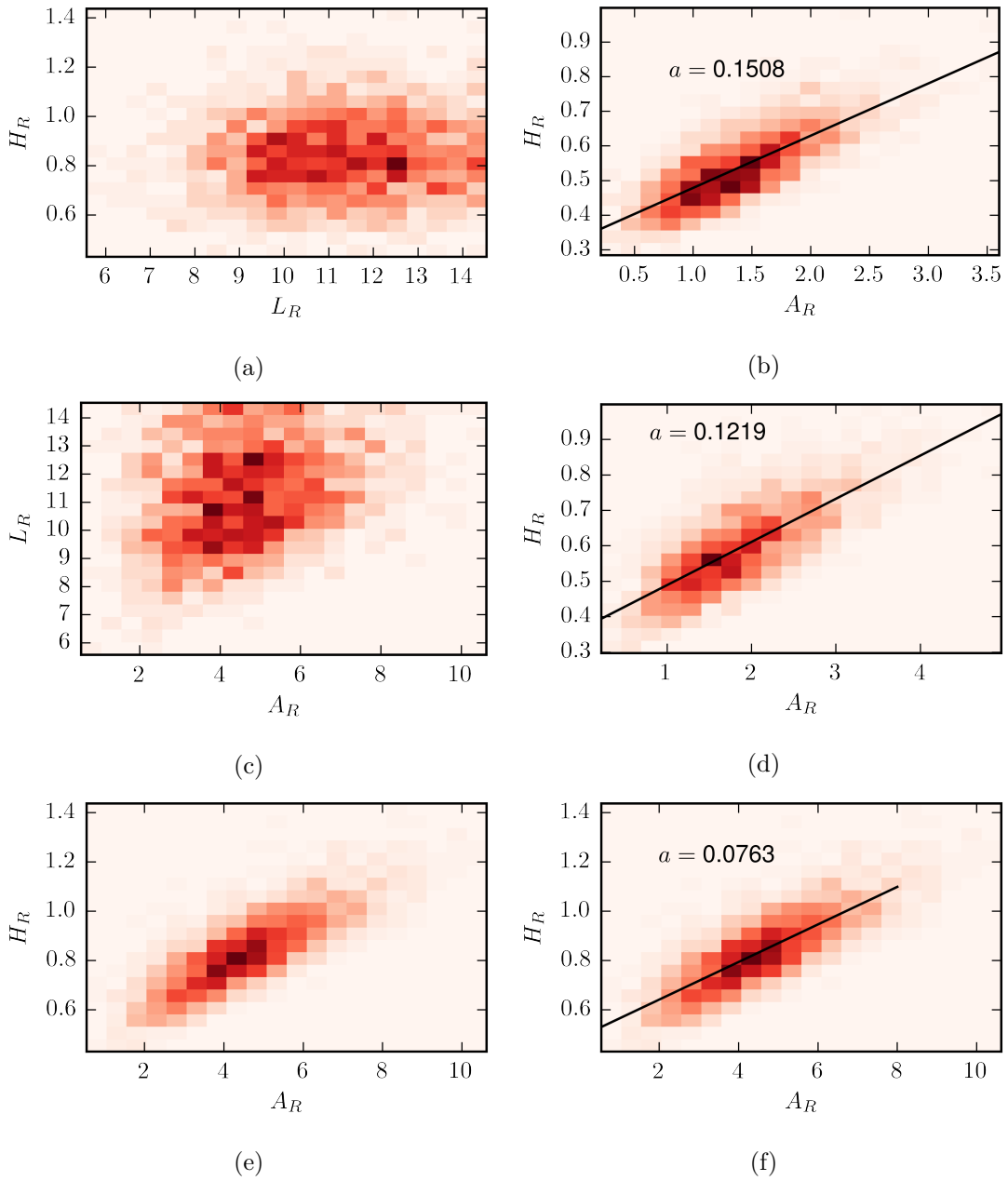

Figure 4.16: Joint probability density function of the dimensions of the recirculation region wake of a $L/H = 4$ rib (a. ,c. ,e.). Joint histogram of area and height of a wake recirculation region for three critical rib lengths($L/H = 6$ b., 4 d., 2 f.). a indicates the slope of the line describing the relationship.

linear relationship evolves with rib length. It is progressively shallower for shortening ribs ($H_R \approx 0.15A_R$ for $L/H = 6$, down to $H_R \approx 0.07A_R$ for $L/H = 2$). This translates in a bubble that is proportionally thinner or stretched in the streamwise direction as rib length decreases. Ribs $L/H = 6$ and 8 both produce the same slope of ≈ 0.15.

4.4 Velocity and pressure fluctuations

The previous sections highlight trends in recirculation region size as well as pressure distribution as a function of rib length purely from a statistical perspective. In cases where the flow reattaches on the top surface, it appears the top region behaves very similarly between cases. However, the behaviour of the wake region depends strongly on rib length.

The instantaneous dimensions of recirculation bubbles of FFS and BFS fluctuate according to well known phenomena (see figures 1.3 and 1.4). In this section, time-resolved measurements are used to determine whether the same mechanisms as FFS and BFS are observed in the flow over ribs. We study the state of the flow along the top surfaces of three critical ribs ($L/H = 1, 4, 8$) before moving our focus downstream into the wake regions.

4.4.1 From leading edge to trailing edge

It is known that variations in size of recirculation regions of FFS are the result of the amount of turbulence present in the shear-layer formed on the edge of recirculation regions, the momentum carried by the flow around the recirculation regions, and the scale of the fluctuations in velocity produced by the separation at the sharp corners (Pearson et al., 2013; Awasthi et al., 2014). We study velocity profiles, velocity frequency spectra and surface pressure spectra obtained near the leading edge of ribs to compare FFS to ribs.

Figure 4.17a shows vertical profiles near the leading edge of stream-wise velocity (U) and 4.17b the magnitude of velocity fluctuations ($T.K.E$) computed as $\overline{u^2 + v^2}$ from PIV measurements normalized by free-stream velocity for cases $L/H = 1, 4, 8$. Three ribs are depicted for visual purposes because intermediate rib lengths follow the trends explained here. Similarly to mean surface pressure distribution and bubble dimensions, vertical profiles near the leading edge show that medium and long ribs produce identical mean velocity, and $T.K.E.$. Both long ribs produce reversed flow up to $y/H = 1.15$ indicated by the local minimum, an acceleration of the flow up to 1.2 U_e at $y/H = 2.25$, and peak $T.K.E.$ at $y/H = 1.2$. The short rib produces reversed flow up to the same height, however the acceleration of the flow is weaker, only up to $1.1U_e$. Peak $T.K.E$, located at the same height for all three cases, is also 15% weaker over the short rib than

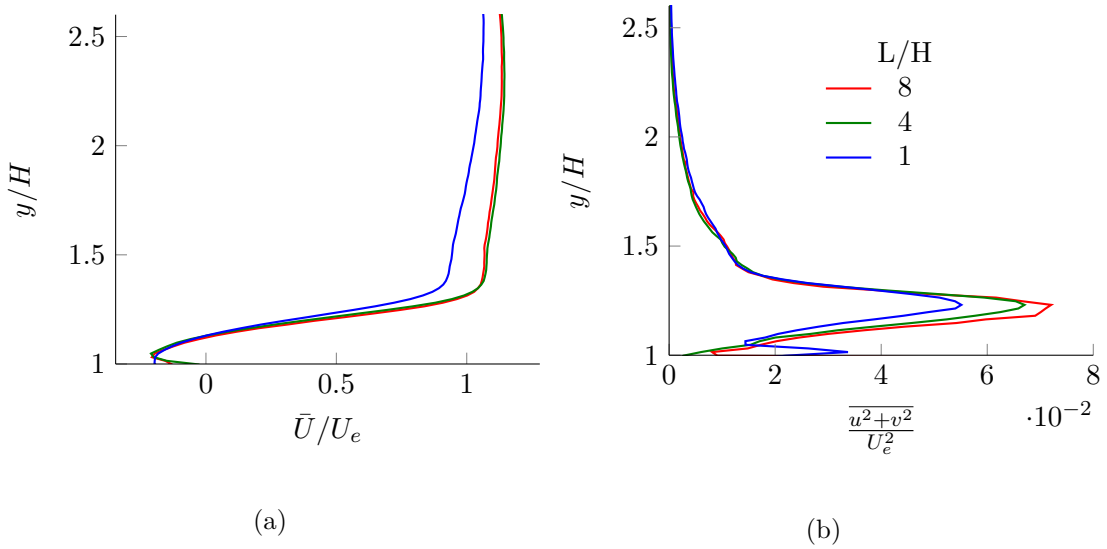

(a) (b)

Figure 4.17: Velocity (a) and $T.K.E$ (b) profiles from PIV measurements at the leading edge of three ribs ($x/H = 0.5$).

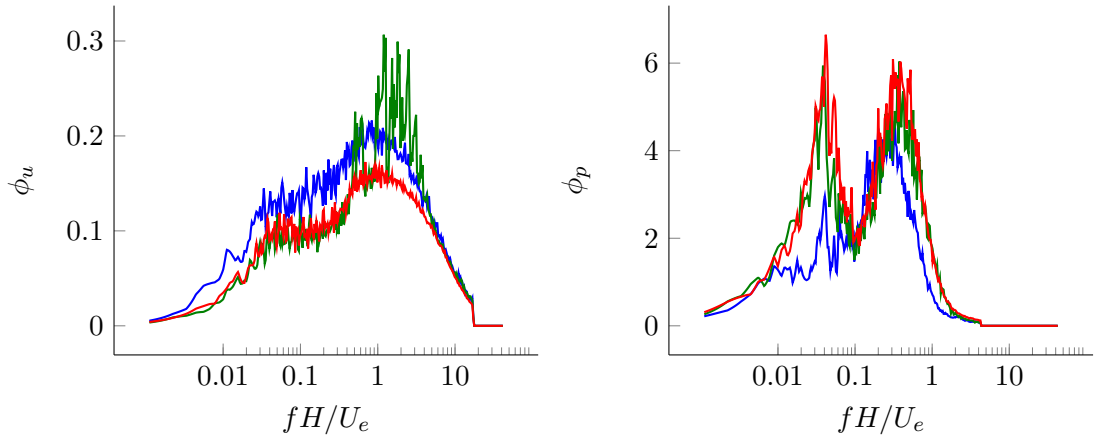

(a) (b)

Figure 4.18: (a) Velocity and (b) pressure spectra obtained at the station nearest to the leading edge ($x/H = 0.5$).

longer ribs. The weaker acceleration of the flow over short ribs is paired with a weak pressure drop (shown in section 4.2.1) near the leading edge. Thus, the short rib causes a weaker disturbance on the incoming flow near the leading edge.

Figure 4.18 contains pre-multiplied velocity and pressure frequency spectra (ϕ_u and ϕ_p) near the leading edge ($x/H = 0.5$) of three ribs of critical length. The velocity spectra are extracted from hot-wire measurements at height $y/H = 1.47$, the upper part of the shear layer, at $x/H = 0.5$. These indicate that two frequencies dominate the flow in this region. The first peak is centred on $fH/U_e = 0.04$, the second on 1. The spectrum of case $L/H = 4$ shows higher magnitude at $fH/U_e = 1$ which is believed to be attributed to electro-magnetic noise in the set-up which was discovered after the measurements.The low frequency portion seems to agree well with the spectrum of $L/H = 8$ showing that

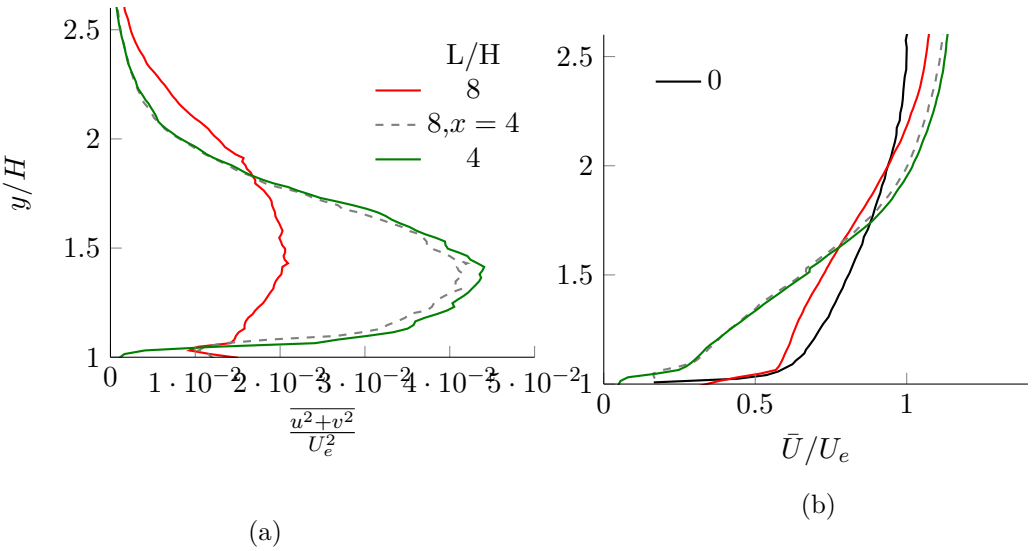

Figure 4.19: Velocity (a) and $T.K.E$ (b) profiles at the trailing edge of two long ribs. For comparison, "8, $x = 4$" corresponds to the profile at $x/H = 4$ on rib $L/H = 8$. In addition, figure (b) contains the streamwise velocity profile in the absence of obstacle ('0' in black).

both ribs produce similar flow unsteadiness near the leading edge. These dominant frequencies observed in velocity spectra are consistent with the observations made by Awasthi et al. (2014) and Farabee and Casarella (1986) on FFS. In the case of blunt leading edges forming a forward-facing step, Kiya and Sasaki (1983) and Cherry et al. (1984) find also a peak in velocity spectra near $St = 1$.

Similarly, pressure spectra near the leading edge show two frequencies dominating surface pressure fluctuations. A low frequency oscillation centred on $fH/U_e = 0.03$, as well as a higher frequency oscillation centred on 0.3. The low frequency peak is similar to that of the low frequency velocity oscillation. The high frequency peak however is at a lower frequency in pressure than velocity. Thus we may expect to see a relationship between low frequency velocity and pressure, but not directly between the higher frequency peaks. The dominant frequencies observed in pressure spectra are consistent with the observations made by Ji and Wang (2012) on FFS. These observations support that the forward-facing portion of a long rib is behaving similarly to a "simple" forward-facing step.

At the trailing-edge of long ribs, one observes that the mean velocity profile is positive throughout, however very different from a flat plate turbulent boundary layer profile (see figure 4.19). It is clear that the trailing edge of the medium rib, $L/H = 4$, is closer to the recirculation region at the top because the velocity is lower in the near-wall region of the profile. Furthermore, the peak intensity of $T.K.E$ is greater by over 65% and is located closer to the surface of the rib. Consequently, from a similar amount of turbulence and velocity at the leading edge, the medium rib shows a lower velocity and more turbulent flow at its trailing edge. In addition to the observation that the

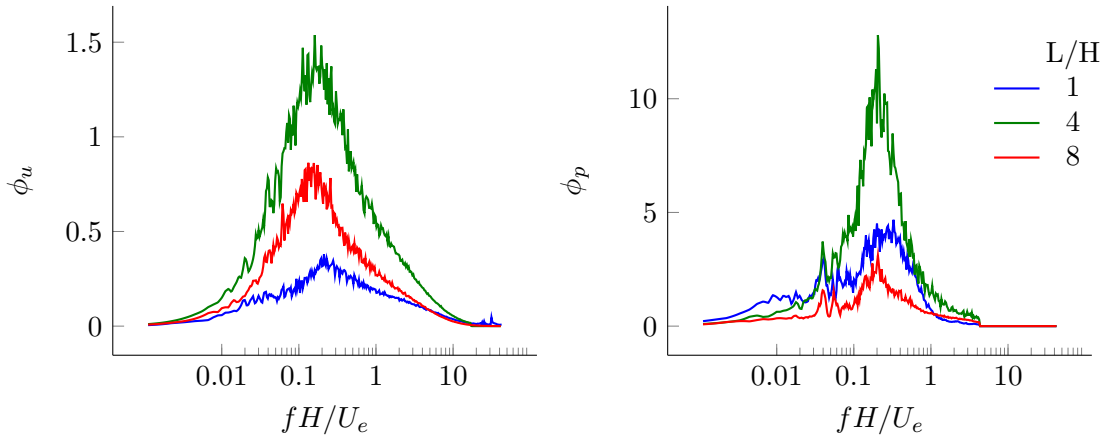

(a) (b)

Figure 4.20: a. Velocity spectra at the trailing edge of ribs $L/H = 4$ and 8 and $x/H = 2$ in the case of $L/H = 1$. b. Pressure spectra obtained at the last station before the trailing edge of all ribs. ($x/H = 0.5$, 3.5 and 7.5 for ribs L/H =1,4 and 8 respectively.)

top region may extend past the trailing edge, this would justify the most unsteady recirculation region dimensions in the wake.

Unlike the leading edge, the velocity spectrum taken at the trailing edge (figure 4.20a.) displays only one peak centred at a reduced frequency which decreases with rib length ($fH/U_e = 0.2$ for $L/H = 1$ to $fH/U_e = 0.17$ for $L/H = 8$). The velocity spectra are measured at $y/H = 1.67$ which is in the outer portion of the shear layer thus avoiding negative velocity measurements. The magnitude of each spectrum confirms that the shortest rib produces the lowest fluctuations and the medium rib the highest at their respective trailing edges. A slight shift in frequency exists between long and medium ribs. This shift is attributed to the distance from the leading edge over which shed vortices grow and rotate slower (Liu et al., 2008). Indeed the medium rib being shorter than the long rib, but convection velocity being comparable, the vortices shed from the leading edge develop over a shorter period of time before reaching the trailing edge.

The surface pressure fluctuations measured near the trailing edge $x/H = 0.5, 3.5, 7.5$ for ribs $L/H = 1, 4, 8$ respectively (Figure 4.20b) indicate that one peak dominates the flow at $fH/U_e = 0.3$ for $L/H = 1$ and 0.18 for longer ribs. However, a comparatively weak oscillation also observed at the leading edge persists at $fH/U_e = 0.03$.

Figure 4.21 presents surface pressure spectra as a function of streamwise location for the three ribs of interest in more synthetic form. Along the streamwise direction, the two peaks observed in ϕ_p at the leading edge become one at the trailing edge, centred on a middle value. The last pressure sensor on the top surface is located $0.5H$ upstream of the trailing edge, and it measures a single peak centred on approximately $fH/U_e = 0.18$, where the anemometer measurements exhibit a single peak centred on $fH/U_e = 0.17$

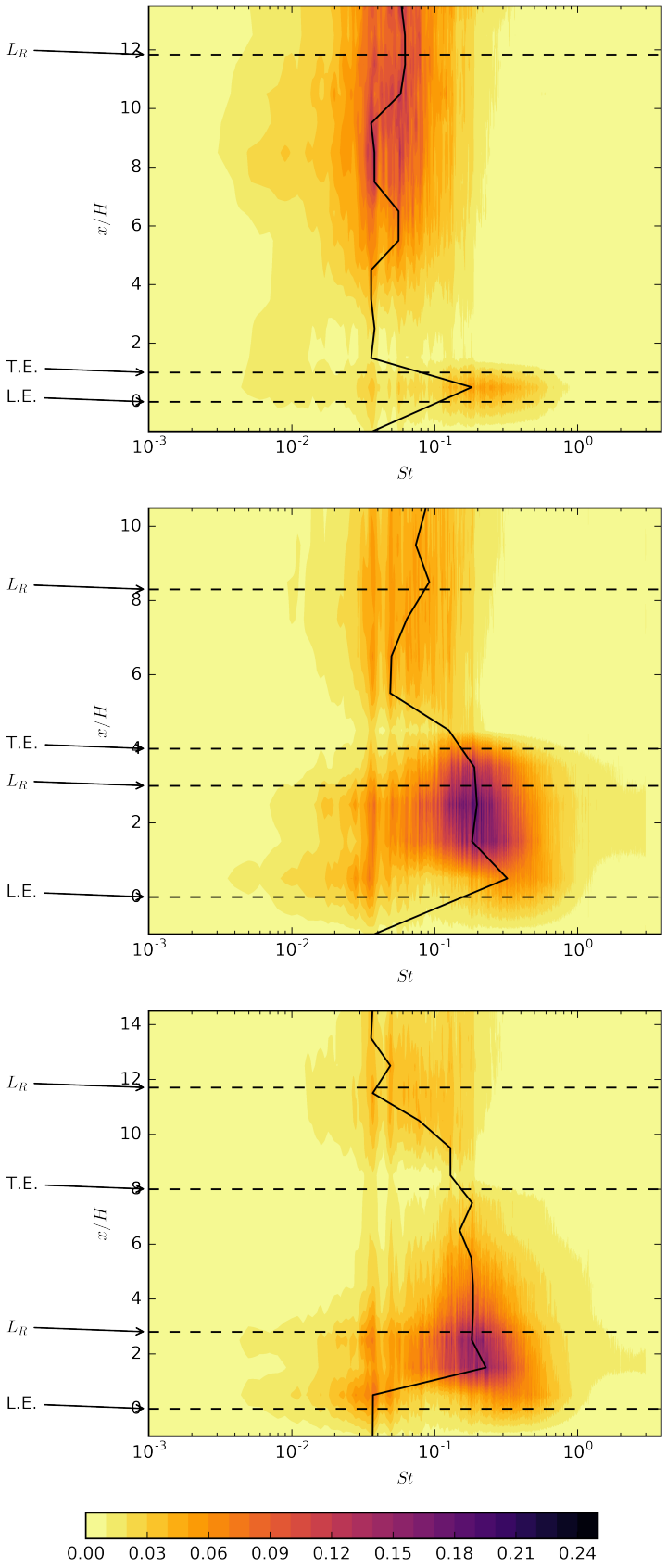

Figure 4.21: Pre-multiplied pressure spectra at the surface of each rib. Top to bottom: $L/H = 1, 4, 8$. The black line links the peak frequency at each streamwise position.

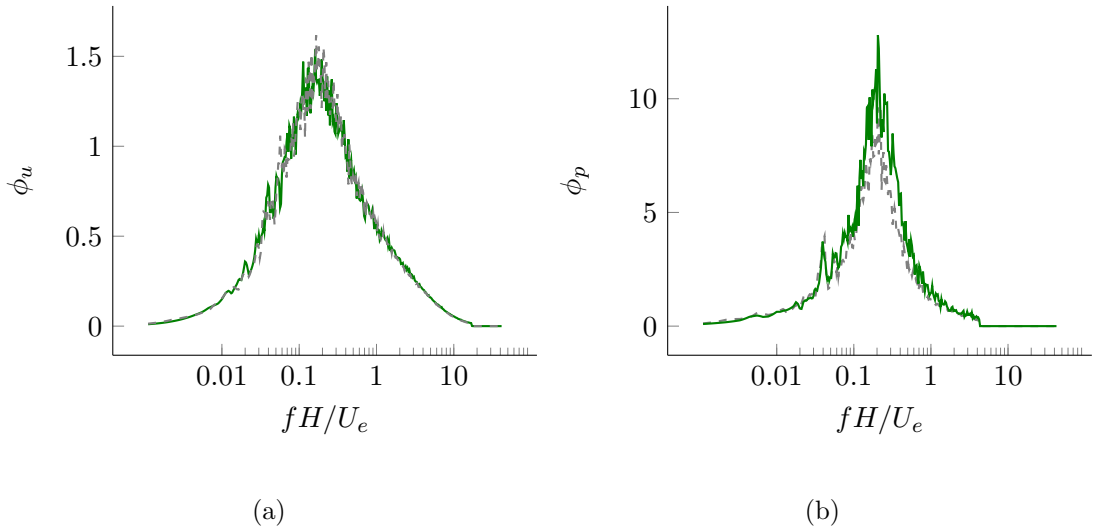

(a) (b)

Figure 4.22: a. Velocity and b. Pressure spectra at location $x/H = 4$ for ribs $L/H = 4$ and 8.

for the longest rib (see figure 4.20). At the trailing edge the intensity of the pressure fluctuations vary with rib length, the medium rib produces the strongest fluctuations visible as a dark purple region in figure 4.21 due to the short distance between mean reattachment point and trailing edge. The long rib shows attenuation of pressure fluctuations along the top surface. The discrepancy in the dominating frequency between long and medium rib observed in velocity spectra is also present in surface pressure spectra and may be explained by the streamwise evolution of fluctuation along the top surface.

It must be noted that velocity and $T.K.E$ profiles at the trailing edge of the medium rib ($L/H = 4$) are identical to those measured at $x/H = 4$ on top of the longest rib ($L/H = 8$), thus indicating that the location of the trailing edge does not affect the flow along the top surface of long ribs (see figure 4.19). We can confirm this by studying the velocity and pressure spectra at $x/H = 4$ for the medium and long ribs in figure 4.22. It is clear the properties of the flow here are identical.

To further study the similarity of top recirculation regions on long and medium ribs, we applied "snapshot" Proper Orthogonal Decomposition (POD) as defined by Sirovich (1987) to the streamwise velocity components on top of the medium rib and the longest rib ($x/H = 0$ to 4 for both). The results (figure 4.23) show indeed that the same POD modes can be observed at least up to mode 7. Beyond mode 7, the modes of the medium rib still look similar to those of the longest rib, but the order in which they appear may be different. This indicates the dominant fluctuations in the flow over the top surface of both ribs are identical. The small changes in mode order and energy is attributed to statistical convergence, 2000 snapshots were used for POD. In the wake region of the medium and long ribs, (figure 4.24) the first modes look similar but not identical. This suggests the wake region behaves similarly but not identically. The large patches of velocity fluctuations present in the first mode indicate that large scales dominate

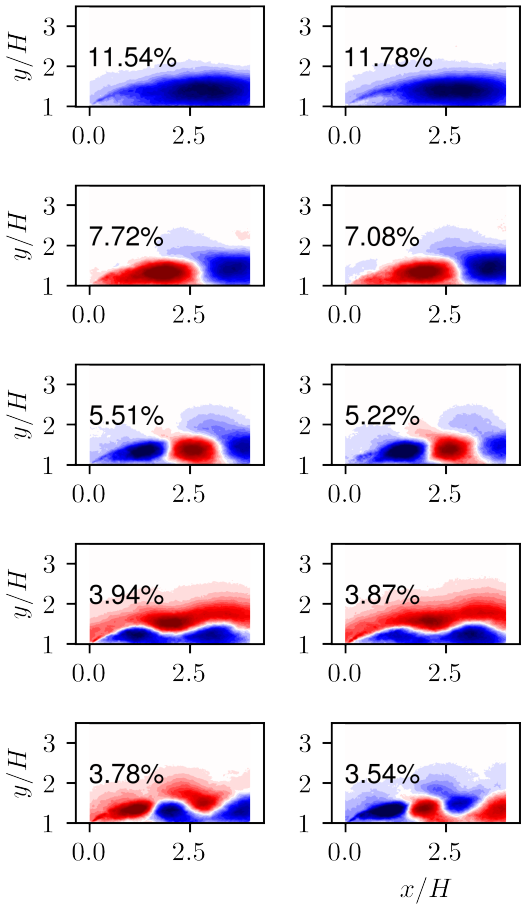

Figure 4.23: POD of streamwise velocity components on the top surface of ribs $L/H = 4$ (left) and 8 (right). No difference is visible between modes until mode 7. The energy fraction associated with each mode is written as a percentage in the inset text.

the wake region. Beyond mode 5, the mode shapes begin to differ significantly, thus indicating the flow behaves differently at smaller scales. More background on POD analysis can be found in appendix A along with modes for the short, medium and long ribs.

4.4.2 From trailing edge to mean reattachment point

Unlike the top region, the wake region exhibits marked discrepancies between the medium and long ribs. Focussing solely on the top surface, the long and medium rib produced indistinguishable velocity and pressure distributions, but only slight changes in surface pressure distribution. In the wake, one may no longer categorize ribs as short or long because the position of the trailing edge forces a more gradual evolution of the flow.

The first shear layer caused by the leading edge separation produces velocity fluctuations which are convected downstream and past the trailing edge. At the trailing edge of long

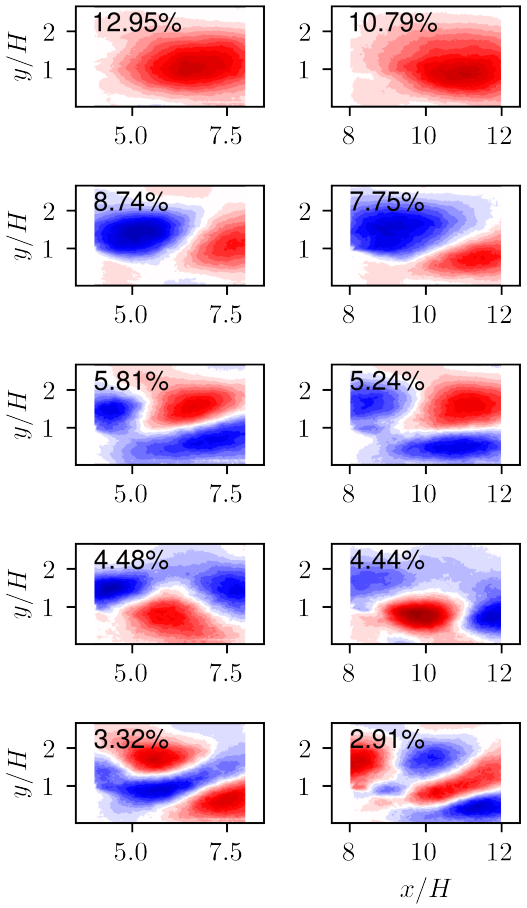

Figure 4.24: POD of streamwise velocity components in the wake of ribs $L/H = 4$ (left) and 8 (right). The energy fraction associated with each mode is written as a percentage in the inset text.

ribs, the backward-facing step-like separation produces a second shear layer, and a second zone of high $T.K.E$ influenced by the unsteady flow from the top surface. Profiles of $T.K.E$ in the wake region of long ribs displayed in figure 4.25 indicate two local maxima: one near or below the level of the top surface, the second between the top surface and $1H$ above it. With stream-wise distance from the trailing edge, the upper maximum tends to diminish while remaining at the same vertical height. The lower maximum on the contrary drops from the level of the top surface down to approximately $y/h = 2/3$ near the mean reattachment point while increasing in magnitude. Further downstream it spreads higher as well as reduces in magnitude. Streamlines indicate that the mean flow descends past the trailing edge through the upper maximum and into the lower maximum $T.K.E$ region. This indicates that turbulent flow may be carried down into the lower region. However, despite the downward mean velocity, the high $T.K.E$ region grows upwards, against the mean flow. High shear is present in this area which maintains the production of $T.K.E$ along the top of the high $T.K.E$ plume. After mean reattachment, where the shear should vanish, diffusion of turbulence allows the high $T.K.E$ zones to

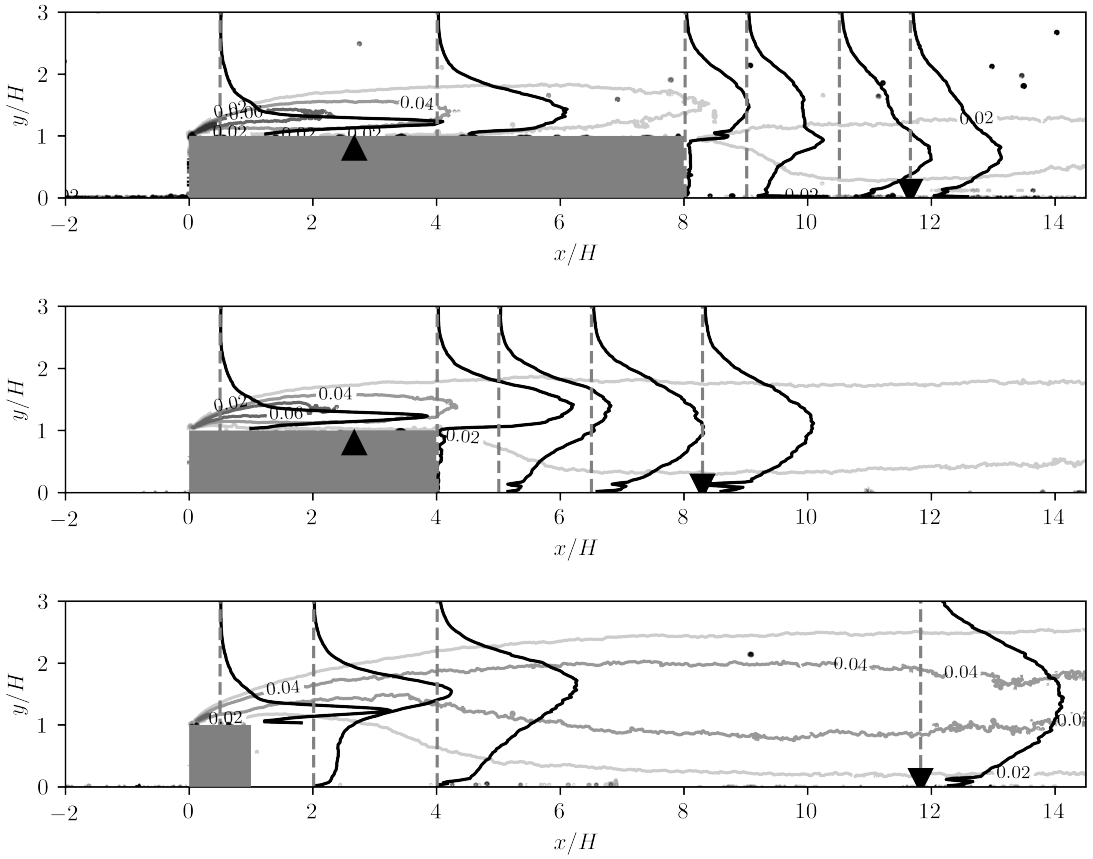

Figure 4.25: Organization of $T.K.E$ above three critical rib lengths ($L/H = 8, 4, 1$ from top to bottom). Contours represent regions of high $T.K.E.$. Lines represent qualitatively the distribution of $T.K.E.$ within these regions and offers a comparison between cases.

grow vertically. The high $T.K.E$ region from the leading edge does not cause the wake region to rise, they meet however as the plumes broaden.

With shorter rib length as displayed by $L/H = 4$, and $L/H = 1$ in figure 4.25, the high $T.K.E$ region emanating from the leading edge merges with that of the wake region to form one region. The two peaks present in vertical profiles in the wake of long ribs disappear in the medium rib. As rib length shortens, there is a tendency for the high $T.K.E$ regions to grow vertically as does the mean recirculation region. The wake region no longer imposes a strong downwards draft on the flow coming from the leading edge. Further downstream, diffusion again causes the upward growth of the plumes of high $T.K.E$.

In the wake of each rib, the downstream plate exhibits very little pressure fluctuations near the obstacle, possibly due to the low magnitude of the flow in the secondary recirculation region. The pressure fluctuations however increase as seen in the P_{rms} data after $1.5H$ on the downstream plate (see figure 4.8). The intensity of surface pressure spectra shown in figure 4.21 show in more detail that the short rib produces a single

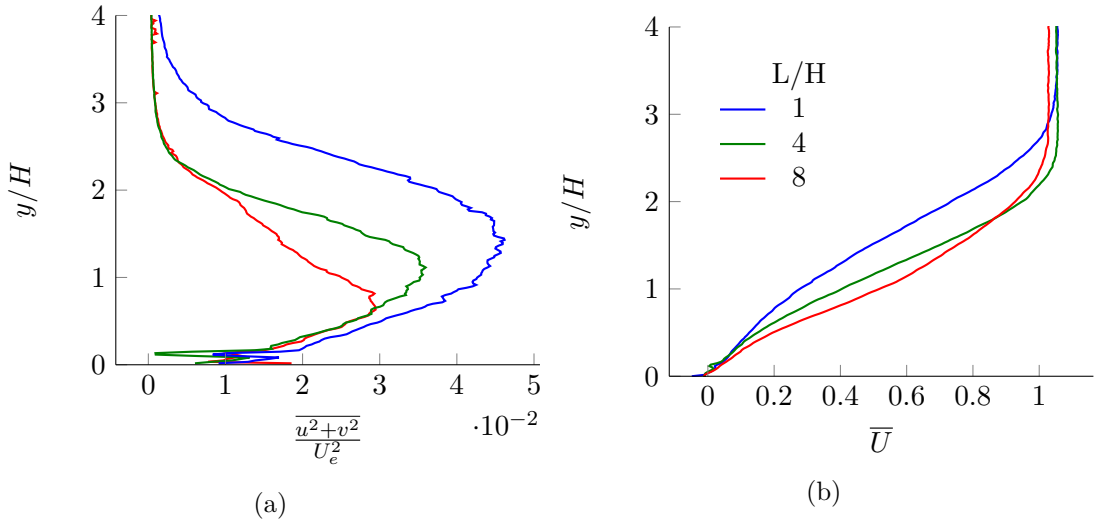

(a) (b)

Figure 4.26: The state of the flow near the mean reattachment point. Comparison of $T.K.E$ (a) and velocity (b) profiles after the mean reattachment point $x/H = 13.5$.

peak which is consistently centred on $St = 0.04$ before and after reattachment of the flow. Peak intensity is shown to be at the mean reattachment point. Medium-length ribs also produce a single peak in surface pressure spectra centred on $St = 0.04$ which is broader than the one produced by the short rib. Finally, the longest rib produces a plateau before the reattachment point between $St = 0.03$ and 0.15, which narrows into a broad peak after the mean reattachment point centred at 0.04. For comparison, studies on backward-facing steps alone report Strouhal numbers of interest in the regions of 0.02, 0.07, and 0.13 respectively associated with shear layer flapping, vortex shedding, and vortex merging Liu et al. (2005) at $Re_H = 33000$. These values are also supported by Eaton and Johnston (1981), and Lee and Sung (2001). Consequently, the backward-facing portion is not behaving directly as a "simple" obstacle would. Indeed, the characteristic frequencies of a forward-facing step are found in the wake of short and medium ribs, but long ribs, where the flow settles along the longer top surface, begin to show characteristic frequencies of BFS.

4.4.3 Mean reattachment point and far wake

Plotting a vertical profile of $T.K.E$ of each rib at the mean wake reattachment point (figure 4.26) highlights short ribs produce the largest amount of $T.K.E$ in the wake. The medium and longest ribs exhibit gradually less $T.K.E$, at gradually lower vertical positions. In comparison with the measurements made near the leading edge, $T.K.E$ at the mean reattachment point in the wake is 24, 58 and 65% weaker for $L/H = 1, 4, 8$ respectively. Despite the similar location of L_R for $L/H = 8$ and 1, the short rib maintains a more consistently high $T.K.E$ level. Velocity fluctuation spectra (figure 4.27) above the mean reattachment point ($y/H = 1.67$) indicate that lower frequencies

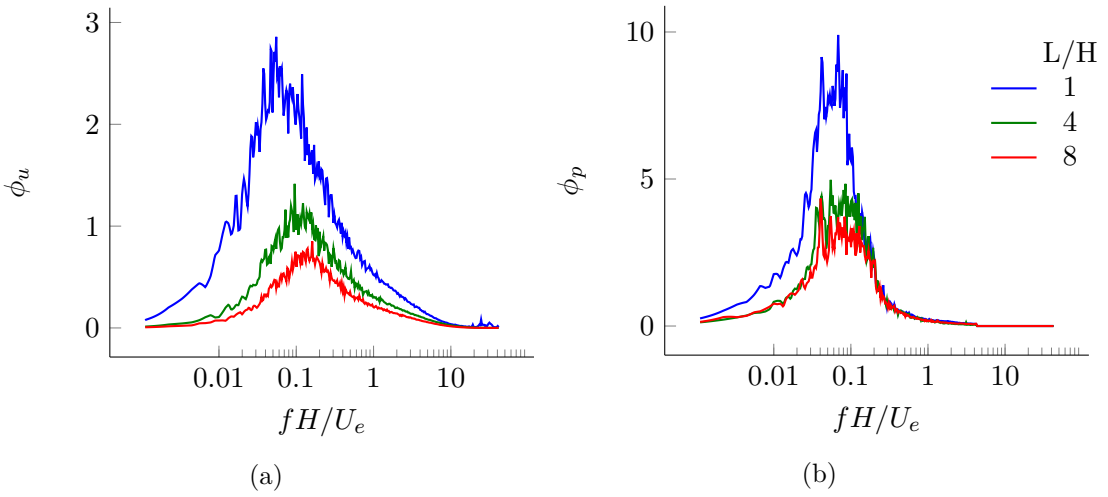

Figure 4.27: (a) Velocity and (b) Pressure spectra at the mean reattachment point in the wake of all ribs.

centred on $St = 0.05$ dominate the wake region of short ribs. The spectra of longer ribs exhibit only one peak centred on $St = 0.12$, while the velocity spectrum of the medium rib displays higher intensity in the lower frequencies than that of the longest rib.

From $T.K.E.$ measurements (figure 4.26 (a)), and the amplitude of the fluctuations in recirculation region dimensions, it is expected that short ribs produce the strongest fluctuations in their wake. These appear both in velocity of the flow, and surface pressure. We may associate this trend with the absence of a boundary layer developing on the top surface which exists in the case of long ribs. This boundary layer reorganizes and dampens the perturbations caused by the top recirculation bubble through the shear it imposes. For this reason, short ribs allow more low frequency shear layer flapping and vertical development of the flow in their wake.

Similarly to Antoniou and Bergeles (1988)'s study of the integral time scale in the wake, we obtained integral time scales at certain locations around ribs. Integral time/length scale is used as an argument of lifespan of turbulence as it is carried downstream with the mean flow. At the leading edge, short ribs exhibit the lowest amount of $T.K.E$, and the ITS of turbulence generated by the shortest rib is similar, or smaller than longer ribs (figure 4.28 (a)). In the wake, the integral time scales shown in figure 4.28 (b) confirm that at the reattachment point, up to approximately $y/H = 1.66$ at $x = L_R$, the short rib exhibits the largest ITS, as well as the largest $T.K.E$. Inspecting the production of $T.K.E$ highlights the sources of $T.K.E$ along streamlines above the ribs. Figure 4.28 (c) compares the streamwise production of $T.K.E$ between the three lengths of interest. It is clear that high concentrated rates of $T.K.E$ production exist near the leading edge of all three ribs. Further downstream, the rates decrease but spread to higher vertical positions behind short ribs than longer ribs. Peak $T.K.E$ production rate is located in the shear layer indicating it is the source of turbulence. This shear is maintained consistently up to the reattachment point of the short rib therefore maintains higher

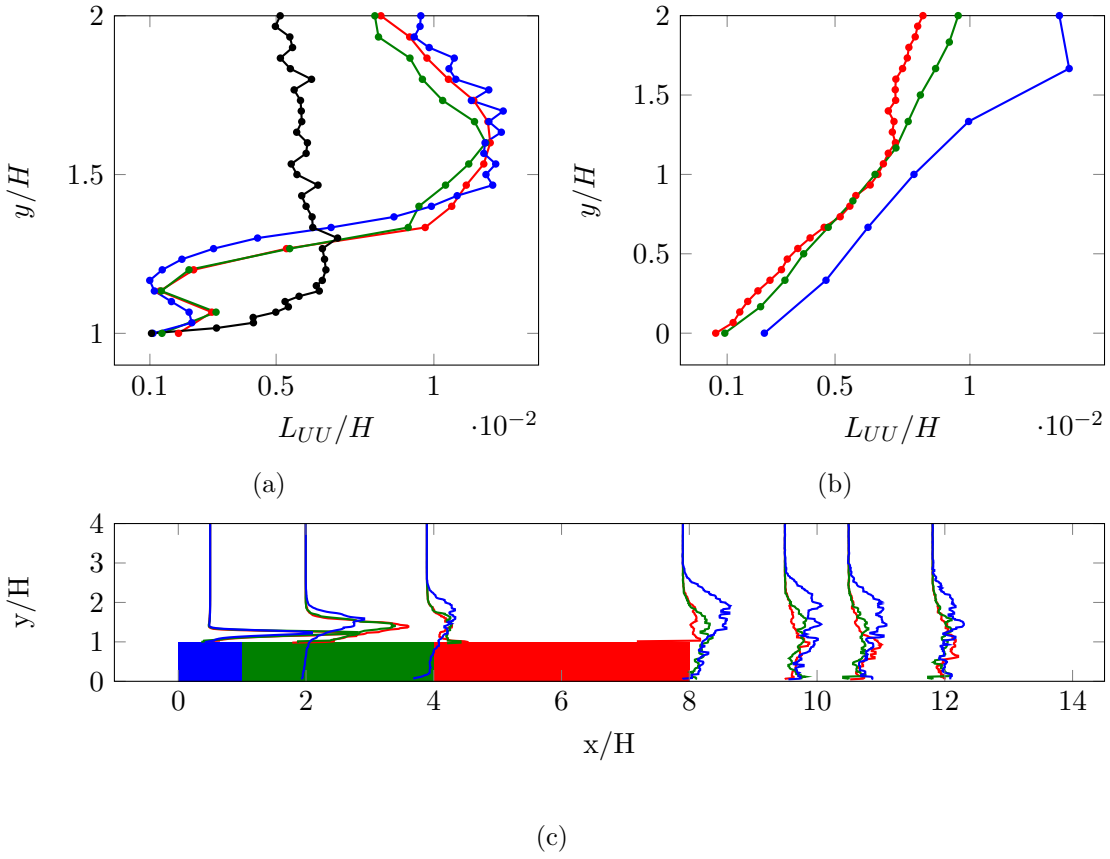

Figure 4.28: (a) Comparison of integral length scales at the leading edge ($x/H = 0.5$), and (b) point of mean reattachment in the wake (x_R). (c) Production rate of $T.K.E$ with streamwise position. Near leading edge amplified by 5, rest by 50.

levels of $T.K.E$ than for long ribs. In the case of long ribs, a higher shear exists near the leading edge. However, it is dissipated as the bubble reattaches to the top surface. A new peak of production appears in the shear layer of the wake region. Overall, less production of $T.K.E$ occurs, justifying the lower amount of $T.K.E$ in the wake of long ribs. The argument of the longer time scales supports the amount of $T.K.E$ in the wake of ribs, but the $T.K.E$ production rate indicates that fluctuations of larger scale are possible in the wake of shorter ribs because the longer shear layer allows larger coherent structures to develop before the reattachment point.

Chapter 5

Effects of free-stream turbulence on separation and reattachment

5.1 Motivation and objective

Surface-mounted ribs have received comparatively less attention than their isolated counterparts the FFS and the BFS. The little literature covering these obstacles describes how they represent many engineering applications where flow conditions might vary. The majority of those studies (Arie et al., 1975a,b; Bergeles and Athanassiadis, 1983; Antoniou and Bergeles, 1988) however study ribs in a low-turbulence steady free-stream flow with a turbulent incoming boundary layer. The presence of the turbulent boundary layer is necessary in studying separation on sharp objects because it produces a repeatable fully turbulent flow separation. A laminar separation that would transition to turbulent in the shear layer would be difficult to reproduce reliably. However, there is a factor intervening in many industrial applications which is not studied in great detail: the presence and its effect of free-stream turbulence (FST) on the response of the flow to the rib. This is partially due to technical difficulties in isolating the pure effect of turbulence, and not a combined effect that turbulence has on the boundary layer impinging the obstacles. With the use of an active grid, we were able to introduce free-stream turbulence at a desired intensity but with little effect on the shape of turbulent boundary layer developing upstream of the obstacle. Several studies have used grids to generate free-stream turbulence (Saathoff and Melbourne, 1997), but we use the grid developed by Eda Dogan and Robert Bleischwitz. Detailed information can be found regarding this grid and the interaction between free-stream turbulence and a turbulent boundary layer in Dogan et al. (2016), as well as Hearst et al. (2016). In essence, the introduction of the active grid produces a thicker boundary layer based on δ_{99}, all else equivalent. Free-stream turbulence also increases turbulence intensity within the boundary layer up to a certain amount. This quantity saturates above a specific FST intensity as is explained

Figure 5.1: Active grid used in the experiment. Varying the rotation rate and direction of each shaft allows varying intensities and scales of turbulence.

by Dogan et al. (2016). Nevertheless, with various turbulence intensities generated by the grid, we are able to maintain key parameters between turbulent cases. Those are detailed in the following section as well as the effects of turbulence on recirculation, and surface pressure distribution.

In this chapter three rib lengths ($L/H = 1, 4$, and 8) are subjected to four levels of free-stream turbulence in order to identify the effects of free-stream turbulence on separation, as well as the importance of rib length on the response to free-stream turbulence. Indeed, the separation caused by a short rib differs from that by a long rib, thus the response to turbulence may differ.

5.2 Incoming flow conditions

In order to study the effect of turbulence on the characteristics of separation and reattachment over the ribs, four flow conditions are studied. The first is without active grid, the following three require the use of the active grid. Figure 5.1 is a picture of the active grid from downstream. It is composed of six horizontal and 11 vertical shafts rotating hollowed wings. Each shaft is driven independently which allows for a broad range of turbulent scales and intensities to be produced.

The boundary layer produced at the location of the leading edge of the obstacle is described in figure 5.2 as well as in table 5.1. It was obtained by hot-wire measurements at the location of the leading edge (x/H) prior to mounting the models. Further information can be found regarding the hot-wire set-up used in section 2.6. In the case of this experiment, six 30-second long acquisitions were made at each vertical position above $x/H = 0$. The vertical positions follow a logarithmic pattern to increase the number of points near the ground where the velocity gradient is strong, and reduce the number of points near the free-stream where the velocity gradient is weak. The data extracted from the hot-wire is temperature-corrected as defined by Hultmark and Smits (2010).

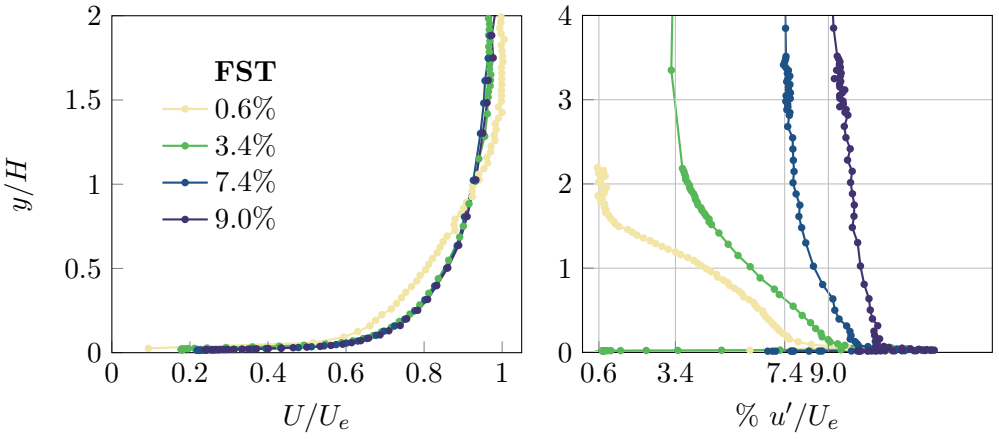

Figure 5.2: Velocity magnitude profile averaged between $x/H = -5.4$, and $x/H = 0$, the location of the leading edge of all obstacles.

This requires a calibration be made pre- and post-experiment. Temperature-dependent gains and offset are then calculated for the temperature before and after the experiment. The temperature drift during the experiment (which can be minimized by preheating the room with the wind-tunnel for a couple of hours) is acquired in parallel with the voltage of the hot-wire. The temperature is then used as a weight to average between the pre- and post-experiment gains and offsets. No filtering is used on the time-series in this case. The mean and standard deviation of the velocity are used to compute the boundary layer profiles reported in figure 5.2. These are normalized by the free-stream velocity.

Table 5.1 contains quantitative information regarding the boundary layer profiles formed with varying free-stream turbulence intensities. The "laminar" case in the left-most column refers to a study without active grid mounted. The "low" case corresponds to the grid being mounted inside the wind-tunnel but not actuated. The flaps are in the open position without motion, only holding torque is applied through the motors. The "medium" corresponds to the grid mounted with the shafts rotating fast at random speeds and switching direction at random intervals. This produces small scales which dissipate quickly. The "high" intensity case is achieved similarly but by rotating and alternating at a slower rate. This in turn produces larger scales at the grid which results in stronger turbulence further downstream where the rib is located. The grid settings correspond to cases "B, C, D" used by Hearst et al. (2016). In the two most turbulent cases (C and D) the direction of rotation was reversed at random between 0.05s and 2.5s, the acceleration of the rotation was randomly set between 50Hz/s and 200Hz/s and final wing velocity was randomly set between 5Hz and 15Hz for 7.4% FST (case C) and 1Hz and 3Hz for 9.0% FST (case D). Nevertheless, the presence of the grid in the wind-tunnel thickens the boundary layer (as defined by δ_{99}), which changes the velocity gradient at the height of the rib ($y/H = 1$). Within the three cases with active grid, the

Turbulence intensity	δ_{99} (mm)	σ_{U_e}/U_e	δ_{99}/H	u'_H/U_e	$\tau_H = \frac{H}{U_H}\frac{dU}{dy}\|_H$	L_x/H
Laminar	42	0.54%	1.39	4.4%	0.25	0.58
Low	101	3.45%	3.35	6.5%	0.1	2.25
Medium	84	7.36%	2.81	9.1%	0.1	3.69
High	61	9.02%	2.02	10.9%	0.1	5.59

Table 5.1: Properties of the incoming boundary layer profiles at the location of the leading edge for all turbulence intensities.

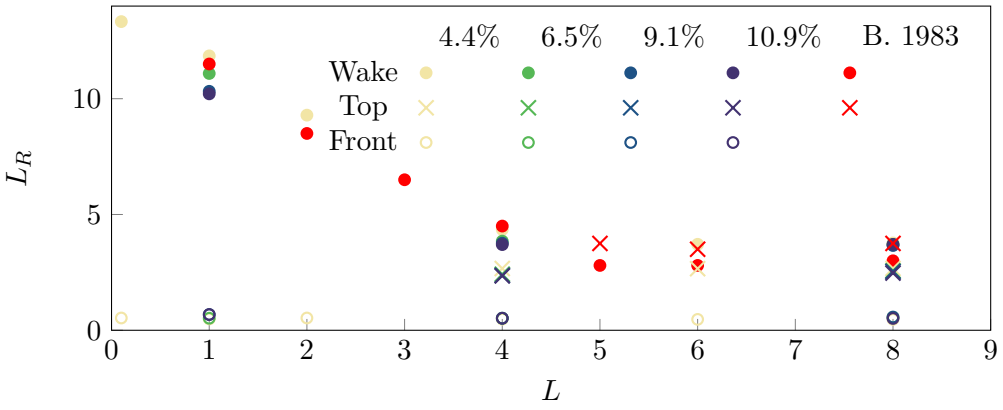

Figure 5.3: Recirculation region lengths of each rib according to turbulence intensity at rib height u'_H/U_e.

velocity gradient represented by the non-dimensionalised shear coefficient τ_H remains similar, only turbulence intensity at the rib height and in the free-stream increase. It must also be noted that the Reynolds number computed with velocity at rib height is identical for all four cases, $Re_H = 17400$. For comparison, the Reynolds number based on free-stream velocity is $Re_\infty \approx 19000$. In the results following, we will be referring to each turbulent case by the turbulence intensity at rib height u'_H/U_e as defined in table 5.1.

5.3 Recirculation region dimensions

5.3.1 Average dimensions

The introduction of the active grid has a non-negligible effect on recirculation around ribs of various aspect ratio. Three ribs were tested $L/H = 1, 4$, and 8 at free-stream turbulence levels varying from 0.6% to 9.0%, or at rib height: 4.4%, 6.5%, 9.1% and 10.9%. Figure 5.3 contains recirculation lengths of the front, top and wake regions as defined in chapter 4. Both the top and wake regions decrease in length with added free-stream turbulence. However, this reduction is proportionally higher for short and medium ribs than long ribs. Table 5.2 contains the percentage decrease in recirculation length of each region for this study. Up to 15% decrease in recirculation region is

u'_H/U_e	6.5 (%)		9.1 (%)		11 (%)	
region	top	wake	top	wake	top	wake
$L/H = 1$		-6%		-13%		-14%
$L/H = 4$	-9%	-11%	-11%	-14%	-12%	-15%
$L/H = 8$	-3%	-2%	-5%	-3%	-7%	-2%

Table 5.2: Proportional reduction in recirculation length of the regions with added turbulence compared with the baseline case for three rib lengths.

achieved for rib length $L/H = 4$ at the highest turbulent intensity whereas the long rib sees a decrease of only 2 to 3%. The linear trend of short ribs and the steady value of long ribs is maintained as observed for the baseline case in chapter 4. However, the recirculation lengths of short ribs with FST is shorter than that observed by Bergeles and Athanassiadis (1983) where the boundary layer was thinner than the rib. The recirculation length of the wake appears to be still longer for long ribs. This would point to the fact that the reduced shear at the height of the rib would produce a reduction in the size of recirculation regions. The added turbulence intensity at a constant shear level would further reduce the size of the recirculation regions.

5.3.2 Statistics of dimensions

The previous section describes that reduced boundary layer shear at rib height leads to smaller recirculation regions. Turbulence intensity further reduces the length of recirculation regions. It is also possible to investigate the statistics of recirculation region dimensions with increased FST. We will study the distribution of recirculation lengths from instantaneous snapshots. This is done by finding the last point downstream where the streamwise velocity component switches from negative to positive values. This will provide insight into the reason why regions shrink. It could be due to a change in the distribution of reattachment points, or a shift upstream of similar distributions.

Due to laser reflections near the surface, the distribution of instantaneous reattachment points is taken at a height of $y/H = 0.1$ above the surface in the wake region. This maintains a qualitative comparison between cases, the exact values will vary if measurements could be made at the surface itself. The instantaneous reattachment points are gathered from 2000 snapshots into 10 bins evenly distributed between the leading edge and the trailing edge, and the trailing edge and the edge of the PIV window for the top and wake regions respectively.

Figures 5.4, 5.5 and 5.6 contains the distribution of instantaneous reattachment point on top and in the wake of the short, medium and long ribs respectively. Along the top surface of the medium and long ribs, it appears the addition of turbulence modifies only slightly the distribution of instantaneous reattachment points. On the contrary, in the wake region of all three ribs, the distributions are broader for each turbulent case versus

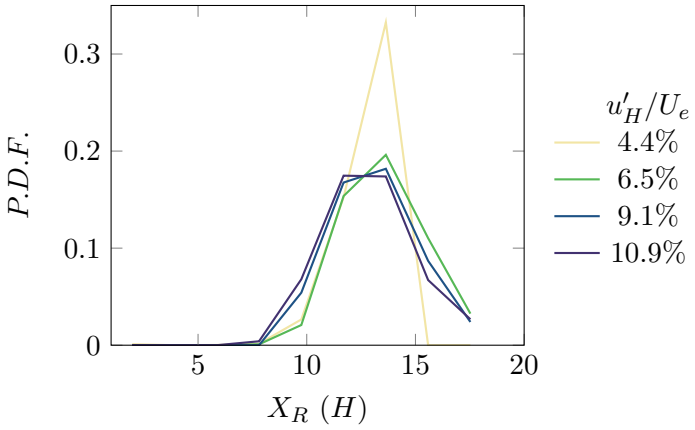

Figure 5.4: Normalized distribution of instantaneous reattachment locations in the wake of the short rib ($L/H = 1$).

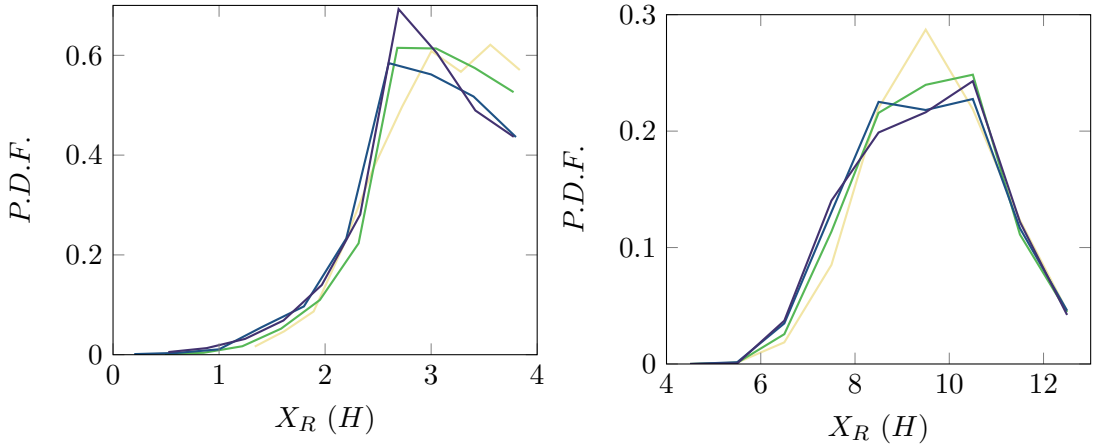

Figure 5.5: Normalized distribution of instantaneous reattachment locations on top (a) and in the wake (b) of the medium length rib ($L/H = 4$).

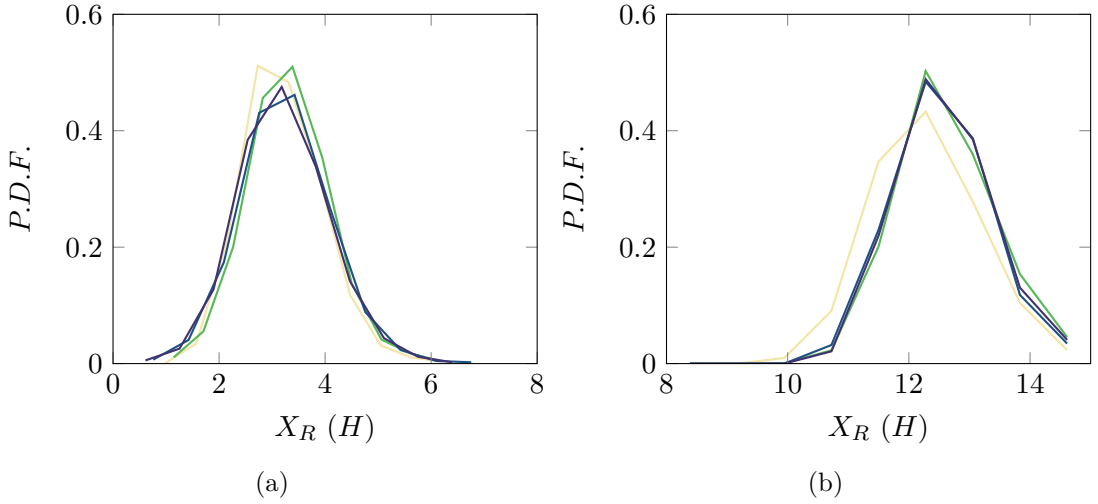

Figure 5.6: Normalized distribution of instantaneous reattachment locations on top (a) and in the wake (b) of the long rib ($L/H = 8$).

the baseline. The shift of the mean value is not clear from observing these histograms, however it is apparent that the variations among turbulent cases are very small. Only in the wake of the shortest rib is it possible to see that increased free-stream turbulence displaces the distribution further left as observed in the mean values. The medium rib seems to show only minimal changes within tolerance.

5.4 Surface pressure distribution

In addition to field velocity, surface pressure measurements were made at the same locations as the case without active grid. Surface pressure distribution provides an indication of the loads exerted on a structure.

Figure 5.7 contains the surface pressure distributions of short, medium and long ribs at each turbulence intensity provided by the active grid. Unlike the reattachment point on the top surface, or in the wake, the evolution of surface C_P is not monotonous with turbulence intensity. Indeed, the peak suction occurring immediately after the leading edge of each rib is subject to both shear in the boundary layer and turbulence intensity. The magnitude first drops significantly as the shear level is varied (introduction of the active grid in the lowest turbulence produced). Then, as the active grid is used to produce higher turbulence levels, the magnitude of the pressure drop increases towards the original value. This is true for all three rib lengths, but more so for shorter ribs than long ribs. In the graph containing the data for the shortest rib it is apparent that the pressure drop is affected between the leading edge, and approximately $6H$ downstream. Further downstream, the pressure distribution of all three cases with the active grid merge before the reattachment point, and remain merged thereafter. The introduction of the grid caused an overall pressure drop by approximately $C_P = -2.64$, whereas the baseline case yielded a pressure drop of $C_P = -1$ in the test-section. This is reflected in the increased power of the wind-tunnel motor required to achieve the same free-stream velocity. The difference in pressure drop is removed by subtracting the value at the most upstream pressure measurement location.

5.5 Discussion: The mechanisms of bubble reduction

It was observed in section 5.3.1 that a thin boundary layer with relatively low shear results in increased in top recirculation region length. This in turn leads to a velocity profile with low momentum at the trailing edge, thus a short wake recirculation region. The opposite is true for a thicker boundary layer, where shear is higher at rib height. A small recirculation region occurs on the top surface, but a long bubble is produced in the wake. In contrast, free-stream turbulence at constant shear produces an overall

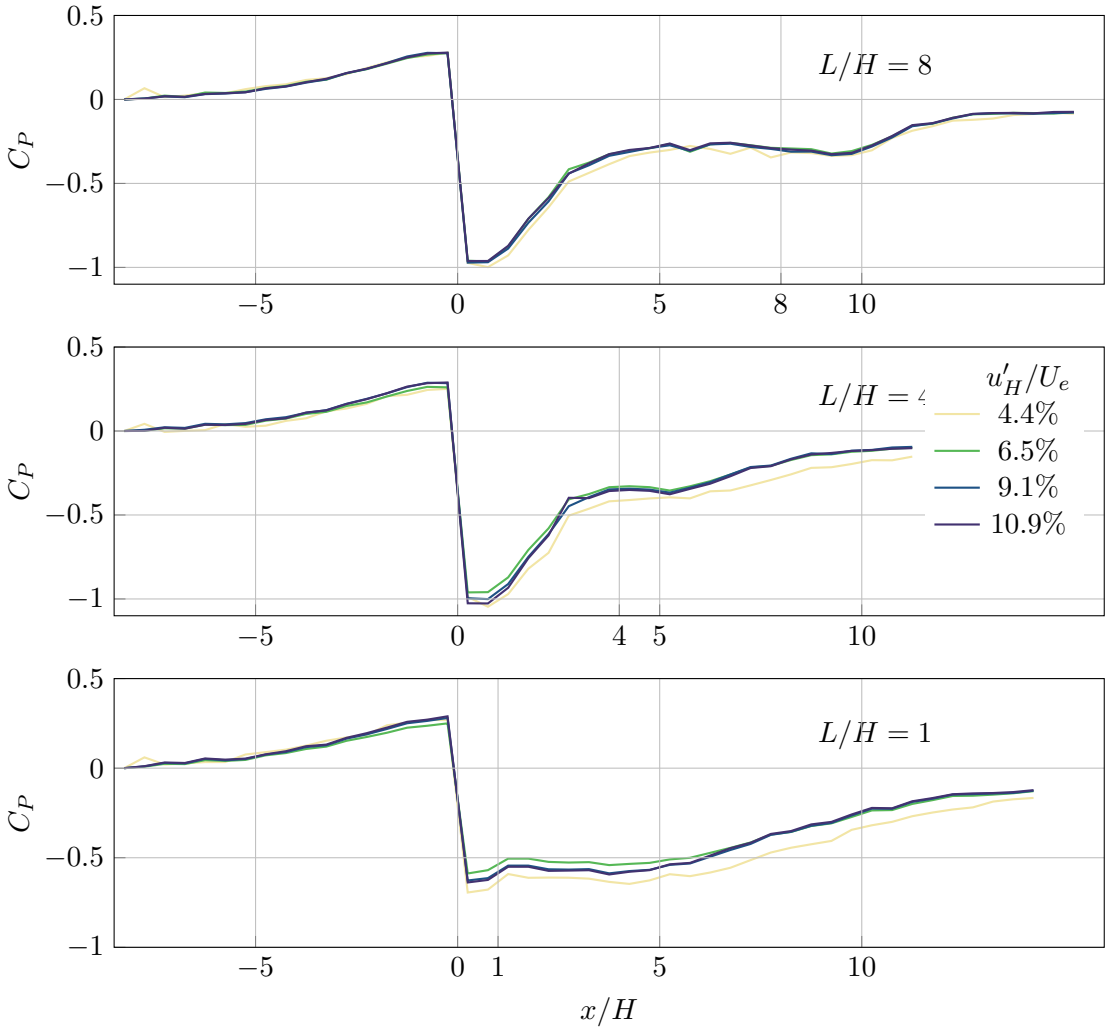

Figure 5.7: Mean surface pressure distribution for every turbulent case. From top to bottom: Long, medium and short rib lengths.

reduction of bubble size. This section illustrates some of the changes that occur with free-stream turbulence and how they may explain the diminished bubble size with FST.

5.5.1 Vertical velocity in the shear layer

The first parameter of interest is the vertical velocity in the shear layers produced by the obstacle. It is a measure of entrainment of irrotational free-stream fluid into the turbulent shear layers and recirculation regions. This in turn affects the spread of shear layers, and the size of recirculation regions.

Figure 5.8 depicts profiles of average vertical velocity V for each FST case. The baseline case is included, as well as the three grid settings. The velocity profiles are extracted

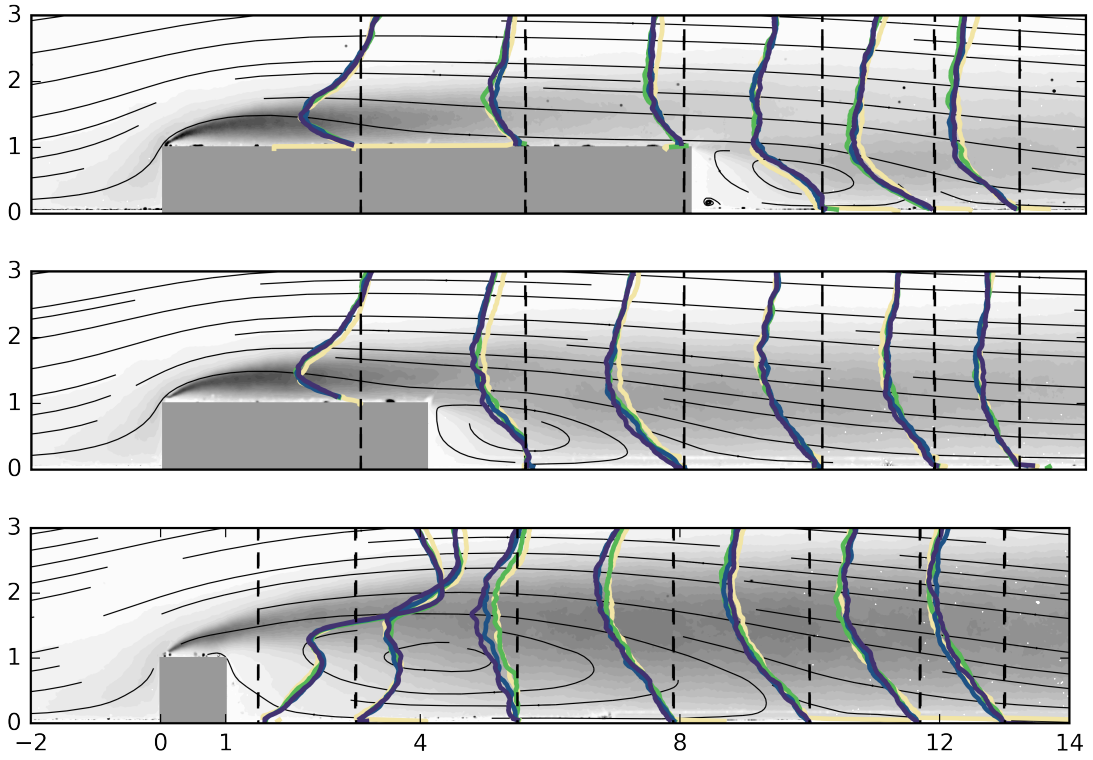

Figure 5.8: Vertical velocity at each dashed line as a function of free stream turbulence.

at each dashed line around which they are drawn. The values are amplified for visual purposes by a factor of 1.5.

The shortest rib exhibits mostly differences in V profile between the centre of the recirculation region and the reattachment point in the wake. Near the obstacle, the bubble appears to show similar shape, and little velocity difference is measurable. Past the centre of the recirculation region ($x/H \approx 4.5$), V becomes mostly negative between y/H =0 and 2.5, but differences are more noticeable between FST cases. Increased FST results in lower V above rib height which is paired with a shorter recirculation region. Downstream of the mean reattachment point ($x_R/H = 11.8$ without active grid) the discrepancies disappear.

The longer ribs produce similar trends with little or no difference on the top surface, but the most marked difference between the centre of the wake recirculation region and the mean reattachment point. This indicates that the top region is not affected noticeably by increased entrainment. On the contrary, the wake region exhibits more entrainment.

The difference between short and long ribs is consistent with the observations made in the mean bubble lengths. However, the variations observed between $L/H = 4$ and 8 are not explained by vertical velocity only. The following sections investigate further parameters which affect recirculation length.

5.5.2 Turbulent mixing in the shear layer

The addition of free-stream turbulence amplifies flow mixing in the shear layers as depicted in figure 5.9. A set level ($1.8\text{m}^2/\text{s}^2$) of cross-flow Reynolds stress term $u'v'$ is plotted above the obstacles for the original laminar case, as well as all three cases with the active grid mounted. It shows that increased free-stream turbulence results in a larger patch for a given level of $u'v'$ thus an increased mixing area. Furthermore, the maximum value at the centre of each patch is increased with FST.

The alterations in $u'v'$ levels vary with rib length. The short rib exhibits only one patch which begins several step heights downstream of the trailing edge. Despite the highest levels of T.K.E. being produced at the leading edge (see chapter 4), mixing through cross-flow fluctuations does not occur until the wake region. Increased FST moves the most upstream point of the contour further upstream. As a result, turbulent mixing occurs closer to the obstacle with increased FST. This in turn brings higher momentum flow on the edge of the recirculation region thus reducing its measured size. The medium and long ribs produce two distinct patches of high turbulent mixing, the first on the top surface, and the second in the wake. Similarly to the short rib, turbulent mixing reaches its highest intensity some distance away from the edges of the obstacle. On the top region, the drawn contour does not reach further upstream with increased FST. On the contrary, it is the downstream edge of the contour which grows further downstream. For the longest ribs this translates in little change before the top reattachment point, but more so before the trailing edge. Thus, the wake region is formed by an incoming flow with more mixing in case $L/H = 4$, and less so for $L/H = 8$ as the region of high mixing ends as the flow reattaches and settles before the trailing edge. In the wake of $L/H = 4$, very little turbulent mixing was measured with the laminar free-stream, but with FST, a strong change in $u'v'$ appears above the wake bubble. This explains why the recirculation length of $L/H = 4$ varies the most among the three cases. The wake of the longest rib exhibits strong turbulent mixing with laminar free-stream, and a marked increase in the area of the $u'v'$ contour with FST. However, the mixing occurs mostly above and downstream of the reattachment point which is consistent with the small changes in recirculation region size.

5.5.3 Production and transport of turbulent kinetic energy

The production and transport of turbulent kinetic energy provide further description of the mechanisms behind the reduction of bubble size with FST. The wake recirculation region length is dominated by increased mixing and entrainment above the reattachment point. However, along the top region the differences are smaller and appear downstream of the mean reattachment point. This focusses the interest on effects free-stream turbulence might have nearer the leading edge.

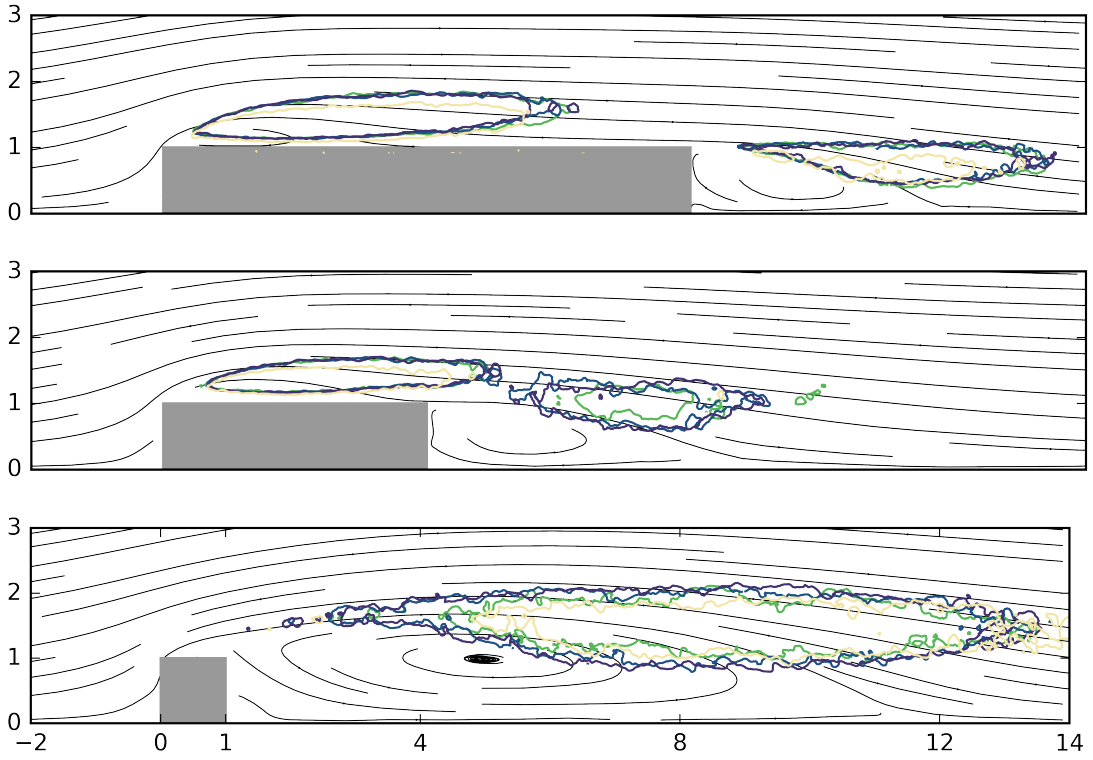

Figure 5.9: Cross flow terms of Reynolds stress indicating mixing in the shear layer as a function of free stream turbulence.

The turbulent mixing described in 5.9 result from a change in turbulent kinetic energy dominated by $u'u'$ and $v'v'$ maximum near the leading edge to $u'v'$ where the shear layers expand above each recirculation region. The regions of high $u'v'$ originate some distance from the leading edge and trailing edge of long ribs, but only from the leading edge of medium and short ribs. Figure 5.10 indicates where production of T.K.E. occurs, and how it is affected by free-stream turbulence. The data is smoothed for this plot by a gaussian filter of 5 vector width.

Near the leading edge of all ribs ($x/H = 0.5$) all three ribs exhibit a step change in production when the grid is installed. With further free-stream turbulence, the production is increased even more, but only marginally. As we travel downstream on the top surface of long ribs, production spreads with the turbulent region and the contrast between FST intensity vanishes gradually by the trailing edge. As the rib ends, a new shear layer is produced, Initially little difference is visible between FST cases, but after the reattachment point, the three turbulent cases stand out from the case without active grid. This means turbulence is produced in the wake and more so for high FST intensity rather than low. Medium ribs produce similar patterns along the top surface, but in the wake region, production is generally more vertically spread, and the peak rises with stream-wise distance from the trailing edge. In addition, FST appears to raise the peak of production too. The contrast between laminar and FST cases is less marked in this

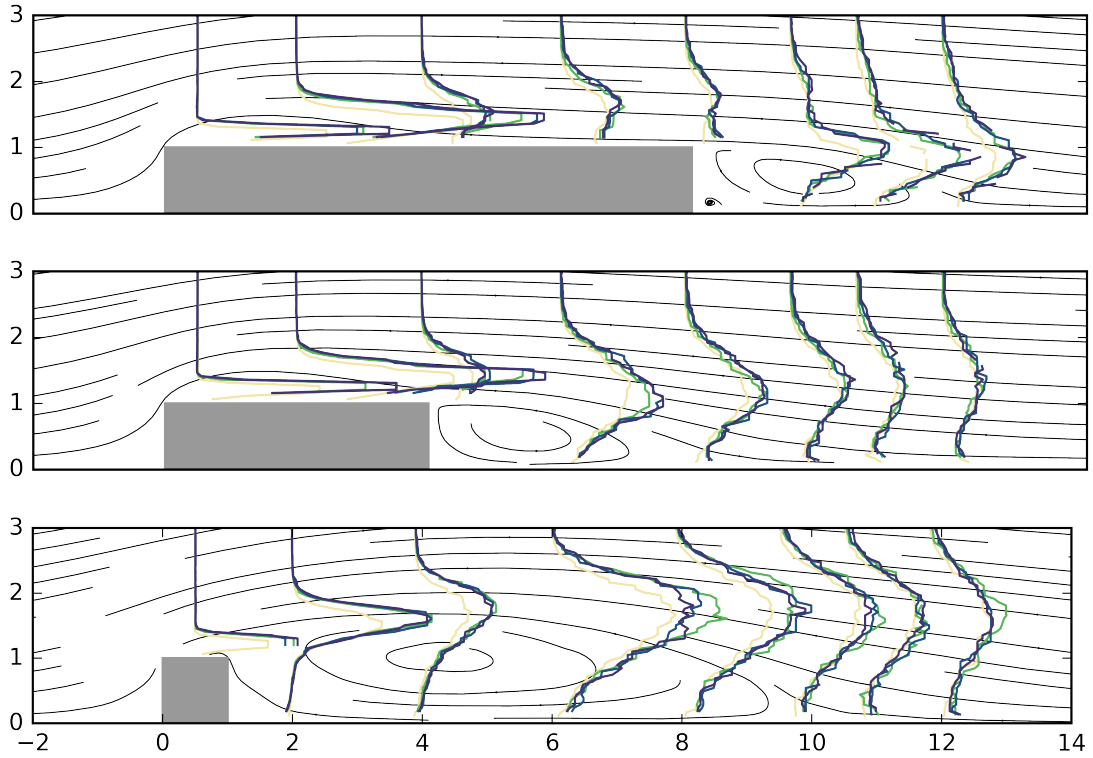

Figure 5.10: Turbulent Kinetic energy production for each rib length with varying levels of free-stream turbulence. A median filter with 1/4H size is applied to the data.

case compared to the longest rib. The shortest rib presents T.K.E. production profiles for FST cases which are distinct from the laminar case from the leading edge up to approximately the centre of the recirculation bubble. There, all four profiles show a peak production rate at $y/H \approx 2$ and the difference between cases vanishes gradually until the mean reattachment point. The rate of production is highest for longer ribs near the leading edge, however the shortest rib maintains production rates for the longest distance downstream of the obstacle.

Similarly to production, one may investigate the behaviour of the transport of turbulent kinetic energy. Figure 5.11 presents the transport of turbulent kinetic energy for three rib lengths and the laminar flow case and three FST cases. In this quantity, no difference is visible between turbulence intensities.

5.5.4 Discussion on $L/H = 8$ and $L/H = 6$ without FST

The wake bubble length of case $L/H = 6$ (3.71) is identical to that of $L/H = 8$ with free-stream turbulence (3.66-3.71) (laminar is 3.77). A comparison of the velocity profiles at the trailing edges shows similarities between $L/H = 8$ with FST, and $L/H = 6$ without FST. Figure 5.12 contains mean velocity profiles and turbulent kinetic energy

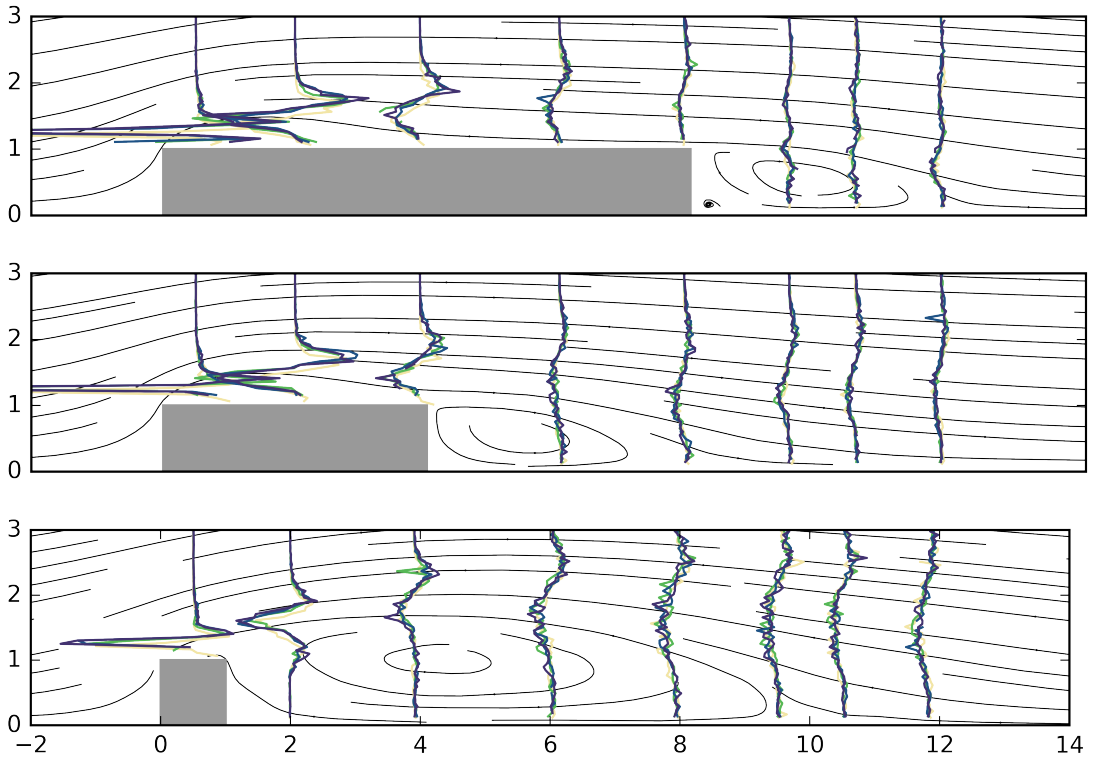

Figure 5.11: Turbulent Kinetic energy transport for each rib length with varying levels of free-stream turbulence. A median filter with 1/4H size is applied to the data.

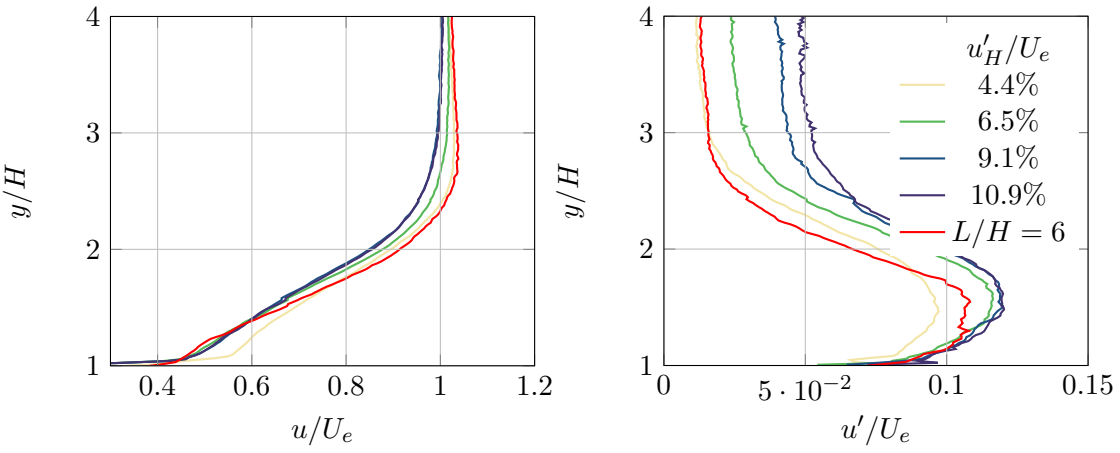

(a) (b)

Figure 5.12: Comparison of the velocity profiles at the trailing edge of $L/H = 8$ at different turbulence intensities, and $L/H = 6$ without the active grid. $L/H = 6$ without active grid produces the same wake recirculation length as $L/H = 8$ with FST.

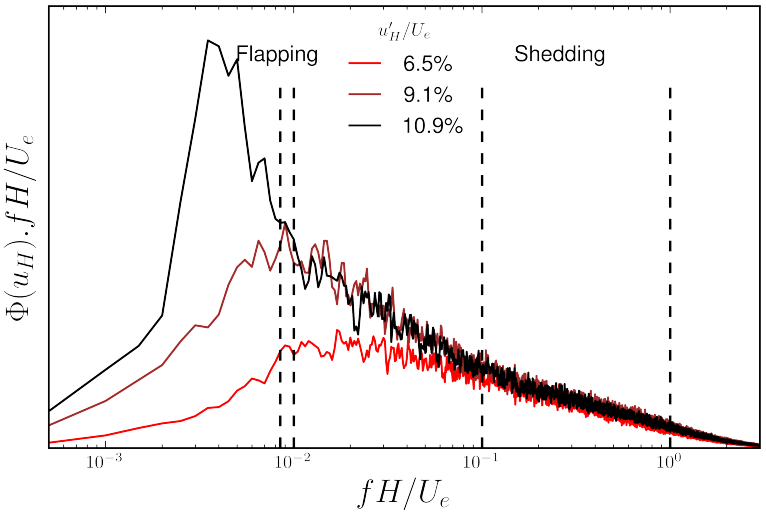

Figure 5.13: Pre-multiplied power spectral density of the incoming velocity at the height of the rib ($y/H = 1$) from hot-wire measurements without the presence of the obstacle. All three levels of FST are represented, as well as the range of natural frequencies of vortex shedding, and shear-layer flapping around ribs of varying length. This indicates FST adds mostly low-frequency fluctuations in the flow which are more likely to interact with the flapping motion than the shedding of vortices.

normalized by free-stream velocity. From these graphs, we can see that the lower portion of velocity and fluctuation profiles from 0 to $y/H = 0.5$ of case $L/H = 6$ match those of case $L/H = 8$ with FST. The top surface of $L/H = 6$ is shorter, therefore the trailing edge is closer to the top recirculation region. This brings more turbulence from the top region to the trailing edge. The shape of the mean velocity profile is also deviated to match those of the cases with FST. Above $y/H \approx 0.5$, the profiles return towards the profiles of $L/H = 8$ without FST.

It is also noticeable that the turbulence levels although increase consistently in the free-stream with the active grid, nearer to the surface the intensity saturates. It appears to become independent of FST above 9% of FST. These observations suggest there is a relationship between the size of a BFS separation region and the lower portion of the incoming flow.

5.5.5 Overlap between forcing frequency and natural frequencies of the rib

The addition of FST to the original flow has an effect which varies with obstacle length. As seen above, short ribs tend to produce shorter recirculation regions as FST increases. On the contrary, longer ribs tend to show fixed recirculation length with increasing FST. The sections above describe how the flow changes with FST around each studied rib and it appears that the reduction in bubble size is associated with increased $T.K.E.$

production, increased $u'v'$ as well as increased vertical flow velocity. These quantities do not explain the contrasting responses from short ribs and the longer ones. It is possible however to identify the reason behind the varying response to FST between each rib by investigating the time or length scales in the flow with FST.

Saathoff and Melbourne (1997) describes the effect of increased FST on a blunt leading edge which produces similar types of recirculation regions as the leading corner of ribs. It is observed that increased fluctuations occur in surface pressure fluctuations with increased FST. The mechanism observed involves a large scale perturbation in the flow impinging the leading edge of the obstacle provoking a roll-up of the shear layer. This phenomenon occurs at naturally in the canonical flow over blunt obstacles, but may be modulated by FST.

It is believed that the same phenomenon occurs on ribs, but rib length has a secondary effect. Indeed, the short rib produces a long shear layer from its leading edge to the downstream surface. Along this shear layer travel smaller scale vortices which are shed from the leading edge. These produce some mixing between the free-stream and the recirculation region. However, it is the flapping of the shear layer which causes the largest amount of mixing thus affecting the recirculation region size. The two phenomena (flapping and shedding) occur naturally at frequencies separated by one to two orders of magnitude. Longer ribs on the other hand produce smaller shear layers where the shed vortices dominate the flapping of the shear layer. This is evident from the previous chapter (4), where a narrow range of frequencies was found near the leading edge related to shear layer flapping, and a range of frequencies associated with vortex shedding which decreases with downstream distance from the leading edge of the rib.

In this study, when introducing FST, fluctuations of large scales are introduced which influence the flapping motion of a shear layer more than the shedding of vortices from the leading edge of a blunt object. Indeed, as the active grid is used to produce higher FST, larger and slower scales are observed at rib height which will directly influence its behaviour. A streamwise velocity spectrum at rib height (See figure 5.13) shows that only reduced frequencies of 0.001 to 0.1 exhibit higher intensity. Previous literature (Cherry et al., 1984) indicates that the flapping motion of the shear layer occurs at a reduced frequency of the order of 0.01. On the other hand, vortex shedding from the leading edge occurs one to two orders of magnitude faster depending on the exact flow conditions, and the streamwise distance of measurements from the leading edge.

These flow conditions are produced by the active grid used in this study, however, it would be interesting to study the effect of FST at a higher frequency, or smaller time scale. It could confirm the hypothesis that fluctuations of similar scale interact without affecting higher or smaller scales. A possible source of information for this would be the study of active flow control where fluctuations at set frequencies are employed to reduce wake regions.

Chapter 6

Spatio-temporal characteristics of separating and reattaching shear layers

We have seen in previous chapters that two phenomena dominate the motions of the separated flow over ribs, the slow shear layer flapping and a higher frequency vortex shedding from the leading edge. These phenomena occur at similar frequencies in surface pressure fluctuations as well as velocity. Consequently, in this chapter we are interested in illustrating the link between surface pressure fluctuations and velocity fluctuations in the flow of a rib of length $L/H = 4$. The length of the rib affects the state in which the perturbations caused by the forward-facing step region reach the wake region. We have selected $L/H = 4$ because it produces the most compact flow separation and the perturbations from the leading edge retain energy in the wake region.

6.1 Spectral analysis of p and u

Using data from chapter 4 where velocity and pressure measurements were made, we may obtain spectra indicating the frequency at which phenomena occur in the flow over rib $L/H = 4$. The pressure spectra are made by using 1s-long windows of four 30s-long signals. These windows overlap overs 0.5s. The sampling frequency of pressure transducers was set to 25.6kHz. The velocity spectra are made using the same parameters from hot-wire data sampled.

The surface pressure spectra indicate that two dominant frequencies stand out. A low reduced frequency of 0.03-0.04 which is nearly constant with streamwise location and a second which is 0.4 at the leading edge and continuously decreases down to approximately 0.07 at the location nearest to the mean reattachment point in the wake. The

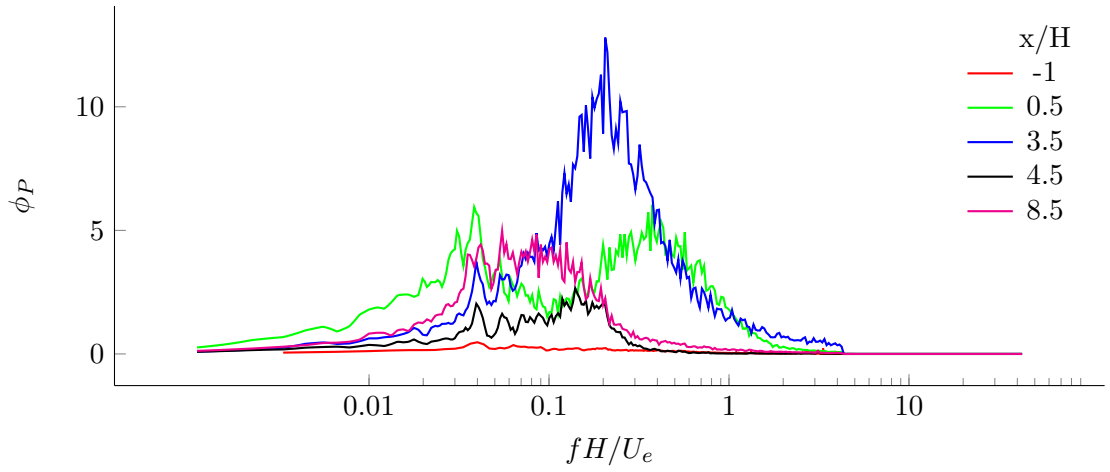

Figure 6.1: Sample pre-multiplied pressure density spectra at the surface of the rib at varying locations marked in the legend (x/H).

intensity associated with the lowest frequency decreases along the top surface but increases at the mean reattachment point. The peak associated with the higher frequency increases at the mean reattachment point on the top surface, and again in the wake region. The behaviour observed with the high frequency peak is consistent with observations on forward-facing steps where vortices shed from the leading edge generate fluctuations in pressure and velocity in this range of frequency, but the frequency associated decreases with streamwise distance from the leading edge as the shear layer grows and the vortices merge into larger, slower structures Cherry et al. (1984).

In a similar fashion to pressure spectra, we investigate velocity spectra. It appears there are also two dominant frequencies of interest near the leading edge which vary with stream-wise position but also vertical distance to the surface of the rib. Figures 6.2a, 6.2c, 6.2b and 6.2d contain velocity spectra acquired at varying height (below, in and above the shear layer stretching above the rib) at the leading edge, trailing edge, mean reattachment point of the top surface and mean reattachment point of the wake region respectively. Near the leading edge, the lower frequency peak in the shear layer is centred on 0.035 whereas the higher frequency peak is higher than that observed in pressure at $fH/U_e = 1$. At the trailing edge, the two peaks have merged in one peak which is centred on the same frequency as that observed in pressure. Finally we observe that frequencies match very well near the mean reattachment points on top and in the wake of the rib. However the wake region appears to fluctuate at half the reduced frequency of the top surface. The correlation between velocity and pressure at these locations is studied in the following section.

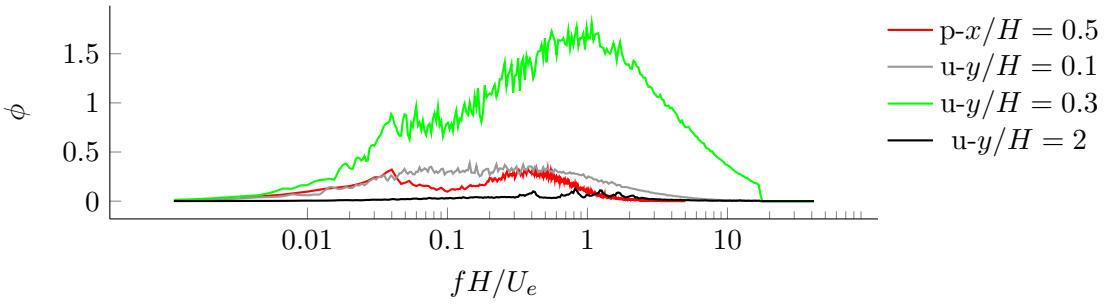

(a) Sample pre-multiplied pressure and streamwise velocity density spectra at the leading edge of the rib at varying locations marked in the legend (y/H).

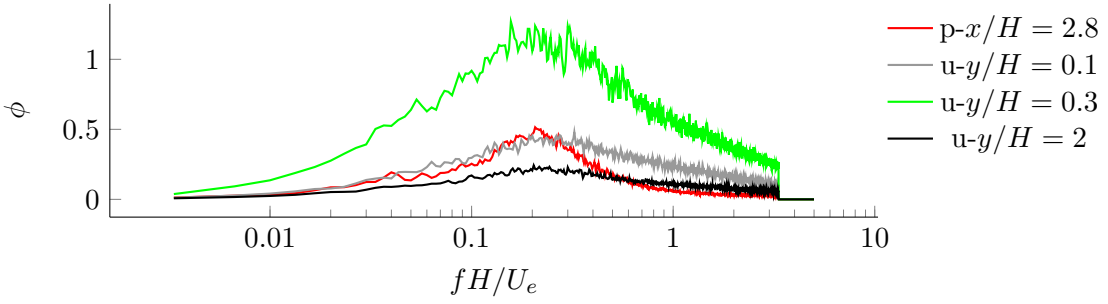

(b) Sample pre-multiplied pressure and velocity density spectra at the reattachment point on the top surface at varying vertical locations marked in the legend (y/H).

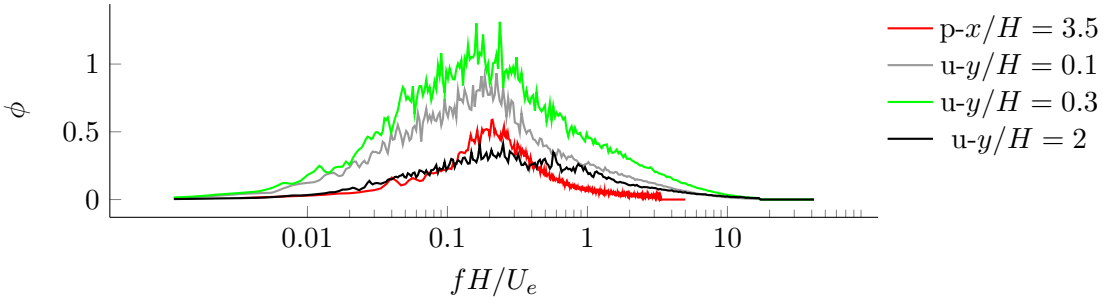

(c) Sample pre-multiplied pressure and velocity density spectra at the trailing edge of the rib at varying locations marked in the legend (y/H).

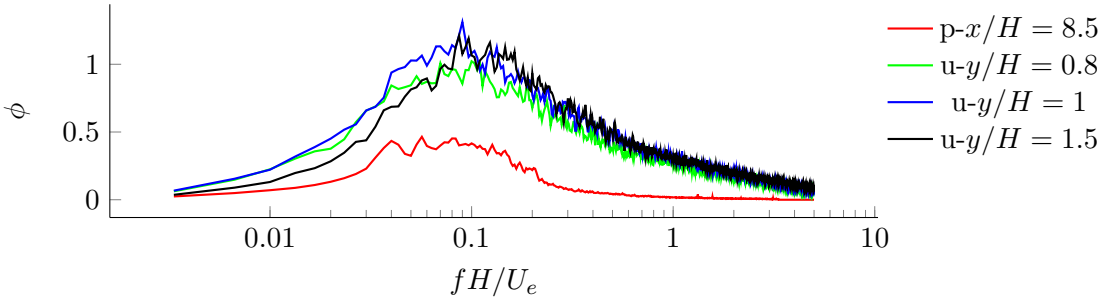

(d) Sample pre-multiplied pressure and velocity density spectra at the reattachment point in the wake region at varying vertical locations marked in the legend (y/H).

Figure 6.2

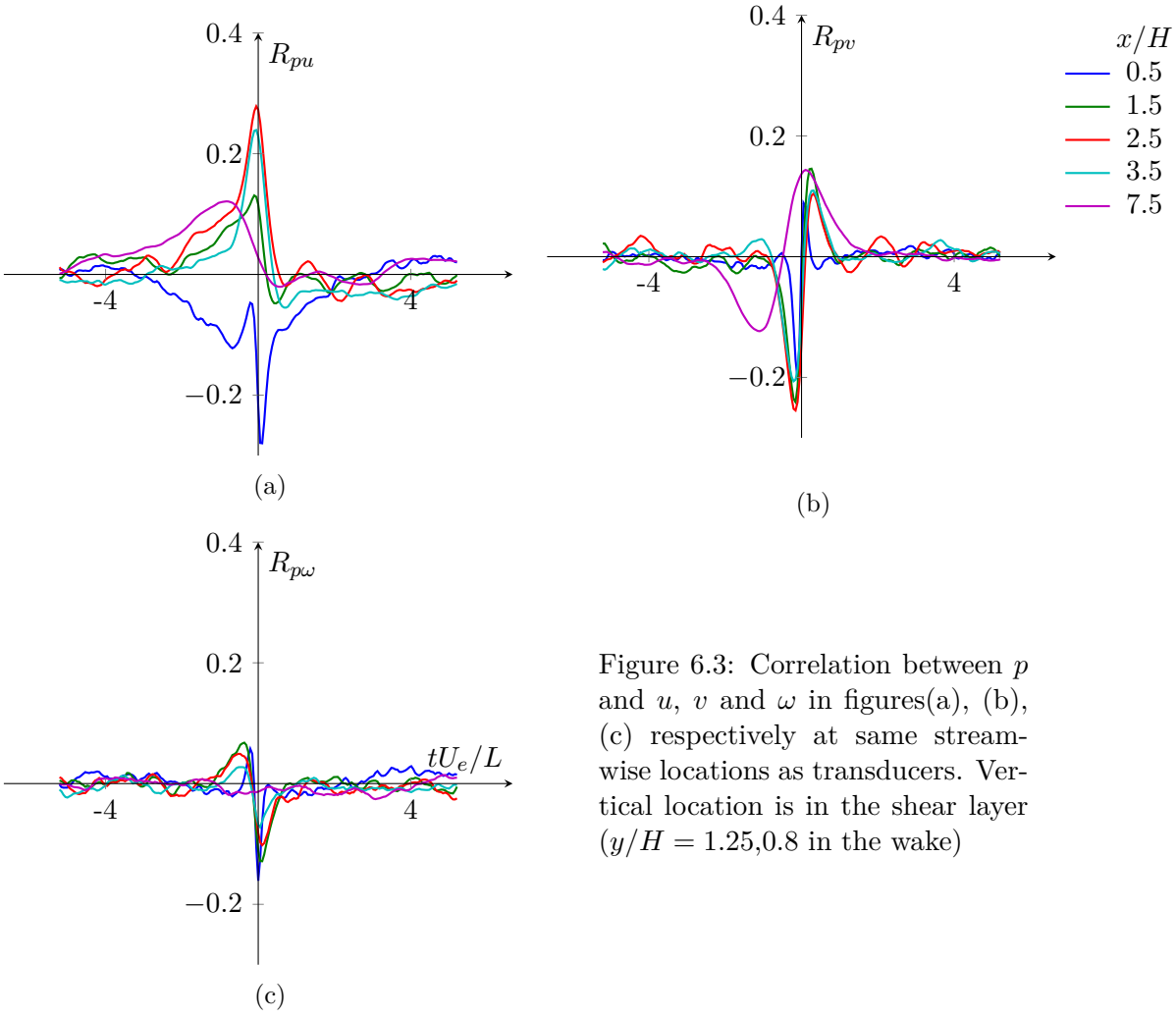

Figure 6.3: Correlation between p and u, v and ω in figures(a), (b), (c) respectively at same stream-wise locations as transducers. Vertical location is in the shear layer ($y/H = 1.25$,0.8 in the wake)

6.2 Correlation between p and u, v, ω

We study correlation between pressure, velocity (u and v) and vorticity at chosen locations to capture the dynamics of the flow.

Figure 6.3 depicts the correlation between pressure and two components of velocity as well as vorticity. The velocity and vorticity signals are extracted above the pressure transducer, in the shear layer ($y/H = 1.25$ or 0.8, on top or in the wake). The correlations show that a delay of 100 samples is sufficient to capture the correlation peaks between p and u the stream-wise component of velocity. This corresponds to a non-dimensional time of $t^* = 5$ where $t^* = \frac{100U_e}{f_s L}$ where $U_e = 10$m/s, $L = 0.12$m and $f_s = 1600$Hz. The correlation tends to be high in the past time-delays meaning the velocity at one location and one time instant has an effect, several time-steps later on the surface pressure. In addition, at every location, the correlation is mostly positive, or mostly negative then it converges to 0 with high time-delays. This means an event in pressure (lower or higher than average values) is associated with a surge in velocity, or a drop in velocity. The first transducer at the leading edge is negatively correlated

with stream-wise velocity, meaning a positive pressure input is associated on average with a negative stream-wise velocity fluctuation. The other transducers are positively correlated and the maximum correlation value is attained at $x/H = 2.5$ and $x/H = 3.5$, between which the mean reattachment point is located. At that location, a positive stream-wise velocity surge is associated with a positive pressure fluctuation.

The correlation between vertical component of velocity and surface pressure produces a lower correlation peak than the stream-wise velocity component, but the shape of the correlation is almost symmetric. This represents a situation where the vertical velocity has an equal but opposite effect before and after the time instant of the pressure value on average. This is very likely due to the passage of vortices or other periodical motion which are made of a negative then a positive vertical velocity fluctuation. The small time-delay is due to the vertical separation between the transducer and the point from which velocity is extracted. Finally, the correlation between vorticity and pressure is lower because of the high noise in gradients obtained from PIV. On average, the correlation with vorticity lasts the shortest amount of time among all three terms analysed here. However, similarly to the vertical velocity component, the correlation seems symmetric with respect to the centre of the correlation window.

Figure 6.4 depicts the correlation between p and u, v or ω at $x/H = 3.5$ at varying vertical positions. The data plotted for seven points between $y/H = 1.1$ and 3.5 covers the lower part of the shear layer (centred on $y/H = 1.5$ at that location) up the free-stream above the rib, where there is less than 2% $T.K.E$. It is apparent that there is little correlation between u and p (figure 6.4a) very far from the step (less than 0.1) but the small correlation stands out clearly from the noise. As the probe location is lowered between $3H$ and $1.1H$, strong negative-only correlation appears which gradually evolves to a positive then negative shape, then a strong positive only correlation. The correlation between vertical velocity and surface pressure is also comparatively small in the free-stream ($y/H = 3.5$) and increases through the shear layer reaching a peak of 0.3 between $y/H = 2$ and 2.3. Closer to the surface of the obstacle it decreases again to lower values. Unlike the streamwise velocity, the vertical velocity correlation remains symmetric at all heights with a negative peak in the negative delays and a positive peak in the positive delays. Finally, the correlation with vorticity evolves with vertical distance from the surface of the rib as well. It reaches a maximum of 0.1 at $y/H = 1.7$ and appears to evolve from negative time delays to positive time delays with increasing heights.

The study of correlation between surface pressure and various velocity measurements above the rib indicates that a wide range of dynamics exist in the flow. Velocity and pressure are correlated both forward and backward in time up to $t^* = 5$ in ways that vary spatially. In the next chapter, we estimate velocity based on pressure measurements, this procedure will require a thorough understanding of the link between these two quantities. In this section, we see that velocity and pressure are correlated over a large period of time, but the correlation depends on the location of transducers and velocity

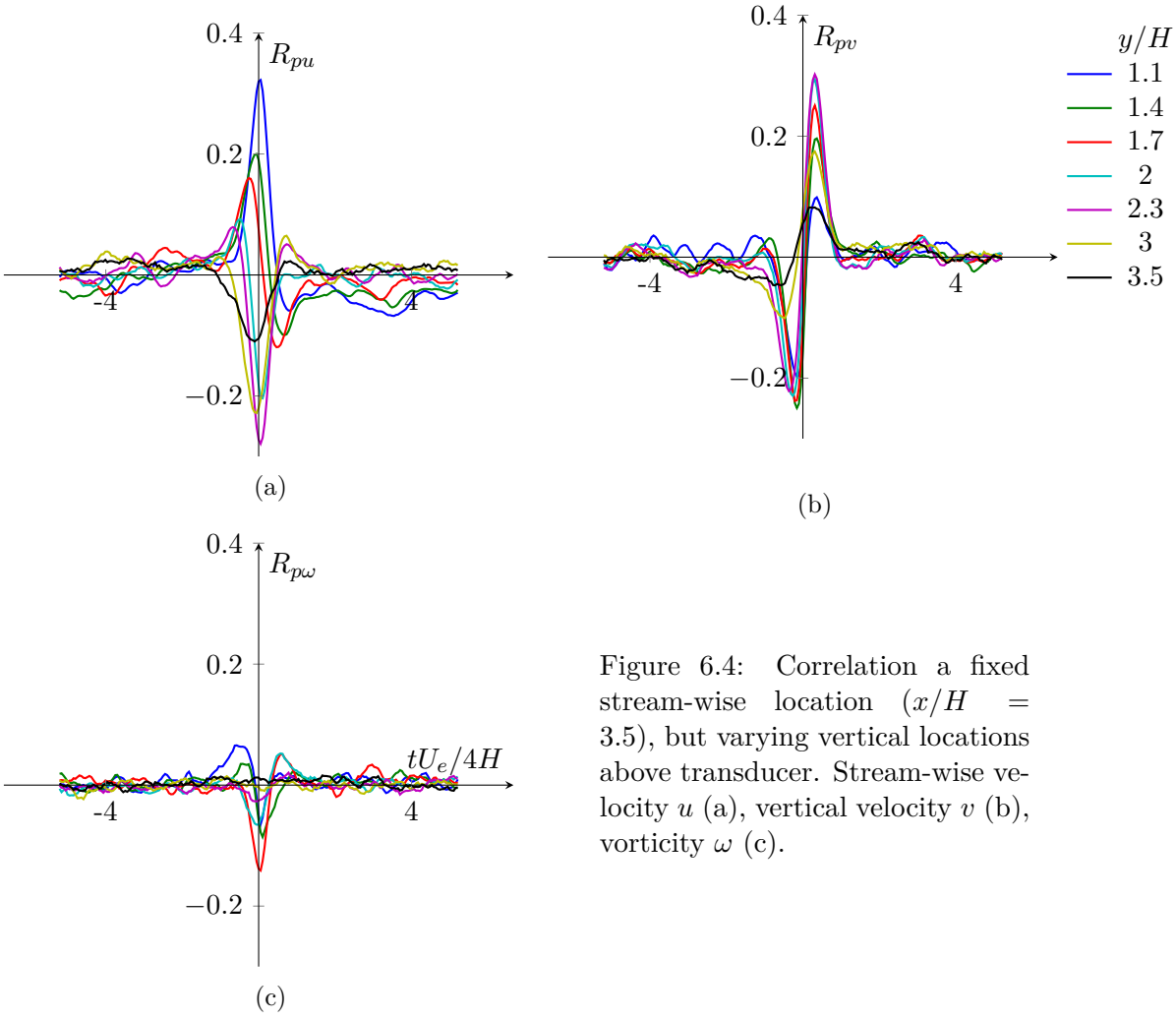

Figure 6.4: Correlation a fixed stream-wise location ($x/H = 3.5$), but varying vertical locations above transducer. Stream-wise velocity u (a), vertical velocity v (b), vorticity ω (c).

points analysed. Thus, the estimator of velocity needs to include a long pressure series while maintaining resolution to capture the various phenomena.

6.3 Conditional averaging of recirculation region area

This section illustrates how the size of the top and the wake bubbles are related to specific patterns in velocity. In order to do so, we measure the instantaneous recirculation area in the velocity field. The time-dependant quantity can be Hilbert transformed to reveal the phase θ of bubble size. We average eight sectors of the phase to show the stages of bubble growth and decay.

Spectra of the time series of each recirculation region area are visible in figure 6.5. These indicate the wake region area fluctuates at the slowest rate of all the dynamics of the flow. The dominating frequency is centred on $fH/U_e = 0.01$. The top region on the other hand presents dynamics occurring at a higher frequency. The dominant frequency is centred on $fH/U_e = 0.04$ which corresponds to the peak observed in the

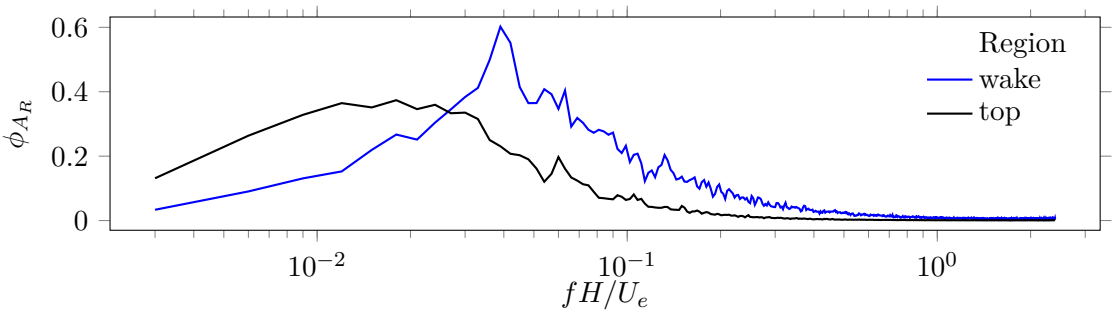

Figure 6.5: Spectra of area of recirculation regions.

shear layer flapping motion reported earlier and in previous studies. With the knowledge of the dominant frequency, we can establish that the Hilbert-transformed signal will be rotating around the origin of the complex plane at a slow rate, mostly linked to the low-frequency dynamics of the flow. Consequently, each phase studied in the next paragraphs represents phases of those slow cycles.

Figure 6.6 illustrates the state of streamwise velocity fluctuations on average for each of the eight phases of top bubble area. This serves as a surrogate for the separation bubble which we can follow Pearson et al. (2013). The maps show a relatively small recirculation region at $\theta = 0$ associated with a large red zone covering the whole top surface. The following phases indicate that the high speed region moves downstream and remains above the wake region. It progressively dissipates at higher phases because it loses coherence with respect to bubble size. While the accelerated flow region moves downstream, a region of slow flow takes position on the top surface and grows from the leading edge to $x/H = 9$ over half of the cycle before moving downstream and being replaced again by a high speed region. Thus, it appears the growth and decay of the top bubble is paired with a pocket of slow or fast flow that grows on the top surface and stretches downstream before disconnecting from the leading edge and travelling downstream. Similarly, figure 6.6 also shows the corresponding phase averaged pressure fields estimated from PIV. The patterns in pressure seem to be coherent only on the top region because the averages show more noise past the trailing edge at every phase. Pressure seems offset in time relative to velocity. Indeed, at phase $\theta = 0$ when the bubble is at its smallest and the velocity is at the highest, pressure shows a low pressure region followed by a high pressure region which tends to decelerate the flow. The periodic acceleration and deceleration of the flow seems maintained this way through the phases.

The phases of the wake region area are also associated with large scale velocity fluctuations. Figure 6.7 shows the eight phases of wake bubble size and the corresponding averaged velocity and pressure fields. The smallest wake region is associated with a large acceleration of the flow and vice versa. There seems to be little link between the state of the flow on top surface and the wake region. This could be due to the difference in frequency at which the two bubbles grow and shrink as can be seen in figure 6.5. A high

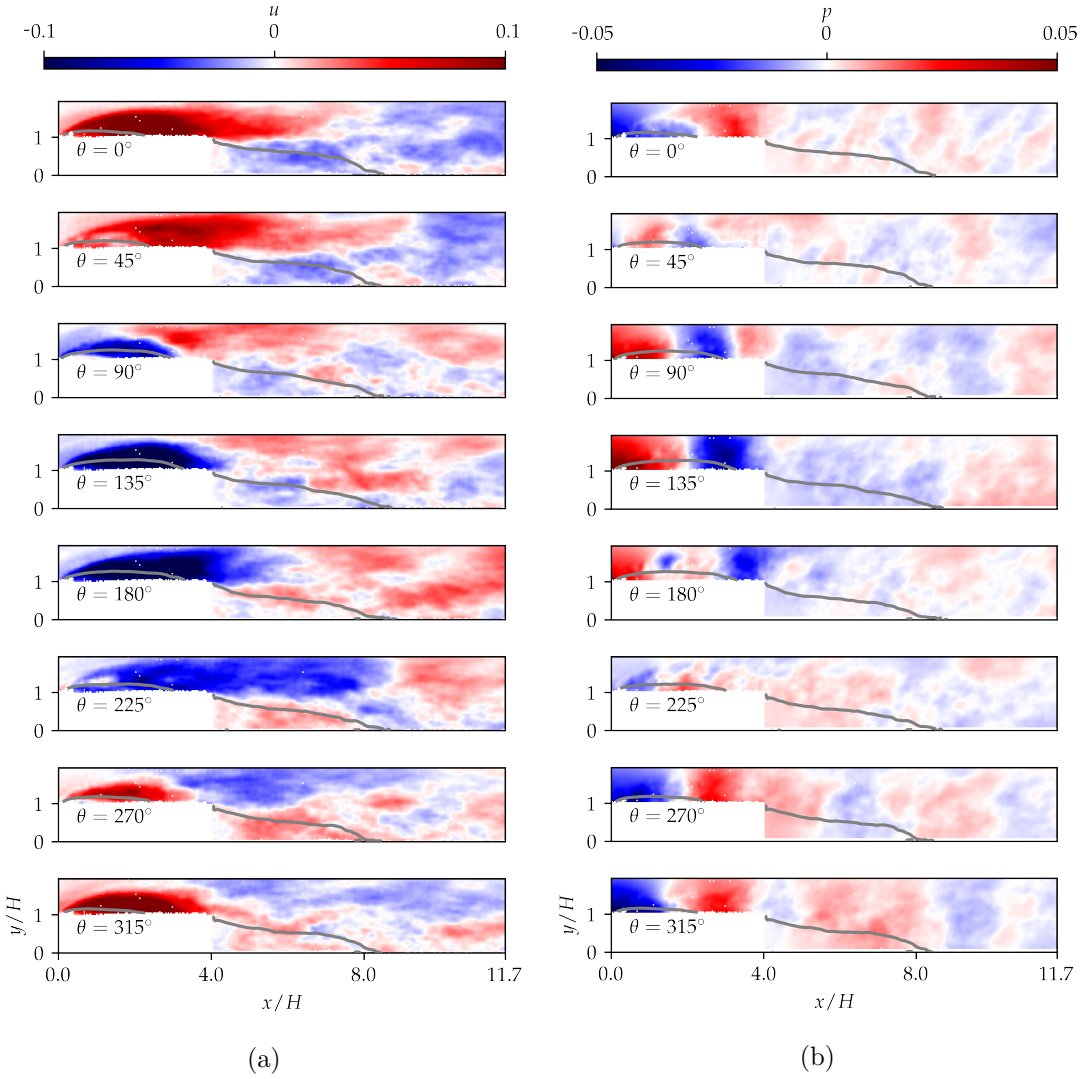

Figure 6.6: Conditional averaging of the streamwise velocity u (a) component and pressure fluctuations p (b) estimated from PIV as a function of top bubble size.

speed region is also made of a low pressure region followed by a high pressure region applying a force opposite to flow direction. The size of these high/low pressure regions is larger in the wake region, but their intensity is lower than in the top region. The regions of accelerated or decelerated flow in the wake appear to grow from the middle of the recirculation region, growing upstream and downstream at the same time before "disconnecting" from the trailing edge and travelling downstream.

6.4 Phase averaging based on velocity criteria

Phase averaging based on bubble area shows that bubbles tend to grow due to low velocity flow pockets growing before moving downstream. We also phase averaged streamwise

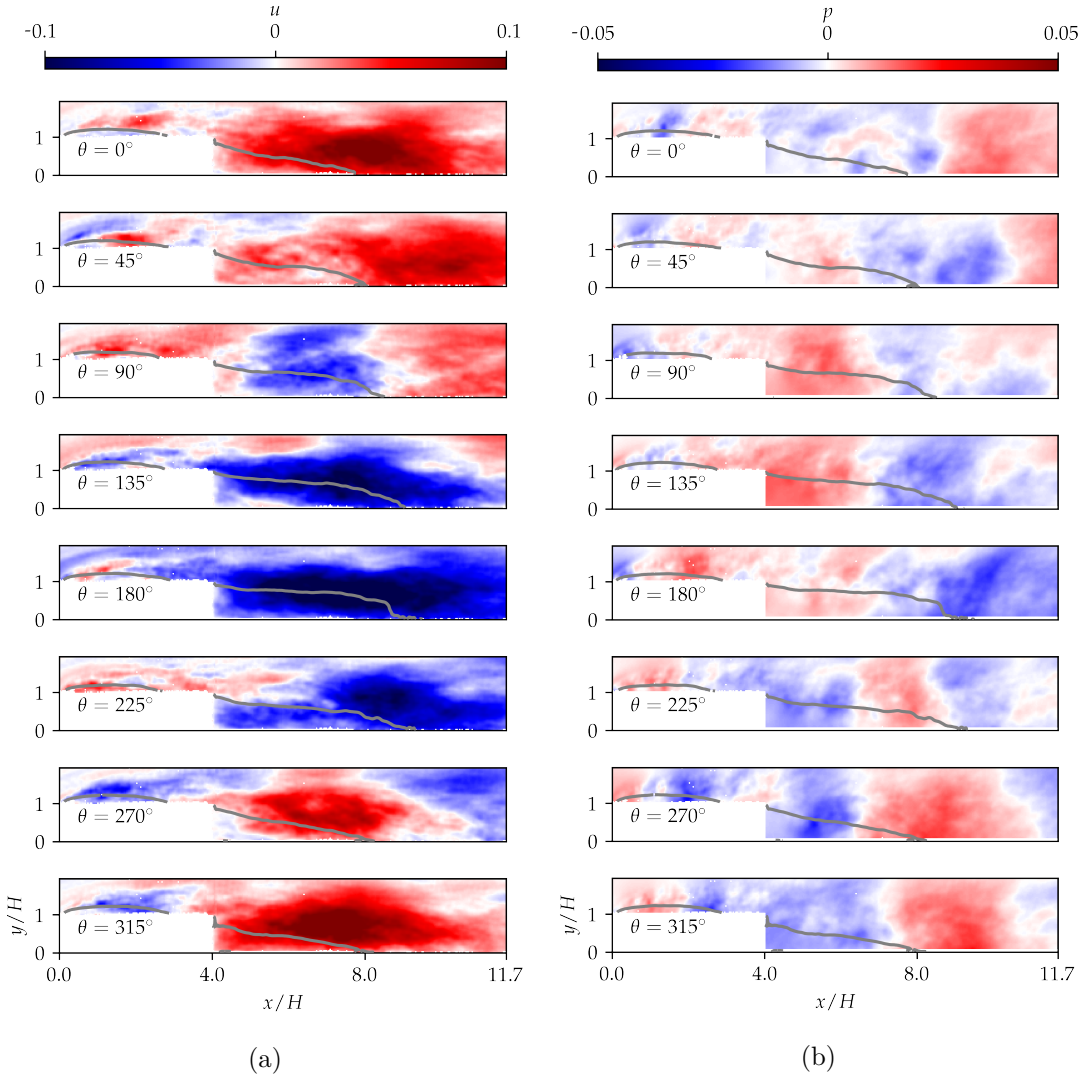

Figure 6.7: Conditional averaging of the streamwise velocity u (a) component and pressure fluctuations p (b) estimated from PIV as a function of wake bubble size.

and vertical velocity components based on velocity at key locations. Velocity was shown earlier to be dominated by two phenomena near the leading edge but only one downstream of the top reattachment point. Consequently, we use three criteria to carry out the phase averages: velocity in the shear layer at $x/H = 0.5$ and $y/H = 1.2$ filtered to preserve the shear layer flapping at $fH/U_e = 0.03$, the same point band-pass filtered to isolate vortex shedding at $fH/U_e = 0.4$, and velocity near the trailing edge at $x/H = 3.5$ and $y/H = 1.2$ with band pass filtering from $fH/U_e = 0.2$ to 0.4.

Figure 6.8 shows similar trends as the previous conditional average in figure 6.6. A high or low velocity in the shear layer is associated with a large high or low velocity region along the top surface and a small or large recirculation region respectively. The uniform regions seem to grow and stretch downstream over the wake region before being replaced by a region of the opposite sign. The opposite region grows from the surface upwards

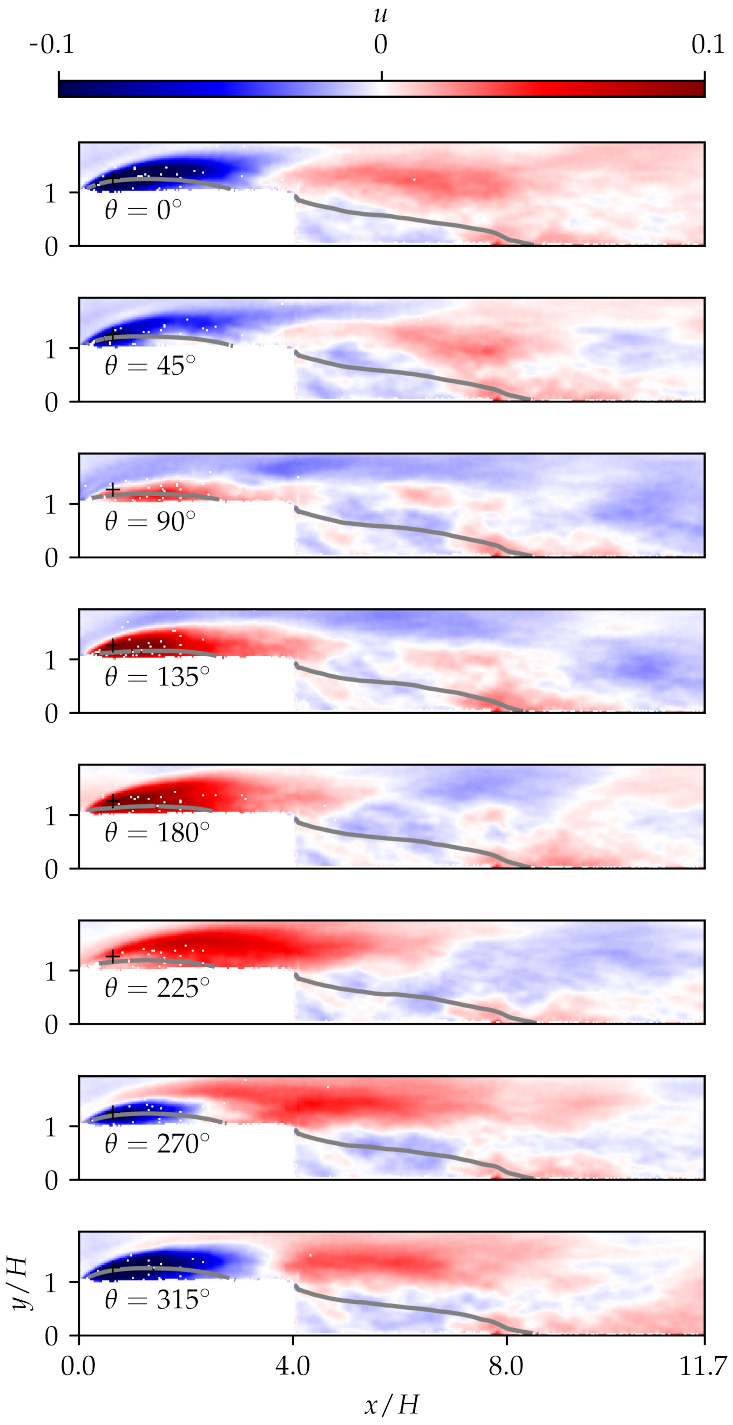

Figure 6.8: Phase average of streamwise velocity u based on velocity in the shear layer near the leading edge indicated by the black cross. The velocity criterion near the leading edge is dominated by two frequencies, here we band-pass filter to preserve the peak at $fH/U_e = 0.03$.

before stretching downstream in turn. The wake region area is not significantly affected by the state of the top region because of the frequency difference which eliminates out of phase motions through averaging.

Figure 6.9 shows the phase average of the highest frequency motion observed in velocity spectra. Phase averaging indicates that this motion is localized to the leading edge and the early stages of the shear layer. The rest of the field of view shows no cyclic motion. The motion was most visible in the vertical velocity component thus it is depicted here. The pattern isolated at $fH/U_e = 1$ is a small succession of up and down motion which quickly dissipates with distance from the criterion point. This reflects how quickly vortices evolve within the shear layer. The growing vortices rotate progressively slower thus causing velocity fluctuations at progressively lower frequencies which are not captured in this phase averaging. These motions have little effect on bubble size, both on top and in the wake.

The third phase average criterion is the vertical velocity component near the trailing edge. Here frequencies from $fH/U_e = 0.2$ to 0.4 are isolated in the velocity time-series to carry out the phase averaging. Figure 6.10 depicts the eight phases of the corresponding cycle. It appears this motion is dominated by large circular patches of high and low vertical velocity. These patterns appear from the second half of the top region $x/H = 2$ and disappear before $x/H = 6$. The size of the top region is affected by this motion because a high velocity zone near the mean reattachment point causes the bubble to close earlier and vice versa. x_R moves by less than $1H$ as a consequence of these motions. The wake region is not noticeably affected.

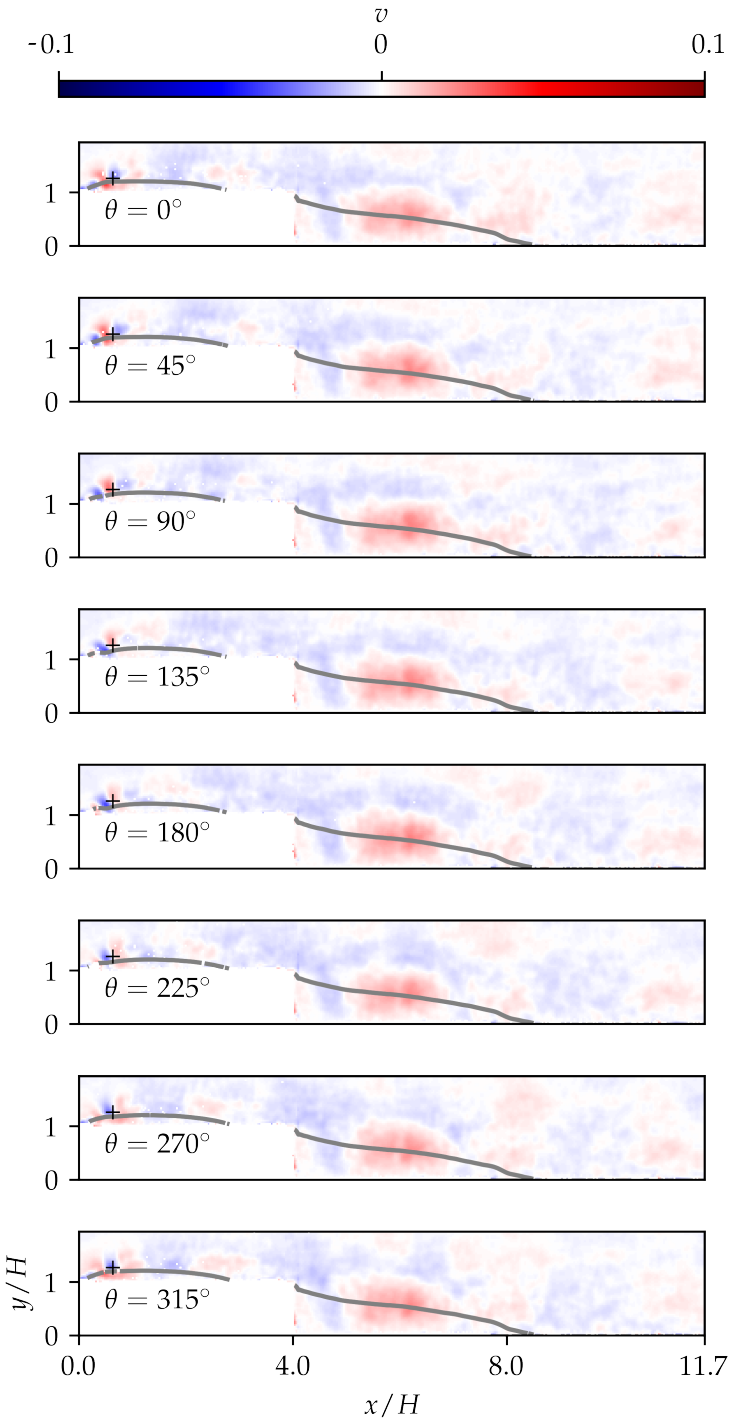

Figure 6.9: Phase average of vertical v velocity based on velocity in the shear layer near the leading edge indicated by the black cross. The velocity criterion near the leading edge is dominated by two frequencies, here we band-pass filter to preserve the peak at $fH/U_e = 1$.

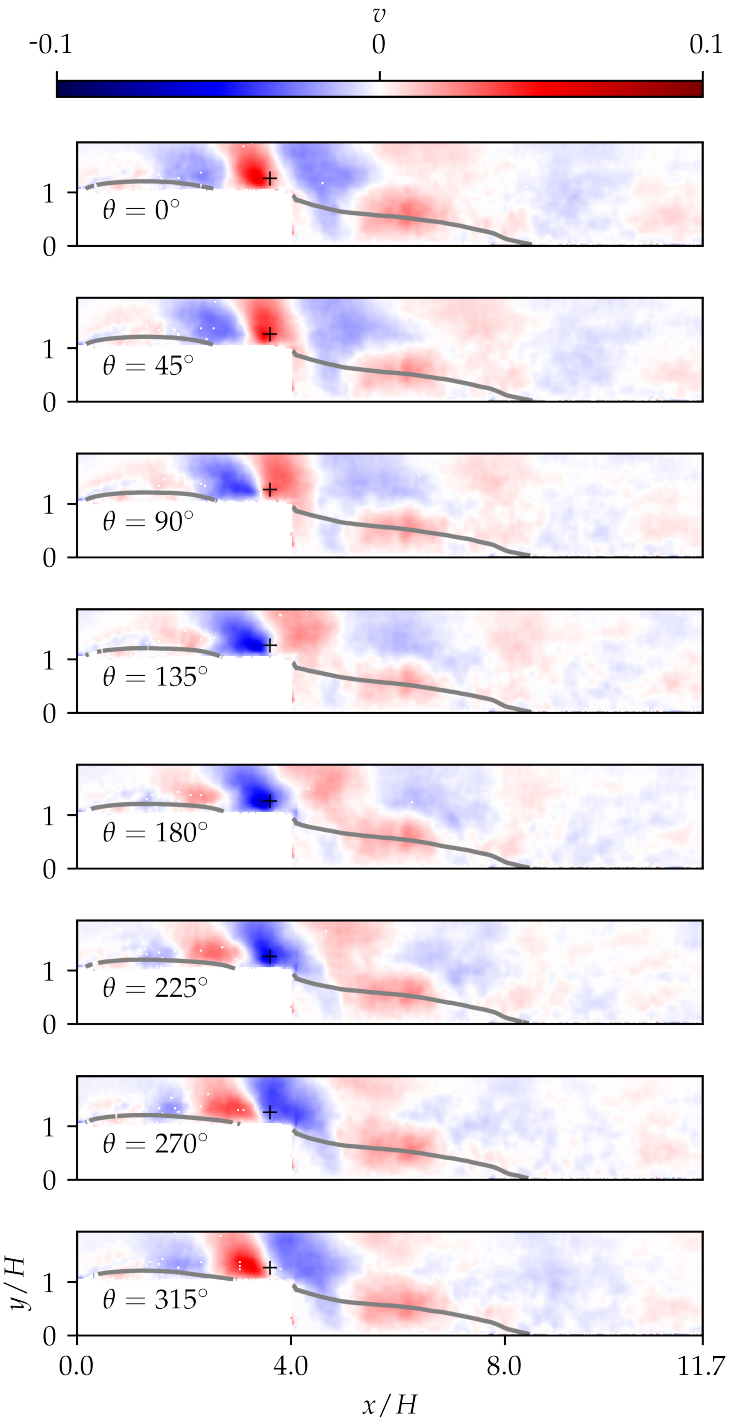

Figure 6.10: Phase average of vertical velocity v based on velocity near the trailing edge indicated by the black cross. The velocity criterion is band-pass filtered to preserve the peak at $fH/U_e = 0.2 - 0.4$.

Chapter 7

Linear estimation of velocity over a rib using surface pressure

In order to study the relationship between surface pressure fluctuations and velocity fluctuations around ribs, we decompose the flow and reconstruct only the velocity fluctuations that are correlated with surface pressure measurements. This provides velocity information which is "filtered" from the velocity fluctuations that are not related to surface pressure. Thus we are not aiming to reconstruct the original flow faithfully, but attempting to extract only the velocity fluctuations linked to surface pressure. Rib $L/H = 4$ studied in detail in chapter 6 is used throughout this chapter.

Other studies have established a relation between surface pressure and velocity measurements. However, this is the first to the author's knowledge with high-speed PIV data over a fully turbulent flow over a rib geometry. Clark et al. (2014) have studied a blunt trailing edge wake with PIV measurements but maintained a low Reynolds number in order to preserve periodic coherent vortex shedding. Lasagna et al. (2013) has studied the flow over a cavity but using hot-wire measurements which are excellent to obtain good statistical convergence and high precision at one location at a time. In our study we attempt to study a complex turbulent flow with PIV measurements which are notoriously noisy but provide the information of a velocity field rather than a single point.

In chapter 6, we studied important design parameters for a linear estimator of the problem at hand. Elements such as pressure sensor location and frequency response of the estimator need to be appropriate for the separated flow over a rib. We observed two types of fluctuations in the pressure and velocity fluctuations which we should include in the estimator

As a preliminary step to designing the estimator, we studied correlation between p and u at chosen locations to confirm the largest time-delay τ_{max} necessary to capture the

dynamics of the flow and peak correlation coefficient R_{max} to establish the quality of the estimation. The study of correlation between surface pressure and various velocity measurements above the rib indicates that a wide range of dynamics exist in the flow which the estimator needs to capture with a number of time delays of up to approximately $t^* = 5$ non dimensional time units. Instead of estimating velocity directly however, we approximate the velocity vector fields to a reconstruction based on a subset of POD modes. In this case, the LSE model will generate POD coefficients for each snapshot given pressure information. This reduces the computational cost of the model.

7.1 Methodology

7.1.1 Proper Orthogonal Decomposition (POD) algorithms

In order to draw a link between surface pressure and velocity, we model the flow. However, in order to reduce the complexity of the problem, we substitute velocity fields with a subset of POD modes.The flow is reconstructed by estimating POD mode coefficients from pressure measurements using a linear estimator. In principle, the POD (Sirovich, 1987) decomposes the stream-wise and vertical velocity components around the rib into a set of orthogonal mode shapes and energy values, or eigenvalues. The reconstruction of velocity fields based on POD modes consists in a weighted sum of POD mode shapes weighted by what is referred to as their energy coefficient. The weight of each shape varies with snapshot, or time. One obtains the value of this weight by projecting the mode shape on a snapshot. The norm of this projection is the energy coefficient of that mode shape for this snapshot.

$$u(x, y, t) = \sum_{i}^{N} a_i(t)\phi_i^u(x, y) \tag{7.1}$$

$$\hat{u}(x, y, t) = \sum_{i}^{n} a_i(t)\phi_i^u(x, y) \tag{7.2}$$

If we select a subset of n POD modes to produce our estimate of velocity, we must only model n variables based on pressure information. As an example, in the case of our high-speed experiment, we obtained $N = 7091$ snapshots for each run, each vector field contains 168×321 grid points, this is a lot more variables to estimate than $n \leq N$ per snapshot.

The decomposition of the flow is made in Python from an adapted version of the Matlab code published by Meyer (2008). It consists in concatenating stream-wise and vertical components of a single snapshot in a single column, then adding all successive snapshots next to each other. The “snapshot” method does not require the samples to be resolved

in time. It is a statistical tool that works even with non time-resolved PIV. The auto-correlation of the matrix containing all the velocities is then computed. The eigenvectors of the auto-correlation matrix are then projected on to the original velocity matrix to obtain mode shapes. These shapes are sorted by the magnitude of their eigenvalue which gives us the ranked POD modes. The modes are represented for $L/H = 4$ in section 7.3.

7.1.2 Correlation of variables

When modelling velocity from surface pressure measurements, it is essential to understand the link between the variables involved. We use POD-based reconstructions of the flow field to obtain velocity. This decomposition may introduce undesirable effects in comparison with a direct estimation of velocity at each grid point. To highlight the effects of using POD, we analyse a few of the governing equations re-written to takes this into account.

First and foremost, the correlation between pressure and velocity needs to be strong in order to establish a link between them.

$$R_{pu}(x, y, \tau) = \frac{\sum_t^N p(t).u(x, y, t + \tau)}{\sqrt{\sum_t^N p(t)^2}\sqrt{\sum_t^N u(x, y, t)^2}} \tag{7.3}$$

The definition of the linear correlation R_{pu} between pressure and velocity is given in equation 7.3. Its denominators can be reformulated as 7.4 and 7.5 with the appropriate normalization by the number of samples N. Results of this cross-correlation may be found in section 6.2. These are encouraging with clear correlation between the two variables. Consequently, we assess also the linear correlation between POD mode energy coefficients and surface pressure measurements.

$$\sigma_p : \sqrt{\overline{p^2}} = \sqrt{\sum_t^N p(t)^2/N} \tag{7.4}$$

$$\sigma_u : \sqrt{\overline{u(x, y)^2}} = \sqrt{\sum_t^N u(x, y, t)^2/N} \tag{7.5}$$

Equation 7.6 reports the computation of linear correlation between surface pressure measurements and POD coefficients. The results also described in section 6.2 show strong correlation between certain modes and certain transducers.

$$R_{pa_i}(i, \tau) = \frac{1}{N}\frac{\sum_t^N p(t)a_i(t + \tau)}{\sigma_p \sigma_{a_i}} \tag{7.6}$$

One may re-write equation 7.3 using the formulation for POD reconstructed velocity. Equation 7.7 describes the results if all modes are used to reconstruct velocity, as such, $u = u^N$.

$$\begin{aligned} R_{pu}(x,y,\tau) &= \frac{1}{N}\frac{\sum_t^N p(t)\sum_i^N a_i(t+\tau)\phi_i^u(x,y)}{\sigma_p\sigma_u(x,y)} \\ &= \frac{1}{N}\frac{\sum_t^N \sum_i^N p(t)a_i(t+\tau)\phi_i^u(x,y)}{\sigma_p\sigma_u(x,y)} \\ &= \frac{1}{N}\frac{\sum_i^N \sum_t^N p(t)a_i(t+\tau)\phi_i^u(x,y)}{\sigma_p\sigma_u(x,y)} \\ &= \frac{\sum_i^N \sigma_{a_i} R_{pa_i}(i,\tau)\phi_i^u(x,y)}{\sigma_u(x,y)} \end{aligned} \tag{7.7}$$

From equation 7.7 it is clear that the correlation between pressure and velocity or mode coefficient are directly related because they are multiplied by constants. Using a subset of n modes will affect the final correlation between reconstructed velocity and surface pressure.

7.1.3 Linear stochastic estimation using multiple sensors and multiple time delays

In order to obtain POD coefficients as a function of p, we create a mathematical link between surface pressure and POD mode coefficients through linear stochastic estimation. This procedure is described by Lasagna et al. (2013). The problem solved can be written as:

$$\hat{a}_i(t) = \sum_k \sum_{j=-n_p}^{n_f} w_j^k p_k(t - j\Delta t) \tag{7.8}$$

w_j^k represents a set of coefficients defined for each time delay j and each sensor k used in the model. These coefficients are obtained by solving a least-squares problem $AX = B$ by minimizing the remainder r such that $r = min(||AX - B||)$. In this definition of the problem, we use time delays from the past and the future to determine the coefficient of the current time step. In other words, $-j\Delta T$ is positive or negative. This is because we are not interested in creating a flow control device for instance where only the past is known, but interested in the relationship between pressure and velocity with the least amount of error possible. Similarly we use as many pressure transducers as available to create the estimator even though this might be sub-optimal in the sense that redundant information is brought by additional sensors. This is related to the correlation between pressure transducers. Indeed, the correlated parts of two pressure signal would be redundant. Only the decorrelated part of the signal from an additional sensor would help create an estimator which is capable of resolving more minute differences.

The direct solution to the least-squares minimization problem can be written with matrix operation as:

$$(A^T A)^{-1} A^T A X = (A^T A)^{-1} A^T B \tag{7.9}$$

$$X = (A^T A)^{-1} A^T B \tag{7.10}$$

On the condition that $(A^T A)^{-1}$ exists.

There are several algorithms available for solving least-squares problems in Python, these save memory and run faster in some instances than explicitly solving the written equation, consequently they will be used (`np.linalg.lstsq`). These provide the solution to X as well as other quantities of interest for our problem such as the remainder of the minimization problem.

Equation 7.10 may be re-written with the notation of the quantities used in the model:

$$W = (P^T P)^{-1} P^T A_i \tag{7.11}$$

where W contains the coefficients by which pressure information is multiplied to obtain estimated coefficients. Pressure information is contained in P, this matrix is formed of a combination of time-delays and sensors. A_i contains the original POD mode coefficients.

The construction of matrix P requires some attention. This dictates the part of the POD coefficient signal that can be estimated and the frequency response or transfer function of the linear estimator. The frequency response of the model is studied in the results section.

P is constructed as vertical columns of pressure measurements from one pressure transducer beginning at a given time step $t = 0 - n_p$ the number of past time steps used. The adjacent column contains the same information but shifted in time by one time step. This procedure introduces the multiple time delays included in the model and is repeated until the desired number of time delays is reached ($n_p + 1 + n_f$, the number of past, current, and future time instants). After the last column of time delays for one sensor, one may append information from a different sensor. The number of time delays included for this sensor may be different to the previous sensor. The model becomes a multi-sensor multi-time delay model. In practical terms, the matrix P can become very large if constructed explicitly, thus it is possible to use tricks to write only the auto-correlation matrix $P^T P$, that is what is used in solving the least-squares problem. The auto-correlation matrix is much smaller if the number of time delays is much smaller than the number of samples. A description of the implications of the auto-correlation matrix in the LSE model is given by Lasagna et al. (2013).

Example of the construction of matrix P:

$$\begin{vmatrix} p_k(0) & p_k(1) & \dots & p_k(n_p+n_f+1) & p_{k+1}(0) \\ p_k(1) & p_k(2) & \dots & p_k(n_p+n_f+2) & \dots \\ \dots & \dots & \dots & \dots & \dots \\ & \dots & \dots & \dots & \\ p_k(N-n_p-n_f-1) & p_k(N-n_p-n_f) & \dots & p_k(N) & p_{k+1}(N-n_p-n_f-1) \end{vmatrix}$$

With a configuration as given in the example above, the corresponding estimated A_i matrix will begin a time step n_p and end at time step $N-n_f$, thus the matrix is reduced by n_p+n_f number of samples and only snapshots n_p to $N-n_f$ can be reconstructed using this method.

One may compute the error between estimated and actual POD coefficients by computing the norm of their subtraction. This quantity (ϵ) will be studied in the results as we build the model as it is dependant on the number of time delays and sensors.

$$\epsilon = ||A_i - P \cdot W|| \tag{7.12}$$

7.1.4 Transfer function/frequency response of the estimator

We will be estimating the mode coefficients $\hat{a_i}$ from surface pressure measurements as per equation 7.8. Our estimator is only able to capture specific frequencies thus it is important to analyse its frequency response. If we take the z transform of 7.8, we obtain:

$$\hat{A}_i(z) = \sum_{k=1}^{T} H_k(z) P_k(z) \tag{7.13}$$

Where H_k is effectively a transfer function associated with transducer k at each $z = e^{-i\omega}$ We are interested in representing how each pressure signal is treated by the estimator in order to produce an estimate of a mode coefficient. In order to do so, we may look at the magnitude of equation 7.13 and obtain the gain of the transfer function between each pressure transducer and $\hat{A}_i$.

$$|\hat{A}_i(z)|^2 = |\sum_{k=1}^{T} H_k(z) P_k(z)|^2 \tag{7.14}$$

The z-transform being complex, we may apply identities for complex numbers to rewrite our equation:
$|\hat{A}_i(z)|^2 = \hat{A}_i \hat{A}_i^*$
Where * denotes the complex conjugate. Applying the same identity to the right-hand

side, and expanding it becomes:

$$|\hat{A}_i(z)|^2 = \sum_{k=1}^{T} |H_k|^2 |P_k|^2 + \sum_{k=1}^{T-1} \sum_{j=k+1}^{T} 2Re\{H_k H_j^* P_k P_j^*\} \tag{7.15}$$

This rather long expression is inconvenient because we cannot separate the P terms from the H in order to look at H and obtain an idea of the gains applied by the estimator to each transducer. So we can re-write the second half involving the real part $Re\{...\}$ of the complex products. Because $(P_k P_j / P_k)^* = P_k^*$, we obtain:

$$|\hat{A}_i(z)|^2 = \sum_{k=1}^{T} |H_k|^2 |P_k|^2 + \sum_{k=1}^{T-1} \sum_{j=k+1}^{T} 2Re\{H_k H_j^* P_k P_k^* (P_j^* / P_k^*)\} \tag{7.16}$$

$$|\hat{A}_i(z)|^2 = \sum_{k=1}^{T} |H_k|^2 |P_k|^2 + \sum_{k=1}^{T-1} \sum_{j=k+1}^{T} 2Re\{H_k H_j^* |P_k|^2 (P_j^* / P_k^*)\} \tag{7.17}$$

$$|\hat{A}_i(z)|^2 = \sum_{k=1}^{T} |H_k|^2 |P_k|^2 + \sum_{k=1}^{T-1} \sum_{j=k+1}^{T} 2|P_k|^2 Re\{H_k H_j^* (P_j^* / P_k^*)\} \tag{7.18}$$

Due to the interchangeability $|P_k P_j^*|^2 = |P_k^* P_j|^2$, we wrote $2Re...$ from the expansion, but the terms independently can be re-written to factor P_k and keep only the ratio P_j / P_k

$$|\hat{A}_i(z)|^2 = \sum_{k=1}^{T} |P_k|^2 \left[|H_k|^2 + \sum_{j=1}^{T} (1 - \delta_{jk}) Re\{H_k H_j^* (P_j^* / P_k^*)\} \right] \tag{7.19}$$

Where δ_{jk} is the Kronecker delta used so we do not include twice $H_k H_k^*$.
This results is of the form:

$$|\hat{A}_i(z)|^2 = \sum_{k=1}^{T} |P_k|^2 |\tilde{H}_k|^2 \tag{7.20}$$

With equation 7.20, we obtain a sum of inputs multiplied by transfer functions which can be looked at conveniently. The transfer function for each pressure transducer includes a term related to the ratio (P_j^* / P_k^*), which is dictated by parameters such as the location of one transducer related to another, as well as the type of flow or the convection from one transducer to the other.

The z-transform H can be computed directly in the form

$$H(z) = w_0^k z^{n_f} + \cdots + w_{n_f+1}^k + \cdots + w_{n_f+1+n_p}^k z^{-n_p} \tag{7.21}$$

Using the coefficients denoted w from the W matrix described in equation 7.8.
For z of magnitude 1, where we evaluate the transfer function, we can apply the identity

between z-transform and Fourier transform and determine:

$$P_k = \sum_{n_p}^{N-n_f} p_k(n) z^{-n} = \sum_{n_p}^{N-n_f} p_k(n) e^{-2\pi n/(N-n_p-n_f-1)} \tag{7.22}$$

Using this definition, we obtain a Fourier transform with $N - n_p - n_f - 1$ points with the Nyquist frequency being 800Hz at our acquisition rate and the minimum being $\frac{1}{N-n_p-n_f-1}$. If we compute the $H(z)$ for the same set of frequencies as P_k, we may multiply all the complex terms for each z and obtain the value of H_k at z. The transfer functions are analysed in the results section after the estimator is made.

7.2 Parameters of the estimator

7.3 POD modes of $L/H = 4$

In this section, we describe the shape of the POD modes and the associated energy distribution. Finally the correlation between POD modes and surface pressure measurements is studied.

We produced snapshot POD modes of streamwise and vertical velocity components as described by Sirovich (1987). The data-set consists in stream-wise and vertical velocity components of 2000 snapshots from the high-speed PIV measurements. The methodology used to decompose the flow is described in more details in section 7.1.1. The result is a set of POD mode shapes Φ_u or Φ_v representing stream-wise and vertical velocity components respectively associated with an average energy proportion. Mode shapes Φ_v are depicted in figure 7.1a with the associated average energy fraction that contributes to the overall fluctuations in the flow. It appears that the most energetic modes are first large trains of ellipsoids in the wake region which reduce in size and appear further upstream as mode number is increased. Higher modes are complex and difficult to associate with any clear type of flow structure. However, the first ones resembles growing and shrinking recirculation regions while mode 5 and above seems to reproduce periodical fluctuations which could be associated with vortex shedding from the leading edge and travelling downstream while growing in size. The projection of each of those modes on a single snapshot produces a set of coefficients a_i which weigh each mode.

POD modes of $L/H = 4$ seem to show a continuous decay of energy with little information standing out. As a result it is believed there are no groups of POD modes which might be connected as is presented in research such as Clark et al. (2014) where a blunt trailing edge produces a vortex street which is dominated by two opposed POD modes. However, POD modes contain important information in the frequency spectrum of their coefficients. Similarly to the velocity spectra, because the POD weights a_i vary in time,

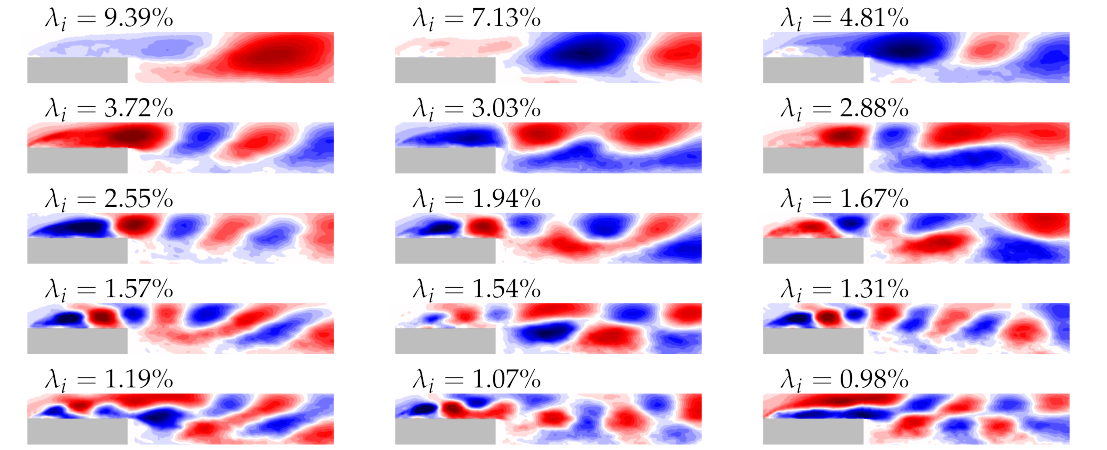

(a)

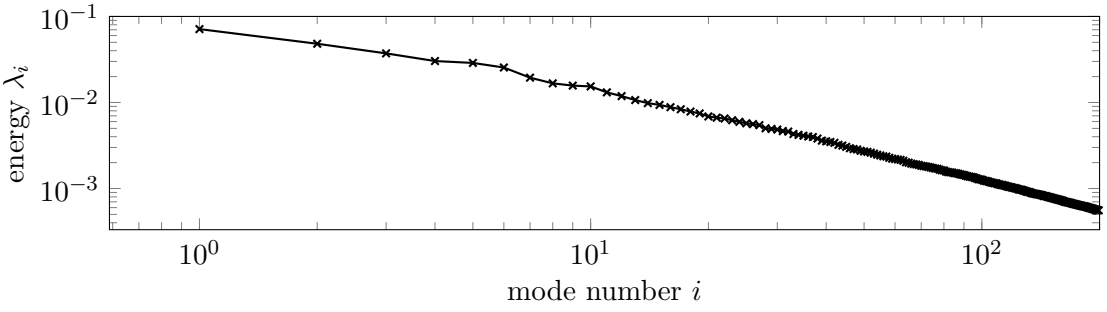

(b)

Figure 7.1: (a) First 15 POD mode shapes of streamwise velocity component u for rib $L/H = 4$. The inset text represents the percentage energy associated with the mode. (b) Average energy distribution associated with each POD mode of the $L/H = 4$ obstacle.

we may compute frequency spectra to identify frequencies of interest in POD coefficients. As an example, figure 7.2 depicts the energy spectra of the coefficients of modes 0, 1, 2 and 3 as illustrated in figure 7.1a compared with surface pressure fluctuations near the leading $x/H = 0.5$. Note that the spectra have been multiplied and offset to produce a clearer illustration of the frequencies of interest. As mode number increases, the magnitude of the energy contained in the spectrum decreases. It appears that the first two modes oscillate at similar frequencies which are centred on the frequency associated with shear layer flapping. Mode 2 exhibits a bi-modal oscillation. The spectrum of its coefficient is dominated by two peaks straddling the lowest peak in the surface pressure spectrum. Higher modes (6, 10, 13, 16) present progressively higher dominating frequencies as well as lower magnitude. The magnitude is not represented accurately in figure 7.2 for illustrative purposes. At mode 16 and above, the dominating frequency of the spectrum is larger than the dominating frequency in the surface pressure. This means the scales of the fluctuations represented by mode 16 and higher are smaller and may have little representation in surface pressure. However, these are smaller scale

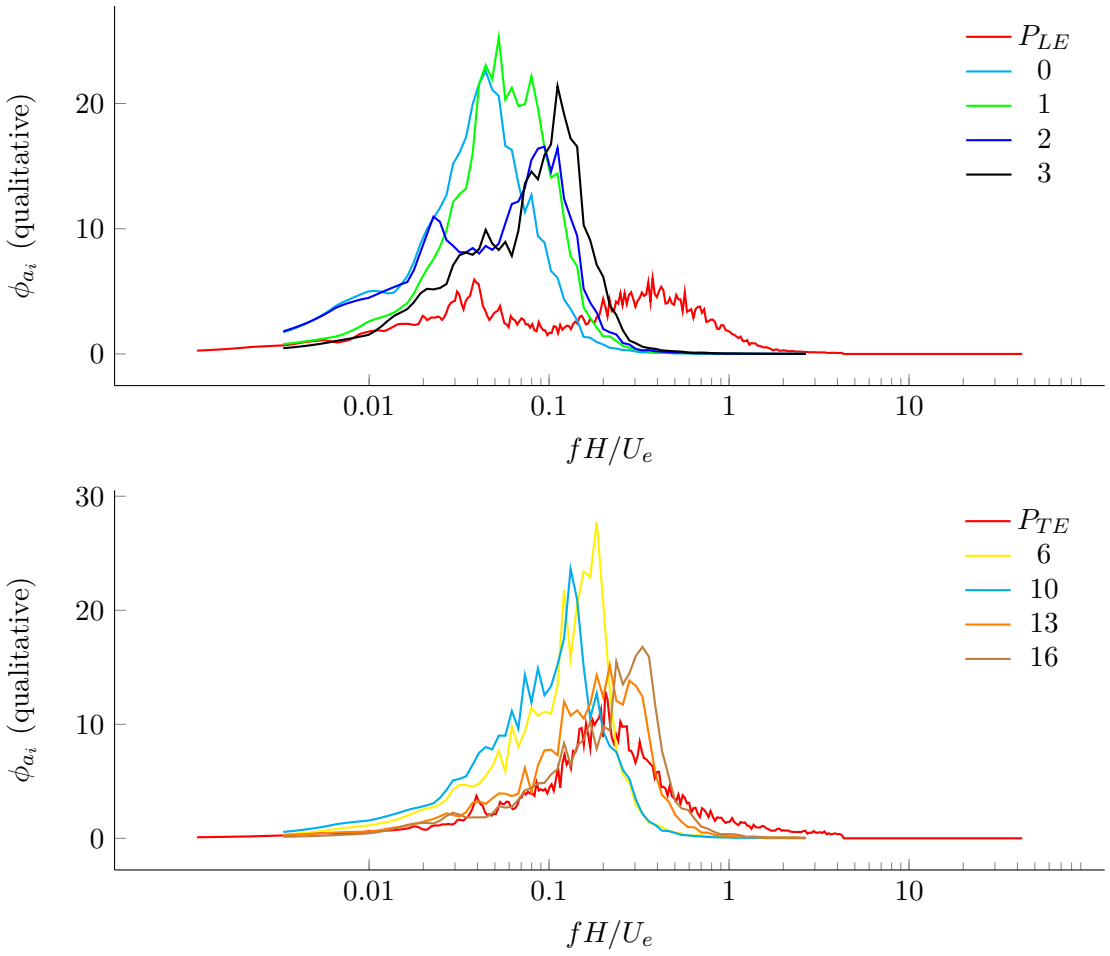

Figure 7.2: Temporal pre-multiplied spectra of POD mode coefficients.The POD spectra are re-scaled for visual purposes and compared to surface pressure measurements.

fluctuations which still contribute a significant amount to velocity fluctuations.

7.3.1 Correlation between POD modes and surface pressure measurements

We may compute the cross-correlation between surface pressure and POD mode coefficients. This is required to understand which mode can be estimated from pressure information. Figure 7.3a depicts the value of maximum cross-correlation coefficient between surface pressure transducer indicated by the colour, and the mode number i. For each mode, the correlation with different transducers varies. This is because the POD modes may represent fluctuations which are localized thus only affecting nearby transducers. Nevertheless, maximum coefficients of up to 0.35 are achieved for mode 6 for instance with surface pressure measurements at location $x/H = 2.5$ which is immediately upstream of the reattachment point. The fluctuations in coefficient of mode 6 are

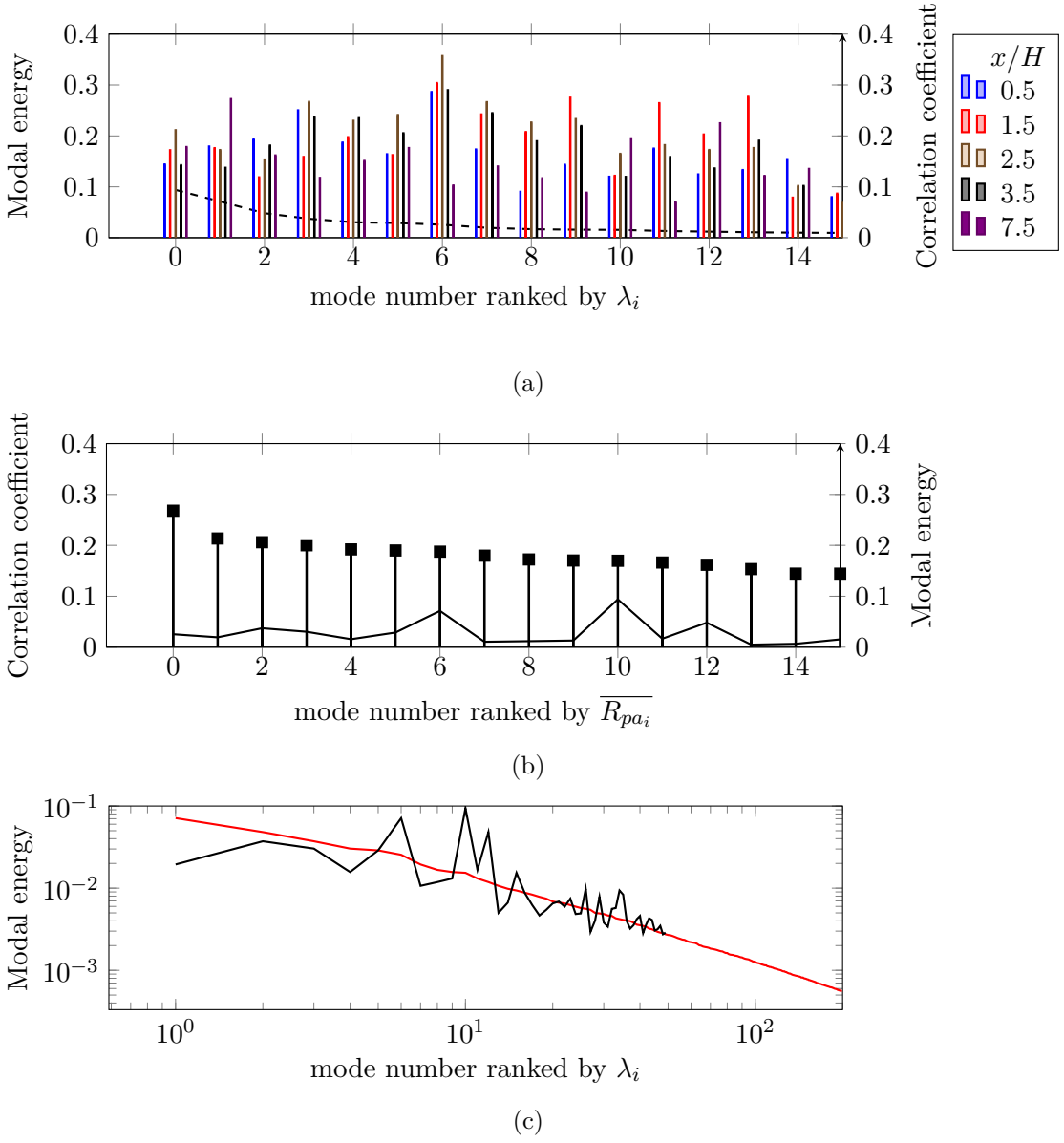

Figure 7.3: (a) Energy of each POD mode as well as correlation value between each mode coefficient and a pressure transducer (histograms). (b) Re-arranged modal energy (black line) ranked by average maximum correlation coefficients (histograms). (c) Model energy ranked by energy (red) and ranked by correlation coefficient (black).

also weakly correlated to the pressure fluctuations at location $x/H = 7.5$. Due to the variability of the correlation, we can already establish that multiple pressure transducers will benefit the overall accuracy of estimation throughout the entire domain. In order to capture a more general sense of the relationship between pressure and mode coefficients, figure 7.3b indicates the maximum correlation coefficient averaged over all the pressure measurements for each POD mode. The modes are re-arranged in decreasing order of average correlation coefficient. In order to relate the correlation-ranked vs the energy-ranked the original energy content of each mode is also plotted in black. In this way, mode 6 becomes the most correlated mode, and the most energetic (mode 0) takes the 11th place in order of correlation coefficient.

In order to reconstruct the flow, one may argue that the most correlated modes should be favoured rather than the most energetic modes. Re-arranging the POD modes by correlation coefficient is only made to indicate which modes will be best correlated statistically speaking. However these may only produce very small contributions in terms of fluctuations if their energy fraction is very small. Consequently, we plot in figure 7.3c both the original energy distribution and the R_{pa_i}-sorted energies and it is visible that at mode 50, the difference in energy between the two ranking methods becomes very small. In other words as the energy per mode decreases the correlation coefficients also appears to decrease which leads to small variations in energy contributions as the ranks are swapped. If one were to use more than 50 modes to reconstruct the flow it is arguable that either ranking methods will result in the same overall result. Later in this study, we will analyse up to 100 modes in the reconstruction, so we maintain mode numbering per decreasing energy, not per maximum correlation coefficient.

7.3.2 Mode estimation based on pressure

In the previous sections, we have established that there is a relationship between the fluctuations in POD mode coefficients with the fluctuations in surface pressure measurements. Therefore, we estimate the POD mode coefficients from pressure information. Section 7.1.3 describes how we build the estimator. It describes that we may use multiple sensors and multiple time-delays per sensor to estimate the coefficient of one single mode. Using more than one time-step and one transducer allows for a reconstruction which will favour some frequencies in the spectrum of reconstructed mode coefficients rather than a single gain of all types of fluctuations (see Lasagna et al. (2013) for a detailed analysis of the spectral response of one vs multiple time-delays per sensor). Adding an extra sensor will also add a condition on which the reconstruction can be based, an extra degree of freedom that should lead to a more detailed reconstruction.

We are faced with the problem of determining the combination time delays that will produce the most accurate representation of the velocity fluctuations correlated with surface pressure. In order to do so, we tested the linear estimation of POD mode

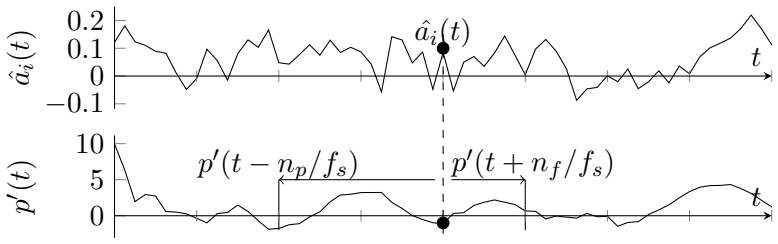

Figure 7.4: Diagram of the timing between estimated POD coefficient and pressure data used in the estimator.

coefficients with all five transducers and varying number of time-delays in the pressure data before and after the time-instant which needs to be estimated. Figure 7.4 contains a schematic of the pressure data selected to reconstruct a_i at time t. n_p represents the number of samples prior to t included from the pressure time-series. n_f represents the number of samples after time t. f_s is the sampling frequency, in our case 1600Hz. $\hat{a}_i$ denotes the estimated mode coefficient where a_i is the original value of the projection of mode i on a velocity snapshot at time t.

In figure 7.5 two examples of the error between estimated and original a_i are represented (mode 0 and 6, left and right respectively). The W matrix is constructed with a "training" dataset and applied on a "validation" dataset which is another batch of snapshots acquired in a different run of the experiment. The top figure illustrates how the error evolves with n_p and n_f between the training dataset and the estimated coefficients of the training dataset $\frac{\overline{(a_i - \hat{a}_i)^2}}{\overline{a_i^2}}$. We apply the same estimator W to a validation dataset and compute its error in the middle figure. Finally, the difference between the validation and estimation errors is represented in the lower figure. The shape of each of those plots is unique for each POD mode, and unique to the combination of sensors used. The location of the minimum error in the validation dataset is the optimal number of samples to use for robust reconstruction without "over-fitting" which leads to error in the validation dataset. The training dataset does not exhibit increased error with additional n_p and n_f because this introduces information in the W matrix such that the least-squares fitting is closer to the original data.

From testing all modes with varying numbers of n_p and n_f, in steps of 1, we may extract the combination which results in the smallest validation error. This test was repeated for an estimator using all five transducers and for estimators using one single pressure transducer to illustrate the improvement in using five transducers instead of one. Figure 7.6 recapitulates these combinations in the form of a window size $(n_p + n_f)$ and window centre $(-n_p + n_f)/2)$ for one sensor located at $x/H = 0.5$ and all sensors. This formulation indicates conveniently whether most of the information in p useful for $\hat{a}_i$ is contained in the past or in the future, and whether many or few p time-delays are needed. From the data collected in figure 7.6, it seems the optimal combination for transducer at $x/H = 0.5$ does not contain much future time delay to improve accuracy

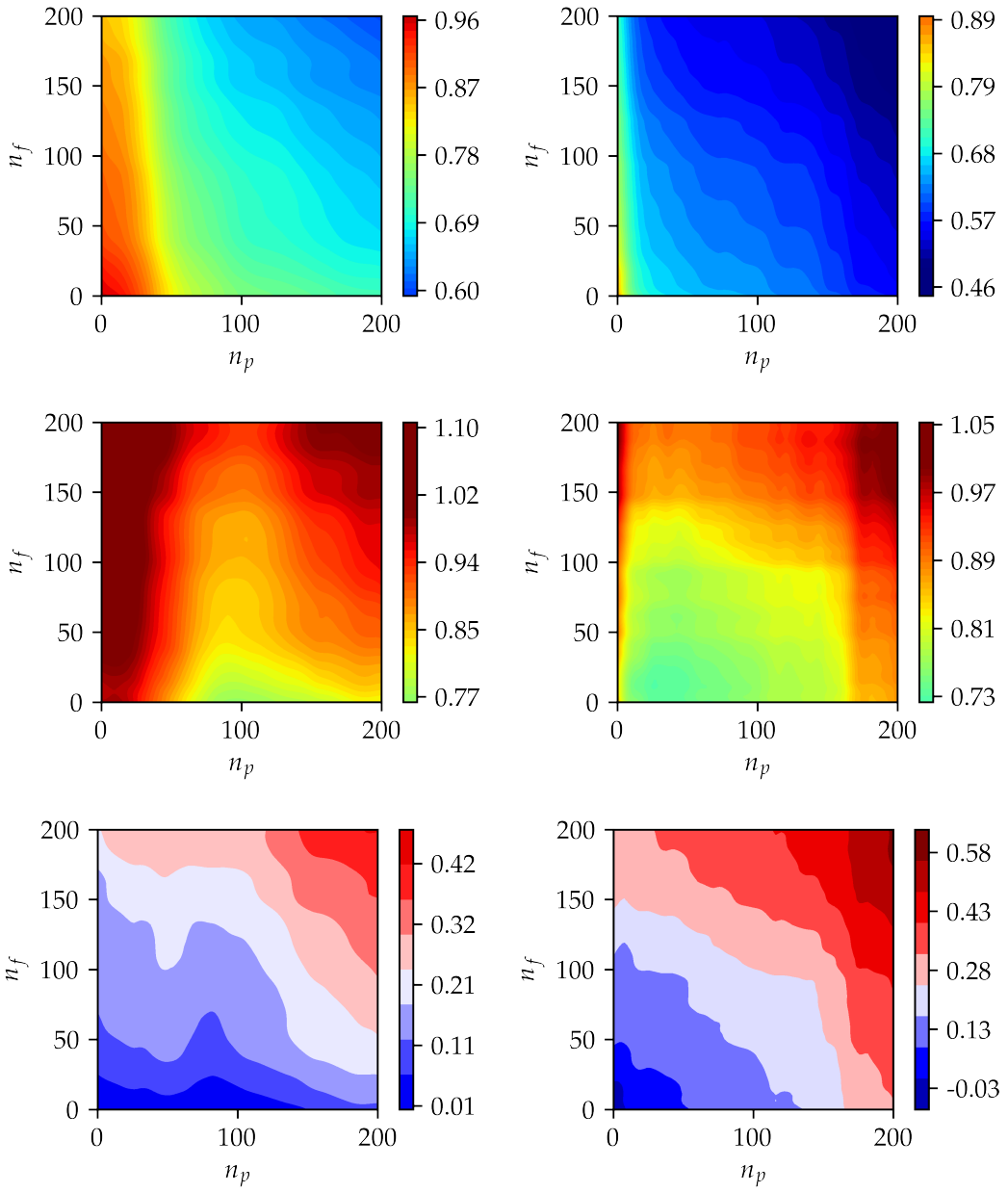

Figure 7.5: Remainder in estimation relative to original POD coefficients as a function of past and future time delays. normalized by original pod coefficients. From top to bottom: estimation dataset then validation dataset, then difference normalized. for mode 0 left, and 6 right.

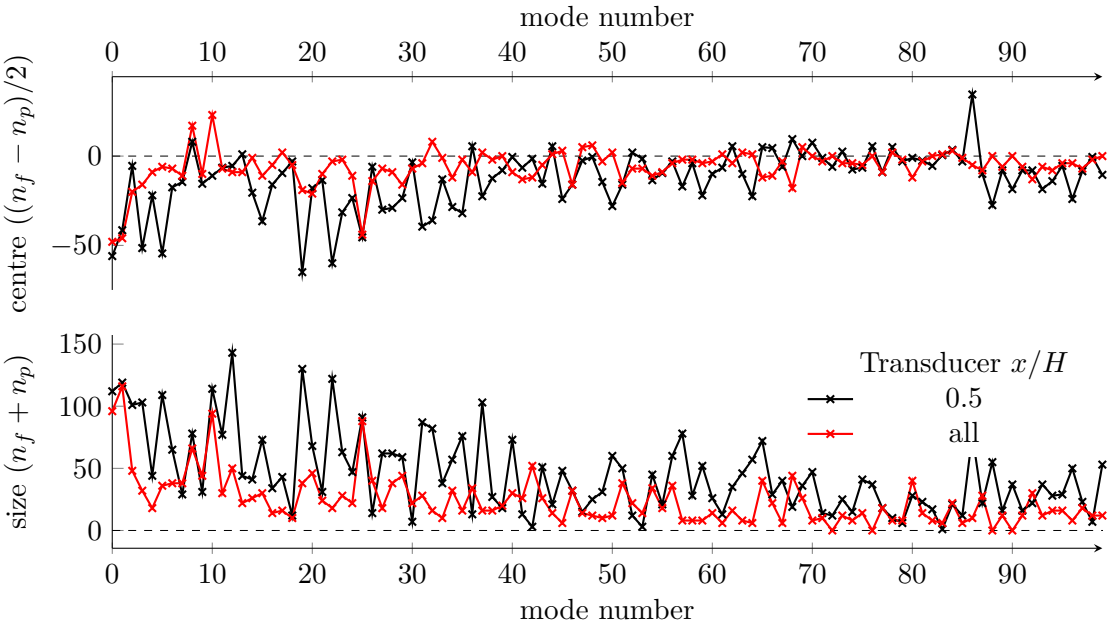

Figure 7.6: Optimal number of time delays for POD modes number used in the linear estimator.

in estimating $\hat{a}_i$ from pressure measurements. In contrast, the combination of all five sensors produces the least error with negative time delays as well as positive time delays.

Using the optimal window of pressure data from five transducers to reconstruct one single mode coefficient, we may compute the resulting error between the original and estimated values. The error is depicted in figure 7.7. The error increases with mode number and it starts very high even for the most correlated modes. No less than 67% error can be achieved for mode 6. Nevertheless, we will analyse further on why this error is so large and how it affects the estimated modes and velocity fields, but it must be reminded that the correlation is low between modes and surface pressure. Therefore, much of the error could be due to the decorrelated parts of the signals, as well as noise. The difference between error on the training and validation datasets is small, it is the area between the black and the red curves.

7.3.2.1 Dependence of estimated $\hat{u}^N$ on number N of POD modes included

With the optimal time-delays found for each mode, one may now estimate the $\hat{a}_i$ coefficients and subsequently reconstruct velocity flow fields with varying number of modes. In this section, we study the effect of the number of POD modes estimated in the resulting reconstructed velocity $\hat{u}^N(x, y, t) = \sum_i^N \hat{a}_i(t)\phi_u(x, y)$.

The correct way to evaluate the error in this case is to compare the error made on a validation data-set, a different data-set to the one used to create the W matrix. Using all

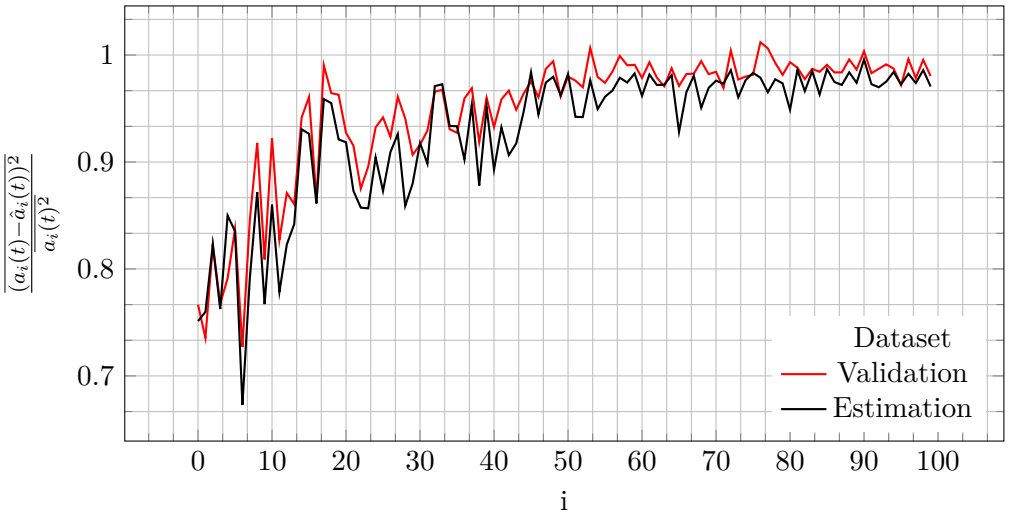

Figure 7.7: Error between original and estimated mode coefficients at the optimal time delays reported in figure 7.6 using all five tranducers to estimate the coefficients.

5 transducers, we reconstructed $\hat{u}^N$ using varying numbers of POD modes N and plotted the average error $\overline{(u(x,y,t)-\hat{u}^N(x,y,t))^2}/\overline{u(x,y,t)^2}$, snapshot by snapshot in figure 7.8 and against the reduced-order version of u $\overline{(u^N(x,y,t)-\hat{u}^N(x,y,t))^2}/\overline{u^N(x,y,t)^2}$ where u^N is a reconstruction of u using N modes with original coefficients rather than the estimated coefficients in figure 7.9.

In figure 7.8 it is visible that adding 1,20 or 100 modes creates a different local error in $\hat{u}^N$ against u. Using only one mode (0) that fluctuates in the wake region results in 85% error in the far wake and over 95% everywhere else. This means the first mode is correlated to surface pressure despite the physical separation between sensors and the estimated region. This illustrates the large number of past time-delays required from pressure to estimate velocity as described in figure 7.6. With 10 modes, the error is reduced near the top surface of the obstacle. This is because higher modes contain smaller fluctuations which are located on top of the rib and which may extend in the wake region. The physical and temporal separation between pressure and velocity is reduced at higher mode numbers. The lowest error is achieved with the largest number of POD modes, at $N = 100$, this is approximately 70% near the pressure measurement locations of $x/H = 2.5$ and 3.5. We observed that the error does not change significantly between $N = 60$ and $N = 100$ so we omitted plots of these values of N for clarity. Because the error varies little at this high number N, we can establish that the flow is reconstructed with the highest detail possible. Any further modes added will contribute little energy and will be only weakly correlated to surface pressure, thus not apparent in $\hat{u}^N$.

In figure 7.9 we compare the estimated data against the reduced-order version of the data-set with the same number of modes N. This allows us to confirm the error on $\hat{a}_i$. Furthermore as N approaches 2000, the maximum number of POD modes, $u^N \approx u$. At

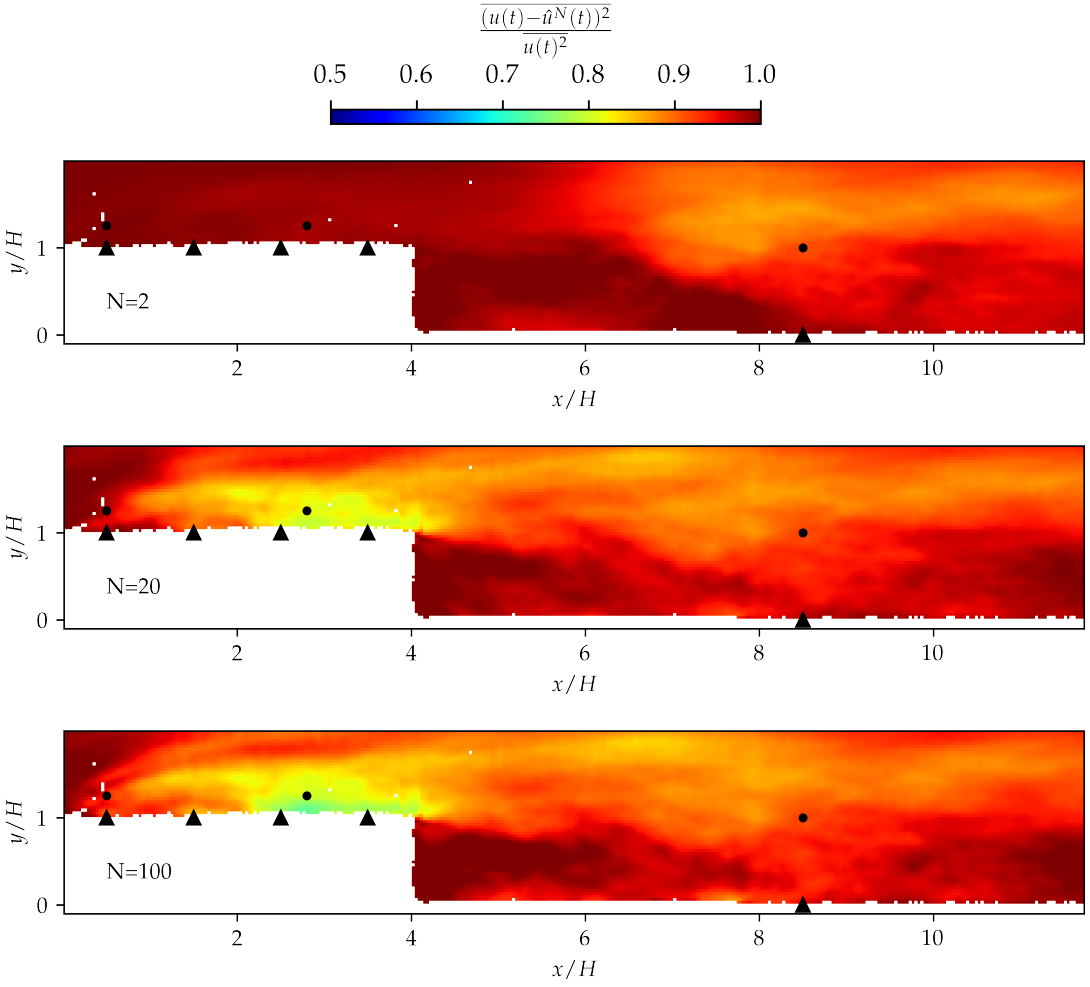

Figure 7.8: Map of difference between estimated and original dataset on validation dataset $\frac{\overline{(u(t)-\hat{u}^N(t))^2}}{\overline{u(t)^2}}$ as a function of number of POD modes used in reconstruction. Top: 2 modes, middle: 10 modes, bottom: 100 modes. Velocity is reconstructed using five pressure sensors indicated by the black triangles. The black dots correspond to the locations from which we extract velocity spectra presented in figure 7.13.

$N = 100$, the lowest error is achieved in the shear layer above $x/H = 0.5$, and around the mean reattachment point on the top surface. This indicates these regions have the strongest effect or correlation with surface pressure. The error increases sharply past the trailing edge, thus the wake region appears independent of the top region in this representation. Only the upper wake region seems to be estimated to some extent. Thus, higher modes describing the wake regions are decorrelated from the transducers on the top surface and the transducer in the wake region.

We repeated the operations with one transducer at a time to show the effect of sensor location and number. Figure 7.10 illustrates the error between u^N and $\hat{u}^N$ or u using the transducer highlighted by the black triangle beneath the surface. With 100 modes, the error is reduced locally near the transducers but using all transducers appears to produce

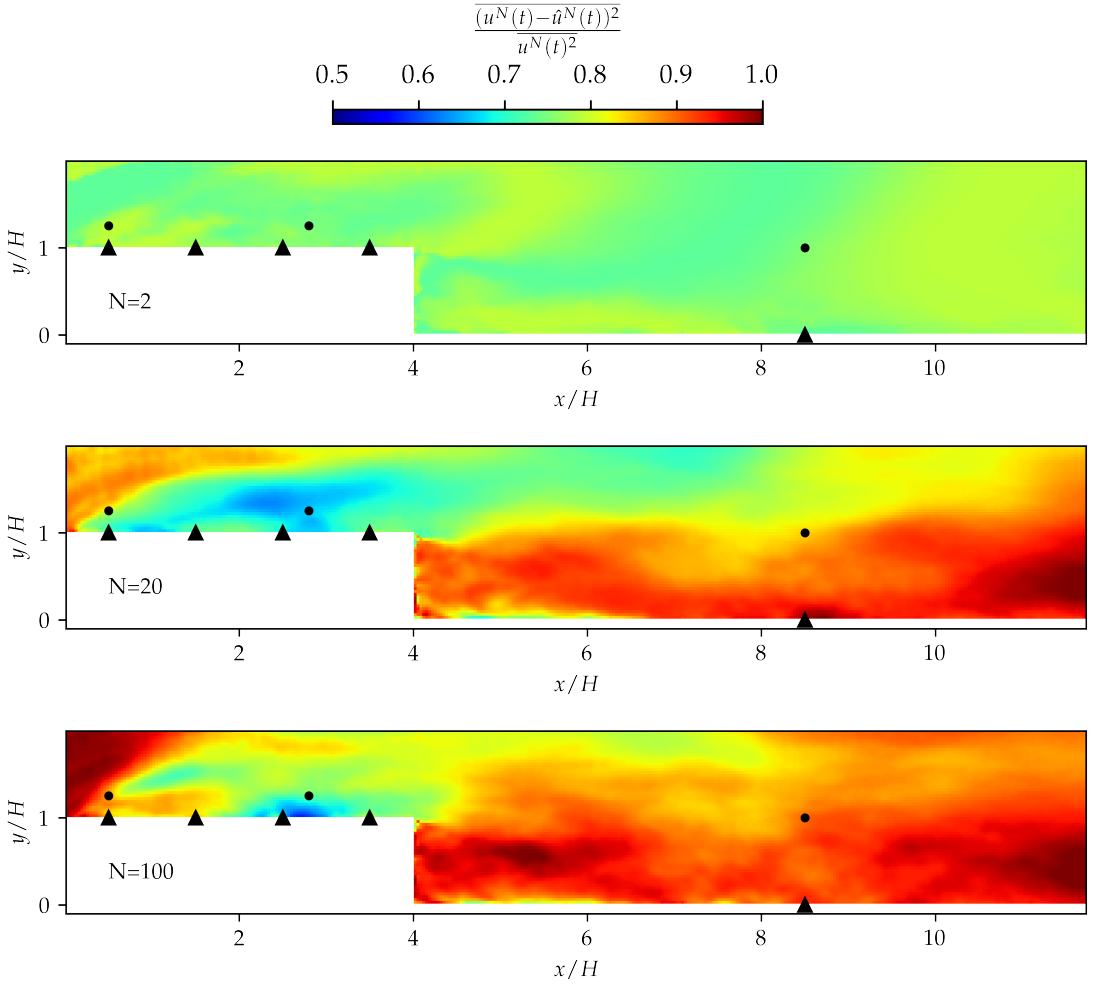

Figure 7.9: Map of difference between estimated and original reduced-order dataset on validation dataset $\frac{\overline{(u^N(t)-\hat{u}^N(t))^2}}{\overline{u^N(t)^2}}$ as a function of number of POD modes used in reconstruction. Top: 2 modes, middle: 10 modes, bottom: 100 modes. Velocity is reconstructed using five pressure sensors indicated by the black triangles. The black dots correspond to the locations from which we extract velocity spectra presented in figure 7.13.

a better result than the addition of five individual transducers. The most upstream transducer produces estimates in the shear layer immediately above, and some degree of estimation at the mean reattachment point of the top surface. This indicates velocity fluctuations near the leading are correlated with the leading edge surface pressure and could be convected downstream to the mean reattachment point. Using the transducer at $x/H = 1.5$ leads to poor overall estimation of $\hat{u}$, the error is smallest above the shear layer but at least 85%. The third sensor from the leading edge ($x/H = 2.5$) produces the least localized error on its own, down to 70% and the estimated region spans from $x/H = 1$ to 8. The fourth tends to produce less error in its vicinity, but high error everywhere else. Finally, the sensor in the wake region leads to very little estimation thus high error on its own.

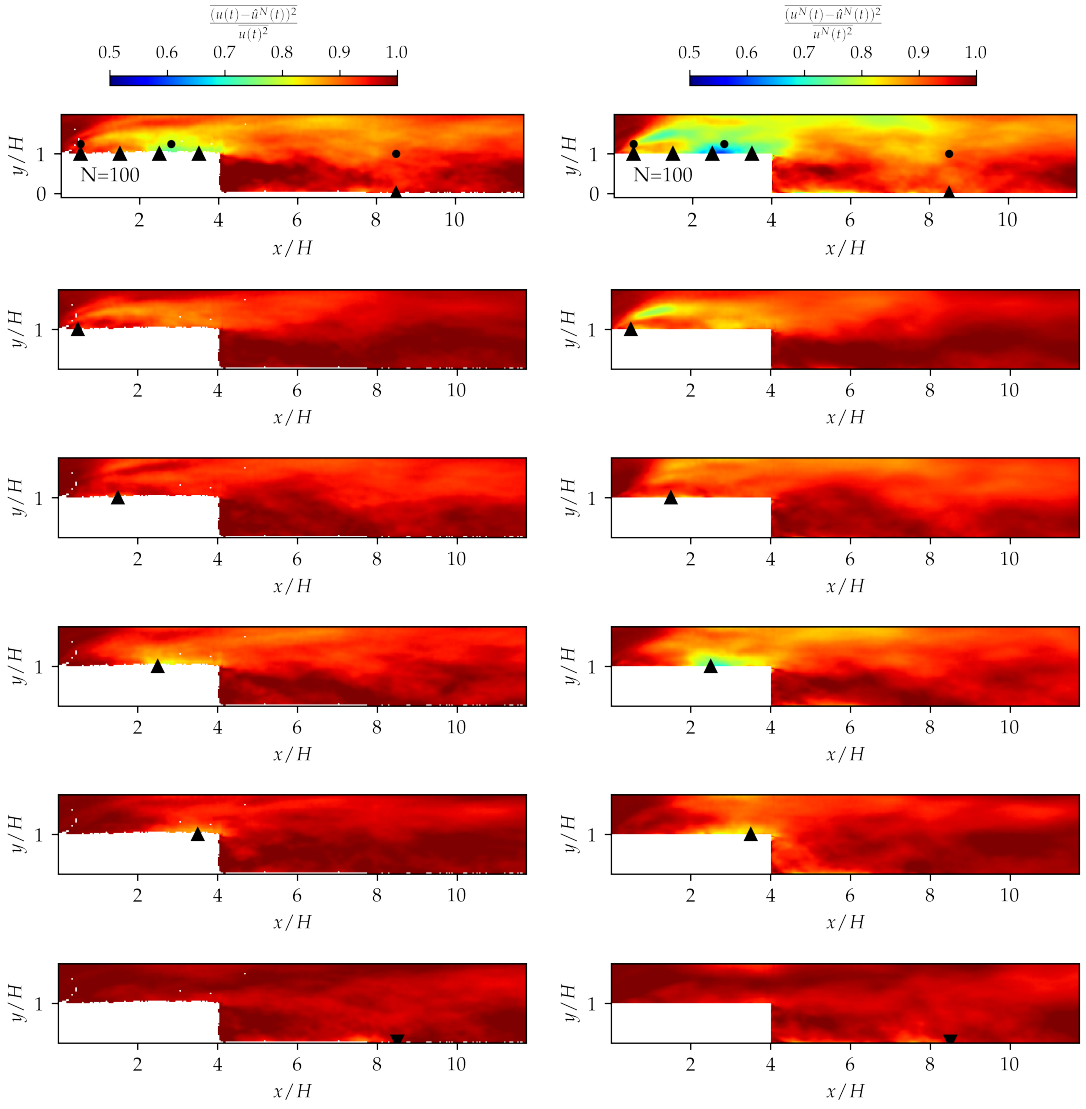

Figure 7.10: Comparison between using all transducers, and one transducer at different location to reconstruct u with 100 modes.

Each black dot in 7.10 represents a location from which we can extract the error as a function of N. This indicates the number of modes necessary to reach the minimum local error. Figure 7.11 contains the errors at these points as a function of mode number using one transducer or all transducers on the validation and estimation data sets compared with u or u^N. These graphs indicate that the error evolves differently at different spatial locations. For instance, near the leading edge, the error compared with u decreases gradually and plateaus at 0.95, whereas compared to u^N the error begins very low and increases gradually before plateauing at 0.9. The same behaviour is observed for multiple spatial locations but the error rises at different rates and due to different modes for each location. It is interesting to notice that adding more modes increases the error compared with u^N because the correlation with higher mode numbers is diminished on average, thus little information is added. In addition, the denominator of the error metric also

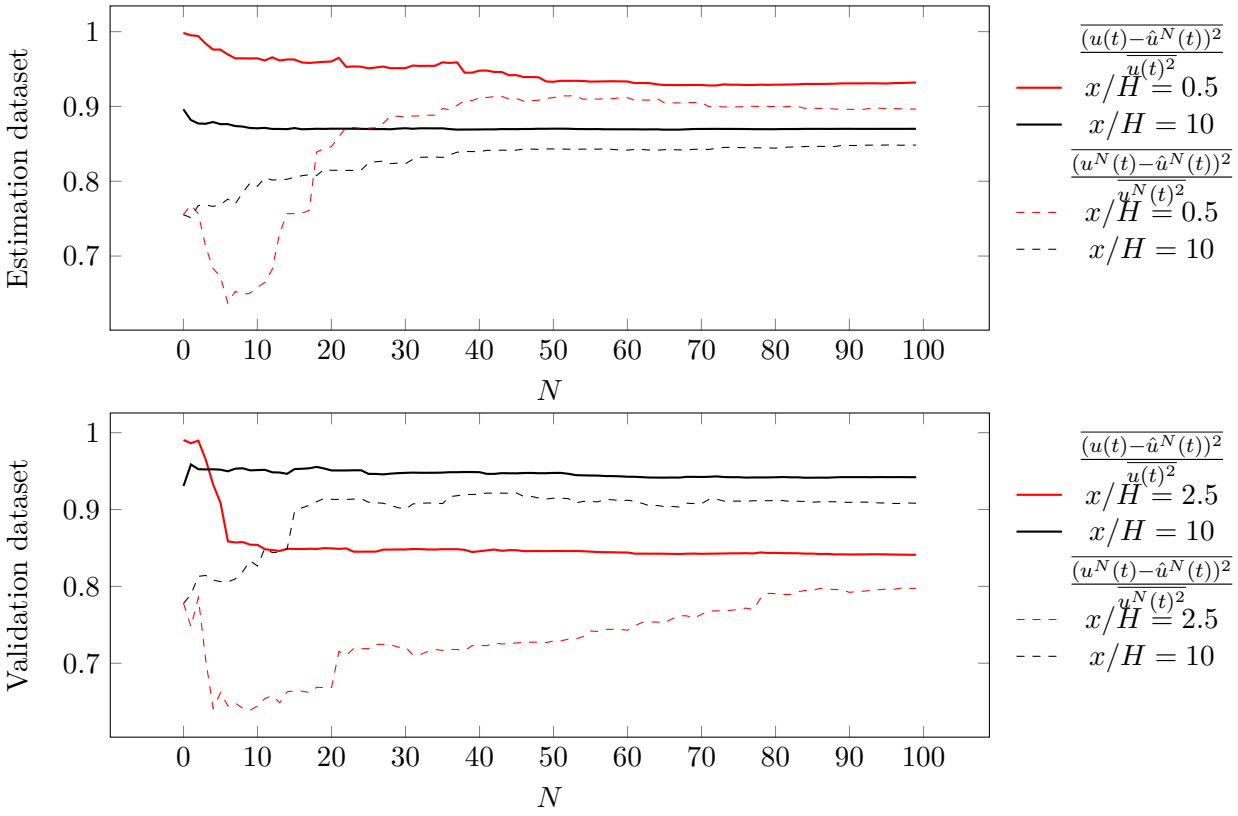

Figure 7.11: Error between estimated $\hat{u}$ and original u or reduced-order u^N as function of number of modes N used in reconstruction. Estimation dataset on top and validation at the Bottom.

varies with N. At $N = 2000$, the errors should converge to a single value which is $\overline{(u - \hat{u}^{2000})^2}/\overline{u^2}$.

Due to the localized nature of the error, we also considered a time and spatially averaged error. It is obtained by spatially averaging the error described with figure 7.8 and 7.9. The result is depicted in figure 7.12. This indicates that the overall error plateaus at mode 32 (grey dashed lines) at a value of 0.92. Thus we could argue that a reconstruction with 32 modes should be sufficient to capture the majority of flow features responsible for dominant pressure fluctuations in our flow of interest. However, analysing the local error in figure 7.10 proves that there is a benefit in using more modes for local phenomena.

In fact, the frequency content of the reconstructed flow shows that there are variations in spectra with higher mode numbers. Figure 7.13 contains a selection of stream-wise velocity spectra from original velocity, reconstructed with fewer modes and estimated then reconstructed with the same number of modes. Three regions are studied, the leading edge, the mean reattachment point on the top surface, and the mean reattachment point in the wake region. Overall, when adding more modes in the reconstruction of u, the stream-wise velocity spectra approach the original spectra. This happens first with medium and low frequencies, finally the high frequencies (small length scales) are still

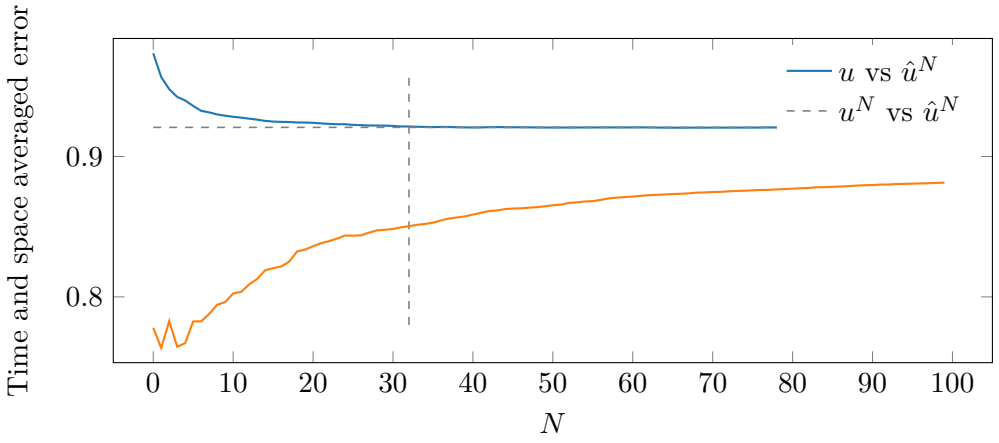

Figure 7.12: Space and time average of the error between $\hat{u}^N$ and u^N or u as function of POD mode number N used in the reconstruction.

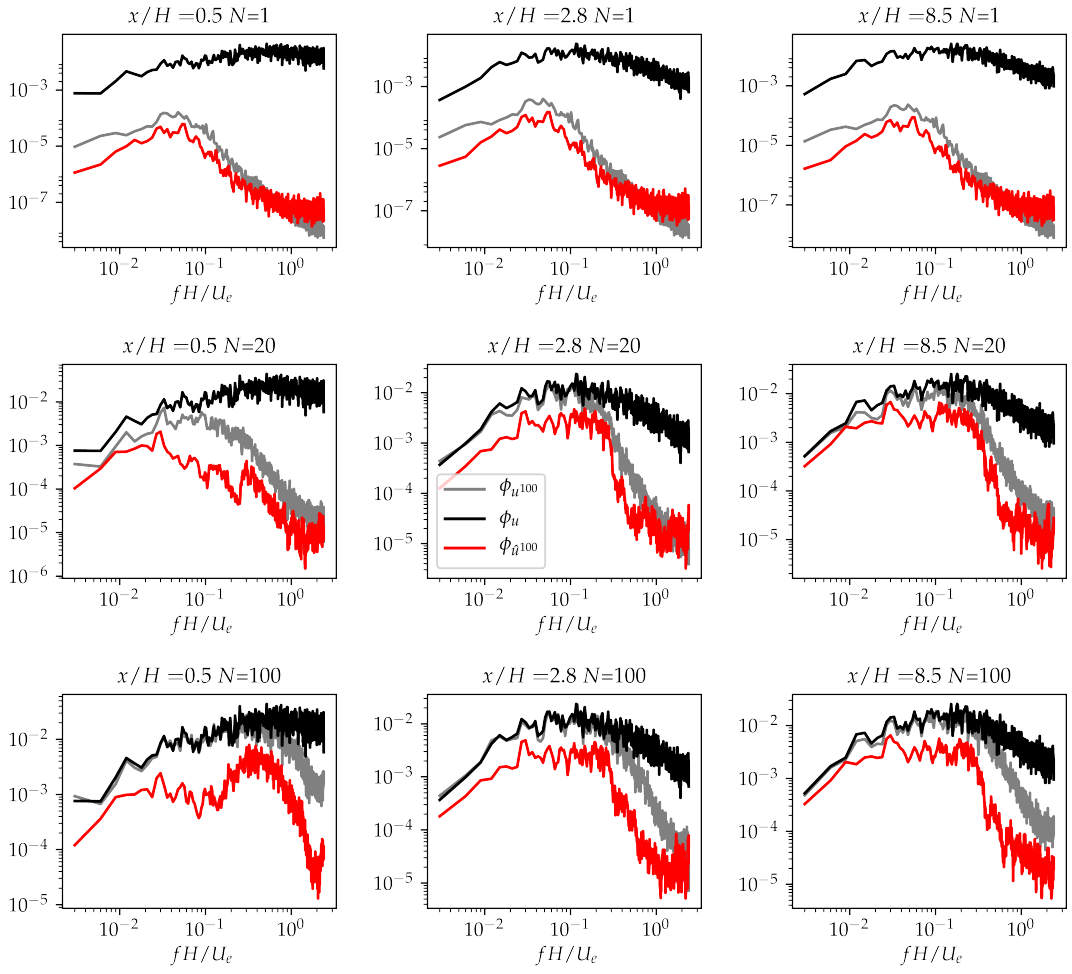

Figure 7.13: Streamwise velocity spectra of reconstructed datasets extracted at the location of black dots shown in figure 7.8 compared with reduced-order and original data. Vertical location is

filtered out because only 100 modes are included. In general, the spectra of estimated velocity follow closely the reduced-order velocity spectra in general, meaning that the modes of interest are well reconstructed with surface pressure. Near the leading edge however, a dip appears clearer with higher N between estimated and the original velocity spectra. This is due to the correlation with surface pressure transducer measurements which captured two peaks (see figure 6.2a) thus privileging a reconstruction with two dominant frequencies. Such spectra are observed in the original velocity very close to the surface of the rib, but not at the sample location in figure 7.13. The area between estimated and original spectra corresponds to the error, and it is now clear where the high error found earlier values stem. Further along the top surface (at $x/H = 2.8$) only one dominant frequency exists which is well captured with 20 POD modes, but 100 modes produces little improvement (or reduction of the area between original and estimation). This confirms the low correlation between high mode numbers and the transducer measurements at that location. Further downstream, at the mean reattachment point in the wake ($x/H = 8.3$) we observe a similar effect to the top region, overall the magnitude of the estimated spectra increases with additional POD modes, but past 20 modes, very little improvement in the estimation of velocity spectra can be seen. Thus the information necessary due to reconstructing fluctuations in the wake region is lost due to poor correlation with the surface pressure both upstream and in the wake. The convection of events which were correlated with pressure from the top surface may reach the mean reattachment region. However, these do not dominate the fluctuations of the wake region.

7.3.2.2 Semi-analytical frequency response of the estimator

Unlike, figure 7.13 which gives an idea of the transfer function between pressure and reconstructed velocity at specific locations. With equation 7.20 one may compute the gain between the signals of each transducer and each mode applied by the estimator. Although the gain between one transducer and the mode signal is computed mostly analytically, the cross-terms contain the ratio between Fourier transforms of discrete pressure signals which are noisy in our case.

Nevertheless, the relation between a mode and a pressure signal gives insight into the effect of velocity fluctuations on surface pressure and how the estimator is performing. Figure 7.14 depicts the gain including cross-terms as computed between pressure signals extracted from locations x_p and mode 0 and 6 (a and b respectively). This gain includes the cross-terms which explains the noise and is non-negligible compared to the $|H|^2$ term. It appears mode 0 is modulated mostly by the signals of $x_p/H = 3.5$, $x_p/H = 0.5$, and slightly by $x_p/H = 2.5$. Mode 6 on the other hand is mostly modulated by pressure measurements at locations $x_p/H = 3.5$, $x_p/H = 0.5$ and $x_p/H = 8.5$. Mode 6 was on average the most correlated mode and mode 0 was the most energetic mode. Mode

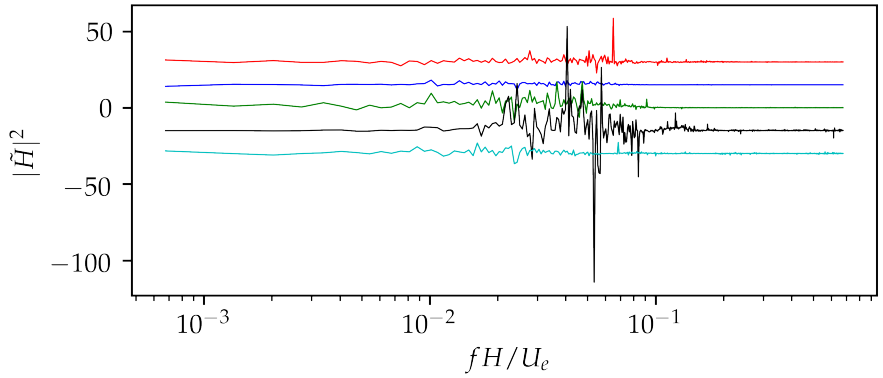

(a)

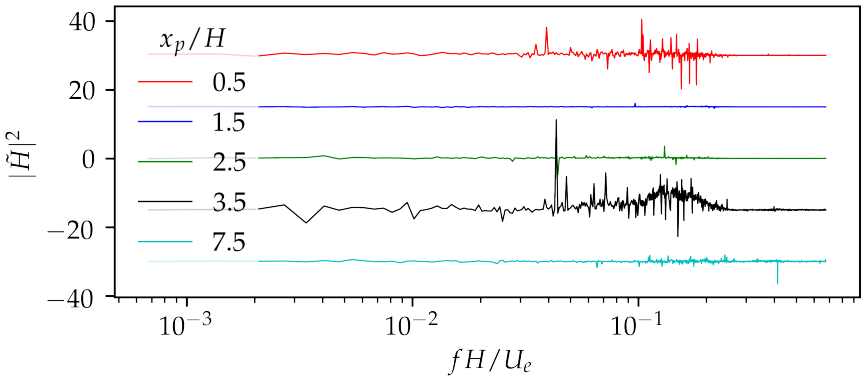

(b)

Figure 7.14: Gain of the transfer functions between mode 0 (a) and 6 (b) and the pressure measurements at location x_p/H.

0 is modulated at frequencies of 0.01 to 0.1, whereas mode 6 is modulated between frequencies of 0.04 and 0.3 mostly. This corresponds to the range of frequencies observed in the spectra of POD mode coefficients. Thus the reconstruction is occurring in the correct range of frequencies for those modes. Many modes can be looked at individually in this way, but these are not represented here. Figure 7.13 can be seen as the overall effect of the estimator on a sum of modes at key locations.

7.3.2.3 Reconstructed velocity field statistics

Finally, to provide an indication of the resulting estimated velocity, we computed statistics of the flow in figure 7.15. The top figure displays the standard deviation of $\hat{u}^{100}$ but with only source of pressure from the location $x_p/H = 2.5$. The figure below shows the same reconstruction using information from all five transducers instead. The figure below shows the original values obtained from the original PIV data. Finally, the bottom figure shows the standard deviation of u^{100}, the reconstructed velocity with 100 POD modes and the original coefficients.

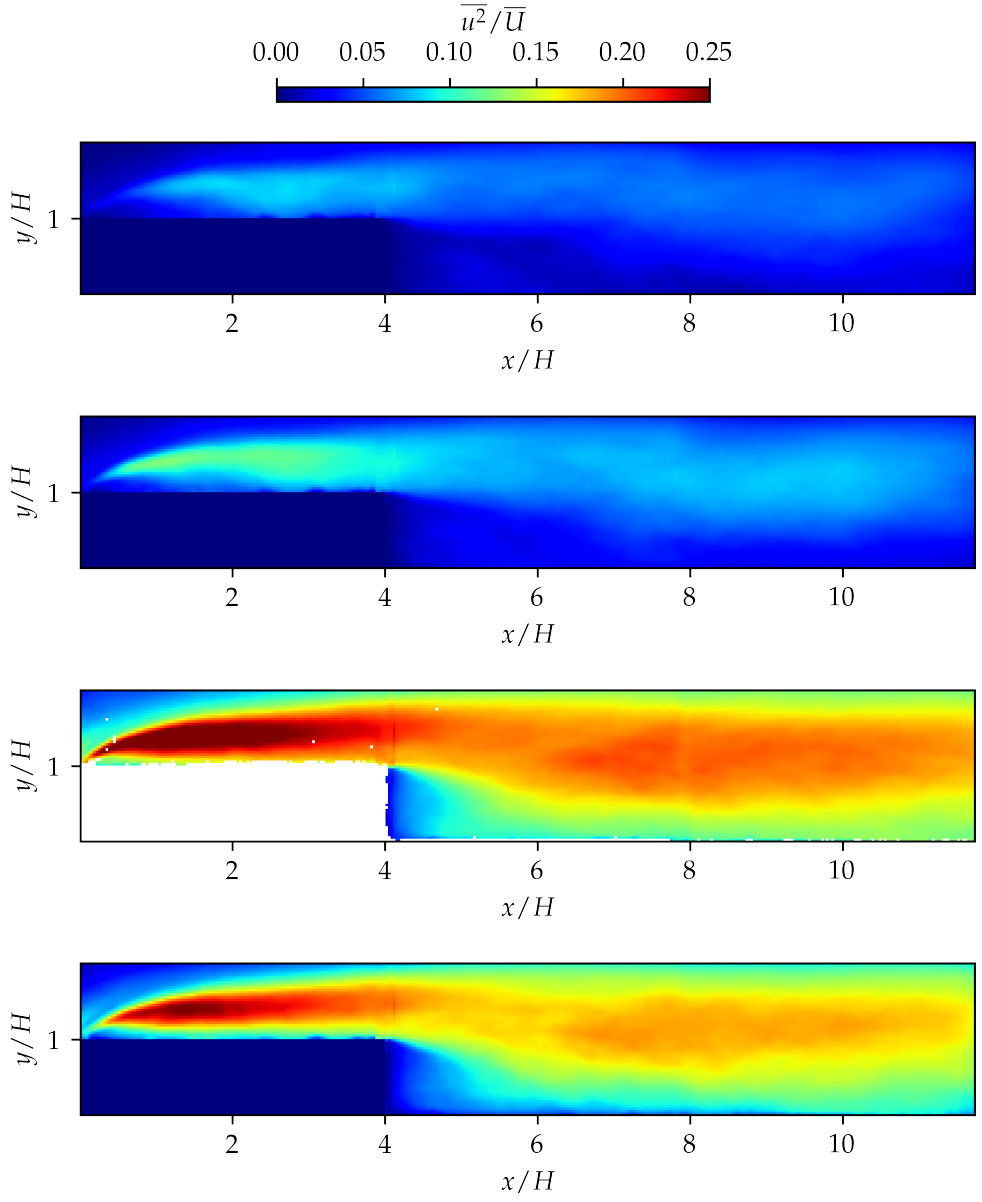

Figure 7.15: Standard deviation of stream-wise velocity component using different methods to reconstruct the flow. Top to bottom: $\hat{u}^{100}$ from transducer at $x_p/H = 2.5$, $\hat{u}^{100}$ from all transducers, original u, reduced-order u^{100}. Reconstructed using 100 modes and the optimal number of time delays for each transducer.

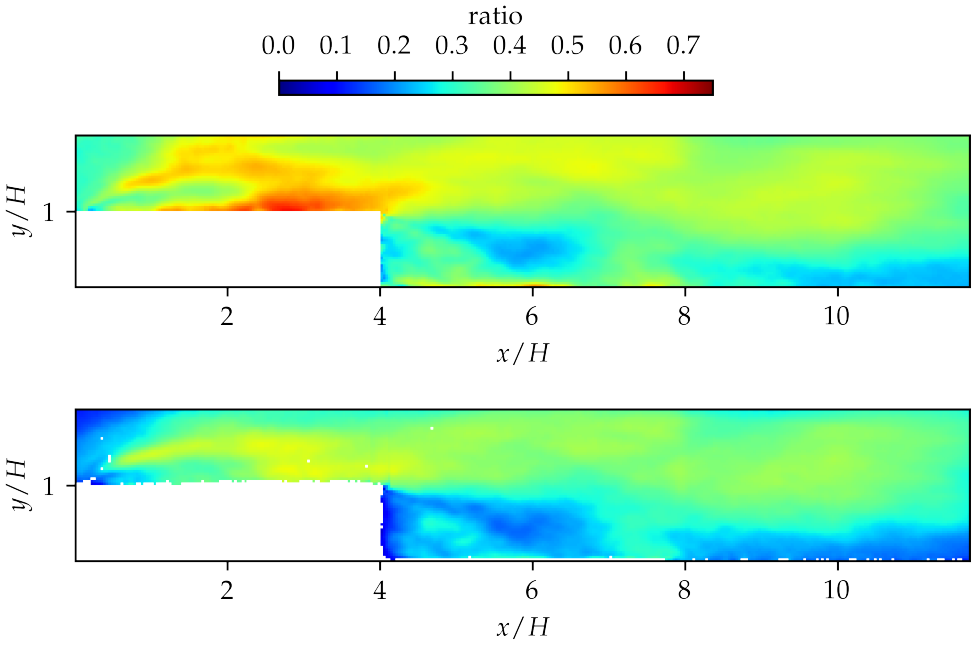

Figure 7.16: Ratio between standard deviation of the reconstructed dataset and the reduced-order velocity equivalent (top) as well as the original dataset (bottom) shown in figure 7.15.

The estimation with only one transducer appears to produce a flow with fluctuations beginning at the leading edge and propagating far downstream, past the end of the PIV measurement window. The strong convective nature of the flow is thus shown. However, the wake region below $y/H = 1$, the level of the top of the rib, presents little fluctuations, and the boundary with the upper parts of the upstream shear layer extending over the wake region is sharp. This suggests the upstream shear layer that is correlated with the pressure fluctuations at the mean reattachment on top does not penetrate the second separation region after the trailing edge of the rib. Additionally, based on one transducer little fluctuations are reproduced inside the recirculation region at the leading edge, only the shear layer is reproduced.

The reconstruction with all transducers shows a different type of flow with fluctuations beginning at the leading edge and extending all the way to the downstream end of the PIV window of measurements, but also including fluctuations inside the recirculation regions at the leading edge and in the wake. Thus we may establish that pressure fluctuations along the top surface of the obstacle can be paired with velocity fluctuations everywhere around the rib, even in the wake region. Nevertheless, these do not dominate the velocity fluctuations that do not affect surface pressure.

Figure 7.16 depicts the ratio between standard deviation of the reconstructed dataset and the reduced-order velocity equivalent (top) as well as the original dataset (bottom) shown in figure 7.15. The top figure indicates that compared with the reduced-order dataset, the reconstructed dataset is most similar to the reduced-order dataset near the

mean reattachment point of the top surface (up to 75% from $x/H = 2$ to 4). The standard deviation of streamwise velocity is lower by approximately 50% in the shear layer near the leading edge compared with the reduced-order dataset. The wake region presents the lowest ratio between the two quantities with less than 25% in the core of the recirculation region ($x/H = 6$).

In comparison with the original dataset, the standard deviation of the reconstructed dataset is more homogeneously lower. Approximately 45% of the standard deviation is reproduced from in the leading edge shear layer to the end of the PIV window. The ratio of standard deviation of u is also lowest in the wake of the obstacle with only 10% between reconstructed and original datasets.

This ratio between standard deviations indicates that statistically speaking the estimator reproduces the 100 POD modes well in regions where pressure is well correlated with velocity. However, the remaining POD modes which are weakly correlated to pressure would contribute a significant amount of fluctuations.

7.4 Motion of the flow affecting surface pressure

Using the linear estimation of velocity as a function of surface pressure, we extracted the part in velocity fluctuations that is correlated with surface pressure. Two phenomena were detected in velocity and pressure in chapter 6: the low frequency shear layer flapping, and the higher frequency vortex shedding. Using the estimated data, we illustrate how these events occur over the rib of $L/H = 4$ from the perspective of surface pressure.

In order to do so, we reconstruct the flow of a validation dataset with 100 modes, and the full pressure fluctuation spectra. Then we phase average the reconstructed velocity fields based on a condition imposed on surface pressure. Selecting the pressure transducer at the leading edge, we band-pass the signal to isolate the low-frequency ($fH/U_e = 0$ to 0.1). The band-passed signal is then Hilbert-transformed such that we obtain complex numbers rotating around the real-imaginary plot as dictated by the oscillation with the largest magnitude, in this case the frequencies close to $fH/U_e = 0.03$. This allows us to split the time-series into eight quadrants and average all the snapshots within each quadrant. As a result, we obtain eight average flow fields of velocity fluctuations correlated with surface pressure which correspond to eight phases of the shear layer flapping phenomenon.

The operation can be repeated by isolating different frequencies in the pressure spectra. Additionally, the condition can be imposed on a different transducer. In this section, we will look at the low and high frequency phenomena of the leading edge sensor, as well as a single frequency for the sensor immediately downstream of the mean reattachment point ($x/H = 3.5$).

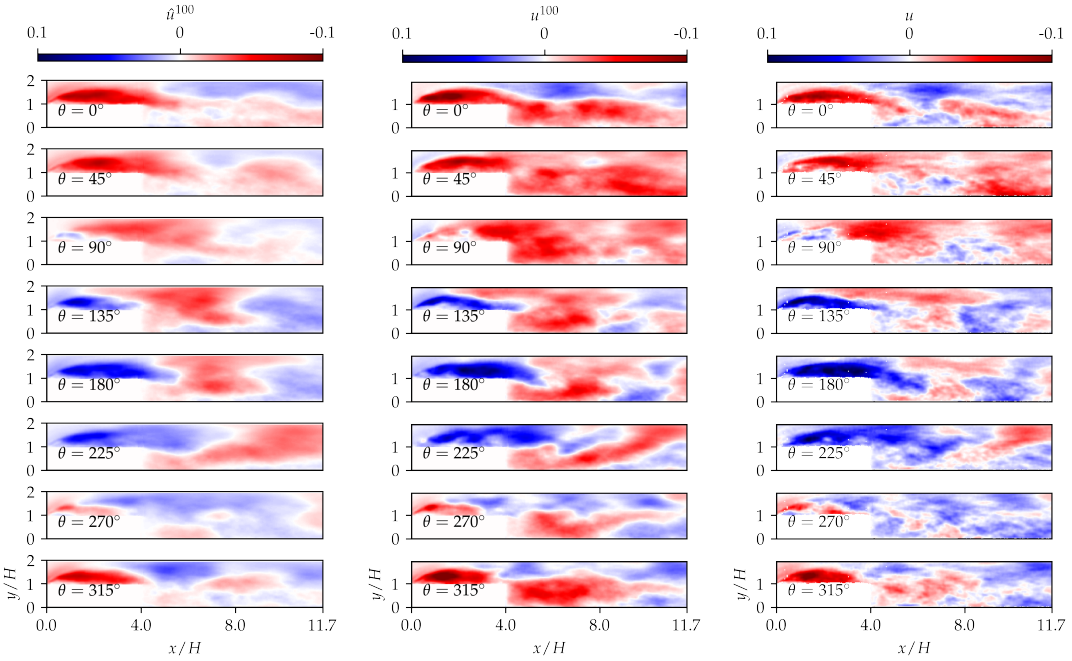

Figure 7.17: Phases of shear layer flapping phenomenon occurring at $fH/U_e = 0.03$ based on phase averaging based on the first leading edge pressure.

Using the first transducer as a criterion for phase averaging, we isolated the frequencies between $fh/U_e = 0$ and 0.1 and phase-averaged the velocity flow fields associated with each pressure measurement. Figure 7.17 shows the average streamwise velocity flow fields associated with the eight phases (θ) of the pressure signal. We repeated the phase averaging for the estimated velocity, conserving only the fluctuations correlated with pressure, the original reduced-order velocity field, and finally the original flow field. It appears from all three velocity datasets that the eight phases in pressure correspond well to eight phases in velocity. Indeed a large acceleration (red ellipsoid) exists over the top surface of the rib at $\theta = 0$ which grows into the wake region before moving downstream and allowing a zone of deceleration to grow in its place. Towards the end of the cycle, the red zone reappears at the leading edge and grows again to cover the top surface. This phenomenon illustrates the effect of shear layer flapping in streamwise velocity.

Similarly, the two original velocity datasets show similar trends although with more noisy patterns. This is due to two main reasons, the estimation of velocity filters the signal significantly as can be seen in the frequency spectra of estimated velocity flow fields. In addition, the phases in shear layer flapping of the original dataset are not necessarily correlated with surface pressure, thus the phase averaging is capturing other fluctuations which do not repeat periodically. The smoothing effect of POD is visible in the phase-averaged reduced-order velocity dataset and show very similar trends along the top region. Some discrepancies occur in the wake region where the flow field is the least correlated with top surface pressure. The original dataset shows the same discrepancies,

however it is noisier. This suggest that modes over number 100 still contain energy, but are not correlated with pressure.

Still using the leading edge pressure transducer as a reference, we isolate frequencies between 0.1 and 1 in figure 7.18. Instead of streamwise velocity component, we found that the phenomenon was clearer in vertical velocity component. Therefore we plot the vertical velocity averages associated with the eight phases in the pressure signal. This situations shows successive upwards and downwards draft with one full cycle over eight phases between positive and negative fluctuations near the leading edge. These fluctuations are reminiscent of small vortices being shed from the leading edge which are also in described in forward-facing step studies (Cherry et al., 1984). The pulses quickly disappear beyond $x/H = 1.5$ showing that only the first $1.5H$ of the top surface experiences vortex shedding in the range of frequency highlighted. The regions downstream do not repeat periodically thus the phase averaging does not capture any consistent fluctuation.

Finally, using the transducer closest to the trailing edge, we isolate pressure fluctuations between $fH/U_e = 0.2$ and 0.4 which should correspond to vortices shed from the leading edge rotating at a slow rate as they grow and travel downstream. This effect has been observed in numerous studies over forward-facing and backward-facing steps. In this case, we also found that the vertical velocity component was the clearest, therefore, in figure 7.19, we plot the eight phases of vertical velocity associated with the eight phases of isolated pressure fluctuations. The result is a train of up and down motions which appears clearly in the second half of the top surface and extends downstream of the trailing edge with little extension into the recirculation region. The ellipsoids vanish with streamwise distance from the trailing edge, and are not visible as clearly by $x/H \approx 6$. In this instance, the patterns repeat over one cycle indicating that they are temporally well aligned with the isolated frequencies.

With linear estimation of POD modes from surface pressure, we were able to reconstruct velocity fluctuations correlated with surface pressure fluctuations. Overall, it appears the estimation of modes is possible if correlation is sufficient. Some discrepancies between the original and reconstructed velocity exist because higher POD modes which contain a significant energy portion are not correlated to surface pressure. As seen in the phase averaging of the flow based on surface pressure, some flow structures which are well correlated with p are well reconstructed both spatially and temporally. Consequently, we may establish that velocity estimation in this turbulent case is possible, although filtering of some velocity fluctuations occurs due to the nature of the input used.

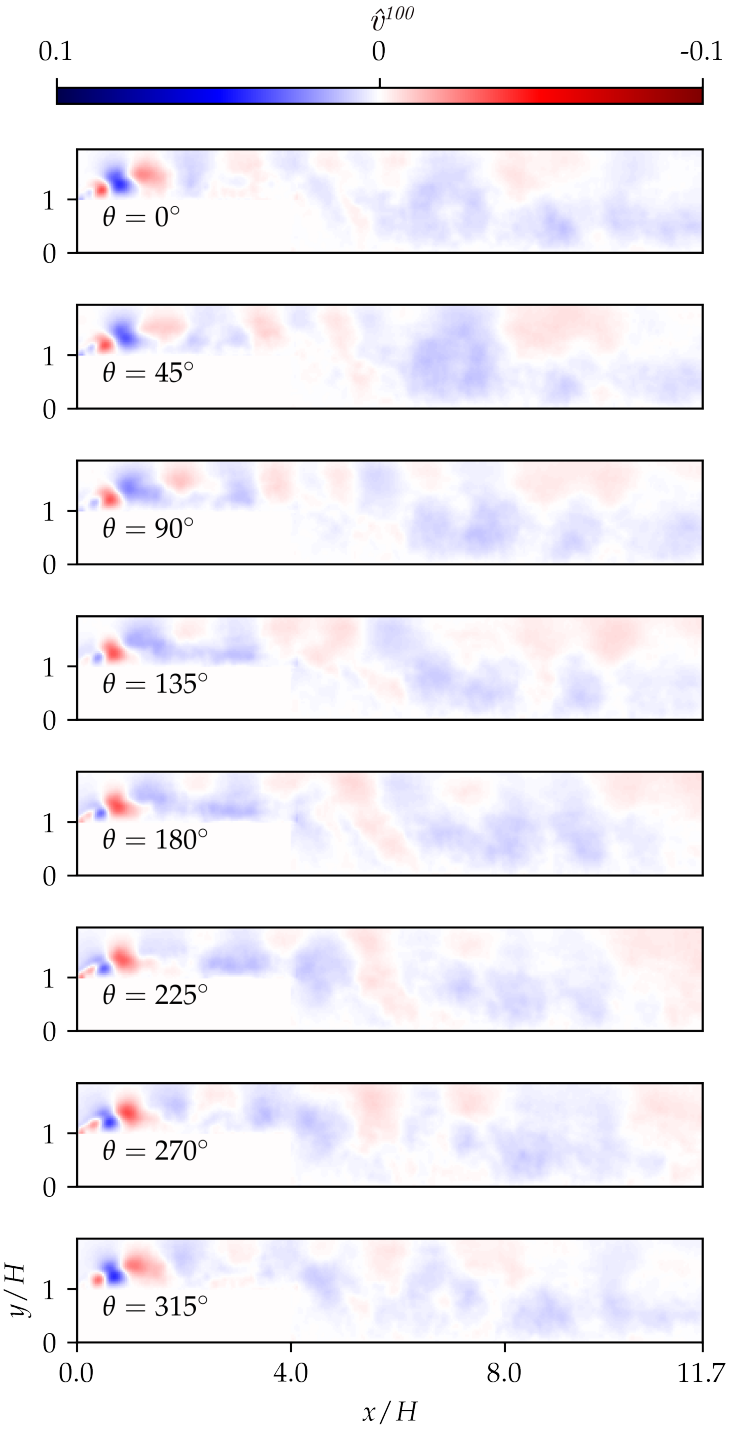

Figure 7.18: Phases of shear layer flapping phenomenon occurring at $fH/U_e = 0.4$ (BP from 33 to 333Hz.) from band-pass filtered data based on the leading edge pressure

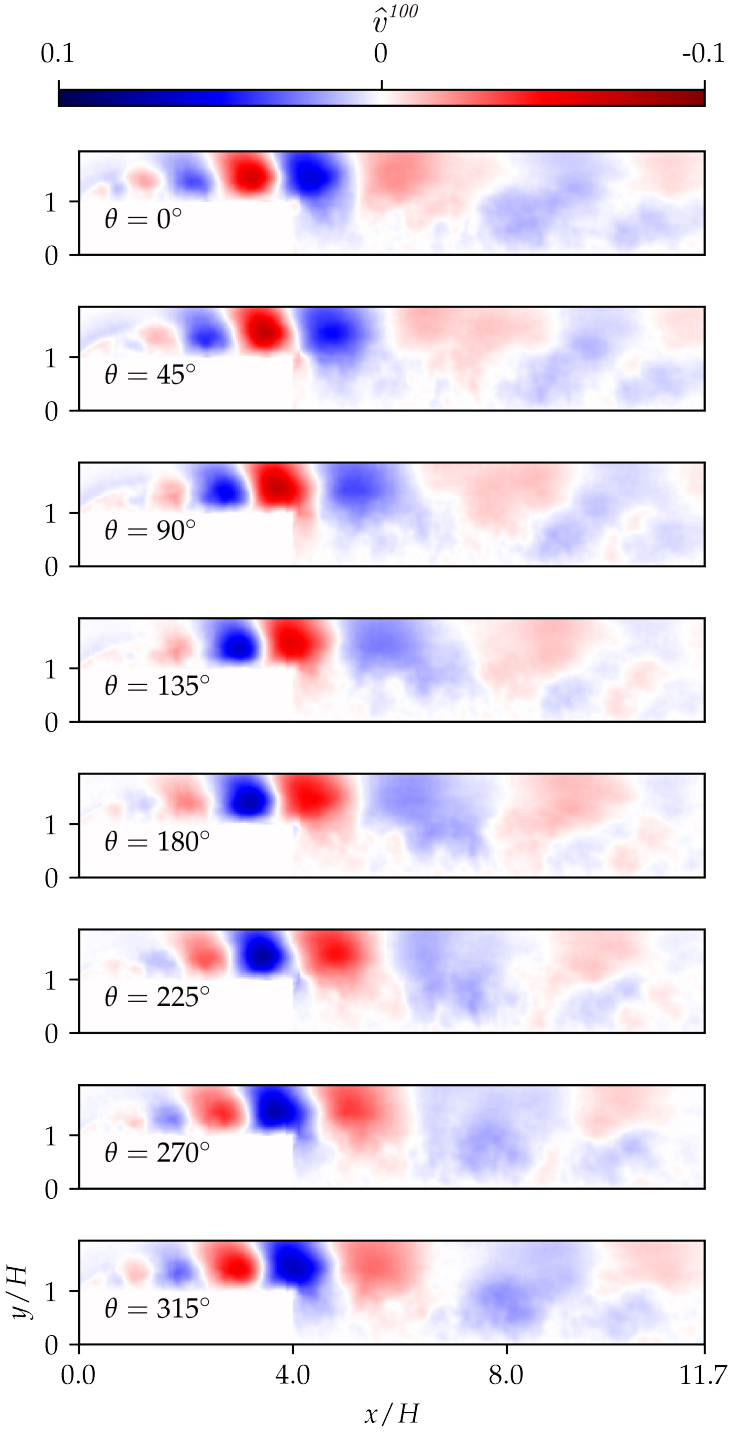

Figure 7.19: Phases of vertical velocity component v phenomena occurring at $fH/U_e = 0.2$ to 0.4 based on sensor at $x/H = 3.5$ and BP between 33 and 200Hz.

Chapter 8

Conclusions and Future work

8.1 Findings

This work tackled the flow over two-dimensional ribs which consist of a forward-facing step followed by a backward-facing step. The interaction between the aerodynamics of these two canonical obstacles leads to complex patterns that vary with rib length.

In order to study the aerodynamics of ribs, four steps were taken that involved multiple forms of velocity and pressure measurements. Four experiments were also carried out to obtain the necessary information using average and fluctuating surface pressure measurements, PIV and hot-wire velocity measurements. In some instance, the pressure and velocity information was acquired synchronously that allowed us to draw links between the two quantities in such a turbulent flow.

The first subject of discussion is the implementation of a method to estimate pressure fields from particle image velocimetry measurements. Using Taylor's Hypothesis, this method enables the estimation of two-dimensional pressure fields from non time-resolved PIV measurements. The method is proven to reliably recreate the statistics of pressure measured at the surface of ribs using pressure transducers. In addition, the method estimates with better accuracy than other commonly used methods. The field pressure information is used to study the general characteristics of separation over ribs.

The second matter is the characteristics of the flow over ribs of varying length. Using statistical analysis, trends identified in previous work by Bergeles and Athanassiadis (1983) were found in this study although with some differences which are explained. Indeed, the length of the recirculation regions caused by ribs follows a linear decrease with increasing rib length up to $L/H = 4$. Longer ribs produce a wake recirculation region approximately half of the length of the bubble behind "simple" backward-facing steps, but seemingly constant. These two trends distinguishing short ribs from long ribs are correlated with the presence/absence of a closed recirculation region on the

top surface. PIV allows the measurements of bubble height and area instantaneously on which the trends were also observed. In addition to trends of the mean quantities, the fluctuation of each quantity was found. It was shown that ribs of medium length produce the most unsteady bubbles because of the occasional merging of top and wake bubbles. Longer ribs produce steadier bubbles because the flow along the top surface stabilizes before reaching the wake region. Shorter ribs seem to produce proportionally steadier recirculation regions because the bubble size is driven by shear layer flapping and vortex shedding from a single corner, rather than two. Temporal analysis of velocity and pressure fluctuations in key locations showed that the top surface of long ribs behaves identically to a forward-facing step in similar flow conditions, and there is no discrepancy in this region between long ribs. In the wake region, some degree of similarity with backward-facing steps was found, but it was very dependent on rib length. Similar analysis showed that shorter ribs produce weaker separation initially than longer ribs. However, shear above the wake region allows larger scale turbulence to develop thus resulting in the most perturbed wake.

The third topic is the effect of free-stream turbulence on the characteristics of the flow. It was found that the size of the recirculation region behind a short rib is more sensitive to free-stream turbulence than that of a longer rib. The wake bubble of the short rib shrank with increased FST, whereas the bubbles of long ribs remained nearly constant. It was identified that FST changes the amount of exchange between the recirculation regions and the free-stream. This occurs because FST modulates the low frequency shear layer flapping mode of recirculation regions. However, the wake bubble of long ribs is not dominated by large shear layer flapping, therefore it was less sensitive to perturbations of that regime.

Finally the relationship between pressure and velocity in the flow over a rib of length $L/H = 4$ was studied. We found that motions of the top recirculation region are not synchronized to the wake region. Bubbles appear to grow in position due to a pocket of slow flow settling after a corner. Above a certain size, these pockets begin to advect downstream to allow a pocket of accelerated flow to take place and compress the recirculation regions. We may also illustrate three typical phenomena observed on FFS on tops of ribs: shear layer flapping which occurs at the lowest frequency, vortex shedding at the highest frequency and the same vortices after some growth, producing oscillations at lower frequencies. These phenomena generated at the leading edge affect the flow separating at the trailing edge, but do not reach the end of the wake region.

Linear estimation of POD modes of velocity based on surface pressure measurements isolated velocity fluctuations with an effect on surface pressure. This study showed that the shear layer flapping and vortex shedding phenomena are captured both in pressure at the top surface and velocity around the rib. Low frequency shear layer flapping can traced to pressure fluctuations near the leading edge as well as the trailing edge. This is because shear layer flapping consists in large pockets of accelerated or decelerated

flow travelling along the top surface of the obstacle, into the wake region. Conversely, vortex shedding is characterized by short and high frequency variations in velocity in the shear layer. These variations grow in size while reducing in intensity and frequency with streamwise distance from their origin, the leading edge.

8.2 Future work

This thesis contains the beginnings of what could be much more detailed analysis. Here are a few directions in which this work could be continued:

- Applying the current measurements to better model the flow over common objects such as hills with wind-farms located on the top surface, or on the lee side. This would improve wind-turbine on-site efficiency predictions.
- The simple geometry of ribs produces a complex flow with a large range of scales. This could potentially be a good test for numerical methods. The different aspects covered in this thesis should be a starting point for validating CFD simulations.
- Several other measurements could be made such as surface skin friction, this would allow a more accurate measurement of the reattachment point as well as add skin friction drag components. Unsuccessful attempts were made to use flexible materials to measure shear stress at the surface of ribs during this work, but the author believes skin-friction is relevant and measurable.
- Studying ribs under freestream turbulence of a much smaller scale thus potentially exciting only the vortex shedding motions without affecting shear layer flapping. This opens the question of flow control where forcing is introduced to dampen oscillations in the flow. As we have seen that two frequencies dominate this flow, perhaps a two-frequency forcing would be appropriate.
- High-speed measurements were acquired for one rib length ($L/H = 4$), it would be relevant to repeat those measurements for different rib lengths.
- Based on the linear estimations of velocity from surface pressure, one could implement closed-loop control systems based on pressure to control or anticipate velocity above the rib.
- One could also use the linear model of the flow to design cheap but realistic inflow conditions for numerical simulations. The use of POD reduces the number of computations necessary to reconstruct the flow of a rib.

Appendix A

POD of velocity around all ribs

The turbulent length scales produced by each rib can be observed in Proper Orthogonal Decomposition (POD) obtained via "snapshot POD" method (Sirovich, 1987). These POD modes do not show physical phenomena, merely the general location where fluctuations occur, and how strong they might be. Figure A.1 shows the cumulative energy distribution for all the modes for each case. It can be seen that a larger number of modes is required for longer ribs to capture 50% of the total kinetic energy. For the short, the medium, and the long rib, 25, 28 and 40 modes are required respectively to reproduce 50% of the total fluctuating kinetic energy. This suggests the fluctuations over long ribs are the most complex, requiring more scales to be described. Figure A.2 represents the first eight POD modes of the three principal rib lengths. The top modes are the most dominant, the ones that contribute the largest kinetic energy of the fluctuations. POD associates the strongest modes with large patches of velocity fluctuations suggesting the strongest fluctuations are associated with large scale velocity fluctuations. In addition to the large strong modes, weaker and weaker modes bring smaller more localized fluctuations.

The longest rib produces pulses of fluctuations which are near its surface and do not expand vertically much in comparison to smaller ribs. The first 8 modes show smaller

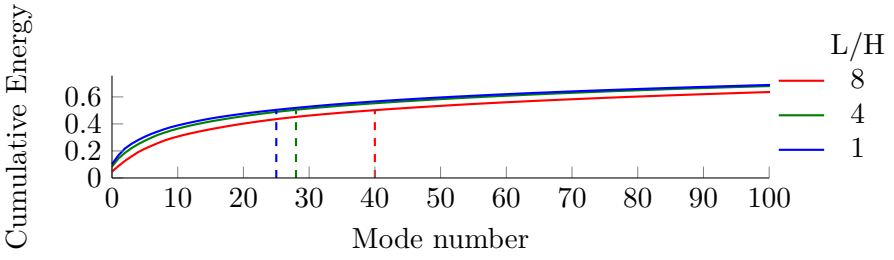

Figure A.1: Cumulative POD energy for each rib length. The dashed line indicates the number of modes required to obtain 50% of the fluctuating $T.K.E.$, respectively 25, 28 and 40 for L/H =1, 4, 8.

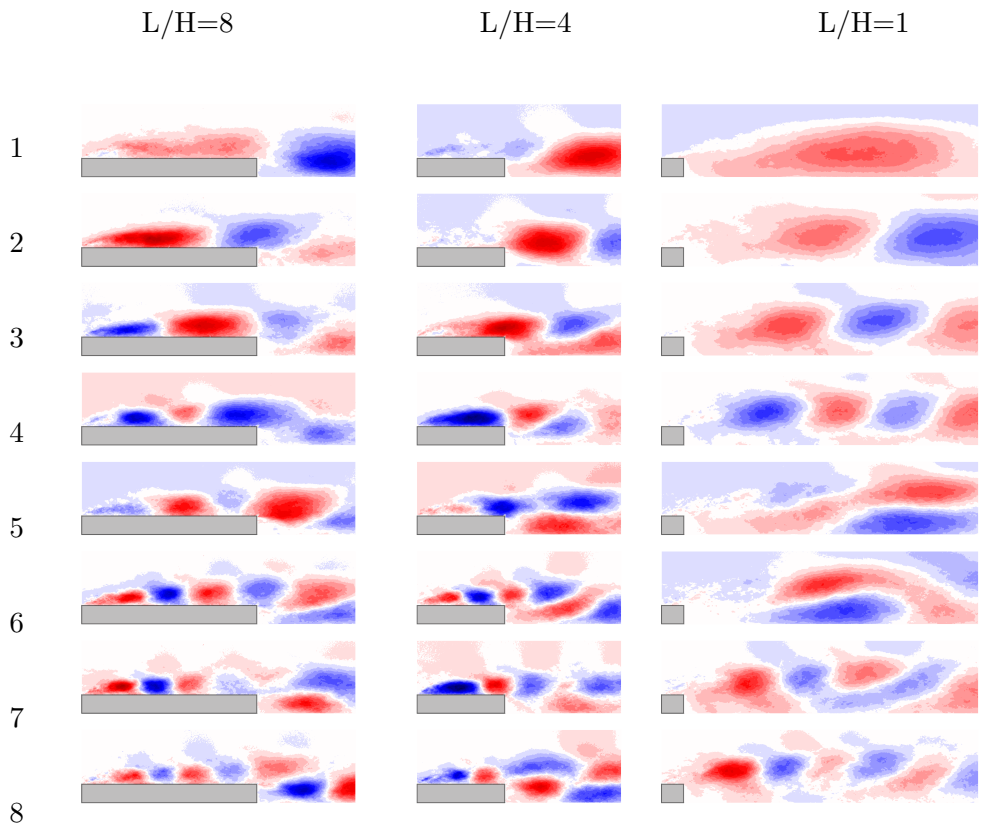

Figure A.2: POD modes obtained for three rib lengths. Increasing mode numbers on the left indicate decreasing magnitude of the energy associated with each mode. Blue indicates negative velocity fluctuation and red the opposite.

and smaller trains of fluctuations aligned in the stream-wise direction. The medium rib (centre) shows differences with the long rib from mode 3 onwards. In mode 3, the pulse of high and low velocity are stacked vertically, rather than aligned in the stream-wise direction. Higher mode numbers (weaker modes) exhibit fluctuations which expand higher vertically. This is similar to the comparison of $T.K.E$ distribution (figure 4.25) and suggests the fluctuations are developing more and further into the free-stream. The first mode of the shortest rib presents one single large velocity pulse where the recirculation region should be. Modes 2, 3, 4 show trains of smaller pulses aligned with the top of the shear layer. The largest scales of velocity fluctuations are clearly visible here. Furthermore, these occur on the shear layer where they may be swept downstream at high velocity. Higher mode numbers show more complex patterns but remain organized.

Observing the POD modes of three critical ribs, it is clear that longer ribs produce smaller scale turbulence which inherently dissipates quicker than larger scale fluctuations, despite stronger initial $T.K.E.$ as reported in figure 4.25. Shorter ribs tend to produce predominantly fluctuations of larger scale in the shear layers which subsist longer, thus being more noticeable far downstream of the rib.

Appendix B

Conditional averaging of the flow.

Pearson et al. (2013) highlighted the effect of incoming turbulent boundary layer on separation of a forward-facing step. It was discovered that low-momentum fluid from the turbulent boundary layer reaching the step accumulates against the vertical face until the bubble of separated flow grows enough to "leak" over the corner of the step. As the front bubble "leaks" over the corner of the step, unusually long but thin separation of the flow occurs. In the context of this study, these periodic events exist as well on ribs, and the shape of the recirculation region on the top surface may have a direct effect on the separation in the wake region.

Sections 4.3.1 and 4.3.2 describe the link between L_r and A_R, and H_R and A_R, but not between L_R and H_R. It appears there may be short or long bubbles, as well as high or low bubbles on top and in the wake of ribs. The states of each of those regions could influence neighbouring regions, and this to a degree varying with rib length. In this section, conditional averaging is used to highlight how the state of a recirculation region may be linked to that of others and to the incoming flow.

Three investigations were carried out involving the momentum of the flow at the leading edge, the top recirculation region area, and the wake bubble area. Each of the three investigations used the first, second or third of the above criteria to gather snapshots in 3 groups: the first below average, the second on average, and third above average value.

The results of the first conditional average are presented in figure B.1. Three conditions are defined based on the momentum of the flow at the leading edge of the rib compared to the mean value. Three groups are extracted for values above, below and within 5% of the mean value. The narrow band is required due to the narrow distribution of values, otherwise insufficient samples would be averaged leading to unconverged averages. Each rib indicates that momentum at the leading edge of the rib is associated with a large region of relatively fast or slow flow stretching approximately from $2H$ upstream to $2H$ downstream of the leading edge. It is supposed that due to the non-time resolved

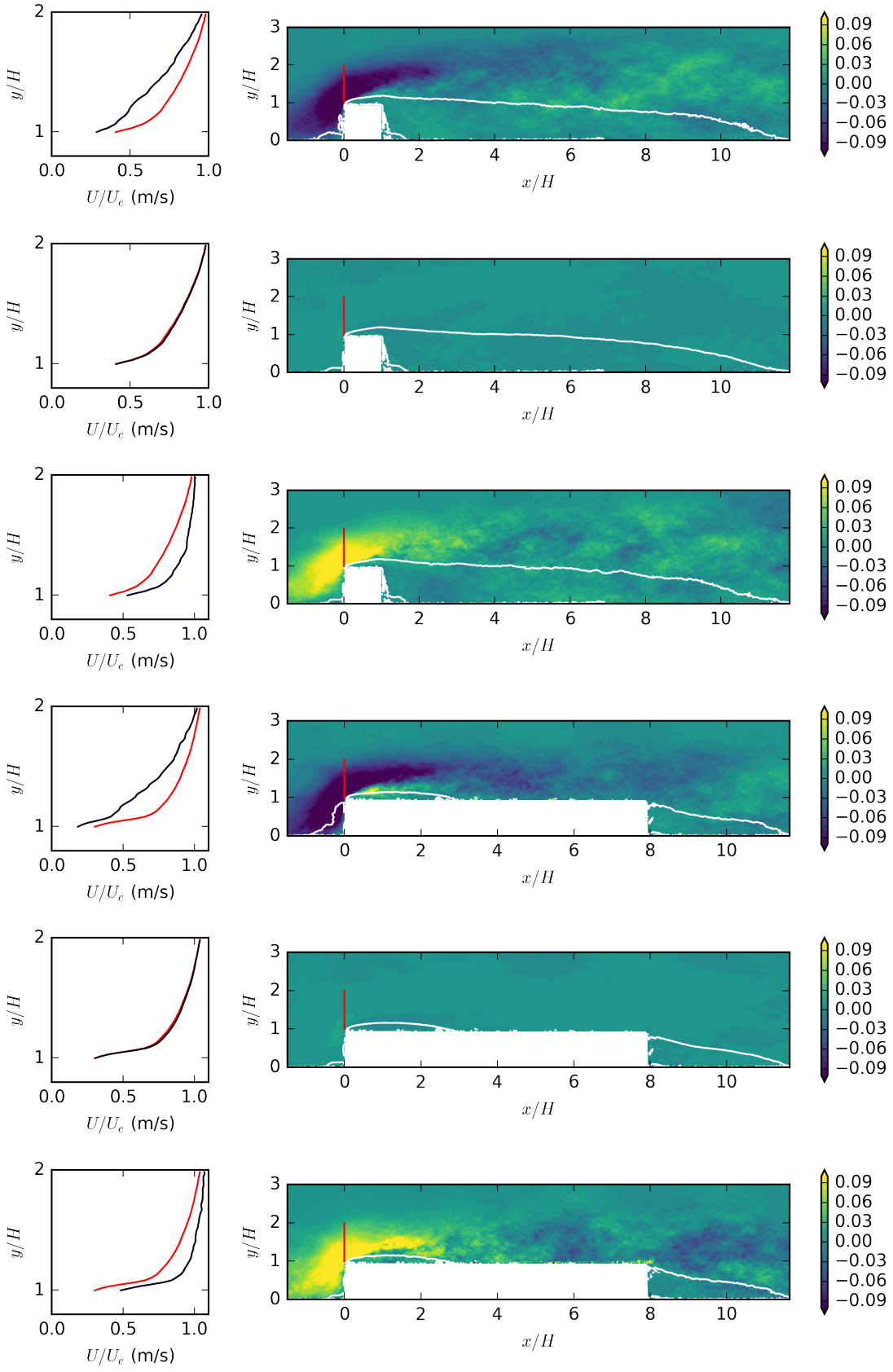

Figure B.1: Conditional averaging of the flow fields based on momentum at the leading edge of the rib. Rib length 1 and 8. White contour describes location of U=0. Graphs display the stream-wise velocity profile of current conditional average in black compared to average velocity in red.

nature of the PIV measurements, this large patch represents conditional averaging of the flow features detected by Pearson et al. (2013) at different stages. Consequently the "leakage" observed by Pearson et al. (2013) is averaged at multiple stages. The result of this averaging is a very small effect on the average flow downstream of the leading edge. Indeed, the recirculation length of the wake region of all ribs varies only by a percent which can be associated with statistical error, and is within measurement uncertainty (recall that the vector spacing is $0.017H$).

The results of the second conditional average are presented in figure B.1. We compare the three long ribs based on the area A_R of the recirculation region defined by $U < 0$. Three groups are made with areas below, above or within 50% of the average recirculation area. Varying size of recirculation region has a direct effect on the top reattachment length. Indeed, for all three ribs with a closed bubble on top, we see an increase from approximately $2H$ to $3.5H$ with a mean value at $2.8H$. In addition to the size of the region, a vertical velocity profile is extracted at the leading and trailing edges of the ribs in each associated graph. This graph indicates that regardless of the condition set on the size of the recirculation region there is no distinction in the velocity profiles at the trailing edge. On the other hand, a small or large recirculation region is associated with an increase or decrease of stream-wise velocity component at the trailing edge respectively. In case $L/H = 4$ this velocity difference reaches the trailing edge unlike case $L/H = 8$ where the difference vanishes before the trailing edge. The condition placed on top recirculation region size affect the wake region of $L/H = 4$ (L_R from 7.93 to 8.2) but not that of the longest rib. This highlights the effect of rib length on the link between recirculation regions.

The last conditional average distinguishes between small medium or large wake recirculation regions. In this case a short ($L/H = 2$), medium and long rib are compared with a threshold set at +/-50% of the mean value. Unlike the previous conditional average, the size of the wake region does not appear to have an effect on the top recirculation region. A large or small recirculation region in the wake is associated with a reduction or increase respectively of streamwise velocity in the window of interest. It is also associated with larger or smaller recirculation regions respectively.

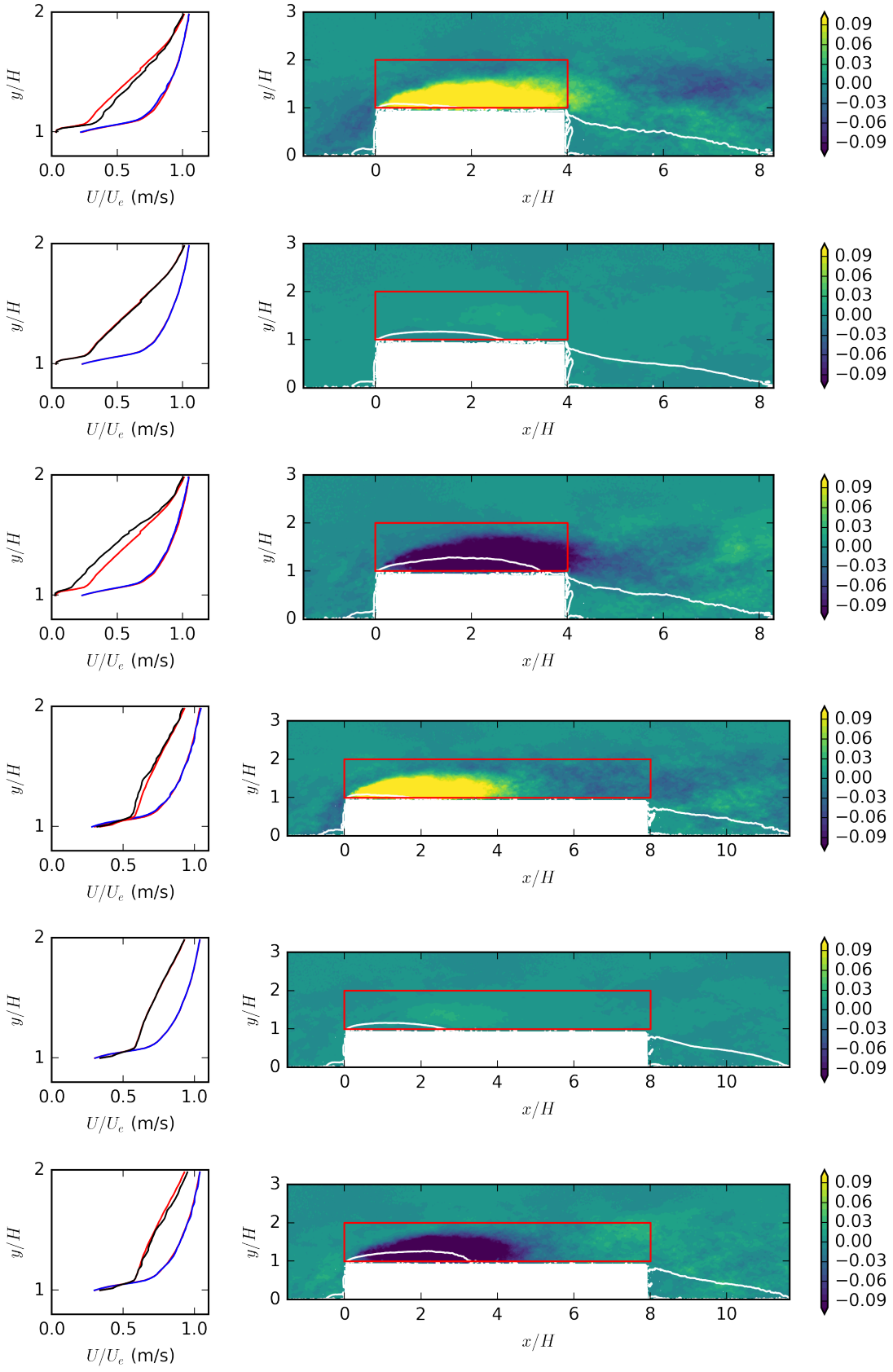

Figure B.2: Conditional averaging of the flow fields based on size of the top recirculation region. Rib length 4 and 8. White contour describes location of U=0. Graph display the streamwise velocity of current conditional average in black compared to overall mean velocity in red.

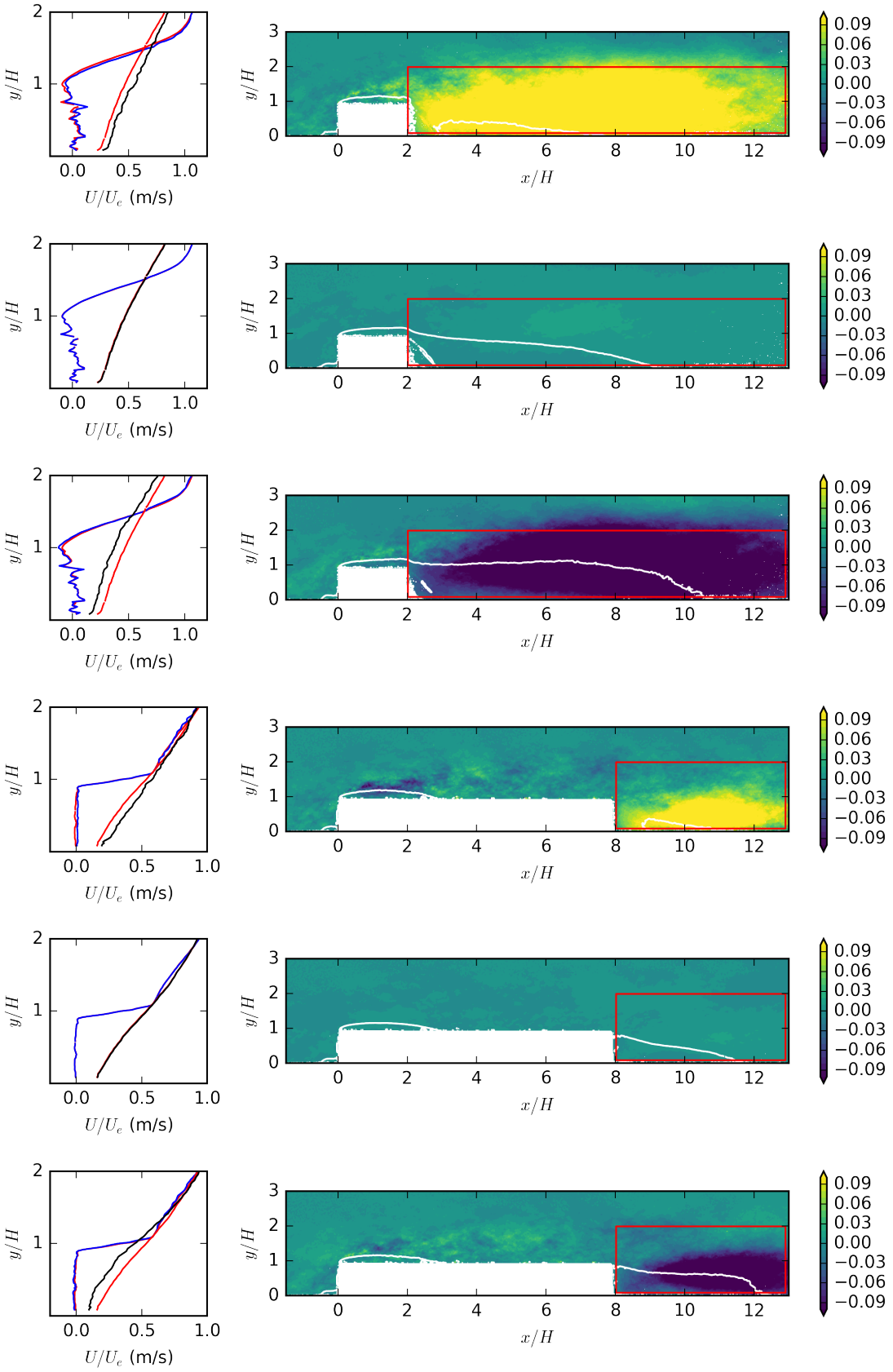

Figure B.3: Conditional averaging of the flow fields based on the size of the wake recirculation region. Rib length 2 and 8. White contour describes location of U=0. Graph display the normalized velocity profile of current conditional average in black compared to average velocity in red.

References

Adams, E. and Johnston, J. (1988). Flow structure in the near-wall zone of a turbulent separated flow. *AIAA journal*, 26(8):932–939.

Antoniou, J. and Bergeles, G. (1988). Development of the reattached flow behind surface-mounted two-dimensional prisms. *ASME Transactions Journal of Fluids Engineering*, 110:127–133.

Arie, M., Kiya, M., Tamura, H., and Kanayama, Y. (1975a). Flow over rectangular cylinders immersed in a turbulent boundary layer: Part 1, correlation between pressure drag and boundary-layer characteristics. *Bulletin of JSME*, 18(125):1260–1268.

Arie, M., Kiya, M., Tamura, H., Kosugi, M., and Takaoka, K. (1975b). Flow over rectangular cylinders immersed in a turbulent boundary layer: Part 2 flow patterns and pressure distributions. *Bulletin of JSME*, 18(125):1269–1276.

Arie, M. and Rouse, H. (1956). Experiments on two-dimensional flow over a normal wall. *Journal of Fluid Mechanics*, 1(02):129–141.

Armaly, B. F., Durst, F., Pereira, J., and Schönung, B. (1983). Experimental and theoretical investigation of backward-facing step flow. *Journal of Fluid Mechanics*, 127:473–496.

Awasthi, M., Devenport, W. J., Glegg, S. A. L., and Forest, J. B. (2014). Pressure fluctuations produced by forward steps immersed in a turbulent boundary layer. *Journal of Fluid Mechanics*, 756:384–421.

Bergeles, G. and Athanassiadis, N. (1983). The flow past a surface-mounted obstacle. *Journal of fluids engineering*, 105(4):461–463.

Blinde, P., Michaelis, D., van Oudheusden B., Weiss, P., de Kat, R., Laskari, A., Jeon, Y. J., David, L., Schanz, D., Huhn, F., Gesemann, S., Novara, M., McPhaden, C., Neeteson, N., Rival, D., Schneiders, J. F. G., and Schrijer, F. (2016). Comparative assessment of PIV-based pressure evalutaion techniques applied to a transonic base flow. In *In Proc. of the 18th Int Symp on Applications of Laser Techniques to Fluid Mechanics*, Lisbon, Portugal.

Bradshaw, P. and Wong, F. (1972). The reattachment and relaxation of a turbulent shear layer. *Journal of Fluid Mechanics*, 52(01):113–135.

Cabral, B. and Leedom, L. C. (1993). Imaging vector fields using line integral convolution. In *Proceedings of the 20th annual conference on Computer graphics and interactive techniques*, pages 263–270. ACM.

Camussi, R., Felli, M., Pereira, F., Aloisio, G., and Di Marco, A. (2008). Statistical properties of wall pressure fluctuations over a forward-facing step. *Physics of Fluids (1994-present)*, 20(7):075113.

Castro, I. and Fackrell, J. (1978). A note on two-dimensional fence flows, with emphasis on wall constraint. *Journal of Wind Engineering and Industrial Aerodynamics*, 3(1):1–20.

Chandrsuda, C., Mehta, R., Weir, A., and Bradshaw, P. (1978). Effect of free-stream turbulence on large structure in turbulent mixing layers. *Journal of Fluid Mechanics*, 85(4):693–704.

Charonko, J. J., King, C. V., Smith, B. L., and Vlachos, P. P. (2010). Assessment of pressure field calculations from particle image velocimetry measurements. *Measurement Science and Technology*, 21(10):105401.

Cherry, N., Hillier, R., and Latour, M. (1984). Unsteady measurements in a separated and reattaching flow. *Journal of Fluid Mechanics*, 144:13–46.

Chun, K.-B. and Sung, H. (1996). Control of turbulent separated flow over a backward-facing step by local forcing. *Experiments in Fluids*, 21(6):417–426.

Clark, H., Naghib-Lahouti, A., and Lavoie, P. (2014). General perspective on model construction and evaluation for stochastic estimation, with application to a blunt trailing edge wake. *Journal of Experiments in Fluids*.

de Kat, R. and Ganapathisubramani, B. (2013). Pressure from particle image velocimetry for convective flows: a taylor's hypothesis approach. *Measurement Science and Technology*, 24(2):024002.

de Kat, R. and Van Oudheusden, B. (2012). Instantaneous planar pressure determination from piv in turbulent flow. *Experiments in fluids*, 52(5):1089–1106.

de Kat, R., van Oudheusden, B., and Scarano, F. (2008). Instantaneous planar pressure field determination around a square-section cylinder based on time-resolved stereo-PIV. In *In Proc. of the 14th Int Symp on Applications of Laser Techniques to Fluid Mechanics*, Lisbon, Portugal.

Dogan, E., Hanson, R. E., and Ganapathisubramani, B. (2016). Interactions of large-scale free-stream turbulence with turbulent boundary layers. *Journal of Fluid Mechanics*, 802:79–107.

Driver, D. M., Seegmiller, H. L., and Marvin, J. G. (1987). Time-dependent behavior of a reattaching shear layer. *AIAA journal*, 25(7):914–919.

Eaton, J. and Johnston, J. (1981). A review of research on subsonic turbulent flow reattachment. *AIAA journal*, 19(9):1093–1100.

Farabee, T. and Casarella, M. (1986). Measurements of fluctuating wall pressure for separated/reattached boundary layer flows. *Journal of Vibration and Acoustics*, 108(3):301–307.

Fuertes, F. C., Cecchi, E., van Beeck, J., and Schram, C. (2014). An inexpensive and versatile technique for wide frequency range surface pressure measurements: an application for the study of turbulent buffeting of a square cylinder. *Experiments in Fluids*, 55(1):1–14.

Fujisawa, N., Tanahashi, S., and Srinivas, K. (2005). Evaluation of pressure field and fluid forces on a circular cylinder with and without rotational oscillation using velocity data from piv measurement. *Measurement Science and Technology*, 16(4):989.

Ghaemi, S., Ragni, D., and Scarano, F. (2012). Piv-based pressure fluctuations in the turbulent boundary layer. *Experiments in Fluids*, 53(6):1823–1840.

Good, M. C. and Joubert, P. (1968). The form drag of two-dimensional bluff-plates immersed in turbulent boundary layers. *Journal of Fluid Mechanics*, 31(03):547–582.

Gurka, R., Liberzon, A., Hefetz, D., Rubinstein, D., and Shavit, U. (1999). Computation of pressure distribution using piv velocity data. In *Workshop on particle image velocimetry*, volume 2.

Hall, S., Behnia, M., Fletcher, C., and Morrison, G. (2003). Investigation of the secondary corner vortex in a benchmark turbulent backward-facing step using cross-correlation particle imaging velocimetry. *Experiments in fluids*, 35(2):139–151.

Hanson, R. E., Buckley, H. P., and Lavoie, P. (2012). Aerodynamic optimization of the flat-plate leading edge for experimental studies of laminar and transitional boundary layers. *Experiments in Fluids*, 53:863–871.

Hearst, J., Gomit, G., and Ganapathisubramani, B. (2016). Effect of turbulence on the wake of a wall-mounted cube. *Journal of Fluid Mechanics*, 804:513–530.

Hosokawa, S., Moriyama, S., Tomiyama, A., and Takada, N. (2003). Piv measurement of pressure distributions about single bubbles. *Journal of Nuclear Science and Technology*, 40(10):754–762.

Hudy, L. M. (2005). *Simultaneous wall-pressure and velocity measurements in the flow field downstream of an axisymmetric backward-facing step*. PhD thesis.

Hudy, L. M., Naguib, A., and Humphreys, W. M. (2007). Stochastic estimation of a separated-flow field using wall-pressure-array measurements. *Physics of Fluids (1994-present)*, 19(2):024103.

Hultmark, M. and Smits, A. J. (2010). Temperature corrections for constant temperature and constant current hot-wire anemometers. *Measurement Science and Technology*, 21(10):105404.

Hussain, A. (1986). Coherent structures and turbulence. *Journal of Fluid Mechanics*, 173:303–356.

Jakobsen, M. L., Dewhirst, T. P., and Greated, C. A. (1997). Particle image velocimetry for predictions of acceleration fields and force within fluid flows. *Measurement Science and Technology*, 8(12):1502.

Jensen, M. (1958). *The model-law for phenomena in natural wind.*

Ji, M. and Wang, M. (2012). Surface pressure fluctuations on steps immersed in turbulent boundary layers. *J. Fluid Mech*, 712:471–504.

Kaiser, H. (1959). *Die Strömung an Windschutzstreifen.* na.

Kim, J., Kline, S., and Johnston, J. (1980). Investigation of a reattaching turbulent shear layer: flow over a backward-facing step. *Journal of Fluids Engineering*, 102(3):302–308.

Kiu, M.-H. and Banks, D. C. (1996). Multi-frequency noise for lic. In *Proceedings of the 7th Conference on Visualization'96*, pages 121–126. IEEE Computer Society Press.

Kiya, M. and Sasaki, K. (1983). Structure of a turbulent separation bubble. *Journal of Fluid Mechanics*, 137:83–113.

Largeau, J. and Moriniere, V. (2007). Wall pressure fluctuations and topology in separated flows over a forward-facing step. *Experiments in fluids*, 42(1):21–40.

Lasagna, D., Orazi, M., and Iuso, G. (2013). Multi-time delay, multi-point linear stochastic estimation of a cavity shear layer velocity from wall-pressure measurements. *Physics of Fluids (1994-present)*, 25(1):017101.

Laskari, A., de Kat, R., and Ganapathisubramani, B. (2016). Full-field pressure from snapshot and time-resolved volumetric piv. *Experiments in Fluids*, 57(3):1–14.

Le, H., Moin, P., and Kim, J. (1997). Direct numerical simulation of turbulent flow over a backward-facing step. *Journal of Fluid Mechanics*, 330:349–374.

Leclercq, D. J., Jacob, M. C., Louisot, A., and Talotte, C. (2001). Forward-backward facing step pair: aerodynamic flow, wall pressure and acoustic characterisation. *AIAA paper*, 2249.

Lee, I. and Sung, H. (2001). Characteristics of wall pressure fluctuations in separated and reattaching flows over a backward-facing step: Part i. time-mean statistics and cross-spectral analyses. *Experiments in Fluids*, 30(3):262–272.

Liu, X. and Katz, J. (2006). Instantaneous pressure and material acceleration measurements using a four-exposure piv system. *Experiments in Fluids*, 41(2):227–240.

Liu, Y., Ke, F., and Sung, H. (2008). Unsteady separated and reattaching turbulent flow over a two-dimensional square rib. *Journal of Fluids and Structures*, 24(3):366–381.

Liu, Y. Z., Kang, W., and Sung, H. J. (2005). Assessment of the organization of a turbulent separated and reattaching flow by measuring wall pressure fluctuations. *Experiments in Fluids*, 38(4):485–493.

Longmire, E., Ganapathisubramani, B., Marusic, I., Urness, T., and Interrante, V. (2003). Effective visualization of stereo particle image velocimetry vector fields of a turbulent boundary layer. *Journal of Turbulence*, 4(24).

Maltby, R. (1962). Flow visualization in wind tunnels using indicators. Technical report, DTIC Document.

Marusic, I., Monty, J. P., Hultmark, M., and Smits, A. J. (2013). On the logarithmic region in wall turbulence. *Journal of Fluid Mechanics*, 716:R3.

Meyer, K. E. (2008). Identify flow structures with proper orthogonal decomposition. online.

Mohsen, A. M. (1967). Experimental investigation of the wall pressure fluctuations in subsonic separated flows. Technical report, DTIC Document.

Moss, D. and Baker, S. (1980). Re-circulating flows associated with two-dimensional steps. *Aeronautical Quarterly*, 31:151–172.

Murai, Y., Nakada, T., Suzuki, T., and Yamamoto, F. (2007). Particle tracking velocimetry applied to estimate the pressure field around a savonius turbine. *Measurement Science and Technology*, 18(8):2491.

Naguib, A., Gravante, S., and Wark, C. (1996). Extraction of turbulent wall-pressure time-series using an optimal filtering scheme. *Experiments in Fluids*, 22(1):14–22.

Orellano, A. and Wengle, H. (2000). Numerical simulation (dns and les) of manipulated turbulent boundary layer flow over a surface-mounted fence. *European Journal of Mechanics-B/Fluids*, 19(5):765–788.

Pearson, D., Goulart, P., and Ganapathisubramani, B. (2011). Investigation of turbulent separation in a forward-facing step flow. In *Journal of Physics: Conference Series*, volume 318, page 022031. IOP Publishing.

Pearson, D., Goulart, P., and Ganapathisubramani, B. (2013). Turbulent separation upstream of a forward-facing step. *Journal of Fluid Mechanics*, 724:284–304.

Phillips, N., Knowles, K., and Bomphrey, R. J. (2015). The effect of aspect ratio on the leading-edge vortex over an insect-like flapping wing. *Bioinspiration & biomimetics*, 10(5):056020.

Pope, S. B. (2000). *Turbulent flows*. Cambridge university press.

Raine, J. and Stevenson, D. (1977). Wind protection by model fences in a simulated atmospheric boundary layer. *Journal of Wind Engineering and Industrial Aerodynamics*, 2(2):159–180.

Raju, K., Loeser, J., and Plate, E. (1976). Velocity profiles and fence drag for a turbulent boundary layer along smooth and rough flat plates. *Journal of Fluid Mechanics*, 76(02):383–399.

Ramaprian, B. and Shivaprasad, B. (1978). The structure of turbulent boundary layers along mildly curved surfaces. *Journal of Fluid Mechanics*, 85(02):273–303.

Roos, F. W. and Kegelman, J. T. (1986). Control of coherent structures in reattaching laminar and turbulent shear layers. *AIAA journal*, 24(12):1956–1963.

Saathoff, P. and Melbourne, W. (1997). Effects of free-stream turbulence on surface pressure fluctuations in a separation bubble. *Journal of Fluid Mechanics*, 337:1–24.

Schanz, Danieland Gesemann, S. and Schröder, A. (2016). Shake-the-box: Lagrangian particle tracking at high particle image densities. *Experiments in Fluids*, 57(5):70.

Schneiders, J. F. G., Pröbsting, S., Dwight, R. P., van Oudheusden, B. W., and Scarano, F. (2016). Pressure estimation from single-snapshot tomographic piv in a turbulent boundary layer. *Experiments in Fluids*, 57(4):53.

Schneiders, J. F. G. and Scarano, F. (2016). Dense velocity reconstruction from tomographic ptv with material derivatives. *Experiments in Fluids*, 57(9):139.

Schröder, A., Schanz, D., Michaelis, D., Cierpka, C., Scharnowski, S., and Kahler, C. (2015). Advances of piv and 4d-ptv 'shake-the-box' for turbulent flow analysis -the flow over periodic hills. *Flow, Turbulence and Combustion*, 95(2-3):193–209.

Sciacchitano, A. and Wieneke, B. (2016). Piv uncertainty propagation. *Measurement Science and Technology*, 27(8):084006.

Sherry, M., Lo Jacono, D., and Sheridan, J. (2010). An experimental investigation of the recirculation zone formed downstream of a forward facing step. *Journal of Wind Engineering and Industrial Aerodynamics*, 98(12):888–894.

Shi, L., Liu, Y., and Wan, J. (2010). Tr-piv measurement of separated and reattaching turbulent flow over a surface-mounted square cylinder. *Journal of Mechanical Science and Technology*, 24(1):421–428.

Sigurdson, L. (1995). The structure and control of a turbulent reattaching flow. *Journal of Fluid Mechanics*, 298:139–165.

Sirovich, L. (1987). Turbulence and the dynamics of coherent structures. part i: Coherent structures. *Quarterly of applied mathematics*, 45(3):561–571.

Smits, A. J. and Lim, T. (2000). *Flow Visualization, Techniques and Examples*.

Spazzini, P. G., Iuso, G., Onorato, M., Zurlo, N., and Di Cicca, G. M. (2001). Unsteady behavior of back-facing step flow. *Experiments in fluids*, 30(5):551–561.

Sundquist, A. (2003). Dynamic line integral convolution for visualizing streamline evolution. *IEEE Transactions on Visualization and Computer Graphics*, 9(3):273–282.

Sychev, V., Ruban, A., VicVSychev, and GL, K. (1998). *Asymptotic Theory of Separated Flows*. Cambridge University Press.

Taylor, G. I. (1938). The spectrum of turbulence. In *Proceedings of the Royal Society of London A: Mathematical, Physical and Engineering Sciences*, volume 164, pages 476–490. The Royal Society.

Troutt, T., Scheelke, B., and Norman, T. (1984). Organized structures in a reattaching separated flow field. *Journal of Fluid Mechanics*, 143:413–427.

van Eimern, J. (1964). *Windbreaks and shelterbelts*. Secretariat of the World Meteorological Organization.

van Oudheusden, B. (2013). Piv-based pressure measurement. *Measurement Science and Technology*, 24(3):032001.

van Oudheusden, B. and al (2007). Evaluation of integral forces and pressure fields from planar velocimetry data for incompressible and compressible flows. *Journal of Experiments in Fluids*, 43:153–162.

Violato, D., Moore, P., and Scarano, F. (2010). Lagrangian and eulerian pressure field evaluation of rod-airfoil flow from time-resolved tomographic piv. *Experiments in Fluids*.

Winant, C. and Browand, F. (1974). Vortex pairing: the mechanism of turbulent mixing-layer growth at moderate reynolds number. *Journal of Fluid Mechanics*, 63(02):237–255.